

Scaling issues in glaciology: addressing subgrid topography

by

©Kevin Le Morzadec

A Thesis submitted to the School of Graduate Studies in partial fulfillment of the requirements for the degree of

Doctor of Philosophy

Department of Physics and Physical Oceanography

Memorial University of Newfoundland

October 2016

St. John's

Newfoundland

Abstract

Ice sheets are a key component of the earth system and disturbances of their state affects various aspects of human activity (e.g. due to sea level rise). Glaciological studies take advantage of paleo-data to improve our knowledge about ice sheet processes. To investigate ice sheet evolution over the timescale of a glacial cycle, 3-D ice sheet models (ISM) are typically run at grid resolutions of five to tens of kilometres. This introduces to-date unquantified errors in sub-grid (SG) ice transport and surface mass balance (SMB, the difference between ice surface accumulation and ablation). Here, I document the impact of ISM resolution on SMB and ice flux in regions of rough topography and develop parametrizations to reduce the associated ISM grid resolution dependency.

For inland regions, I develop a new flow line SG model which uses hypsometric curves, a statistical summary of the topography, to describe the variability of SMB. The 1-D mass transport for the SG model is computed with the shallow ice approximation. I test this model against high resolution simulations from the 3-D ISSM model over regions of 30 km by 60 km. Using SG topographic information improves the SMB and flux representation, however, depending on the regional topographic characteristics, the new SG model simulates ice volumes 45 % lower to 15 % higher than simulated by the ISSM. An ensemble of last glacial cycle simulations for the North American ice complex shows increases of up to 35m eustatic sea level equivalent in ice volume with inclusion of the SG model.

For coastal regions, glacial valley geometry and density impact ice drainage. Decreasing the model resolution from 1 km to 5, 10 and 25 km overestimates the ice drainage and creates some lags in the timing of ice growth and decay. Modifying ice flow parameters reduces the excess of drainage on the order of 20 % at 5 and 10 km resolution and by 5 % at 25 km resolution. Simulations at 25 km resolution still have a lag of one to three thousand years in growing ice after an interstadial period.

Acknowledgements

A huge thanks to my supervisor, Lev Tarasov. Despite a rough start and a project that took a bit longer than we would have wished for, I have learned more than I expected. Thank you for your restless pursuit for precision and for always finding time in your busy schedule to improve my scientific/modelling knowledge, my communication skills, and my critical reflection.

Thanks to all the people that have passed through the glacial systems dynamics group while I was part of it: Tristan, Rob, Mark, Taimaz, Ryan, Benoit, and Heather, you have all made this project a little bit easier.

Thanks to the ISSM team, especially Mathieu Morlighem and Helene Seroussi, for helping me with one of the models I used. Without you this project would have taken much more time than it did.

I am thankful for all the friends that I have met along the way while constructing this project who worked hard on keeping me sane; particularly Justin and Arnault, who shared my passion for outdoor activities, whatever the conditions. To Celine, Raoul, AJ, Arnault (you again!), and all the others for the numerous discussions, dinners, and parties we shared.

Thanks to all my friends from previous life experiences. Thank you to my lifelong friends Mael, Brieg and the ones I met during my first encounter with the world of science; with whom I shared a lot of experiences in the mountains, downtown or just growing up.

To Stacey, thanks for being close to me over the last few years, for believing in me, supporting me no matter what, and never (rarely?) complaining about my lack of free time. Thanks to your family as well and to Dracula for his warmth during this time.

Finally, thanks to my parents and my sister for being amazing, always supporting my decisions, and helping me to get through them no matter what.

Table of Contents

Abstract	ii
Acknowledgments	iii
Table of Contents	vii
List of Tables	x
List of Figures	xxi
1 Introduction	1
1.1 Motivation and overview	1
1.2 Subgrid processes relevant to the evolution of an ice sheet	5
1.2.1 Ice Dynamic	5
1.2.2 Sliding laws	8
1.2.3 Grounding line	9
1.2.4 Calving and ocean-melt	9
1.2.5 Surface Mass Balance	10
1.2.6 Fjords and outlet glacier	11
1.2.7 Subgrid processes analyzed in this work	14
1.3 Parameterization Methods	14
1.4 Objectives	16
1.5 Thesis structure	17
1.6 Co-authorship statement	17
2 Subgrid fjords in ice sheet models	19
2.1 Introduction	19
2.2 Model description	23
2.2.1 PSU/GSM model	23
2.2.2 Ice Sheet System Model (ISSM)	26
2.2.3 Boundary conditions	26
2.3 Experimental design	28
2.3.1 Fjord geometry impact	31
2.3.2 Model sensitivities: resolution, order of ice dynamics approximation, and sliding law exponent	31

2.3.3	Model resolution dependency minimization	31
2.4	Results	32
2.4.1	Fjord geometry impact	32
2.4.2	Model sensitivities: resolution, order of ice dynamics approxi- mation, and sliding law exponent	36
2.4.2.1	Model resolution dependency	36
2.4.2.2	Higher order ice dynamical physics	40
2.4.2.3	Sliding law exponent impact	44
2.4.3	Model resolution dependency minimization	45
2.4.3.1	Hard bed parameters	45
2.4.3.2	Soft bed sliding parameter and basal topography up- scaling methods	47
2.5	Conclusion	55
2.6	Author contribution	57
2.7	Acknowledgements	57
	Appendix A Thermodynamic impact	57
3	A new sub-grid surface mass balance and flux model for continental- scale ice-sheet modelling: validation and last glacial cycle	60
3.1	Abstract	60
3.2	Introduction	61
3.3	Model description	63
3.3.1	Sub-grid model	63
3.3.1.1	Hypsometric curves	63
3.3.1.2	Surface mass balance	65
3.3.1.3	Ice thickness evolution	66
3.3.1.4	Model limitations	67
3.3.2	GSM	68
3.3.3	GSM and sub-grid model coupling	69
3.3.3.1	Interaction between the sub-grid model and the GSM	70
3.3.3.2	Sub-grid model activation/deactivation	71
3.3.4	Ice Sheet System Model (ISSM)	72
3.4	Sub-grid model performance and tests	72
3.4.1	Comparison with ISSM	73
3.4.1.1	Inclined plane test	73
3.4.1.2	Rocky Mountains test	73
3.4.2	Test of alternative parameterizations	74
3.5	Behaviour of the sub-grid model in the Glacial Systems Model (GSM)	78
3.5.1	Last glacial cycle simulations over North America	79
3.5.2	Sensitivity of the model to different flux and coupling parameters	81
3.6	Conclusions	84
4	Conclusion	89

4.1	Summary	89
4.2	Future work	91
A	Supplementary material for: Subgrid fjords in ice sheet models	94
A.1	Forcings	94
A.1.1	Basal topography	94
A.1.1.1	Realistic fjord	94
A.1.1.2	Synthetic fjords	96
A.1.1.3	Reasoning for the selection of the synthetic fjords	99
A.1.1.4	Example of one real and one synthetic fjord at different resolutions	107
A.1.2	Present day and LGM temperature and precipitation	110
A.1.2.1	Interpolation definition	110
A.1.2.2	PD and LGM temperature and precipitation fields	110
A.1.3	Climate parameters	112
A.1.4	Upstream boundary forcing	113
A.1.4.1	Geothermal heat flux during inception	115
A.2	PSU/GSM parameter vector	116
A.2.1	Impact of the flow enhancement coefficient for shelf flow (fnshelf)	116
A.2.2	Impact of the calving and sub-shelf melt parameters	116
A.2.3	Example of the impact of the flow enhancement coefficient for shelf flow, calving and sub-shelf melt parameters	117
A.3	Experimental design	117
A.3.0.1	Soft bed parameters	117
A.4	Results	120
A.4.1	Fjord geometry impact	120
A.4.1.1	Ice volume evolution	121
A.4.1.2	Statistics	123
A.4.2	Model sensitivities: resolution and order of ice dynamics approximation	129
A.4.2.1	Model resolution dependency	129
A.4.2.2	Higher order ice dynamic physics	135
A.4.3	Resolution dependency minimization	137
A.4.3.1	Hard bed parameters	137
A.4.3.2	Soft bed parameters and basal topography upscaling methods	141
A.4.4	Thermodynamic off on	144
B	Supplementary material for: A new sub-grid surface mass balance and flux model for continental-scale ice-sheet modelling: validation and last glacial cycle	146
B.1	Surface mass balance module	146
B.2	Results for the stepwise regression fit	149

B.3	Surface elevation and velocities on an inclined plane when different numbers of hypsometric bins are used (Fig.B.1)	151
B.4	Percentage of hypsometric bins jumps (Fig.B.2)	151
B.5	Sensitivity to number of hypsometric bins at steady state for six different regions in the Canadian Rockies (Fig.B.3)	152
B.6	Ice evolution on an inclined plane for different forcings (Fig.B.4)	153
B.7	Sensitivity to different subgrid (SG) model parameterizations (Fig.B.5)	154
B.8	Results for a simulation where more ice is generated when the SG model is activated (Fig.B.6)	156
B.9	Maximum positive and negative differences (Fig.B.7)	156
B.10	Ice volume redistribution on coarse grid (Fig.B.8)	157

Bibliography **158**

Acronyms

CFL	Courant-Friedrichs-Lewy.
CG	Coarse Grid.
DEM	digital elevation model.
e.s.l.	Eustatic Sea Level.
EISMINT	European Ice Sheet Modelling Initiative.
ELA	Equilibrium Line Altitude.
GCM	General Circulation Model.
GEBCO	General Bathymetric Chart of the Oceans.
GRIP	Greenland Ice-core Project.
GSM	Glacial Systems Model.
HO	Higher Order.
hs	surface elevation.
ISM	Ice Sheet Model.
ISSM	Ice Sheet System Model.
LGM	Last Glacial Maximum.
MC	maximum conservation.
PDD	Positive Degree Day.
PMIP	Paleoclimate Modelling Intercomparison Project.
RMSE	Root Mean Square Error.
RSL	Relative Sea Level.
SC	Surface Conservation.
SG	subgrid.
SIA	Shallow Ice Approximation.
SLR	Sea Level Rise.
SMB	Surface Mass Balance.
SSA	Shallow Shelf Approximation.
VC	Volume Conservation.

List of Tables

2.1	Ice Sheet System Model (ISSM) and PSU/GSM capabilities showing the differences between each model.	23
2.2	Lists of the baseline parameter vector. Values are rounded to 2 decimal places.	25
2.3	Experiment design summary.	30
2.4	Surface elevation Root Mean Square Error (RMSE) at 5, 10, and 25 km resolution compared to the 1 km resolution simulations using the linear sliding law. The data are averaged over all the synthetic fjords and over the whole time series (TS), over the first stadial (SD) and over the first interstadial (ISD). The surface elevation RMSE percentage is given compared to the average ice thickness at 1 km resolution.	36
2.5	Optimal hard bed sliding coefficient.	46
2.6	Sum over time of the total ice volume difference and surface elevation RMSE between the base run and the optimal Fnslid/Fnflow parameters. Linear sliding law.	46
2.7	Optimal soft bed sliding coefficient.	48
2.8	Ice volume difference and surface elevation RMSE between the base run and the optimal Fnsed/Fnslid/Fnflow parameters. Linear sliding law.	49
3.1	Differences between our new SG model and Marshall and Clarke (1999)/Marshall et al. (2011) models.	64
A.2	Total ice volume difference between the base run and different fnshelf parameters showing a impact of less than 1 % (on average) of differences between simulations using the parameters tested (listed in table A.1) and simulation using the baseline parameter vector.	116
A.3	Total ice volume difference between the base run and different calving and sub-shelf melt parameters showing a impact of less than 1 % (on average) of differences between simulations using the parameters tested (listed in table A.1) and simulation using the baseline parameter vector.	116
A.1	Lists of the baseline parameter vector. Values are rounded to 2 decimal places.	118

A.4	Lists of soft bed parameter tested when using a linear or a quadratic sliding law.	119
A.5	Total ice volume evolution differences between regions with different characteristics and a region with a 5 km wide and 100 km long strait fjord (reference fjord) using a linear sliding law. Fjords with a wider area or with multiple fjords drain more ice than fjords with narrower fjords or increase resistive stresses (compared to the reference fjord).	125
A.6	Total ice volume evolution differences between regions with different characteristics and a region with a 5 km wide and 100 km long strait fjord (reference fjord) using a quadratic sliding law. Fjords with a wider area or with multiple fjords drain more ice than fjords with narrower fjords or increase resistive stresses (compared to the reference fjord).	126
A.7	Surface elevation RMSE differences between regions with different characteristics and a region with a 5 km wide and 100 km long strait fjord (reference fjord) using a linear sliding law. The errors are proportional to the differences is the fjords area and resistive stresses generated by the shape of the fjords compared to the reference fjord.	127
A.8	Surface elevation RMSE differences between regions with different characteristics and a region with a 5 km wide and 100 km long strait fjord (reference fjord) using a quadratic sliding law. The errors are proportional to the differences is the fjords area and resistive stresses generated by the shape of the fjords compared to the reference fjord.	128
A.9	Surface elevation RMSE at 5, 10 and 25 km resolution compared to the 1 km resolution simulations using the quadratic sliding law. The data are averaged over all the synthetic fjords and over the whole time series (TS), over the first stadial (SD) and over the first interstadial (ISD).	129
A.10	Improvement generated with the optimal Fnslid/Fnflow parameters in the representation of total ice volume and surface elevation RMSE compared to the simulation using the baseline parameter vector. Quadratic sliding law.	139
A.11	Total ice volume difference and surface elevation RMSE between the base run and the optimal Fnsed/Fnslid/Fnflow parameters. These results show the reduction of errors generated with the optimization of the parameter vector twice large for the total ice volume than for the surface elevation RMSE. Reductions in the total ice volume difference are on average around 50 % at 5 km resolution, 20 % at 10 km resolution and 25 % at 25 km resolution. Quadratic sliding law.	142
A.12	Total ice volume difference between simulation with the thermodynamic model turn OFF (with cold base or warm base) and ON.	144
B.1	Stepwise regression fit results	150

List of Figures

1.1	Diagram of the important processes taking place during the growth and retreat of an ice sheet. Courtesy of Frédéric Parrenin.	3
1.2	Present day topography showing the density of fjords in the west coast of Fennoscandia.	12
2.1	Basal topography of a fjord region at different resolutions.	21
2.2	Topography for three different synthetic fjord regions.	28
2.3	Different fjord characteristics impact compared to a 5 km wide and 100 km long fjord. The left panel shows the ice volume differences. The right panel shows the surface elevation RMSE. Red represents the average and standard deviation over 50 kyr, blue at the end of inception (111 to 107 ka) and green at the end of the first interstadial event (102 to 100 ka). These simulations use the baseline parameter vector and a linear (Lin) sliding law. The x axis represent the different fjords region listed in Section A.1.1.2 of the supplement. The boldface 5 km fjord, in the x axis, represents limit between regions generating less ice than the reference fjord and the region with more ice.	33
2.4	Range of ice evolution generated with different fjord characteristics. These simulations use the baseline parameter vector and a linear (Lin) sliding law.	35
2.5	Average and standard deviation (over 50 kyr) ice volume differences between simulation at: a. 5 km, b. 10 km and c. 25 km resolution and 1 km resolution simulations. Simulations use a sliding law. The boldface 5 km fjord, in the x axis, represents limit between regions generating less ice than the reference fjord and the region with more ice.	38
2.6	Resolution impact on the ice volume. Examples for a region with no fjords (a. S10), with one 5 km wide and 100 km long fjord (b. S4) and five 2 km wide fjords (c. S3). These simulations use the baseline parameter vector and linear (Lin) sliding law.	39
2.7	Ice velocity fields at 5 km resolution (left panel) and 25 km resolution (central panel) compared to a 1 km resolution simulation at different time slices. The panel on the right side shows the surface, base and velocity evolution in the 25 and 1 km resolution simulations. These simulations use the baseline parameter vector and linear (Lin) sliding law over the region with five 2 km wide fjords.	41

2.8	Ice volume evolution over some of the topographic regions presented on Fig.A.1. Different ice dynamics approximation are used in different models. Red lines are generated with the PSU/GSM model using the hybrid Shallow Ice Approximation (SIA)/Shallow Shelf Approximation (SSA) at high resolution (HR). Blue lines are generated with the ISSM model using the Higher Order (HO) approximation at HR. Green lines are generated with the ISSM model using the SIA approximation at CR.	43
2.9	ice volume for a region with two 5 km wide and 100 km long fjords (left panel) and a 5 km wide and 100 km long fjord with 2 branches (right panel). Solid lines represent a simulation with a linear sliding law while dotted lines represent a simulation with a quadratic sliding law.	44
2.10	Surface elevation RMSE between simulations using a linear or quadratic sliding law for a region with two 5 km wide and 100 km long fjords (left panel) and a 5 km wide and 100 km long fjord with 2 branches (right panel).	45
2.11	ice volume evolution with the baseline parameter vector (left panel) and the optimal sets of slidhardC and flowC parameters (right panel). These simulations use the linear (Lin) sliding law. The different colours represent different resolutions.	46
2.12	Surface elevation RMSE (compared to the 1 km resolution simulation) when using the baseline parameter vector (dotted lines) and the optimal sets of slidhardC and flowC parameters (solid lines). The different colours represent different resolutions. These simulations use the linear (Lin) sliding law.	47
2.13	Metric (normalized ice volume differences plus normalized surface elevation RMSE compared to the 1 km resolution simulation using the base parameter vector) averaged over time and all the synthetic fjords. The left panel shows the impact of different topography interpolation methods (deepest fjord depth, <i>Deepest</i> , fjord depth average, <i>FjordAvg</i> , the average between the deepest depth in the fjord, <i>DeepGenMean</i> , the average between the fjord average and the box average, <i>FjordMeanGenMean</i> , and the box average, <i>Box</i>) when the 0.1 km/yr basal sliding coefficient is used. The right panels focus on the impact of parameters when the box average is used for the interpolation. These simulations use the linear (Lin) sliding law.	48
2.14	Ice volume differences (average and standard deviation over 50 kyr) between simulations at: a. 5 km, b. 10 km and c. 25 km resolution and 1 km resolution simulations. Simulations use the baseline (blue) or the optimized (red) parameters vector and the linear (Lin) sliding law. The boldface 5 km fjord, in the x axis, represents limit between regions generating less ice than the reference fjord and the region with more ice.	50

2.15	Surface elevation RMSE differences (average and standard deviation over 50 kyr) between simulations at: a. 5 km, b. 10 km and c. 25 km resolution and 1 km resolution simulation. Simulations use the baseline (blue) or the optimized (red) parameters vector and the linear (Lin) sliding law. The boldface 5 km fjord, in the x axis, represents limit between regions generating less ice than the reference fjord and the region with more ice.	51
2.16	Ice volume evolution in a region (S3) with five 2 km wide, 100 km long fjords using the baseline parameter vector (left panel) and the optimal set of parameters (right panel). These simulations use the linear (Lin) sliding law.	52
2.17	Ice volume evolution in a region (S1) with a 10 km wide, 100 km long fjord using the baseline parameter vector (left panel) and the optimal set of parameters (right panel). These simulations use the linear (Lin) sliding law.	52
2.18	Surface elevation RMSE evolution (compared to the 1 km resolution simulation) using the baseline (dotted lines) and the optimal (solid lines) parameter vector . These simulations use the linear (Lin) sliding law over a region (S1) with a 10 km wide, 100 km long fjord (left panel) and a region with five 2 km wide, 100 km long fjords (right panel).	53
2.19	Results from a simulation using optimized parameters. Ice velocity fields at 5 km resolution (left panel) and 25 km resolution (central panel) compared to a 1 km resolution simulation at different time slices. The panel on the right side shows the surface, base and velocity evolution in the 25 and 1 km resolution simulations. These simulations use the baseline parameter vector and linear (Lin) sliding law over the region with five 2 km wide fjords.	54
A.1	Ice evolution over region 7, from Fig.A.1, when the thermodynamic model is turned on (red line), off with warm base (blue line) and off with cold base (green line).	58
3.1	Schematic representation of the effective width of the 7th hypsometric bin for a region of 10 km by 10 km. Each square represents a high resolution (1 km) grid cell. The numbers define the hypsometric bin these SG grid cells belong to. The total length of all red lines (14 km) represents the effective width for the 7th bin.	66
3.2	Communication between the GSM and the SG model for one Coarse Grid (CG) cell.	70
3.3	SG model vs. ISSM differences over an idealized inclined plane terrain. Average ice thickness differences (SG model - ISSM) are presented for simulations using different temperatures, desertification effect factors and number of hypsometric bins.	74

3.4	Topography characteristics for six regions over the Canadian Rockies. (a) summarizes surface elevations, (b) the hypsometric curves, and (c) the mean slope for each hypsometric bin.	75
3.5	Ratio of the SG model over ISSM total ice volume for six different regions in the Rockies as a function of hypsometric bins. The simulations were run until steady state with a constant sea level temperature of 0 °C and a desertification effect factor of 0.5. The steady state ice thicknesses, velocities and slopes from the ISSM and the SG model (using 10 hypsometric bins) are presented in Fig. B3 in the Supplement.	76
3.6	Average ice thickness in metres for different topographic regions in the Rockies. Results are shown for the ISSM, the regression model (generated by the stepwise regression fit including only the standard deviation of the topography) and the SG model using 10 hypsometric bins.	77
3.7	Average ice thickness root mean square error (RMSE) between the ISSM and the SG model for different topographic regions. Simulations are run over 2 kyr using a constant precipitation rate of 1 m/yr and a sea level temperature forcing of 0 °C. Different SG parameterizations are presented. Para 1 is the standard deviation of the topography parameterization (Eq. 3.6) and Para 2 the lowest hypsometric slope parameterization (Eq. 3.7).	78
3.8	Surface elevation generated by the ISSM (solid blue line), the SG model with no flux term, using 5 and 10 hypsometric bins, (dotted lines) and the SG model including the flux term (solid thin red line). These simulations use a constant sea level temperature of 0 °C and a desertification effect factor of 0.5. Results are shown at steady state after 2 kyr for six different regions with different topographic characteristics.	79
3.9	Elevation comparisons when the SG model is turned on (blue) or off (red) at different time steps using the parameter vector nn9894. h_d 10 years is the CG surface elevation after 10 years. h_{dhyps} 10 years is the SG surface elevation. h_b is the basal elevation. (a) and (b) represent cases where the Equilibrium Line Altitude (ELA) is above and below the coarse grid surface elevation.	80
3.10	Ensemble mean (solid red line) and standard deviation (dotted blue line) eustatic sea level equivalent of the total ice volume differences when the SG model is turned on and off, for an ensemble run over the last glacial cycle.	81
3.11	Ice field during inception at 115 ka for a simulation using one of the parameter vectors that generates best fits to the calibration constraints (nn9894). (a) Ice thickness with SG turned on. (b) Ice thickness differences between simulations with the SG model turned on and off. Zero differences are presented in the same colour as the continent. . .	82

3.12	Ice field at 50 ka for a simulation using parameter nn9894. (a) Ice thickness with SG turned on. (b) Ice thickness differences between simulations with the SG model turned on and off.	83
3.13	Total ice volume evolution for a simulation using parameter vector nn9894. “flux on” and “flux off” both include the SG surface mass balance calculations but the latter has no SG ice fluxes. “NofluxOut” has SG on, but no SG ice flux between coarse grid cells. The “SG OFF” line is most of the time hidden under the “flux off” line.	84
3.14	Ice volume evolution for a simulation over North America (parameter vector nn9894) with the SG model turned on during inception. “our flux” represents the flux code used in our SG model and “Marshall flux” the flux code used in Marshall et al. (2011) experiment. “flux off” represents the simulation with no ice flux between SG bins and “NofluxOut” has no SG flux between coarse grid cells (but SG fluxes within each coarse grid cell are still enabled).	85
3.15	Total ice volume evolution for a simulation over North America during inception with the SG model turned on (SG on) using the parameter vector of run nn9927. Different methods of ice redistribution at the CG level are compared. VC is for ice volume conservation, SC for surface elevation conservation and maximum conservation (MC) uses the maximum of the previous two methods. “SG off” represents a run where the SG model has been turned off.	86
3.16	Total ice volume evolution for a simulation using parameter vector nn9894. Different curves represent simulations with different minimum altitude variation thresholds used for the SG activation.	87
A.1	Basal topography representing real fjord topography.	95
A.2	Different number of fjords.	96
A.3	Different fjord width.	96
A.4	Different number of bends.	96
A.5	Different fjord width at the mouth of the fjord.	97
A.6	Regions with no fjords and with an inclined fjord.	97
A.7	Different number of branches.	97
A.8	Different branches length.	98
A.9	Different fjord length.	98
A.10	Different depth profile.	98
A.11	Fjord id 6. Amplitude 12 km over 60 km.	99
A.12	Fjord id 7. Amplitude 15 km. 3 sinusoid over 60 km.	99
A.13	Fjord id 17,4, 18. Different fjords length. A.13(a) 50 km long fjord. A.16(c) 100 km long fjord. A.13(e) 150 km long fjord.	100

A.14	Different depth profiles applied to the synthetic fjord region 4 (a.). b. represent the depth profile used in all the synthetic fjord regions, except for region 20 where profile c. is applied (called "deep short") and region 19 where profile c. is applied (called "shallow").	101
A.15	Different depth variations along the fjord center for different regions.	102
A.16	Fjord id 5, 4, 1. Different fjords width. A.16(a) 2 km width. A.16(c) 5 km width. A.20(c) 10 km width.	103
A.17	Fjord id 8.1 km width at the mouth to 5 km upstream. Reduction done over 15 km.	104
A.18	Fjord id 9. 12 km width at the mouth to 5 km upstream. Reduction done over 60 km.	104
A.19	Fjord id 15,12,16,12,13. Branches are 2 km wide and 10 (A.19(b)), 20 (A.19(e)), and 30 (A.19(d)) km long. A.19(e),A.19(f), A.19(g) 20 km length branches.	105
A.20	Fjord id 1, 2, 3. Different number of fjords. A.20(c) one 10 km width fjord. A.20(d) two 5 km width fjord. A.20(e) five 2 km width fjord. .	106
A.21	Fjord id 11. 30 degrees angle	106
A.22	Fjord 7 basal topography at different resolutions.	107
A.23	Fjord 7 mask at different resolutions.	108
A.24	Basal topography for synthetic fjord 2 at different resolutions.	109
A.25	Present day temperature and precipitation fields at 25 km resolution.	110
A.26	Last glacial maximum temperature and precipitation fields at 25 km resolution.	111
A.27	Latitudinally constant present day temperature and precipitation fields at 25 km resolution.	111
A.28	Latitudinally constant last glacial maximum temperature and precipi- tation fields at 25 km resolution.	111
A.29	Climate forcing parameters.The parameters $Tdiff$, $Pfac$ are glacial indexes (see Section A.1.2.1) and $sealev$ represent the sea level evolution.	112
A.30	Climate forcing parameters starting during inception starting at start- ing at 116.6 ka. The parameters $Tdiff$, $Pfac$ are glacial indexes (see Section A.1.2.1) and $sealev$ represent the sea level evolution.	112
A.31	Upstream ice thickness (a.), temperature (b.) and velocity forcing (c.). $Uavg$ represents the vertically and latitudinally average velocity in the x direction (left to right on the topography maps). $Vavg$ represents the vertically and latitudinally average velocity in the y direction (bottom to top on the topography maps). $Ubase$ and $Vbase$ represent the latitudinally average velocities at the base of the ice.	113

A.32	Upstream ice thickness (a.), temperature (b.) and velocity forcing (c.) used in inception simulations. U_{avg} represents the vertically and latitudinally average velocity in the x direction (left to right on the topography maps). V_{avg} represents the vertically and latitudinally average velocity in the y direction (bottom to top on the topography maps). U_{base} and V_{base} represent the latitudinally average velocities at the base of the ice.	114
A.33	Near basal geothermal heat flux evolution. Positive values have an upward heat flux).	115
A.34	Total ice volume evolution over fjord region 7 for different fnshelf parameters (left panel) and for different calving and sub-shelf melt parameters (right panel) showing the limited impact of these parameters on the total ice volume evolution.	117
A.35	Fjord characteristics impact compared to a 5 km wide and 100 km long fjord showing a relation between the fjord area and resistive stresses to the ice drainage. The left panel shows the total ice volume differences. The right panel shows the surface elevation RMSE. Red represents the average and standard deviation over 50 kyr, blue at the end of inception (111 to 107 ka) and green at the end of the first interstadial event (102 to 100 ka). These simulations use the baseline parameter vector and a quadratic (Quad) sliding law. The x axis represent the different fjords region listed in Section A.1.1.2 of the supplement. The boldface 5 km fjord, in the x axis, represents limit between regions generating less ice than the reference fjord (on the left) and the region with more ice (on the right).	120
A.36	Range of ice evolution generated with different fjord characteristics. These simulations use the baseline parameter vector and a quadratic (Quad) sliding law.	121
A.37	Impact of fjord regions with a. different number of fjords with different width as shown in Fig.A.2 and b. one fjord of different width as shown in Fig.A.3 on the total ice volume evolution. These simulations use the baseline parameter vector and a linear (Lin) sliding law.	121
A.38	Impact of fjord regions with a. different fjord length as shown in Fig.A.9 and b. different width at the mouth of the fjord as shown in Fig.A.5 on the total ice volume evolution. These simulations use the baseline parameter vector and a linear (Lin) sliding law.	122
A.39	Impact of fjord regions with a. fjord direction as shown in Fig.A.6 and b. different number of bends in the fjord as shown in Fig.A.4 on the total ice volume evolution. These simulations use the baseline parameter vector and a linear (Lin) sliding law.	122

A.40	Impact of fjord regions with a. different number of branches as shown in Fig.A.7 and b. one branch of different length as shown in Fig.A.8 on the total ice volume evolution. These simulations use the baseline parameter vector and a linear (Lin) sliding law.	123
A.41	Impact of fjord regions with different depth profile as shown in Fig.A.14 on the total ice volume evolution. These simulations use the baseline parameter vector and a linear (Lin) sliding law.	123
A.42	Fjord characteristics impact for: a. a simulation at 5 km resolution, b. a simulation at 10 km resolution and c. a simulation at 25 km resolution compared to a 1 km simulation of a 5 km wide and 100 km long fjord. Red represents the average and standard deviation over 50 kyr, blue at the end of inception (111 to 107 ka) and green at the end of the first interstadial event (102 to 100 ka). These simulations use the baseline parameter vector and quadratic (Quad) sliding law.	130
A.43	Fjord characteristics impact on the surface elevation RMSE for: a. a simulation at 5 km resolution, b. a simulation at 10 km resolution and c. a simulation at 25 km resolution compared to a 1 km simulation of a 5 km wide and 100 km long fjord. Red represents the average and standard deviation over 50 kyr, blue at the end of inception (111 to 107 ka) and green at the end of the first interstadial event (102 to 100 ka). These simulations use the baseline parameter vector and linear (Lin) sliding law.	131
A.44	Fjord characteristics impact on the surface elevation RMSE for: a. a simulation at 5 km resolution, b. a simulation at 10 km resolution and c. a simulation at 25 km resolution compared to a 1 km simulation of a 5 km wide and 100 km long fjord. Red represents the average and standard deviation over 50 kyr, blue at the end of inception (111 to 107 ka) and green at the end of the first interstadial event (102 to 100 ka). These simulations use the baseline parameter vector and quadratic (Quad) sliding law.	132
A.45	Resolution impact on the total ice volume. Examples for a region with no fjords (a. S10), with one 5 km wide and 100 km long fjord (b. S4) and five 2 km wide fjords (c. S3). These simulations use the baseline parameter vector and quadratic (Quad) sliding law.	133
A.46	Ice velocity fields at 5 km resolution (left panel) and 25 km resolution (central panel) compared to a 1 km resolution simulation at different time slices. The panel on the right side shows the surface, base and velocity evolution in the 25 and 1 km resolution simulations. These simulations use the baseline parameter vector and quadratic (Quad) sliding law over the region with five 2 km wide fjords.	134

A.47	Ice thickness differences between ISSM simulations solving the HO model for ice flow and PSU/GSM simulations solving the hybrid SIA/SSA model at the end of inception after a 5000 years. Results are shown for topographic regions 1, 7, 3, and 4 presented on Fig.A.1. The HO model generates more ice than the hybrid SIA/SSA model.	135
A.48	Vertically average velocity differences between ISSM simulations solving the HO model for ice flow and PSU/GSM simulations solving the hybrid SIA/SSA model at the end of inception after a 5000 years run. Results are shown for the topographic regions 1, 7, 3, and 4 presented on Fig.A.1. The HO model generates higher velocities than the hybrid SIA/SSA model in the fjords.	136
A.49	Impact the combination of different flow enhancement factor (flowC) and the hard bed sliding coefficient (slidhardC) on simulations run at, a. 5 km resolution, b. 10 km resolution, and c. 25 km resolution. A lower metric (defined in Section 2.4.3) represent a better fit to the 1 km resolution simulation. The red cross represent the lowest differences compared to the high resolution simulations. Sliding is represented as a linear flow law.	137
A.50	Impact the combination of different flow enhancement factor (flowC) and the hard bed sliding coefficient (slidhardC) on simulations run at, a. 5 km resolution, b. 10 km resolution, and c. 25 km resolution. A lower metric (defines in Section2.4.3) represent a better fit to the 1 km resolution simulation. The red cross represent the lowest differences compared to the high resolution simulations. Sliding is represented as a quadratic flow law.	138
A.51	Total ice volume evolution at different resolutions with: a. the baseline parameter vector and, b. the optimal sets of slidhardC and flowC parameters. These simulations use the quadratic (Quad) sliding law. The main difference compared to the 1km resolution simulation at the end of inception, between 112 and 98 ka, are reduced to a few percents with the optimum parameter set. The optimization did not reduce the differences in the 25 km resolution simulation after 102 ka.	139
A.52	Surface elevation RMSE (compared to the 1 km resolution simulation) when using the baseline parameter vector (dotted lines) and the optimal sets of slidhardC and flowC parameters (solid lines). The different colours represent different resolutions. These simulations use the quadratic (Quad) sliding law. The surface elevation RMSE are significantly improve only in the 25 km resolution simulation, however high errors remains.	140

A.53	Metric (normalized total ice volume differences plus normalized surface elevation RMSE compared to the 1 km resolution simulation using the base parameter vector) averaged over time and all the synthetic fjords. The left panel shows the impact of different topography interpolation methods (deepest fjord depth, <i>Deepest</i> , fjord depth average, <i>FjordAvg</i> , the average between the deepest depth in the fjord, <i>DeepGenMean</i> , the average between the fjord average and the box average, <i>FjordMeanGenMean</i> , and the box average, <i>Box</i>) when the 0.1 km/yr basal sliding coefficient is used. This shows that the <i>Box</i> average method generate the small errors in ther of total ice volume and surface elevation RMSE compared to the 1 km resolution simulation. The right panels focus on the impact of parameters when the box average is used for the interpolation. These simulations use the quadratic (Quad) sliding law. The optimum parameters presented in table 2.7 of the main paper are extracted from Fig.A.53(b)	141
A.54	Total ice volume evolution in a region (S3) with five 2 km wide, 100 km long fjords using: a. the baseline parameter vector and, b. the optimal set of parameters. These simulations use the quadratic (Quad) sliding law. Fig.A.54(b) shows a reduction in the differences in amplitude and timing of the total ice volume between coarse and high resolution simulations.	142
A.55	Total ice volume evolution in a region (S1) with a 10 km wide, 100 km long fjord using: a. the baseline parameter vector and, b. the optimal set of parameters. These simulations use the quadratic (Quad) sliding law. Fig.A.55(b) shows a reduction in the differences in amplitude and timing of the total ice volume between coarse and high resolution simulations.	143
A.56	Surface elevation RMSE evolution (compared to the 1 km resolution simulation) using the in a baseline (dotted lines) and the optimal (solid lines) parameter vector. These simulations use the quadratic (Quad) sliding law over: a. a region (S1) with a 10 km wide, 100 km long fjord and, b. a region with five 2 km wide, 100 km long fjords. Fig.A.56(b) shows a reduction in the differences in amplitude and timing of the total ice volume between coarse and high resolution simulations.	143
A.57	Impact of the thermodynamic component of the model at different resolution for fjord region 7.	145
B.1	Sensitivity to the number of hypsometric bins for an experiment using a sea level temperature set to 0 °C and the desertification factor to 0.5. a. shows the surface elevation and b. the velocity profiles after 2 kyr.	151

B.2	Average percentage of hypsometric bin jumps in the 21 regions analyzed when different numbers of hypsometric bins are used. "Hypsometric bin jumps" is used to represent some high resolution adjacent grid cells that belong to non-adjacent hypsometric bins.	151
B.3	Comparison of ice grid cell characteristics when different hypsometric bins are used in the SG model. Steady state results are shown (after 2 kyr simulation) for six different regions. a. displays the surface elevation, b. the ice thickness, c. the velocities and d. the slopes. The solid black line represents the bed topography using 30 hypsometric bins. The solid blue lines are for ISSM results. The other lines correspond to the SG model results using 5 (dashed green lines) and 10 (dashed-dotted red lines) hypsometric bins. The differences between the 10 and 30 bins runs are too small to be differentiated.	152
B.4	Surface elevation and velocities evolution over an inclined plane for the ISSM and the SG model. Simulations use a sea level temperature forcing of 0 °C and an elevation desertification factor of 0.5 in a and c , and 0 in b and d.	153
B.5	Comparison of ice grid cell characteristics when different parameterizations are used in the SG model. Result are shown at steady state after 2 kyrs of simulation for six different regions. a. displays the surface elevation, b. the ice thickness, c. the velocities and d. the slopes. The solid black line represents the bed topography using 30 hypsometric bins. The solid blue lines are from ISSM runs. The other lines correspond to the SG model results with no additional parameterization (dashed red lines), the parameterization of the velocities at every bin (Para 1, solid cyan lines) and the parameterization of the slope at the lowest bin (Para 2, dashed-dotted green lines). 10 hypsometric bins are used throughout.	155
B.6	Ice thickness comparison at 50 ka, using a parameter vector that gives an increase of ice thickness when the SG model is used. a. Ice thickness when SG is activated. b. Ice thickness difference between simulations with the SG model turned on and off.	156
B.7	Ice volume evolution using the ensemble parameter vectors that give the maximum positive (red) and negative (blue) differences between simulations with the SG model activated or not.	156
B.8	Total ice volume evolution for a simulation over North America with the SG model turned on (SG on) using the parameter vector of run rn9894. Different methods of ice redistribution at the CG level are compared. "VC" is for ice volume conservation, "SC" for surface elevation conservation and "MC" uses the maximum of the previous two methods. "SG off" represents a run where the SG model has been turned off.	157

Chapter 1

Introduction

1.1 Motivation and overview

Ice fields (ice sheets, ice shelves, ice caps and glaciers) are a key component of the earth system and changes in their state can impact society and ecosystems. The most obvious impact is that the water released by the melting of grounded ice is a key contributor to [Sea Level Rise \(SLR\)](#). The complete melting of the Antarctica and Greenland ice sheets could potentially contribute approximately 58 metres and 7 metres, respectively, to global sea levels ([Lemke et al., 2007](#); [Fretwell et al., 2013](#)). Recent projections of [SLR](#) for the end of century range between 0.26 and 1.2 m ([Church et al., 2013](#); [Horton et al., 2014](#)). The relative contribution of ice sheet mass loss to sea level rise has increased from 15% between 1993 and 2003 ([Lemke et al., 2007](#)), to about 40% since 2003 ([Cazenave and Llovel, 2010](#); [Schrama et al., 2014](#)). When considering that tens of millions of people live in regions already exposed to coastal flooding ([Neumann et al., 2015](#)), it is clear that sea level projections will have major socio-economical repercussions.

Changes in the cryospheric state also affect the rest of the climate system ([Alley, 1991](#); [Turner, 1997](#)). The influx of meltwater can alter ocean circulation with associated regional climate impacts ([Broecker and Denton, 1989](#); [Stouffer et al., 2006](#)). Ice sheet evolution also results in changes in the area of snow and ice, which directly affects surface albedo. Albedo changes alter temperatures ([Barnett et al., 1989](#)) and sometimes atmospheric stability ([Dewey, 1977](#)).

Ice sheet and glacier mass loss has other direct societal impacts beyond those of rising sea level. Glacial melt-water plays an important role in socio-economic activities

such as hydro-power production (Lambrecht and Mayer, 2009; Hirsch et al., 2014) and agricultural production (Parry et al., 2007; Chaulagain, 2015). Calving, the breaking off of ice at the terminus of an ice field, creates hazards for ship navigation, as in the region of LeConte glacier (Motyka et al., 1998). The increase of icebergs released is also a threat for fixed marine infrastructures (Barber et al., 2014). Additionally, the potential of iceberg rolling can result in local tsunamis (MacAyeal et al., 2011). These examples show how important it is to understand and predict ice sheet/glacier behaviour.

Analyzing the evolution of ice fields requires data collected in the field or by remote sensing (using aircraft or satellites) (Das et al., 2014) and numerical models (Tarasov and Peltier, 2007; Pollard and DeConto, 2009; Larour et al., 2012; Cornford et al., 2013). Ice sheet evolution is slow relative to the instrumental record length. The last glacial cycle lasted approximately 120 000 years. Therefore, the information extracted from instrumental data is of limited usefulness in our understanding of the physical phenomena involved. To improve our knowledge about ice sheet processes, glaciological studies take advantage of paleo-data such as relative sea level proxies, dated moraines, dated deglacial indicators, and information present in ice and marine sedimentary cores. In this study, I focus on numerical models as they have the advantage of creating complete spatial and temporal depictions of ice sheet evolution. Moreover, they can predict future evolution while field data can only describe past and present states. These complementary approaches are starting to be more frequently synthesized into calibration of numerical models against observational data sets (Tarasov et al., 2012; Stroeven, 2016).

Due to the complex processes at play and the range of time and spatial scales, glaciological system models, which are used to represent the evolution of ice sheets, are computationally expensive and highly non-trivial to construct. To model a full glacial cycle, a typical (shallow ice, shallow shelf approximation) ice sheet model simulation at 10 km resolution takes at least on the order of 16 days with 16 processor cores (assuming 50% efficient parallelization). The behaviour of, and interactions between, complex physical phenomena such as ice dynamics, basal sliding, thermodynamics, surface mass balance, isostatic rebound, basal hydrology, ice calving, ocean melt, grounding lines migration, geothermal heat flux and climate (Fig.1.1) must be accurately described. In addition, these processes involve a range of spatial scales on the order of one metre to hundreds of metres (e.g. basal hydrology and ice calving) to thousands of metres (an ice sheet can be several kilometres deep and over thousands of kilometres wide).

Temporal scales range from hourly (e.g. calving events) to millennial (e.g. glacial isostatic rebound). To work around the limited computational resources, current [Ice Sheet Model \(ISM\)](#) simulations are done either at high resolution (on the order of one hundred metres, locally, to a few kilometres) to predict the evolution of the current ice sheets over the next century or at coarse resolution of ten to tens of kilometres (e.g. [Pollard and DeConto, 2012](#); [Tarasov et al., 2012](#); [Colleoni et al., 2014](#)) to reproduce the past glacial cycles (on the order of one hundred thousand years).

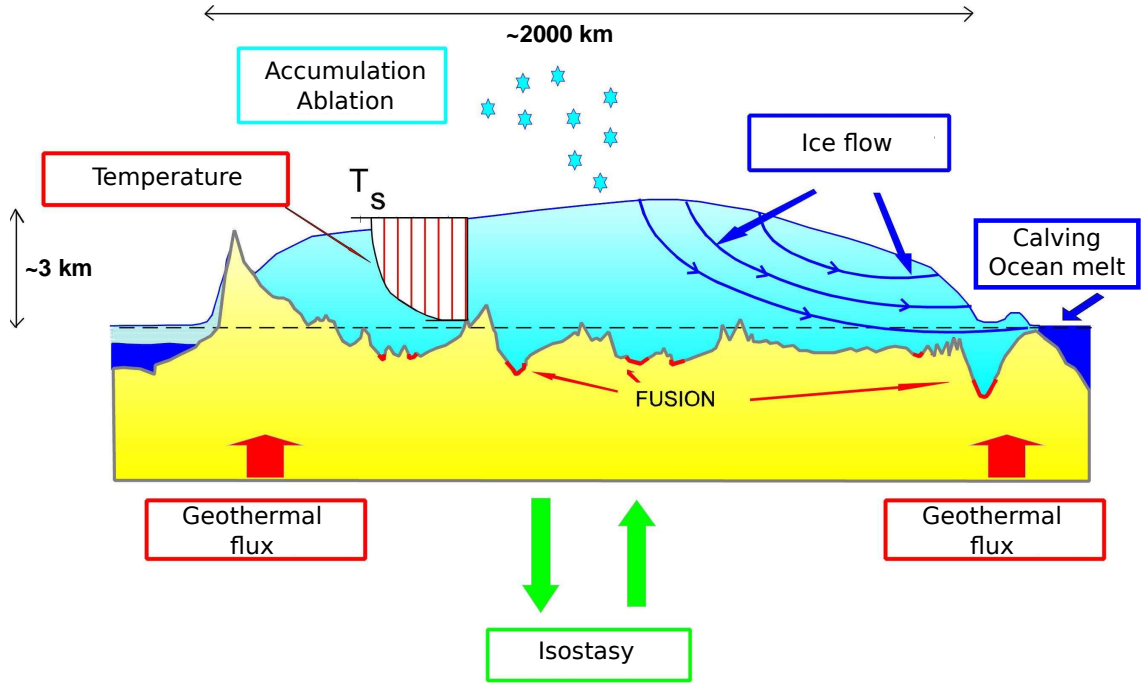


Figure 1.1: Diagram of the important processes taking place during the growth and retreat of an ice sheet. Courtesy of Frédéric Parrenin.

I focus on glacial cycle scale coarse-resolution simulations in this thesis for two reasons. First, the reconstruction of the last glacial cycle can help us improve our knowledge about processes involved in ice sheet evolution. Second, simulations run to present day can constrain the glacial isostatic adjustment signal (the response of the solid earth due to changes in surface load over glacial cycles) that contaminates estimates of ice sheets mass loss from both laser altimetry and/or gravimetric approaches (e.g. using Gravity Recovery and Climate Experiment - GRACE observations).

My study also, in part, addresses a broader context in that any model of complex environmental phenomenon will have [subgrid \(SG\)](#) processes requiring some form of

parametric representation. More broadly still, all numerical models have uncertainties that need to be quantified in order to interpret their predictions. These uncertainties can be categorized into structural and parametric errors. Structural errors come from processes not well represented due to a lack of knowledge, a necessity for approximation (i.e. to reduce the computational demand) or a coarser resolution than the process of interest scale. Parametric errors relate to incomplete sampling of the parameter space when calibrating model parameters against limited observational constraints (which have their own associated uncertainties). A model prediction has no value without an associated uncertainty estimate (though often this estimate is only implicit and therefore ambiguously communicated and interpreted). Increasingly, model-based studies are quantifying uncertainties related to parametric errors (e.g. [Hebeler et al., 2008](#); [Tarasov et al., 2012](#); [Applegate et al., 2012](#); [Pollard et al., 2015](#)). In this work, I focus on numerical ISMs structural uncertainties.

Any model of complex environmental systems has structural uncertainties generated by SG processes that are, by definition, not resolved by the discretized equations that computationally approximate the physical dynamics of the system. ISMs have long been known to have sensitivity to grid resolution (e.g. [Tarasov and Peltier, 1997b](#); [Rutt et al., 2009](#); [Durand et al., 2009b](#); [Horton et al., 2014](#)). Accurate modelling of such systems must determine if the SG processes' variability is relevant for the given context and needs to be parameterized. Variability of processes just below the resolved scale are the most likely sources of resolution dependent model error. For example, a fjord on the order of 5 km wide is not resolved in a 10 km resolution simulation but drains half of the ice in that grid cell and the geometric details of that fjord are likely important for the actual flow. On the other hand, one thousand 1 m scale bedrock bumps with a single coarse grid cell can easily be subsumed into a basal slide parameter.

In continental glacial system, the potentially most important SG processes are located at the boundary of the ice sheet where ice masses can change rapidly. These processes are surface mass balance in regions of rough topography, ice drainage through fjords or other outlets on the order of 1 km wide or less, grounding line migration, ice calving and basal hydrology.

In this thesis I document the impact of ISM's resolution on ice flux in fjords and surface mass balance. I also reduce the ISM's resolution dependency due to these SGs processes via compensatory parameterizations. Section 1.2 presents the different SGs processes important in ice sheet evolution and explains my choice to focus on fjords

and surface mass balance. The different downscaling methods used to parameterize SGs processes, and the specific ones used in this work, are presented in Section 1.3. Section 1.4 summarizes the objectives and scientific questions tackled. The thesis structure is given in Section 1.5.

1.2 Subgrid processes relevant to the evolution of an ice sheet

1.2.1 Ice Dynamic

The flow of ice is governed by the conservation of momentum which for this context takes the form of the Stokes equation. This equation is computationally expensive to solve. By a perturbative expansion in surface aspect ratio, some terms of the full equation can be neglected and much computationally cheaper simplified equations may be used, with accuracy dependent on relevant scales, stress regimes, and boundary conditions. The hierarchy of simplified equations most often used in ice sheet models is described below. For context, order of magnitude scales for ice sheets are:

$$\text{Horizontal } extent = 1000 \text{ km}$$

$$\text{Vertical } extent = 1 \text{ km}$$

$$\text{Horizontal } velocity = 10 \text{ m a}^{-1}$$

$$\text{Vertical } velocity = 0.1 \text{ m a}^{-1}$$

and therefore with an aspect scale of 1/1000.

Stokes Equation

The general momentum equation can be written as

$$\rho \frac{d\mathbf{u}}{dt} = \nabla \cdot (\boldsymbol{\tau}) + \mathbf{f} \quad (1.1)$$

\mathbf{u} ¹ is the velocity vector, $\boldsymbol{\tau}$ the internal stresses (surface stresses) and \mathbf{f} the external volume forces (gravity is the only non negligible external force). Here $\boldsymbol{\tau} = \boldsymbol{\tau}' + P\mathbf{I}$,

¹In this document, bold characters represent a vector.

where τ' is the deviatoric stress, P the pressure, and \mathbf{I} is the unit matrix. The ice constitutive equation relates the strain rate to the shear stress:

$$\tau' = 2\mu\dot{\epsilon} \quad (1.2)$$

Here $\dot{\epsilon}$ is the strain rate and μ the effective viscosity. The strain rate tensor is defined as

$$\dot{\epsilon}_{ij} = \frac{1}{2} (\partial_j u_i + \partial_i u_j) \quad (1.3)$$

where i and j are indexes corresponding to x , y and z .

The effective viscosity μ follows the generalized Glen's flow law:

$$\mu = \frac{B}{2\dot{\epsilon}_e^{1-\frac{1}{n}}} \quad (1.4)$$

where B is the ice rigidity, n is Glen's flow law exponent (typically set to 3), and $\dot{\epsilon}_e$ is the effective strain rate.

The acceleration component of the momentum equation is relatively negligible for ice sheets. As such, the substitution of the ice constitutive equation into the momentum equation 1.1 reduces to

$$\nabla \cdot (2\mu\dot{\epsilon}) + \nabla \cdot (P\mathbf{I}) + \mathbf{f} = 0 \quad (1.5)$$

This is the Stokes equation. In a Cartesian coordinate system this equation is written as

$$\frac{\partial}{\partial x} \left(2\mu \frac{\partial u}{\partial x} \right) + \frac{\partial}{\partial y} \left(\mu \frac{\partial u}{\partial y} + \mu \frac{\partial v}{\partial x} \right) + \frac{\partial}{\partial z} \left(\mu \frac{\partial u}{\partial z} + \mu \frac{\partial w}{\partial x} \right) - \frac{\partial P}{\partial x} = 0 \quad (1.6a)$$

$$\frac{\partial}{\partial x} \left(\mu \frac{\partial u}{\partial y} + \mu \frac{\partial v}{\partial x} \right) + \frac{\partial}{\partial y} \left(2\mu \frac{\partial v}{\partial y} \right) + \frac{\partial}{\partial z} \left(\mu \frac{\partial v}{\partial z} + \mu \frac{\partial w}{\partial y} \right) - \frac{\partial P}{\partial y} = 0 \quad (1.6b)$$

$$\frac{\partial}{\partial x} \left(\mu \frac{\partial u}{\partial z} + \mu \frac{\partial w}{\partial x} \right) + \frac{\partial}{\partial y} \left(\mu \frac{\partial v}{\partial z} + \mu \frac{\partial w}{\partial y} \right) + \frac{\partial}{\partial z} \left(2\mu \frac{\partial w}{\partial z} \right) - \frac{\partial P}{\partial z} - \rho g = 0 \quad (1.6c)$$

First Order Approximation (Blatter/Pattyn Model)

Over the entire ice sheet, the shear stresses τ_{xz} and τ_{yz} are small compared to the normal stress τ_{zz} (hydrostatic approximation). The blue term of equation 1.6c can then be neglected.

The spatial variation of the vertical velocities are significantly smaller than the spatial variation of the horizontal velocity. Therefore the green terms of equation 1.6a and 1.6b can also be neglected.

Using these two simplifications, the Stokes equation can be reduced to

$$\frac{\partial}{\partial x} \left(2\mu \frac{\partial u}{\partial x} \right) + \frac{\partial}{\partial y} \left(\mu \frac{\partial u}{\partial y} + \mu \frac{\partial v}{\partial x} \right) + \frac{\partial}{\partial z} \left(\mu \frac{\partial u}{\partial z} \right) - \frac{\partial P}{\partial x} = 0 \quad (1.7a)$$

$$\frac{\partial}{\partial x} \left(\mu \frac{\partial u}{\partial y} + \mu \frac{\partial v}{\partial x} \right) + \frac{\partial}{\partial y} \left(2\mu \frac{\partial v}{\partial y} \right) + \frac{\partial}{\partial z} \left(\mu \frac{\partial v}{\partial z} \right) - \frac{\partial P}{\partial y} = 0 \quad (1.7b)$$

$$\frac{\partial}{\partial z} \left(2\mu \frac{\partial w}{\partial z} \right) - \frac{\partial P}{\partial z} - \rho g = 0 \quad (1.7c)$$

These equations are used in high resolution models such as BISICLES or [Ice Sheet System Model \(ISSM\)](#) (the former is described in chapter 2 and 3). In this document the term high resolution is used for resolution of 1 km. The disadvantage of these models is the required computational expense. With ISSM, a 500 years simulation of the Greenland ice sheet using a resolution of the order of 5 km at the coast and around 30 km in the interior takes 40 hours with 240 processor cores ([Larour et al., 2012](#)).

Shallow Shelf Approximation (SSA)

In regions of low basal drag, i.e. ice shelves and ice streams, the ice slides over the base with little vertical shear above it. This plug like flow can be described in more simplified form by removal of the vertical shear terms (in red in equation 1.6a and 1.6b), resulting in the Shallow Shelf approximation ([MacAyeal, 1989](#)):

$$\frac{\partial}{\partial x} \left(2\mu \frac{\partial u}{\partial x} \right) + \frac{\partial}{\partial y} \left(\mu \frac{\partial u}{\partial y} + \mu \frac{\partial v}{\partial x} \right) - \frac{\partial P}{\partial x} = 0 \quad (1.8a)$$

$$\frac{\partial}{\partial x} \left(\mu \frac{\partial u}{\partial y} + \mu \frac{\partial v}{\partial x} \right) + \frac{\partial}{\partial y} \left(2\mu \frac{\partial v}{\partial y} \right) - \frac{\partial P}{\partial y} = 0 \quad (1.8b)$$

$$\frac{\partial}{\partial z} \left(2\mu \frac{\partial w}{\partial z} \right) - \frac{\partial P}{\partial z} - \rho g = 0 \quad (1.8c)$$

Shallow Ice Approximation (SIA)

For most of the ice sheet's interior (specifically away from the ice dome centre and the ice sheet boundary), the vertical shear stress gradient and the driving stress dominate.

Under the [SIA](#), the Stokes equation therefore simplifies to

$$\frac{\partial}{\partial z} \left(\mu \frac{\partial u}{\partial z} \right) - \frac{\partial P}{\partial x} = 0 \quad (1.9a)$$

$$\frac{\partial}{\partial z} \left(\mu \frac{\partial v}{\partial z} \right) - \frac{\partial P}{\partial y} = 0 \quad (1.9b)$$

$$-\frac{\partial P}{\partial z} - \rho g = 0 \quad (1.9c)$$

The [Glacial Systems Model \(GSM\)](#) (described in chapter 2), uses these equations. These models are computationally efficient, and can easily be run over full glacial cycles. However, they are inaccurate for ice shelves, grounding lines, and the non “shallow” conditions at ice sheet margins.

Hybrid Shallow Shelf/Shallow Ice Approximation

The [SIA](#) and the [SSA](#) are valid for complementary stress regimes of an ice sheet and can be combined in the same model (e.g. [Pollard and DeConto, 2009](#), PSU/GSM described in chapter 3). Regions with low basal stress are treated with the [SSA](#) and regions with high basal stress are subject to the [SIA](#).

1.2.2 Sliding laws

Due to inaccessibility, there is limited understanding of basal motion controls. At the base of ice sheet, ice moves relative to the solid earth following two different mechanisms. It either slides over the bed or the bed itself is deformed. A combination of these two processes can also occur. For sliding over hard bedrock, [Weertman \(1957\)](#) suggests that depending on the size of the bumps on the bedrock, below or above approximately 1 m, sliding occurs either by melting and refreezing respectively upstream and downstream of the bump or by enhanced creep around the bump. [Lliboutry \(1958\)](#) added a third possibility where ice separates from the bed due to cavitation. These idealized processes can be represented by different powers of the basal stress dependence on the basal velocity with exponents of 1 to 4 ([Cuffey and Paterson, 2010](#); [Fowler, 2010](#)). Physically, there is also a dependence on basal effective pressure but due to the frequent lack of a fully coupled accurate representation of basal hydrology, this dependence is usually ignored. Basal ice displacement can also occur due to deformation of the sediment at the base of the ice. Laboratory and field studies

suggest that sediment can be characterized as a Coulomb plastic material (Iverson et al., 1998; Cuffey and Paterson, 2010) in which basal motion only occurs upon attainment of a yield stress dependent on the effective pressure. The basal drag does not increase with increasing basal velocities above this threshold. The stress threshold depends on the characteristic of the subglacial till that is not easily accessible under current ice sheets. The effective pressure varies widely with the subglacial hydrology state that to date lacks an accurate representation.

1.2.3 Grounding line

The grounding line is the transition zone between grounded and floating ice. The grounding line retreats with the thinning of the ice at the marine boundary, reducing the basal stresses which can lead to an acceleration of the upstream outlet glacier or ice stream. Accurate representation of grounding-line dynamics is therefore required for confident modelling of the marine margins of grounded ice sheets and glaciers, especially given rising concerns about the stability of the West Antarctic Ice Sheet (Joughin et al., 2014).

Durand et al. (2009a) found that a resolution higher than one hundred metres is required for an accurate representation of grounding line migration. Continental ISM simulations using a fixed grid at resolutions on the order of kilometres can exhibit large errors in the grounding line representation (Vieli and Payne, 2005). To reduce these errors, Schoof (2007) developed a parameterization of the ice flux at the grounding line based on the ice thickness and longitudinal stresses. This method is however valid only for near-steady-state evolution (Pattyn et al., 2012). To work around resolution constraints that can not be met in continental ISMs, some simulations use moving grids or adaptive mesh refinement. Moving grids allow grid points to coincide exactly and follow the grounding line position (Hindmarsh and Le Meur, 2001; Vieli and Payne, 2005; Drouet et al., 2013). Adaptive mesh refinement increase the grid resolution as needed around the grounding line (Goldberg et al., 2009).

1.2.4 Calving and ocean-melt

Calving is responsible for approximately 45% of Antarctic mass loss (Rignot et al., 2013; Depoorter et al., 2013) and approximately 50% of Greenland total mass loss. Moreover, it likely played a critical role in the rapid disappearance of the Northern

hemispheric ice sheets at the end of the last ice age (Pollard, 1984).

Calving representation in models has progressed from nonphysical parameterizations (based on water depth, Brown et al., 1983; Pelto and Warren, 1991; Vieli et al., 2001; Van der Veen, 2002) to relations based on stresses and strain rates (Amundson and Truffer, 2010; Levermann et al., 2011; Bassis and Ma, 2015). Calving has also been represented as a stochastic process (Bassis, 2011).

Difficult physical access and complexity challenges the attainment of a universal calving law that can represent the different frequency and size of calving events at the grounding line and at the marine margins of ice shelves/ice tongues (Lazzara et al., 1999; Jacobs et al., 1986). A consequent amount of work is being done to improve our understanding of calving and its representation in ice sheet models (Levermann et al., 2011; Bassis, 2011; Albrecht et al., 2011; Winkelmann et al., 2011; Pollard and DeConto, 2012; Bassis and Ma, 2015).

Over the last decade, submarine melting has received a lot of attention as it has been shown to be as important as calving. Rignot et al. (2010) found submarine melt rates comparable to calving rate in four central West Greenland glaciers. In Antarctica, ocean-melt is responsible for at least 55% of the total ice loss (Rignot et al., 2013; Depoorter et al., 2013). At the terminus of tidewater glacier LeConte, Alaska, this amount is even higher (57%, Motyka et al., 2003). Bartholomaeus et al. (2013) also reported that at least half of ice lost at the terminus of an Alaskan glacier can be due to submarine melt. In Greenland, the ocean melt is responsible for 20% to 75% of frontal ice loss depending of the fjord considered. In addition, the ocean melt can significantly modify the geometry of a floating tongue (Straneo et al., 2011; O’Leary and Christoffersen, 2013) and modify the stresses responsible for calving. However, poor representation of the submarine basin circulation and temperature along with sparse observational constraints limits the accuracy of the results generated by these relations (Jenkins, 2011; Xu et al., 2012; Sciascia et al., 2013).

1.2.5 Surface Mass Balance

The mass balance of a glacier is the net mass change of ice during a period of time. Precipitation, sub-shelf accretion, refreezing and ice inflow are the processes increasing the ice mass; whereas, ice can be removed through surface melt, basal melt, calving, submarine melt, and ice flow into the neighbouring regions. Surface mass balance takes into account only the removal of ice through surface melting (ablation) and

accumulation through precipitation and refreezing. This is often computed using a positive degree day method (Tarasov and Peltier, 1999b) or an energy balance model (Hock, 2005). The degree day method is most frequently used to date as it has a much lower computational demand and requires only mean monthly temperatures and precipitation (the variation of hourly temperatures around the monthly mean are usually approximated by a normal distribution).

To reproduce the last glacial cycle, precipitation and temperature fields are required over the past millennia. Reconstruction/representation of past climate is the largest source of uncertainty in the context of glacial cycle ice sheet modelling. The representation can be performed by interpolating between present day and the last glacial maximum using a glacial index generated from data found in ice cores and/or biosphere indicators. Alternatively, temperature fields are extracted from simplified climate models coupled with the ice sheet model (Tarasov and Peltier, 1999a; Ganopolski and Calov, 2012). Precipitation field forcings can be similarly generated from present day rates and General Circulation Model (GCM) simulations, often with additional temperature or elevation dependencies (e.g. Budd and Smith, 1981).

In addition to the uncertainties in temperature and precipitation fields, running ISM simulations at coarse resolution introduce potentially significant but to date poorly quantified errors in the results generated. ISMs used in a continental scale glacial cycle context are typically ran at horizontal resolutions of about five to tens of kilometres (Pollard and DeConto, 2012; Tarasov et al., 2012; Colleoni et al., 2014). At such resolutions, mountain peaks such as the Rockies are smoothed at best to bumps in a plateau (Payne and Sugden, 1990). If the mean altitude is below the equilibrium line altitude, the ice ablation and rain to snow fraction of precipitation are over-estimated (e.g. Tarasov and Peltier, 1997a). In addition, the surface slopes are lower, reducing the ice flow into lower regions. The effect of topography shading or direct insolation is different in a plateau region than in a terrain with rough topography. Thus coarse resolution can lead to significant temporal and spatial errors in ice sheet inception as well as growth (Rind et al., 1989; Verbitsky and Oglesby, 1992; Marshall and Oglesby, 1994).

1.2.6 Fjords and outlet glacier

Fjords are deep topographic features defined by steep cliffs on their sides and soft sediment beds carved into the bedrock by outlet glaciers flowing into the ocean. Their

widths span hundreds of metres to ten kilometres and can reach up to two hundred kilometres inland. They have the same characteristics as rivers in term of meander, tributaries (or branches), and changes in width.

Fjords play an important role in the mass loss of ice sheets through ice discharge in the ocean (Luckman et al., 2006; Rignot and Mouginot, 2012; Csatho et al., 2014) and are a common feature along the coast of current and past ice sheets (Fig.1.2 shows an example along the west coast of Fennoscandia). The soft sediment at the base of a fjord combined with the sudden reduction of resistive stresses during calving events can enable ice velocities up to 25 km/yr (Rosenau et al., 2013) draining a substantial fraction of an ice sheet. For instance, Jakobshavn Isbrae, one of Greenland’s main outlet glacier, drains approximately 6.4% of the ice sheet (Rignot and Kanagaratnam, 2006).

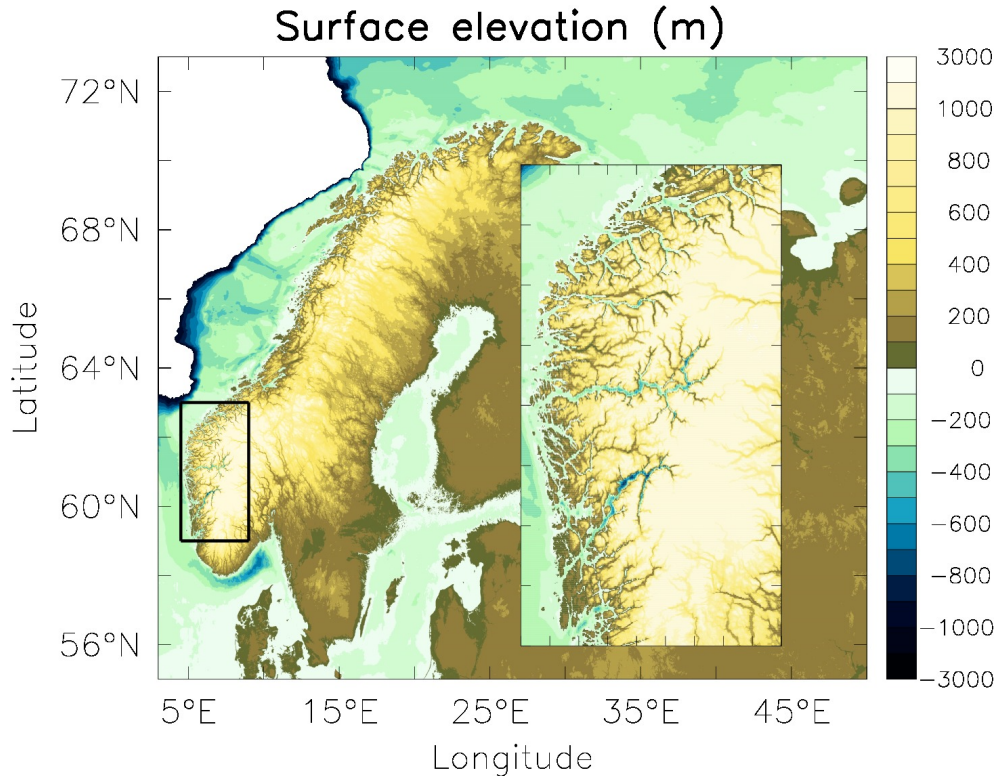


Figure 1.2: Present day topography showing the density of fjords in the west coast of Fennoscandia.

Many factors have been previously identified as influencing the ice dynamics in fjords. These factors can be glacier-specific (e.g. geometry, catchment area and the presence or absence of an ice tongue) or due to the climatic or oceanic characteristics

(e.g. air temperatures, ocean temperatures, fjord circulation and sea ice) (Weertman, 1974; Hughes, 1986; Meier and Post, 1987). Despite recent progress (Carr et al., 2013b,a), the importance of each factor on ice discharge is still unclear.

Identifying the impact of fjord geometry characteristics on ice dynamics in fjords will determine how much detail is needed about the topography underneath current ice sheets. Basal topography underneath Antarctica and Greenland are derived at 1 km resolution through interpolation of ground penetration radar data (Fretwell et al., 2013) and mass conservation algorithms (Bamber et al., 2013; Morlighem et al., 2014). However, the sparse availability of ice thickness in some regions limits the quality of these data with resultant uncertainties of the order of hundreds to a thousand metres. Durand et al. (2011) found that the vertical basal topography variation has to be resolved at a kilometre scale for the accurate representation of outlet glacier evolution. However the effect of the fjord geometry has, to date, not been quantified. What errors are introduced by a 10 km grid resolution representation of fjord areas? What is the magnitude of errors in ice flux near the margin of an ice sheet due to the use of such resolution? Are the number of fjords, the change in width, the number of bends, the presence of branches or the fjord orientation (compared to the ice flow) important characteristics to take into account?

In addition, with their large topographic differentials and their order one kilometre wide and tens of kilometres long scales, fjords can potentially have strong grid resolution sensitivity in current and foreseeable glacial cycle models that run at five to tens of kilometre resolution. Nowicki et al. (2013) suggests an influence of model resolution on the dynamics of narrow fast-flowing outlet glaciers drainage, however its impact has never been quantified.

It is even unclear how one should regrid a fjord when upscaling from a high resolution digital elevation model (DEM) to a coarser resolution ISM grid. In a coarse resolution grid (for example 10 km), a box average of the topography reduces the depth of valley and the heights of peaks. A subgrid fjord would then be made wider and shallower. A wider fjord representation could erroneously increase ice flux. However, the fjord (or valley) depth being reduced delays the occurrence of warm based conditions during a stadial period. To compensate for the under or overestimation of the ice flux, the depth of the fjord or the basal drag parameters could, for example, be adjusted. If the coarse representation of the fjord overestimates the ice flux, this error might be compensated on a continental scale by the lack of representation of smaller fjords.

1.2.7 Subgrid processes analyzed in this work

Over the past decade, significant improvements have been achieved in our understanding and representation of calving, the grounding line, and ocean melt, but there has been relatively little work addressing the other **SG** processes discussed above. Despite the potential importance of surface mass balance at **SG** scales, [Marshall and Clarke \(1999\)](#) is the only study, to date, that attempted to improve its representation in a continental ice sheet model by incorporating a **SG** model that accounted for **SG** topographic information. The impact and accuracy of this **SG** model has yet to be quantified. The model was only validated against observations of a glacier located in the region used for tuning the parameterization ([Marshall et al., 2011](#)). Moreover, the exchange of ice between the **SG** and **Coarse Grid (CG)** models was identified as a potentially important source of error ([Marshall and Clarke, 1999](#)), but its impact was not documented.

Drainage of ice through fjords occurs at a scale smaller than the resolution of most current continental models. However, no modelling study has to date explored the impact of fjord characteristics on ice drainage nor has there been examination of options for improving their representation in continental scale models.

Sliding is another **SG** process that lacks understanding concerning the impact of its representation with different laws in an **ISM**. It is to date unclear what sliding law is appropriate for ice sheet modelling. We examine the impact of linear versus quadratic basal velocity dependence on shear stress.

This work aims to improve our understanding of the impact of the surface mass balance, fjord ice dynamics and sliding **SG** processes. This information is then used to reduce the **ISM** scale dependency in a continental glacial cycle scale context.

1.3 Parameterization Methods

Representation of subgrid processes is a general challenge in the modelling of complex environmental systems. Parameterizations are used to model physical processes not well understood and/or not resolved within the scale of the model. In meteorology, for example, clouds, orographic drag, and turbulence in the atmosphere are processes that must be parameterized. This challenge of accounting for or inferring subgrid behaviour is also faced by downscaling. Downscaling is a method which derives information at a local scale from variables generated at a coarser scale. There are two main approaches

(as described in [Xu, 1999](#)). Dynamical downscaling resolves the [SG](#) process while statistical downscaling parameterizes the [SG](#) process.

- In dynamical downscaling, output from a coarse resolution model is used to drive a higher resolution model. The result of these models are more accurate than statistical downscaling but are computationally expensive.
- Statistical downscaling, typically less computationally demanding than dynamical downscaling, has been presented by [Wilby and Wigley \(1997\)](#) in three categories: regression methods, pattern based approaches, and stochastic approaches. Regression methods establish a linear or nonlinear relations between subgrid scale parameters and the large scale variable. Pattern based approaches use subgrid information to classify the different variable behaviour and then use the coarse information to identify each class. Stochastic approaches introduce stochastic noise conditioned on large scale variables to represent the subgrid spatial and temporal variability of the subgrid process and/or fields (e.g. to represent the transport by turbulent eddies not resolved in an ocean GCM).

As fjord are features present at the margin of the ice sheet, the resolutions issues could be overcome using dynamical downscaling via adaptive mesh refinement (e.g. BISICLES, [Cornford et al., 2013](#)) . This approach is however too computationally expensive to run simulations on a continental scale over a glacial cycle. The complexity of ice discharge through fjords combined with the coarse resolution of [ISMs](#) requires the use of a statistical downscaling method.

[SG](#) information has been used in the literature in different ways to represent physical processes occurring at a smaller scale than the model resolves. The [SG](#) processes to parameterize in this thesis are all dependent on the topography. Using the Fourier transformation of the bed elevation and slopes, [Li et al. \(2010\)](#) derive two parameters to represent the roughness of the topography, at the base of an ice sheet, in a coarse grid cell. [Nijzink and Savenije \(2016\)](#) used [SG](#) information to categorize each grid cell into a set number of landscape classes that impact the coarse grid cell in different ways. That method could potentially be used to represent calving. Another example uses a non-Gaussian (i.e. with skewness and kurtosis) probability density function distribution to represent the topographic distribution in a grid cell used to compute the fraction of the coarse grid cell covered with snow ([Waland, 1996](#)). [Marshall and Clarke \(1999\)](#) used the same approach representing the topography with a subgrid

hypsothetic curve (a statistical summary of the topographic distribution in a given coarse grid cell), to improve surface mass balance and flux in a continental scale ice sheet model. Finally, Calov et al. (2015) proposed a SG ice discharge parameterization that increases ice discharge proportionally to the ice thickness and the distance to the closest ocean boundary. Using SG topographic information could improve that last approach to take into account the presence or not of fjords.

Parameterization schemes are developed by first identifying the important SG variable(s) that impact the process and then extracting or positing a relation between the high resolution variable(s) and the coarse resolution process. Ice drainage is affected by the presence or lack of fjords and their geometry. To improve the representation of ice flow, I use SG information about the fjord characteristics to modify the ice discharge via different sliding and flow parameters. Surface mass balance is influenced by ice flux and the topography elevation and slope. I use elevation and slope information from a hypsothetic curve and a parameterization of the ice flow to improve the representation of ice accumulation, melt, and flow within a coarse resolution grid cell.

1.4 Objectives

In this project, I focus on errors generated by the ice dynamic and sliding representation and resolution errors due to the surface mass balance in regions of rough topography and ice drainage in fjord regions with different geometries.

I address the following questions:

- What is the impact of fjord geometry on ice discharge?
- What is the impact of higher order ice dynamics physics on fjord discharge?
- What is the impact of basal sliding representation on ice discharge?
- What is the resolution dependence of modelled fjord ice discharge?

Based on the (albeit incomplete) answers to the above, I build a subgrid parameterization to improve the representation of ice drainage in fjords and a new subgrid surface mass balance and flux model for purely terrestrial regions of rough topography (mountain ranges).

1.5 Thesis structure

This thesis is written in manuscript format, as opposed to a traditional thesis format. Hence, a more focused literature review is done in the introduction of each chapter.

Chapter 2, in preparation for publication, compares the sensitivity of **ISM** results to grid-resolution and ice flow approximation for topographically rough marine boundary contexts (i.e. fjords). A parameterization is developed to minimize the model scale dependency. The performance of this parameterization is tested over an independent set of different fjord regions.

Chapter 3, published in Geoscientific Model Development, describes the subgrid model developed for mountainous region and quantifies the impact of subgrid mass-balance and ice fluxes on glacial cycle ensemble results for North America. No easy solutions to accurately capture these impacts are found. Furthermore, **SG** process representation and associated parametric uncertainties are shown to have significant impacts on coarse resolution model results for last glacial cycle simulations of the North American ice complex.

An overall summary of the body of work and future steps are presented in Chapter 4.

1.6 Co-authorship statement

Dr. Lev Tarasov developed the initial idea and direction of the project. Dr. Lev Tarasov is an associate professor with the Department of Physics and Physical Oceanography at Memorial University and holds a Canada Research Chair.

The core of the GSM model was provided by Dr. Lev Tarasov. The PSU/GSM model was initially provided by Dr. Dave Pollard from Penn State University and modified by Dr. Lev Tarasov and Dr. Robert Briggs during his time at Memorial University. The ISSM model was provided by Dr. Mathieu Morlighem, an assistant professor at the Earth System Science Department at the University of California, and Dr. Helene Seroussi, NASA Postdoctoral Fellow from the Jet Propulsion Laboratory at the California Institute of Technology.

Authorship for the research paper presented in Chapter 2 is in the following order: Kevin Le Morzadec (thesis author), Dr. Lev Tarasov (thesis supervisor). Dr. Tarasov developed the initial idea and direction of the project. The development of the

parameterization and analysis was performed by Mr. Le Morzadec. The manuscript was prepared by Mr. Le Morzadec and critically reviewed/edited by Dr. Tarasov.

Authorship for the research paper presented in Chapter 3 is in the following order: Kevin Le Morzadec (thesis author), Dr. Lev Tarasov (thesis supervisor), Dr. Mathieu Morlighem and Dr. Helene Seroussi. Mr. Le Morzadec, designed the experiments with assistance from Dr. Tarasov. Kevin Le Morzadec developed the [SG](#) model code and performed the simulations. Kevin Le Morzadec and Lev Tarasov coupled the [SG](#) model into the [GSM](#). Mathieu Morlighem and Helene Seroussi supported [ISSM](#) installation and helped build a new surface mass balance module for the [ISSM](#). Kevin Le Morzadec prepared the manuscript with contributions from Lev Tarasov and the other co-authors. Lev Tarasov heavily edited the manuscript.

The thesis as a whole was critically reviewed Dr. Tarasov.

Chapter 2

Subgrid fjords in ice sheet models

2.1 Introduction

Marine-terminating glaciers flowing through glacial valleys play a crucial role in the mass loss of ice sheets (Luckman et al., 2006; Rignot and Mouginot, 2012; Csatho et al., 2014). Since 1996, a half to a third of the mass loss in Greenland has been through ice discharge (Van Den Broeke et al., 2009; Enderlin et al., 2014). Jakobshavn Isbrae itself, one of Greenland’s main outlet glaciers, drains approximately 6.4% of the Greenland ice sheet (Rignot and Kanagaratnam, 2006). However, uncertainties remain over the impact of glacial valleys topographic characteristics to ice drainage. Here we focus on fjords, deep and long submerged glacial valleys, which drain ice into the ocean and are densely populated at the marine margin of ice-sheets (see Morlighem et al. (2014) for an example around Greenland).

Many processes have been previously identified as influencing the time evolution of ice flow through fjords (Weertman, 1974; Hughes, 1986; Meier and Post, 1987). These can be glacier-specific (e.g. geometry, catchment area, and the presence of an ice tongue) or due to the climatic or oceanic forcing (e.g. air temperatures, ocean temperatures, fjord circulation, and sea ice). Despite recent studies confirming the need to take into account a combination of these factors to model ice discharge through outlet glaciers (Carr et al., 2013b,a), the importance of each factor on drainage is still unclear.

Over the last decade some of these processes, such as submarine melting (Motyka et al., 2003; Holland, 2010; Rignot et al., 2010; Motyka et al., 2011; Straneo et al., 2011; O’Leary and Christoffersen, 2013; Bartholomaus et al., 2013; Sciascia et al.,

2013), calving (Benn et al., 2007; Amundson and Truffer, 2010; Levermann et al., 2011; Bassis, 2011; Bassis and Ma, 2015), grounding line migration (Schoof, 2007; Pattyn et al., 2012; Gladstone et al., 2012), air temperature (Carr et al., 2013a), and the presence of sea ice or ice mélange (Moon et al., 2015) have received a lot of attention.

However, neighbouring glaciers under the same climatic and regional oceanic constraints show different retreat rates that can not be explained only by differences in submarine melt (Carr et al., 2014; Bartholomaus et al., 2016) indicate the importance of glacier-specific factors such as the fjord geometry. The impact of glacier-specific factors are increasingly being recognized (Jamieson et al., 2012; Bevan et al., 2012; Carr et al., 2013a). A clear understanding of the impact of fjord geometry on ice discharge will determine what level of detail is needed about the topography underneath current ice sheets. For example, the shape of the basal topography (over-deepening or the presence of a sill) influences rapid retreat (Enderlin et al., 2013b,a). Depending on the resistive stresses provided by fjord wall geometry, glaciers on reverse bed slopes can undergo a rapid retreat or be stable (Weertman, 1974; Gudmundsson et al., 2012; Jamieson et al., 2012; Carr et al., 2015). The impact of the glaciers width at the glacier front on ice drainage is also unclear. Some studies find a strong correlation between glacier front width variability in time and the retreat rates (Carr et al., 2014) while studies over different regions (McFadden et al., 2011; Carr et al., 2013b) show that it is not a primary factor controlling retreat (McFadden et al., 2011; Carr et al., 2013b). The impacts of other fjord characteristics on ice flow, such as: five 2 km fjords compared to one 10 km fjord, fjord width variation along the glacier, and fjord orientation compared to ice flow, is also undocumented. Despite its potential importance, no study to date has explored the impact of fjord characteristics on ice drainage. Here we document the impact of fjord geometry characteristics on ice evolution.

In addition, even with a good understanding of the fjord geometry impact on ice drainage, in a continental-scale glacial cycle context, ice sheet models (ISMs) currently run at resolutions of about five to tens of kilometres (Pollard and DeConto, 2012; Tarasov et al., 2012; Colleoni et al., 2014). Therefore they do not resolve ice dynamics in fjords. Ice sheet models (ISMs) have long been known to have sensitivity to grid resolution (e.g. Tarasov and Peltier, 1997b; Rutt et al., 2009; Durand et al., 2009b). With their large vertical differentials, length scales of one hundred km, and width scales hundreds of metres to ten kilometres, fjords can be expected to be loci of this grid resolution sensitivity. Nowicki et al. (2013) finds an influence of model resolution

on the computation of narrow fast-flowing outlet glaciers drainage, however its impact has never been quantified. In addition, coarse grid cells that partially include a fjord represent a complex topographic region with only one elevation data point (see Fig.2.1). If the fjord is ignored that grid cell does not drain enough ice. Alternatively, if the grid cell is treated as a fjord, the drainage area is overestimated. The fjord depth is, however, underestimated, delaying the occurrence of a warm base during a stadial period. No studies have explored the appropriate depth to represent a SG fjord in a coarse grid cell.

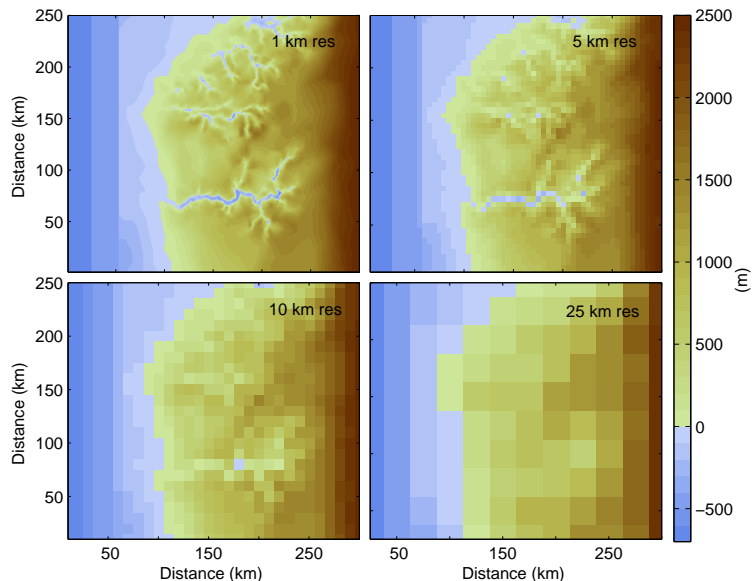


Figure 2.1: Basal topography of a fjord region at different resolutions.

The representation of ice dynamics through fjords in ISMs is also limited due to the ice velocity and subglacial process representation in the models. Studies (Pattyn et al., 2008, 2012; Feldmann et al., 2014) have compared the different dynamical approximations for computing ice velocity on a continental-scale but their impact on a regional scale is not clear. Subglacial processes, such as basal motion due to bed deformation and/or sliding, and subglacial hydrology (with its impact on basal drag) have an important role in flow dynamics (Clarke, 2005); however, we have limited knowledge of the influence of each process on ice drainage (Phillips et al., 2008; Damsgaard et al., 2013; Ingólfsson et al., 2015). Various ice sheet models represent the sliding laws differently using power laws, with exponents ranging from one to four, or Coulomb plastic laws (Cuffey and Paterson, 2010; Fowler, 2010) but the impact of the exponent choice lacks clear documentation in the literature.

As fjords are features present at the margin of the ice sheet, the resolutions issues could be overcome using an adaptive mesh refinement scheme as implemented in the BISICLES model (Cornford et al., 2013). This would allow one to run the model at coarse resolution over the major part of the ice sheet and increase the resolution where details are needed. This approach is however too computationally expensive to run ensemble simulations on a continental glacial cycle scale. Therefore glacial cycle ISMs, especially for large ensemble calibration contexts (e.g. Tarasov et al., 2012), will continue to be run at coarse resolution for the foreseeable future. Given this, it is worthwhile to examine the extent to which parametrizations can account for the impact of subgrid fjords in ISMs. Calov et al. (2015), for example, proposes a subgrid ice discharge parameterization increasing ice discharge proportionally to the ice thickness and the distance to the closest ocean boundary. This approach ignores subgrid information.

Various approaches have been used to summarize subgrid information for coarse resolution modelling of environmental systems. For example, some studies infer probability distributions from the high resolution data (Walland, 1996), to parameterize subgrid processes at coarser resolution, or use the ratio of high frequency to low frequency spatial variance of the feature of interest to take into account its impact in the coarse resolution cell (Guo et al., 2015). Others use the Fourier transformation of the bed elevation and slopes to derive parameters representing the roughness of the topography (Li et al., 2010). The SG information can also be used to classify coarse grid cells in classes that have the same behaviours (e.g. Nijzink and Savenije, 2016). Here we scale the sliding coefficient proportionally to the relative fjord area extent in a coarse grid cell and test different upscale regriding techniques.

To improve the ice drainage representation through fjords in coarse resolution ISMs we address the following questions:

- What is the impact of fjord geometry on ice discharge?
- What is the spatial resolution dependence of modelled fjord ice discharge?
- What is the impact of higher order physics on fjord discharge?
- What is the impact of the sliding power law exponent on ice evolution?
- To what extent can parameterization calibration and the appropriate choice of basal topography upscaling compensate for model grid resolution dependency?

2.2 Model description

The main experiments use the PSU/GSM model described in Section 2.2.1. This model uses hybrid shallow ice and shallow shelf (ice stream and ice shelves) approximations to the full Stokes momentum balance. To test the impact of these approximations, we compare the results of the PSU/GSM model with a model that uses a higher order ice dynamics representation (the *ISSM* model described in Section 2.2.2). The differences between the *ISSM* and PSU/GSM are summarized in Table 2.1.

Table 2.1: *ISSM* and PSU/GSM capabilities showing the differences between each model.

	PSU/GSM	<i>ISSM</i>
<i>Grid</i>	Regular	Finite element
<i>Resolution</i>		
High resolution	1 km	1 km inside the fjords, 20 km outside the fjords
Coarse resolution	runs at 5, 10, and 25 km	25 km
<i>Ice dynamic</i>	SIA-SSA	Higher Order (HO) or SIA
<i>Thermal model</i>	Activated or Deactivated	Deactivated (unstable)
<i>GIA model</i>	Local adjustment or Deactivated	Not implemented (Jan 2016)
<i>Calving</i>	Ice removed for depth > 200m or tidewater, ice shelves, thin ice parameterization	Ice removed for depth > 200m
<i>Basal drag</i>	Exponent 1,2 Weertman type law for soft, hard bed with an exponential transition from cold to warm base	Exponent 1 Weertman type law with an exponential transition from cold to warm base
<i>Ice rheology</i>	Huybrechts (1998) parameterization plus an enhanced factor (Briggs et al., 2013)	Table p.75 in Cuffey and Paterson (2010)
<i>Grounding line</i>	Schoof (2007) parameterization	Flotation criterion
<i>Vertical layers</i>	11	10

2.2.1 PSU/GSM model

The PSU/GSM model, described in detail in [Briggs et al. \(2013\)](#) and [Pollard and DeConto \(2009, 2012\)](#), is a thermodynamically coupled ice flow model. The ice rheology parameterization follows [Huybrechts \(1998\)](#) with an enhancement parameter as in [Briggs et al. \(2013\)](#). The grounding line treatment is taken from [Schoof \(2007\)](#). To

focus on the impact of fjords in the ice evolution, calving is treated by removing ice for depth greater than 200 m. Basal drag is based on a Weertman power law with an exponential dependency on temperature for the cold to warm based transition. The bedrock response to surface loading is visco-elastic. The surface mass-balance model, described in [Le Morzadec et al. \(2015\)](#), is based on [Tarasov and Peltier \(1999a, 2002, 2003, 2006\)](#); [Tarasov et al. \(2012\)](#). In this study, temperature and precipitation are derived from their fields at present day (PD) and at Last Glacial Maximum (LGM) as described in [Tarasov and Peltier \(2004b\)](#) (section [A.1.2.1](#) of the supplement summarizes how the precipitation and temperature time series are generated from these parameters and shows an example of the February PD and LGM temperature and precipitation; Section [A.1.2.2](#)).

Table [2.2](#) presents the PSU/GSM baseline parameter vector used in the high resolution reference simulation. Most of the vector components are from a best-fitting subset member from an ongoing calibration of the GSM (as completed for North America in [Tarasov et al. \(2012\)](#)) over Eurasia. We select the sliding coefficients used in the sliding power law to match typical basal sliding velocities of 1600 m/yr velocity at 20 KPa in a fjord (soft bed, `slidsoftC`) and a 20 m/yr velocity at 50 KPa over hard bedrock (`slidhardC`) ([Cuffey and Paterson, 2010](#)). The flow enhancement parameter, that accounts for different ice fabric, is set to 4.28 for grounded ice and 0.42 for ice shelves. These values are in accordance with the [Ma et al. \(2010\)](#) study that suggested a ratio of 1/9 between the grounded ice and ice shelf enhancement factor. Values between 2 to 6 are present in the literature for the grounded ice enhancement parameter ([Ma et al., 2010](#); [Cuffey and Paterson, 2010](#); [Greve and Hutter, 1995](#); [Letréguilly et al., 1991](#); [Huybrechts et al., 1991](#)).

We examined the sensitivity of ice volume to the ice shelf flow enhancement parameter (`shelfflowC`) and the sub-shelf melt/calving parameters (CM). The results show no significant impact of the ice shelf flow enhancement parameter and the sub-shelf melt/calving parameters on the ice volume evolution (less than 1% differences compared to the simulations using the original parameter vector, see section [A.2](#) in the supplement). Details on the experiment and results are presented in Section [A.2](#) of the supplement.

PSU/GSM simulations have a time step of 0.02 yr for the high resolution (1 km) simulations and 0.05 yr for the coarse resolution (5, 10, and 25 km) experiments. Running the coarse resolution model with a time step of 0.02 yr instead of 0.05 yr does not impact the model results. A [Courant-Friedrichs-Lewy \(CFL\)](#) condition modifies

Table 2.2: Lists of the baseline parameter vector. Values are rounded to 2 decimal places.

Definition	Parameter	Linear	Quadratic
Ice dynamics			
soft bed basal sliding coef.	slidsedC	8	0.4
hard bed basal sliding coef.	slidhardC	4	8
Flow enhancement coef. for grounded ice	flowC	4.28	4.28
Flow enhancement coef. for shelf flow	shelfflowC	0.42	0.42
Calving and sub-shelf melt (CM)			
Maximum calving velocity, tidewater glacier	calvmaxV/10	0.28	0.28
Grounding line zone SSM coef. (large shelves)	SSMGLz1C	1.18	1.18
Shelf front SSM coef. (large shelves)	SSMfrontC	2.89	2.89
Grounding line zone SSM coef. (large shelves)	SSMGLz1C	1.33	1.33
Ice shelf calving minimum thickness threshold	Hshelfcrit	0.64	0.64
Ice shelf calving coef.	shelfcalvC	2.35	2.35
Thin ice calving temperature-dependent coef.	calvthinC	0.41	0.41
Ice shelf calving sub-Hshelfcrit enhancement coef.	shelfcalv2C	0.19	0.19
Shelf front melt climate-dependence coef.	SSMfrontTC	0.67	0.67

the time step as needed to avoid instabilities.

2.2.2 Ice Sheet System Model (ISSM)

The **ISSM** is a finite element 3-D thermomechanically coupled ice flow model [Larour et al. \(2012\)](#). For this study, the surface mass balance and the climate forcing are computed as in the PSU/GSM model (see section 2.2.1). The mass transport is computed according to the depth-integrated form of the continuity equation. Using the ice constitutive equation, the conservation of momentum provides the velocities. The Blatter–Pattyn **HO** and the **SIA** compute the velocities in this study. A hybrid **SIA - SSA** model could not be used as it does not support a flux boundary condition evolving in time. The grounding line is parameterized using the flotation criterion. Basal velocity is proportional to the basal stress (driving stress in the **SIA**) following a Weertman power law with an exponent of 1, specifically as follows:

$$u_b = C\tau_b f(T_i), \quad (2.1)$$

where C is the sliding coefficient and is set to the PSU/GSM model sliding coefficient (see Section 2.2.1). The relation of the basal velocity to the ice temperature T_i and the temperature at the pressure melting point T_{pmp} is given as

$$f(T_i) = \exp\left(\frac{T_i - T_{pmp}}{0.5}\right) \quad (2.2)$$

The thermodynamics module had to be turned off due to excessive computation time and the occurrence of instabilities during the spinup runs (resulting in the much more complicated experimental design of this study). The ice rheology is determined using [Cuffey and Paterson’s \(2010, p.75\)](#) table 3.4. Calving is represented by melting all the ice over the ocean at depth higher than 200 m. The model runs using ten vertical levels and a time step of 1 yr (adjusted in accordance to a **CFL** condition).

2.2.3 Boundary conditions

We use two sets of basal topography representing realistic fjords and idealized synthetic fjords, the latter to isolate geometric impacts on ice flow. Our model grid has a dimension of 300 km in the x direction by 250 km in the y direction. The synthetic set includes 20 fjords with different individual characteristics to span those observed (see Section [A.1.1.3](#) in the supplement which shows figures of the real fjords that guided

our choices). Fig.2.2 shows an example of three synthetic regions (see Section A.1.1.2 in the supplement for a full list of fjords). The set of realistic topographies (Fig.A.1 in the supplement), are extracted from the [General Bathymetric Chart of the Oceans \(GEBCO\)](#) 30 arcsec resolution DEM ([Centre, 2010](#)) (approximately 1 km in the y direction and 450 m in the x direction in the regions of interest) along the western coast of Norway. Eight coastal regions were selected to include fjords with different characteristics, such as the number of fjords, curvature, length, number of tributaries and presence or absence of a sill. Reference region number 5 has no fjords. At the upstream boundary, the topography is raised by 500 m above the highest topography along the boundary to force an ice flow toward the mouth of the fjord. The topography is linearly interpolated over 1 degree in longitude between this synthetic ridge and the topography toward the ocean front. The [GEBCO](#) coordinates are converted into Cartesian coordinates approximating the Earth as a perfect sphere with radius of 6370 km. Fjords are arbitrarily selected as inland regions, at least 20 km long, bound between two steep faces.

For the PSU/GSM simulations at 5, 10, and 25 km resolution, we generate a fjord mask, for each region analyzed, representing the percentage of high resolution (1 km) fjord cells in each coarse grid cell. Fig.A.22 and A.23 of the supplement shows an example of a fjord region, and its related fjord mask, at different resolutions.

A [GSM](#) simulation (a description of the [GSM](#) model is given in Chapter 2, Section 3.3.2) of the Eurasian ice sheet during the last glacial cycle, that gave some of the best fits to the calibration constraints (run id nn56111), provides the glacial cycle forcings and initial conditions. To isolate the impacts of fjords, all regions are subject to the same forcing extracted from region 7 of run nn56111. We selected region 7 as it represents a typical fjord region. Simulation nn56111 provides the climate forcing parameters $Tdiff$, $Pfac$, and $sealev$ controlling the temporal evolution of the climate fields (the time series of these parameters are presented in supplemental Fig.A.30). The underlying climate forcing (i.e. before imposing topographic gradients) is averaged along the y direction (i.e. cross flow, see Fig.A.27 and A.28 in the supplement) to isolate flow response to topography.

The near basal geothermal heat flux is a spatial average extracted from [Pollack et al. \(1993\)](#). An example of its evolution over time is presented in Fig.A.33 of the supplemental.

The intent of choosing these forcings is to simulate ice evolution with archetypal realistic features but not to replicate what happened over the fjord regions analyzed.

The upstream ice velocities and ice thickness forcings (shown in Fig.A.31 of the supplement) are averaged along y direction to avoid fjord response contamination from lateral variations (i.e. for fjords running diagonal relative to general flow and upstream boundary). This forced upstream ice flux reduces the dynamic range of the modelled ice flow. The velocities in the y direction along the sides of the domain is set to 0 to conserve mass.

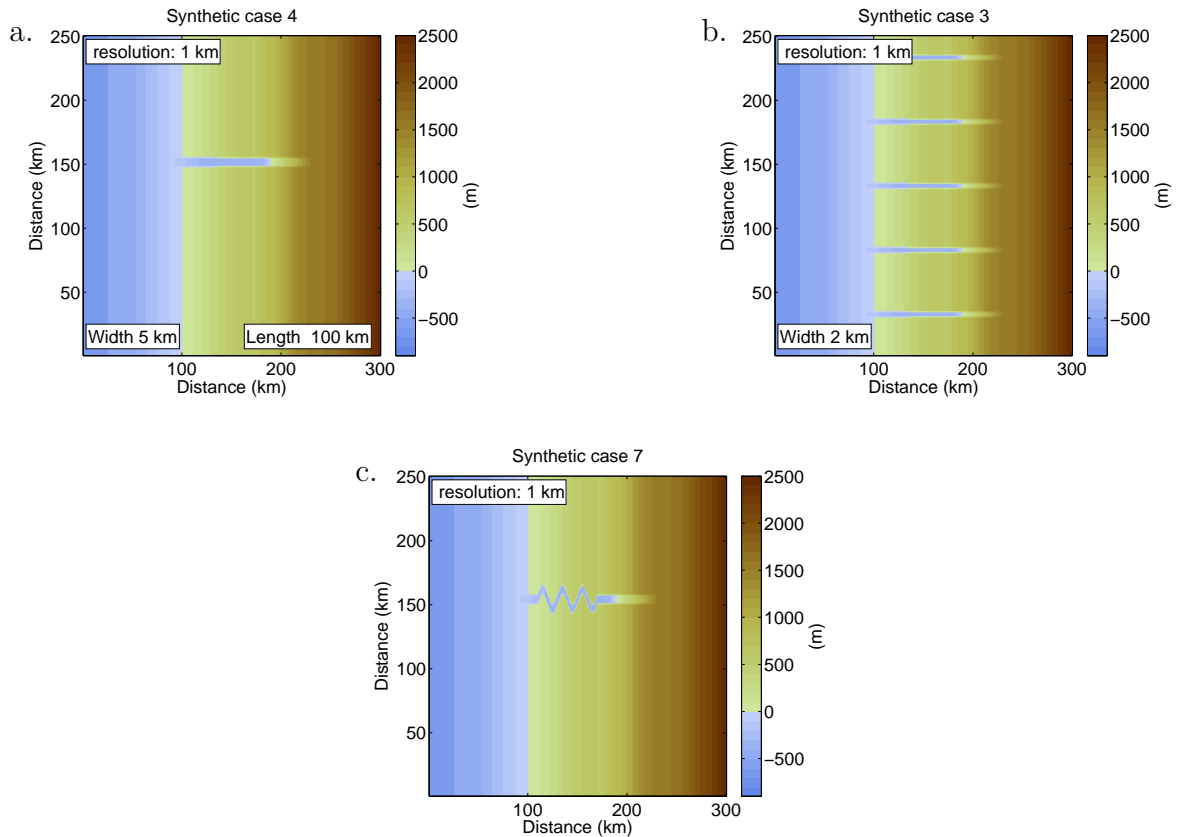


Figure 2.2: Topography for three different synthetic fjord regions.

2.3 Experimental design

Our first set of experiments explores the impact of fjord geometry on ice flux. The second set of experiments documents the model capabilities, in term of resolution and ice dynamic, to represent ice evolution in fjords regions. A third set of experiments is used to develop a new parameterization that minimizes the model resolution dependency. Table 2.3 gives a summary of the experimental design.

Field measurements show that ice acts as a non-linear viscous material (where the strain rate varies proportionally to the power, higher than 1, of the shear stress) for displacement over a hard bed while displacement over a soft bed is determined mainly by the movement of the underlying sediment that act as a Coulomb plastic material (where the shear stress is linearly proportional to the strain rate) after an initial stress adjustment (Cuffey and Paterson, 2010). Studies (presented in Cuffey and Paterson, 2010) have shown that a linear law between the basal velocity and the stresses perhaps better approximates sliding over soft bed while a cubical or quadratic law is better over hard bed. As the PSU/GSM model does not have the ability to apply different sliding exponent over different regions and the impact of the exponent in the sliding law is not well documented in the literature, the following experiments are performed first with a linear law and then with a quadratic law.

In all our experiments, except if stated otherwise, the simulations are run from 120 ka to 70 ka¹ with the baseline parameter vector. We selected that time frame as it represents two stadial and interstadial events.

¹In this chapter, “kyr” is used to represent time intervals and “ka” for time before present day.

Table 2.3: Experiment design summary.

	PSU/GSM res (<i>km</i>)	ISSM res (<i>km</i>)	Topography	Climate	Ice temperature	Simulation
Fjord geometry	1, 5, 10, 25	-	Synthetic	constant along y axis	evolving	120 ka to 70 ka
Resolution	1, 5, 10, 25	-	Synthetic	constant along y axis	evolving	120 ka to 70 ka
Higher order physics	1	1	Real	Real	constant	120 ka to 115 ka
Sliding law	1, 5, 10, 25	-	Synthetic	constant along y axis	evolving	120 ka to 70 ka
Minimize scale dependency	1, 5, 10, 25	-	Synthetic	constant along y axis	evolving	120 ka to 70 ka

2.3.1 Fjord geometry impact

The impact of fjord geometry is tested using the 20 synthetic fjord regions (see Fig.2.2 and Section A.1.1.2 in the supplement). The PSU/GSM is run at 1 km. We evaluate the impact of the different fjord characteristics by comparing the ice volume and surface elevation (hs) Root Mean Square Error (RMSE) of each fjord relative to a straight fjord 100 km long and 5 km wide.

2.3.2 Model sensitivities: resolution, order of ice dynamics approximation, and sliding law exponent

We examine the resolution impact comparing ice volume, surface elevation RMSE, and velocity fields from PSU/GSM simulations at coarse resolution (5, 10, and 25 km) with the same variables from simulations at high resolution (1 km). In the coarse resolution simulations, the soft bed sliding coefficient (slidsedC) is reduced proportionally to the fjord area in each cell using the fjord mask described in Section 2.2.3.

To quantify the impact of higher order ice dynamics, we compare the ice volume differences generated with PSU/GSM and ISSM at each time step during a 5 kyr simulations of the last glacial inception (starting at 116.6 ka). We apply the same climate forcing over the nine real fjord regions. ISSM simulations are done at high resolution (1 km inside the fjords to 20 km away from the fjords) solving the HO model for ice flow. We use the HO model in the fjords as it is computationally less expensive but still in good agreement with Full-Stokes models (Pattyn et al., 2008). PSU/GSM simulations are done at 1 km resolution with the baseline parameter vector deriving the velocities using the hybrid SIA/SSA. The thermodynamic model is turned off in both models as it leads to instabilities in the ISSM.

The resolution impact experiments are performed with both linear law and quadratic laws. We use these simulations to document the impact of the sliding exponent on the ice volume and surface elevation evolution.

2.3.3 Model resolution dependency minimization

To test possible grid resolution sensitivity compensation for the PSU/GSM, we use the same model setup as for the resolution impact experiments. We sequentially apply different values of: the flow enhancement parameter over grounded ice, the sliding parameter over hard bed, the sliding parameters over soft bed as well as the five

following methods to upscale the basal elevation at coarse resolution (5, 10, and 25 km) from a high resolution DEM. The coarse resolution basal elevation is, in turn, set to: the box average of the high resolution (1 km) data, the deepest depth in the fjord(s), the fjord depth average, the average between the fjord average and the box average, and the average between the deepest depth in the fjord and the box average. We first isolate the impact of the flow enhancement factor for grounded ice and hard bed sliding parameter in simulations over the synthetic fjord region that does not include a fjord. The flow enhancement factor parameter is adjusted between 1.5 and 9. The hard bed sliding coefficient is set to values equivalent to a basal sliding speed of 1 to 80 m/yr at 50 KPa driving stress. We then extract the optimum sliding parameter for hard beds and the flow enhancement factor that minimizes the differences in ice volume and the surface elevation RMSE (both compared to the results of the high resolution simulations). With these "optimum" hard bed and flow enhancement parameters, we test the response to the soft bed sliding parameter over all the synthetic fjord regions using coefficients corresponding to velocities ranging from 0 to 9000 m/yr at 20 KPa driving stress (table A.4 in the supplement presents the list of values tested).

2.4 Results

2.4.1 Fjord geometry impact

The comparison of a simulation over a region with a fjord 5 km wide and 100 km long (referred as the "reference fjord" simulation) with simulations over regions with different fjord characteristics is presented in Fig.2.3. Tables A.5, A.7, and A.8 in the supplement present detailed ice volume differences and surface elevation RMSE for each fjord region. The fjord geometries have similar impacts on the ice evolution when using a quadratic or linear law so we focus here on the results generated with the linear law (the results generated with the quadratic law are shown in Section A.4.1 of the supplement).

The surface elevation RMSE and ice volume show different trends in their response to various fjord characteristics. For example, the "diagonal" orientation (relative to upstream ice flow) fjord shows a stronger response in the RMSE than in the ice volume. The larger RMSEs are, partly, due to the different location of the diagonal fjords compared to the straight fjord. Thus some caution is needed in interpreting the various comparison metrics.

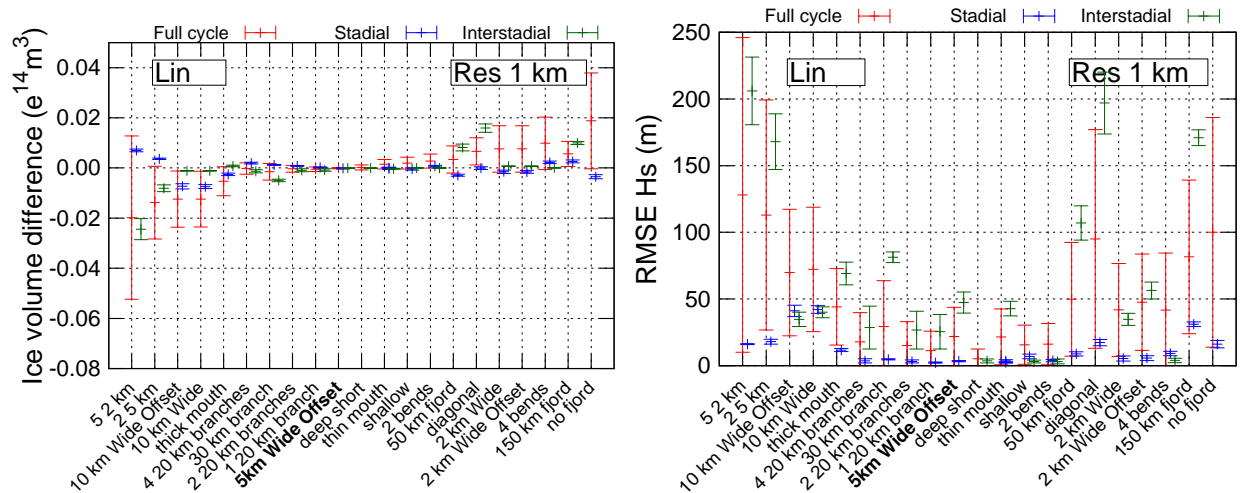


Figure 2.3: Different fjord characteristics impact compared to a 5 km wide and 100 km long fjord. The left panel shows the ice volume differences. The right panel shows the surface elevation **RMSE**. Red represents the average and standard deviation over 50 kyr, blue at the end of inception (111 to 107 ka) and green at the end of the first interstadial event (102 to 100 ka). These simulations use the baseline parameter vector and a linear (Lin) sliding law. The x axis represent the different fjords region listed in Section A.1.1.2 of the supplement. The boldface 5 km fjord, in the x axis, represents limit between regions generating less ice than the reference fjord and the region with more ice.

The comparison with a region with no fjords shows the necessity of taking into account the effect of a fjord while representing ice evolution (see Fig.2.3 and 2.4). Over a 50 kyr simulation period a simulation without a fjord builds, on average, 8.2% (with a standard deviation of 9.8%) more ice than the reference simulation. During stadial periods, this difference is 33.7%.

A comparison of regions with smaller fjords (in length or width) or fjords generating more resistive stresses (such as a fjord with more bends, in a diagonal or with a thin mouth) shows that the total ice volume is higher than with a straight fjord. This is expected as these regions have a smaller drainage basin or more resistance due to side walls position variation. The differences can be up to 3% (with a standard deviation of 3.4%) for a fjord with 4 bends, which is smaller than the differences when the fjord is not taken into account.

Regions with a larger fjord area (either because of wider fjords, multiple fjords, a wider terminus or branches) drain more ice. The ice volume, on average, can be up to 9.6% lower than with a straight fjord (with a standard deviation of 13.1%, for the case of five 2 km wide fjords). The difference in ice volume increase with the area of the fjord and the area of the fjords drainage basin. The ice volume in a region with five 2 km fjords is 2% lower than in a region with one 10 km wide fjord.

To compare the impact of fjord characteristics to another process affecting the ice evolution we compare simulations turning on and off the thermodynamic model. We perform a set of simulations with cold base fjords and a second set with warm base fjords. The results and experiment details are described in Appendix A. During stadial events having a cold or warm base in the fjords increases or reduces the ice volume by an order of magnitude of 20% compared to a simulation where the ice temperature evolves. We find differences of 13.6% (with a standard deviation of approximately 15%) between a region with no fjords and a region with five 2 km wide fjords. These differences show that the fjord geometry characteristics are of the same order of magnitude as the thermodynamic impact.

These results suggest that the fjord characteristics have to be taken into account when modelling ice evolution over fjord regions (see Fig.2.4 for a summary of the range of impacts; the detailed time series of the differences in ice volume between the reference fjord and all the fjord regions analyzed is shown in Section A.4.1.1 of the supplement). However, as our analysis is based over regions of 300 km by 250 km, the implication of ice drainage through fjords over an ice sheet needs further attention.

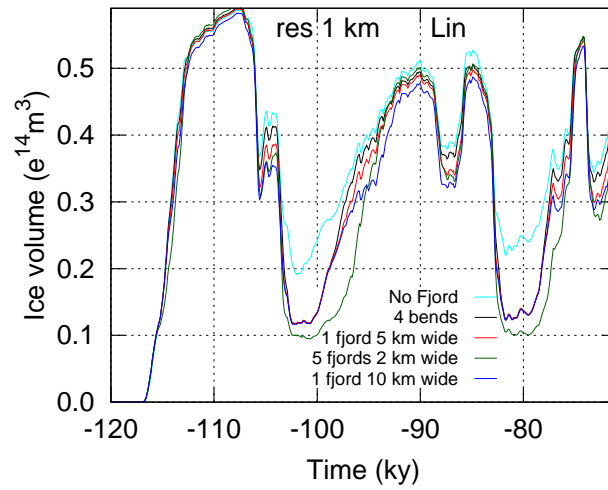


Figure 2.4: Range of ice evolution generated with different fjord characteristics. These simulations use the baseline parameter vector and a linear (Lin) sliding law.

2.4.2 Model sensitivities: resolution, order of ice dynamics approximation, and sliding law exponent

2.4.2.1 Model resolution dependency

Modelling ice evolution in fjord regions with the PSU/GSM model at different resolutions shows a clear dependency of the surface elevation **RMSE** (compared to the 1 km) on the resolution. 25 km resolution simulations produce misfits to the 1 km resolution simulations three times higher than at 5 km resolution (see Table 2.4). Surface elevation **RMSE** and total ice volume differences misfits to the 1 km resolution simulations also increase with the complexity of the fjord system.

Table 2.4: Surface elevation **RMSE** at 5, 10, and 25 km resolution compared to the 1 km resolution simulations using the linear sliding law. The data are averaged over all the synthetic fjords and over the whole time series (TS), over the first stadial (SD) and over the first interstadial (ISD). The surface elevation **RMSE** percentage is given compared to the average ice thickness at 1 km resolution.

res (km)	RMSE hs (m)						RMSE hs percentage (%)					
	TS		SD		ISD		TS		SD		ISD	
	avg	std	avg	std	avg	std	avg	std	avg	std	avg	std
5	60.6	18.8	38	2.43	50.7	0.941	11	4.46	4.69	0.343	11.5	0.941
10	92.6	16.4	83.3	6.38	112	2.34	17.6	4.98	10.3	0.879	25.6	2.34
25	147	11.3	108	4	146	5.57	31	7.07	12.4	0.534	30.3	5.57

Table 2.4 shows the impact of resolution on the simulation of ice evolution over the 20 synthetic fjords when using a linear sliding law (using a quadratic sliding law gives the same resolution impacts, see table A.9 in the supplement). The average and standard deviations are over the whole time series (TS), the first stadial (from 111 to 107 ka, SD) and the first interstadial (from 102 to 100 ka, ISD). Over any time interval, the average surface elevation **RMSE** (compared to the 1 km) increases with resolution. The **RMSE** (as a percentage compared to the mean ice thickness in the 1 km resolution simulation) response to grid resolution is approximately proportional to the resolution to the power 0.65 (11 % at 5 km resolution, 17.6 % at 10 km resolution and, 31 % at 25 km resolution).

Comparing the ice volume evolution between coarse resolution and 1 km resolution simulations (Fig.2.5) shows differences of the same order of magnitude for synthetic

fjord regions with a single fjord. However, the regions with multiple fjords (five 2 km ford and two 5 km fjords), which effectively drain ice from a larger area of the grid, have higher ice volume differences between coarse and high resolution simulations. This suggest that the fjord geometry characteristics impact of a single fjord found in Section 2.4.1 are partly accounted for in coarse resolution simulations with the basal sliding coefficient parameterization based on the fjords area. However, differences increase proportionally to the number of fjords in a region (i.e. while maintaining equal total fjord area). We draw the same conclusions when looking at the surface elevation RMSE data (Fig.A.43 in the supplement). In addition, all simulations, at 5 and 10 km resolution, in regions including at least one fjord show an underestimation of the ice volume at coarse resolution. In 25 km resolution simulations, the ice volume is underestimated on average over time but is overestimated during some interstadial events (such as the end of inception around 110 ka, see Fig.2.6). In contrast to the underestimation of ice volume in coarse resolution simulations over fjord regions, the ice volume in region with no fjords is over or underestimated compared to the high resolution simulation depending of the time step analyzed. These conclusions suggests an excessive drainage of ice through grid cells with SG fjords. This might be due to insufficient reduction of the soft bed sliding coefficient (done proportionally to the fjord area) to mitigate the overestimation of the fjord width at coarse resolution. Alternatively, the underestimation of the ice volume in coarse resolution simulations could be the result of shallower fjord generated from averaging the high resolution topography data. We test these two possible explanations in Section 2.4.3 by applying different soft bed sliding coefficient and different methods to upscale the fjord basal topography at coarse resolution. We draw the same conclusions about the model scale dependency when analyzing the total ice volume difference and the surface elevation RMSE using a quadratic sliding law instead of a linear sliding law(see Fig.A.42 and A.44 in the supplement) instead of a linear sliding law.

The model resolution dependency can also be observed in the timing misfits of different stages of the ice evolution, such as the beginning and end of stadial or interstadial events (Fig.2.6). For a region with no fjords or with a single fjord (independently of its characteristics), the timing of the ice evolution in 1, 5 and 10 km resolution are similar. For 25 km simulation, however, there is a lag of a few thousand years after the first interstadial (around 100 ka). For a region with multiple fjords, all the coarse resolution simulations have a lag of approximately 3 ky during the beginning of the second interstadial period (around 98 ka). We find the same

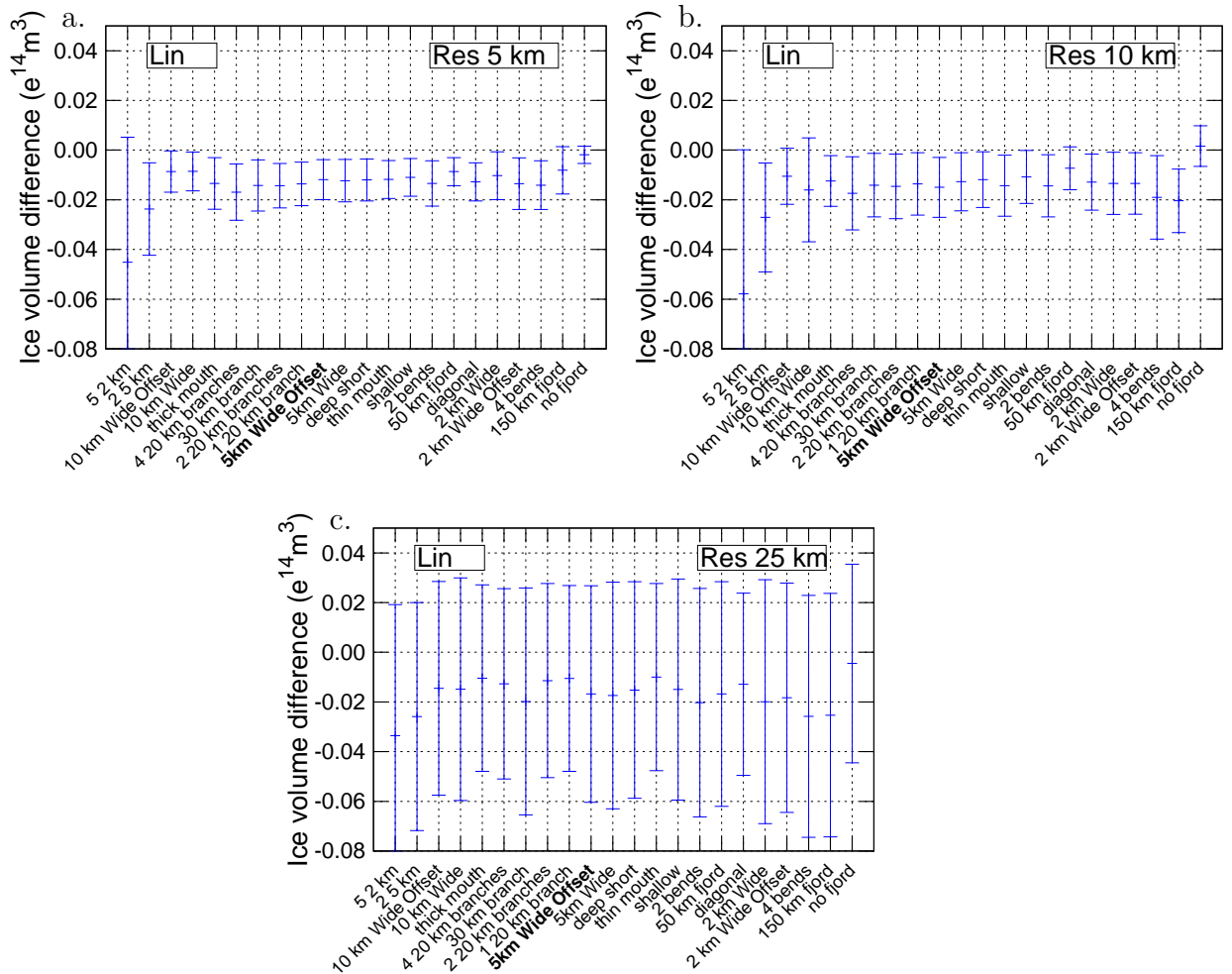


Figure 2.5: Average and standard deviation (over 50 kyr) ice volume differences between simulation at: a. 5 km, b. 10 km and c. 25 km resolution and 1 km resolution simulations. Simulations use a sliding law. The boldface 5 km fjord, in the x axis, represents limit between regions generating less ice than the reference fjord and the region with more ice.

resolution impact when using a quadratic sliding law (see Fig.A.45 in the supplement) instead of a linear sliding law.

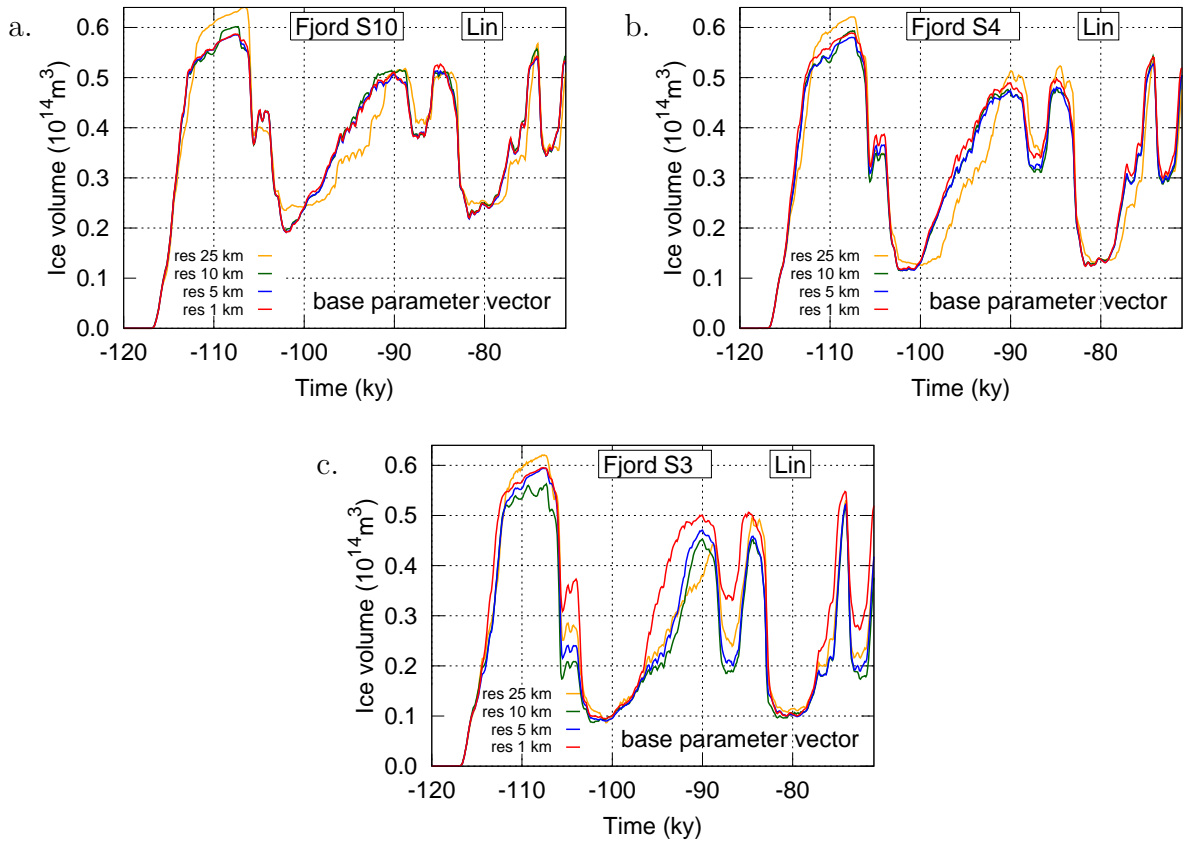


Figure 2.6: Resolution impact on the ice volume. Examples for a region with no fjords (a. S10), with one 5 km wide and 100 km long fjord (b. S4) and five 2 km wide fjords (c. S3). These simulations use the baseline parameter vector and linear (Lin) sliding law.

The impact of resolution on the velocity fields differs non-linearly with resolution and time (see Fig.2.7). We find the same trends when using a quadratic sliding law (see Fig.A.46 in the supplement). One explanatory factor is that the fjords are shallower at coarser resolution. This leads to thinner fjord ice during inception, keeping a cold base (lower velocities) for longer compared to the 1 km resolution simulations. At the end of inception, at approximately 110 ka, the velocities are underestimated or overestimated at coarse resolution depending on the surface elevation profile and the extent of the floating ice at the mouth of the fjord. At the end of an interstadial event (approximately 100 ka), the velocities in the fjords are overestimated at 5 km resolution and underestimated at 25 km resolution. No pattern could be distinguished

relating the velocity fields to the resolution and the fjord characteristics.

2.4.2.2 Higher order ice dynamical physics

We examine here the impact and performance of different approximations of the Full-Stokes equation used to model the ice dynamics in an ice sheet model.

The ice volume growth rate in the beginning of inception is similar when using the HO model or the hybrid SIA/SSA model (see Fig.2.8). Once the fjord starts to be covered with ice, the ice growth rate decrease by the order of 10 % in the hybrid compared to the HO model.

After a 5000 year simulation, most of the differences in the velocity field are in the fjords (see Fig.A.48 of the supplement) and the ice volume in the simulation using the hybrid SSA/SIA model is, on average, 7.7% lower than when using the HO model (averaged over the 7 real fjord regions considered, with a standard deviation of 1.4 %, Fig.2.8). The spatial variations, showing the same results, are presented in Fig.A.47 of the supplement. The surface elevation root mean square error (RMSE) is, on average, 280 m (with a standard deviation of 32 m) which is 41 % (with a standard deviation of 8.8 %) of the average ice thickness of the HO model simulation.

Due to the non-linearity of the model, the ice volume differences and the surface elevation RMSE observed between simulations using the hybrid and the HO models could grow over time if the upstream influx of ice was not forced, increasing the importance of the higher order terms. However, some of the differences could also come from model differences such as the grids (finite element vs. regular) or grounding line parameterizations.

Calov et al. (2015) found that ice sheet models based on the SIA overestimate the ice volume of an ice sheet. Another experiment over the Greenland ice sheet (Pattyn et al., 2013) suggests that using the HO approximation reduces the ice lost by 20 % compared to the SIA which is coherent with our comparison (compare blue and green lines on Fig.2.8). They suggest that these differences are due to the inclusion of membrane stresses in the HO model. In our results, the PSU/GSM (which includes membrane stresses) generates ice volumes closer to the SIA ISSM simulations than to the HO ISSM simulations. In an intercomparison model study, Pattyn et al. (2013) shows that pure membrane models (SSA or hybrid SSA/SIA with a Schoof (2007) grounding line parameterization) produce larger ice sheets than a Full-Stokes or HO model because no vertical shearing is taken into account at the grounding line (no

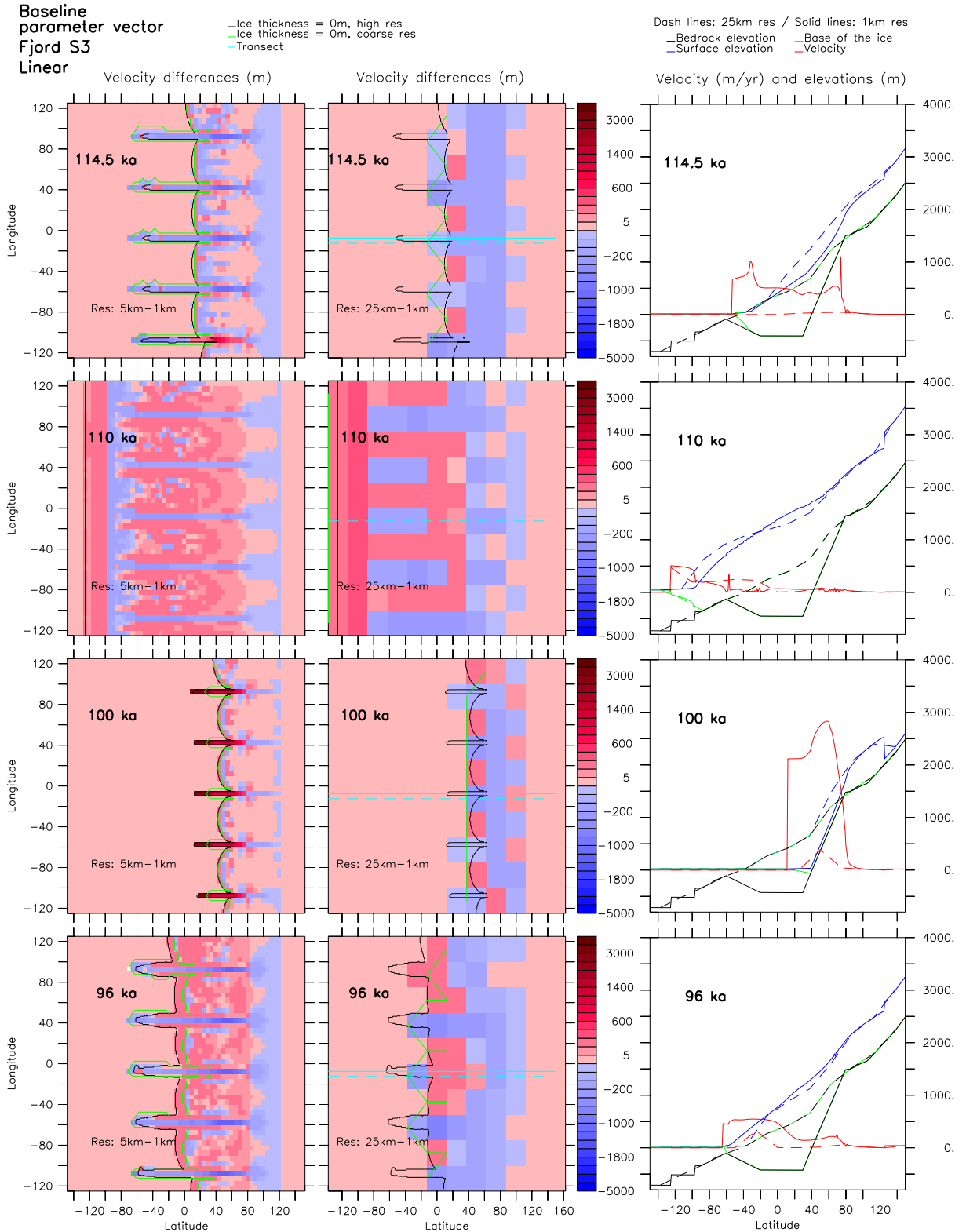


Figure 2.7: Ice velocity fields at 5 km resolution (left panel) and 25 km resolution (central panel) compared to a 1 km resolution simulation at different time slices. The panel on the right side shows the surface, base and velocity evolution in the 25 and 1 km resolution simulations. These simulations use the baseline parameter vector and linear (Lin) sliding law over the region with five 2 km wide fjords.

shearing leads to more viscous ice that reduces the ice drainage in the ocean). Our results contradict that of the above study, but our experiment focused on regions of 300 km by 250 km and not a full ice sheet.

The validity of using the hybrid model for continent-scale glacial cycle experiments where a large ensemble of simulations are required for the model calibration is unclear. To investigate this issue, continental scale simulations are needed, comparing the impact of HO and hybrid SSA/SIA models over the scale of an ice sheet and around the ice/ocean margin.

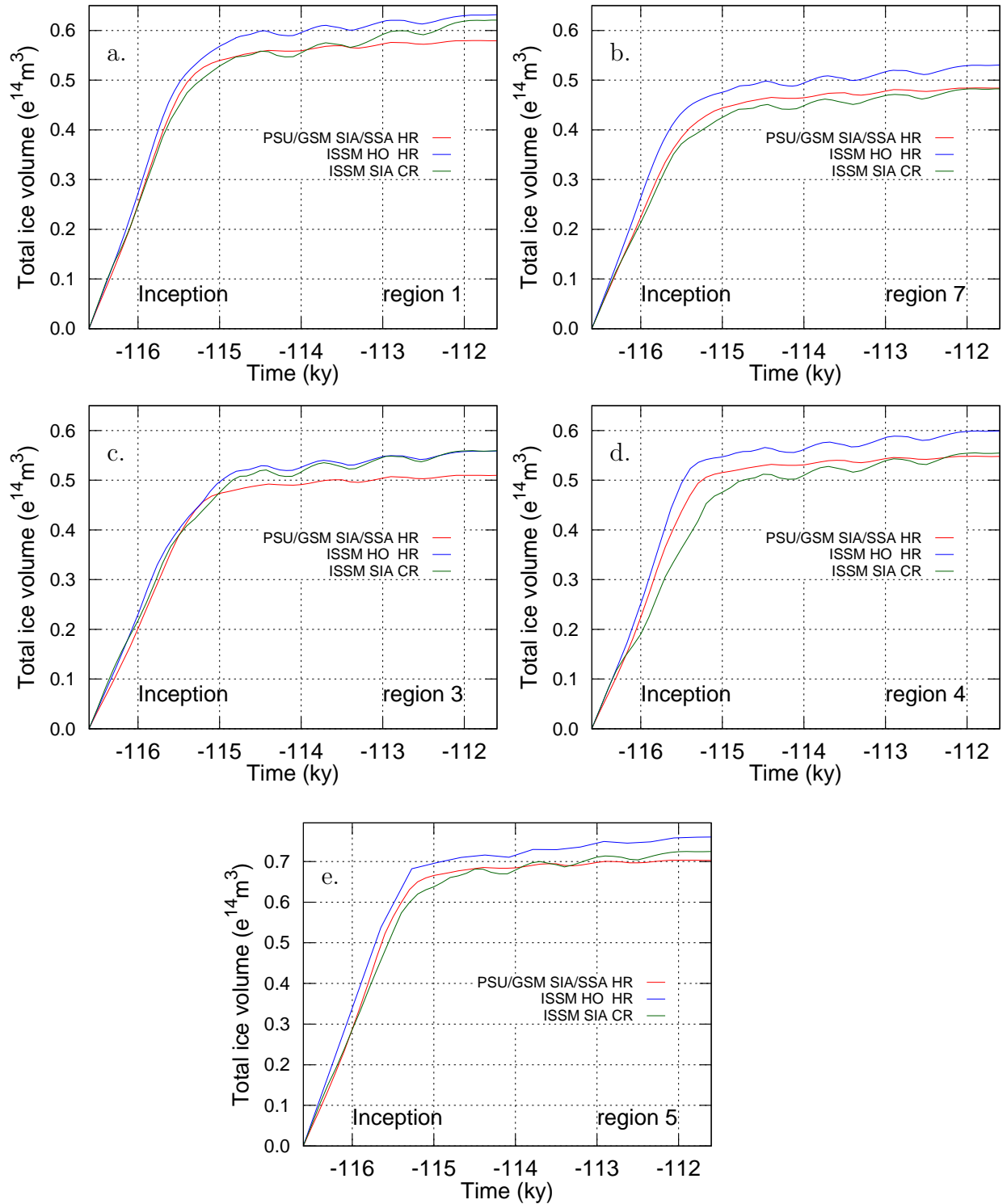


Figure 2.8: Ice volume evolution over some of the topographic regions presented on Fig. A.1. Different ice dynamics approximation are used in different models. Red lines are generated with the PSU/GSM model using the hybrid SIA/SSA at high resolution (HR). Blue lines are generated with the ISSM model using the HO approximation at HR. Green lines are generated with the ISSM model using the SIA approximation at CR.

2.4.2.3 Sliding law exponent impact

Using the optimized parameters at each resolution (generated in Section 2.4.3, we compare simulations with the linear and quadratic laws. Fig.2.9 and 2.10 show the typical responses that we observe over the range of fjord regions analyzed. The differences generated when different sliding laws are used are of the same order of magnitude as the resolution impact. As these differences would be larger if the upstream boundary were not forced, it is essential to improve constraints on the appropriate form of the sliding law used in ice sheet models.

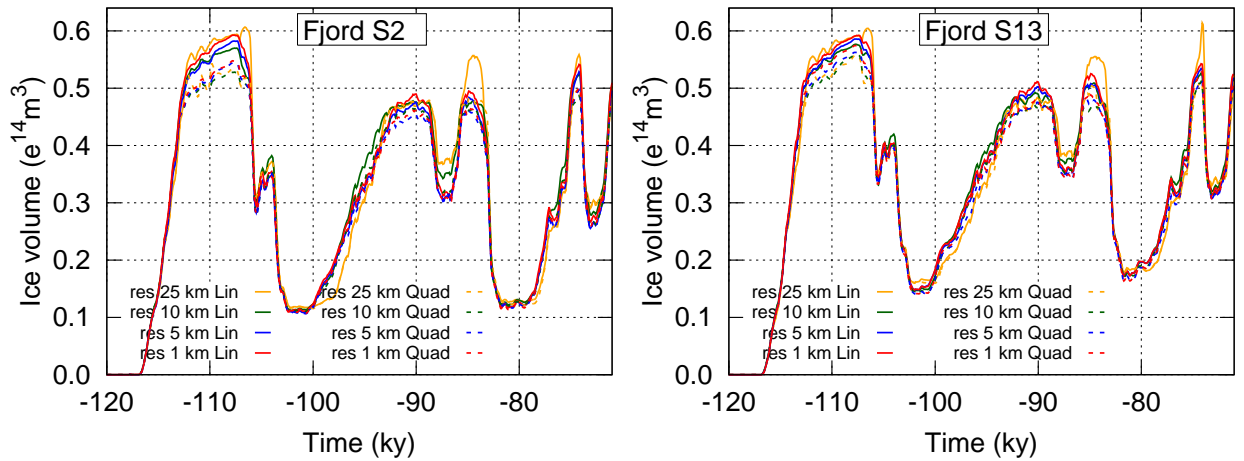


Figure 2.9: ice volume for a region with two 5 km wide and 100 km long fjords (left panel) and a 5 km wide and 100 km long fjord with 2 branches (right panel). Solid lines represent a simulation with a linear sliding law while dotted lines represent a simulation with a quadratic sliding law.

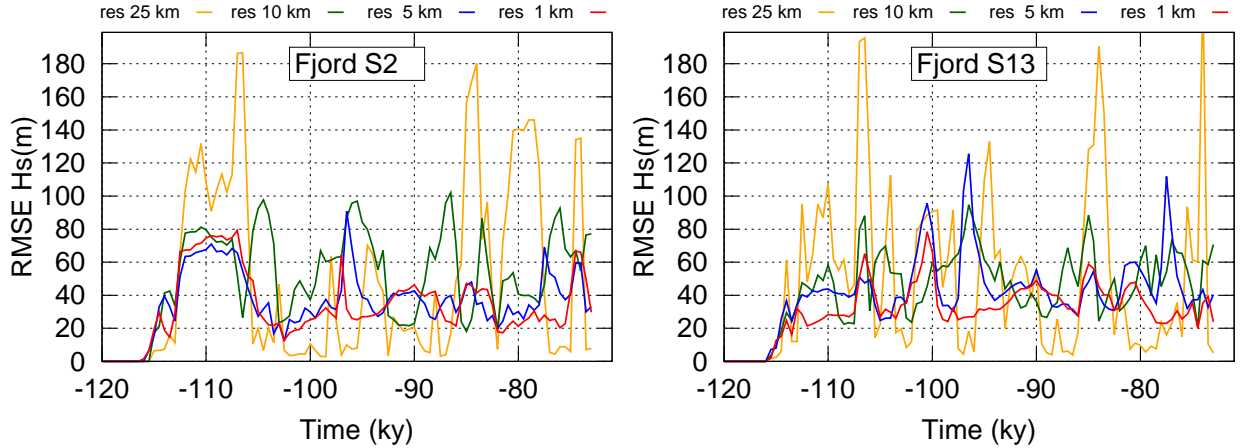


Figure 2.10: Surface elevation [RMSE](#) between simulations using a linear or quadratic sliding law for a region with two 5 km wide and 100 km long fjords (left panel) and a 5 km wide and 100 km long fjord with 2 branches (right panel).

2.4.3 Model resolution dependency minimization

To compare the performance of each coarse simulation against those of high resolution simulations that use the baseline parameter vector, we compute the ice volume differences and the surface elevation [RMSE](#). The final metric is defined as the sum of these two normalized quantities. The normalization is done over the mean of their value across all regions, resolutions and time steps. The conclusions inferred using the [SIA](#) instead of the hybrid [SSA/SIA](#) model, using real fjord data instead of synthetic regions, and generating the misfits metric using the ice flux [RMSE](#) instead of the surface elevation [RMSE](#) are the same as the ones presented in this section.

2.4.3.1 Hard bed parameters

Table [2.5](#) presents a list of optimal parameter sets that minimize the model errors at 5, 10, and 25 km compared to the 1 km reference simulation in a region with no fjords. Of all the parameter sets tested (presented in Section [2.3](#)), the optimal sets of parameters are the ones generating the lowest value of our previously defined metric (see Fig. [A.49](#) and [A.50](#), in the supplement, for a map of this metric for all sets of parameters tested).

When running the model at 25 km resolution, the optimal parameter vector reduces the ice volume and surface elevation [RMSE](#) by approximately 10% (see details in table [2.6](#)). At 5 and 10 km resolution, the baseline parameter vector gives good agreement

Table 2.5: Optimal hard bed sliding coefficient.

Resolution	Flow enhancement	Sliding law			
		Linear coefficient 10^{-4} m/yr/Pa	50 kPa vel equivalent	Quadratic coefficient 10^{-9} m/yr/Pa ²	50 kPa vel equivalent
5 km	4	4	20 m/yr	8	20 m/yr
10 km	3.5	6.5	32.5 m/yr	10	25 m/yr
25 km	8	1	5 m/yr	2	5 m/yr

with the 1 km resolution simulation (see Fig.2.11, and A.52). The optimal set of parameters improves slightly the 10 km resolution simulation. At 5 km resolution, the optimal set of parameters improves the simulation using the quadratic sliding law (see table A.10 and Fig.A.50 in the supplement) but the baseline set of parameters is already the optimum with the linear sliding law. Except for the 5 km resolution simulation, we find improvement of the same order of magnitude when using a quadratic law (see table A.10 and Fig.A.51 and A.52 in the supplement).

Table 2.6: Sum over time of the total ice volume difference and surface elevation RMSE between the base run and the optimal Fnslid/Fnflow parameters. Linear sliding law.

	res (km)	Volume diff		hs RMSE (m)	
		sum (10^{14} m ³)	Improvement (%)	sum (m)	Improvement (%)
Base	5	1.4		2030	
Optimal	5	1.6	-11.8	2090	-2.88
Base	10	3.1		5260	
Optimal	10	3.2	-3.83	4850	7.95
Base	25	16		12400	
Optimal	25	14	11.2	11100	10.4

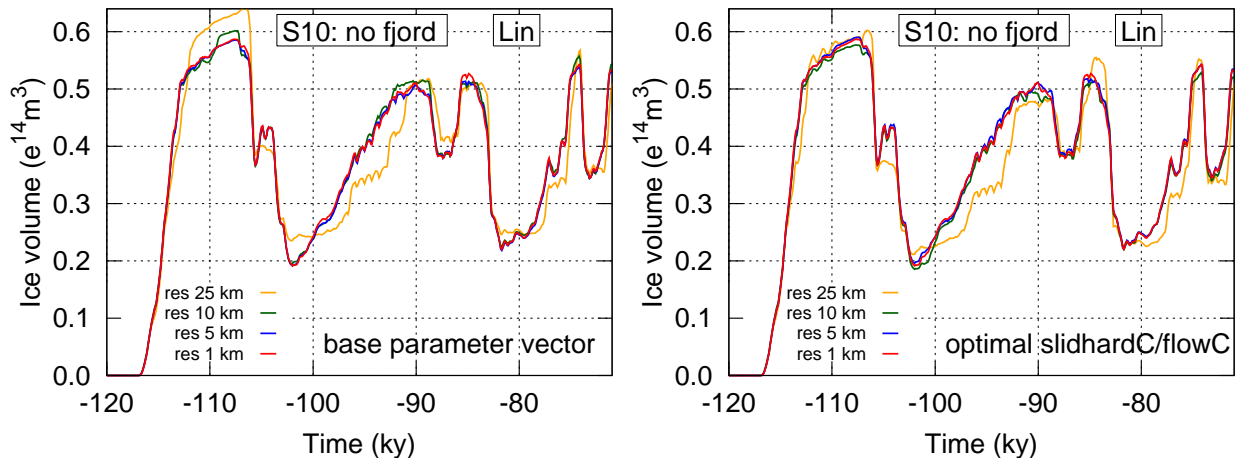


Figure 2.11: ice volume evolution with the baseline parameter vector (left panel) and the optimal sets of slidhardC and flowC parameters (right panel). These simulations use the linear (Lin) sliding law. The different colours represent different resolutions.

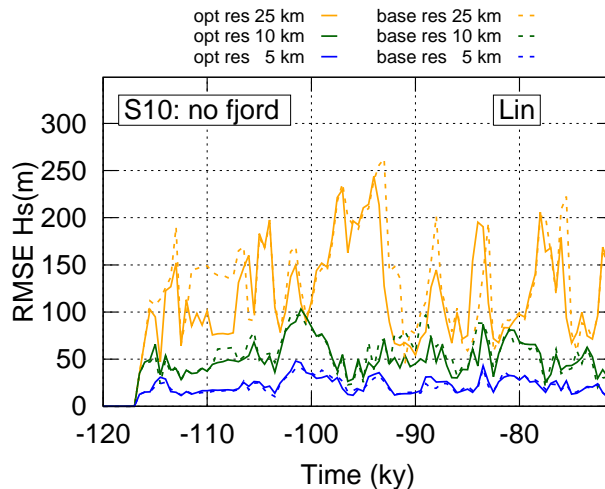


Figure 2.12: Surface elevation **RMSE** (compared to the 1 km resolution simulation) when using the baseline parameter vector (dotted lines) and the optimal sets of `slidhardC` and `flowC` parameters (solid lines). The different colours represent different resolutions. These simulations use the linear (Lin) sliding law.

2.4.3.2 Soft bed sliding parameter and basal topography upscaling methods

In the set of experiments performed to reduce the grid dependency by modifying the soft bed sliding parameters, the flow enhancement factor and the hard bed sliding coefficient are set to the values presented in table 2.5.

Fig.2.13(a) shows the impact of the different methods used to upscale the basal elevation from the 1 km resolution grid to the coarse resolution grids. With the soft bed sliding parameters tested the box average gives smaller errors than when using the deepest depth in the fjord(s), the fjord depth average, the average between the fjord average and the box average, or the average between the deepest depth in the fjord.

For each resolution, we extract the sliding coefficient that most reduces the misfits with the 1 km resolution simulations from Fig.2.13(b). Table 2.7 summarizes the optimum sliding coefficients at each resolution.

Table 2.8 shows the misfit reduction with optimum parameter usage in coarse resolution simulations (relative to the 1 km resolution reference simulation). We find the same response when using a quadratic law instead of a power law (see table A.11 in the supplement). At each resolution, Fig.2.14 and 2.15 show the approximately same improvement for all fjords. However, at 5 km resolution, the surface elevation **RMSE** of the five 2 km fjords region (which drains ice from a broader region than

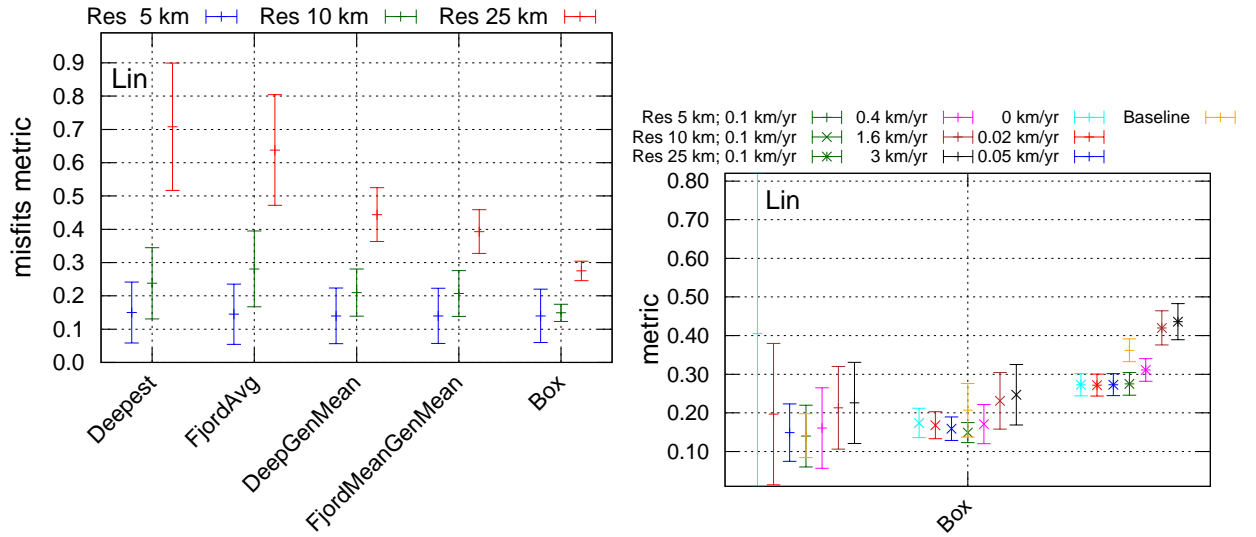


Figure 2.13: Metric (normalized ice volume differences plus normalized surface elevation RMSE compared to the 1 km resolution simulation using the base parameter vector) averaged over time and all the synthetic fjords. The left panel shows the impact of different topography interpolation methods (deepest fjord depth, *Deepest*, fjord depth average, *FjordAvg*, the average between the deepest depth in the fjord, *DeepGenMean*, the average between the fjord average and the box average, *FjordMeanGenMean*, and the box average, *Box*) when the 0.1 km/yr basal sliding coefficient is used. The right panels focus on the impact of parameters when the box average is used for the interpolation. These simulations use the linear (Lin) sliding law.

Table 2.7: Optimal soft bed sliding coefficient.

Resolution	sliding law			
	Linear coefficient	20 kPa vel	Quadratic coefficient	20 kPa vel
5 km	2	400 m/yr	0.025	100 m/yr
10 km	0.5	100 m/yr	0.0125	50 m/yr
25 km	0.5	100 m/yr	0.005	20 m/yr

any other fjord regions) after optimization is still approximately three times larger than the errors in any other region. This shows the limitation of our optimization in a region densely populated by fjords.

Table 2.8: Ice volume difference and surface elevation [RMSE](#) between the base run and the optimal Fnsed/Fnslid/Fnflow parameters. Linear sliding law.

		Volume diff				hs RMSE (m)			
		(10^{14} m^3)		Improvement (%)		(10^{14} m^3)		Improvement (%)	
	res (km)	avg	std	avg	std	avg	std	avg	std
Base	5	0.014	0.016			60.6	19.2		
Optimal	5	0.0054	0.0089	49.7	52.7	37.2	17.3	24.1	27.2
Base	10	0.014	0.02			92.6	16.6		
Optimal	10	0.0088	0.0079	19.4	73.3	65.4	31.9	17	28.6
Base	25	0.037	0.032			147	15.9		
Optimal	25	0.021	0.022	25	69.6	121	70.5	4.97	41.8

After optimization of the parameters, the ice volume time series follows the 1 km resolution simulations more closely (see Fig.2.16 and 2.17). For some regions, however, the 25 km resolution simulation still has a lag during the beginning of stadial events (see Fig.2.17). Net improvement can also be observed in the surface elevation [RMSE](#) (see Fig.A.56), but the 25 km resolution simulation still performs poorly compared to the 5 and 10 km resolution. The average surface elevation [RMSE](#) at 25 km resolution is still on average twice as large as at 10 km resolution (see table 2.8). This suggests that, even with our optimization, running ice sheet system models at 10 km instead of 25 km resolution should be considered if computational resources permit.

In section 2.4.1 we described the impact of fjord characteristics on the ice volume evolution at different resolution. As a first attempt to reduce the resolution dependency, we take into account only the total fjord area in a region. As the region with multiple fjords (five 2 km fjords) is the only one showing significant errors after optimization.

The ice velocities differences between coarse resolution simulations and the high resolution simulations with the optimized parameter vector (Fig.2.19) are of the same order of magnitude as with the baseline parameter vector (Fig.2.7). The velocity fields are still overestimated in fjord regions. We are currently running experiments to explore the impact of optimizing the sliding coefficient using the ice flux differences in addition to the surface elevation differences between the coarse resolution simulations

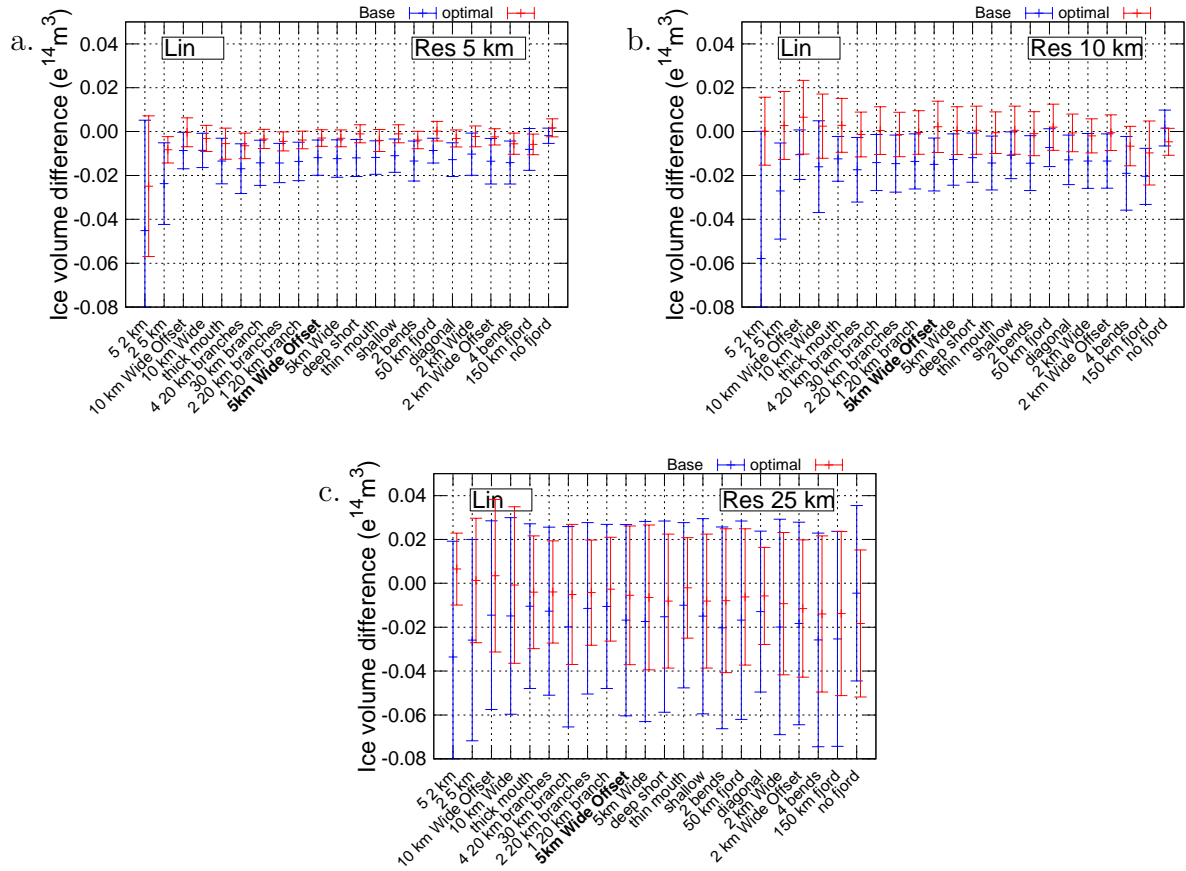


Figure 2.14: Ice volume differences (average and standard deviation over 50 kyr) between simulations at: a. 5 km, b. 10 km and c. 25 km resolution and 1 km resolution simulations. Simulations use the baseline (blue) or the optimized (red) parameters vector and the linear (Lin) sliding law. The boldface 5 km fjord, in the x axis, represents limit between regions generating less ice than the reference fjord and the region with more ice.

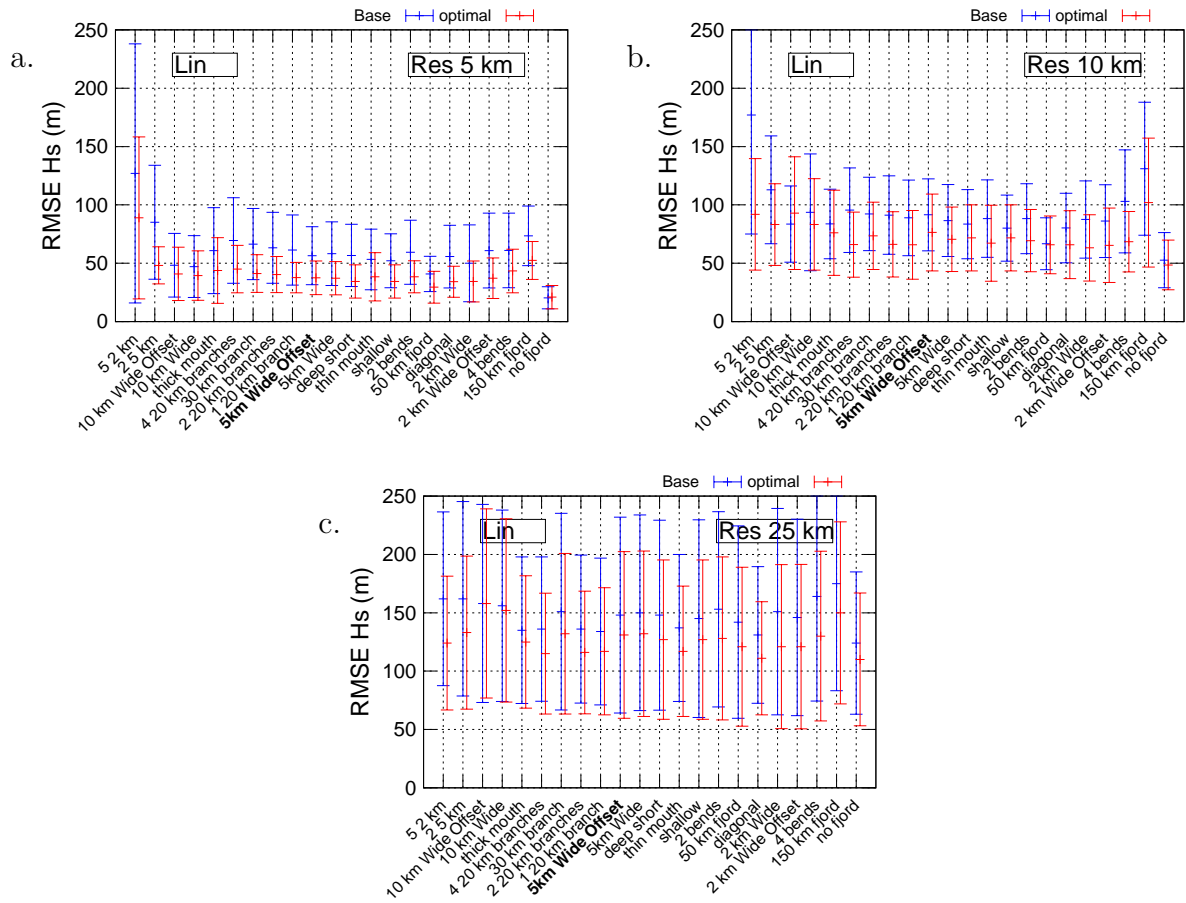


Figure 2.15: Surface elevation RMSE differences (average and standard deviation over 50 kyr) between simulations at: a. 5 km, b. 10 km and c. 25 km resolution and 1 km resolution simulation. Simulations use the baseline (blue) or the optimized (red) parameters vector and the linear (Lin) sliding law. The boldface 5 km fjord, in the x axis, represents limit between regions generating less ice than the reference fjord and the region with more ice.

and the reference simulations.

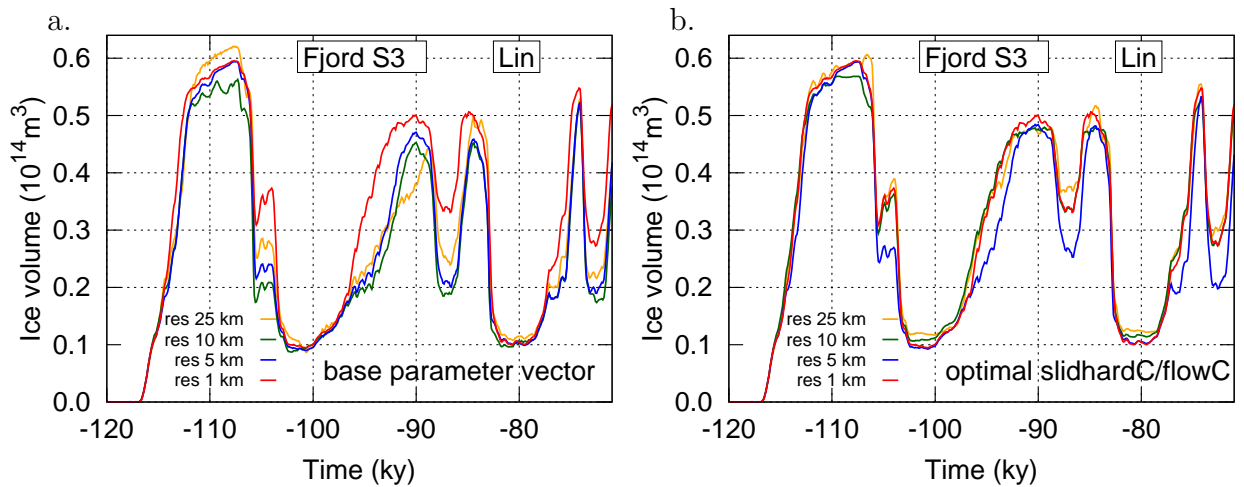


Figure 2.16: Ice volume evolution in a region (S3) with five 2 km wide, 100 km long fjords using the baseline parameter vector (left panel) and the optimal set of parameters (right panel). These simulations use the linear (Lin) sliding law.

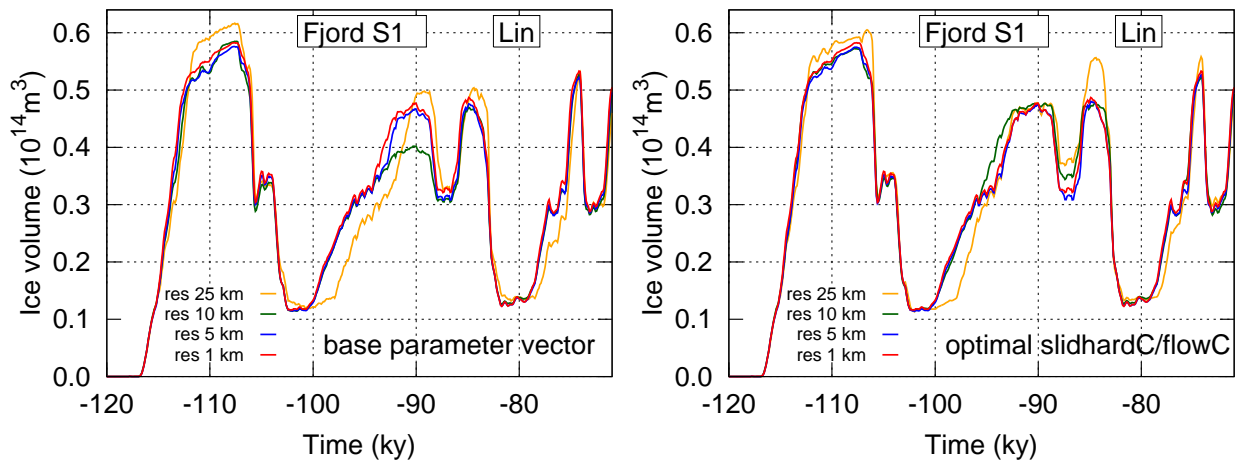


Figure 2.17: Ice volume evolution in a region (S1) with a 10 km wide, 100 km long fjord using the baseline parameter vector (left panel) and the optimal set of parameters (right panel). These simulations use the linear (Lin) sliding law.

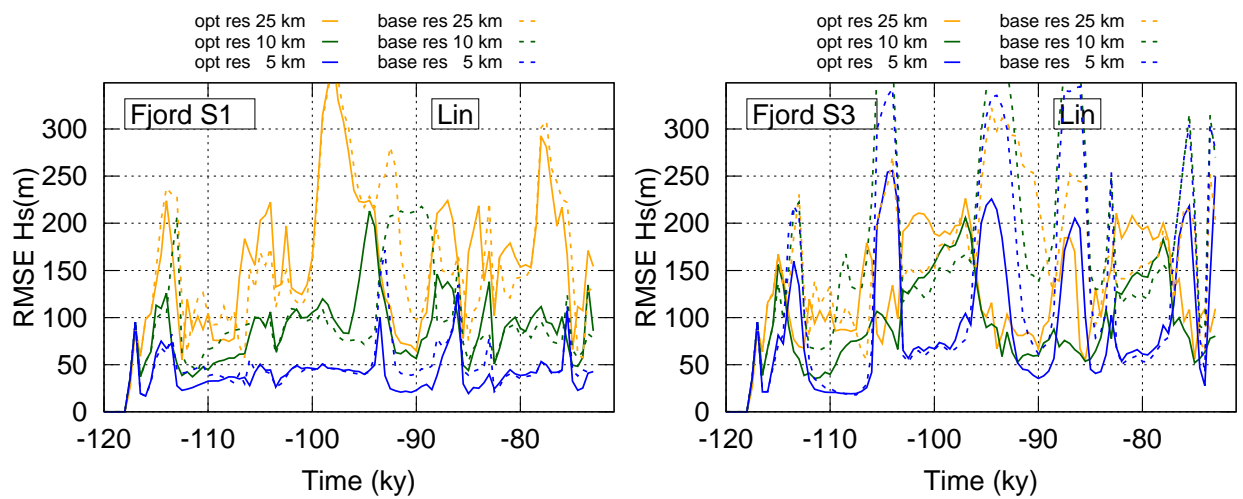


Figure 2.18: Surface elevation [RMSE](#) evolution (compared to the 1 km resolution simulation) using the baseline (dotted lines) and the optimal (solid lines) parameter vector . These simulations use the linear (Lin) sliding law over a region (S1) with a 10 km wide, 100 km long fjord (left panel) and a region with five 2 km wide, 100 km long fjords (right panel).

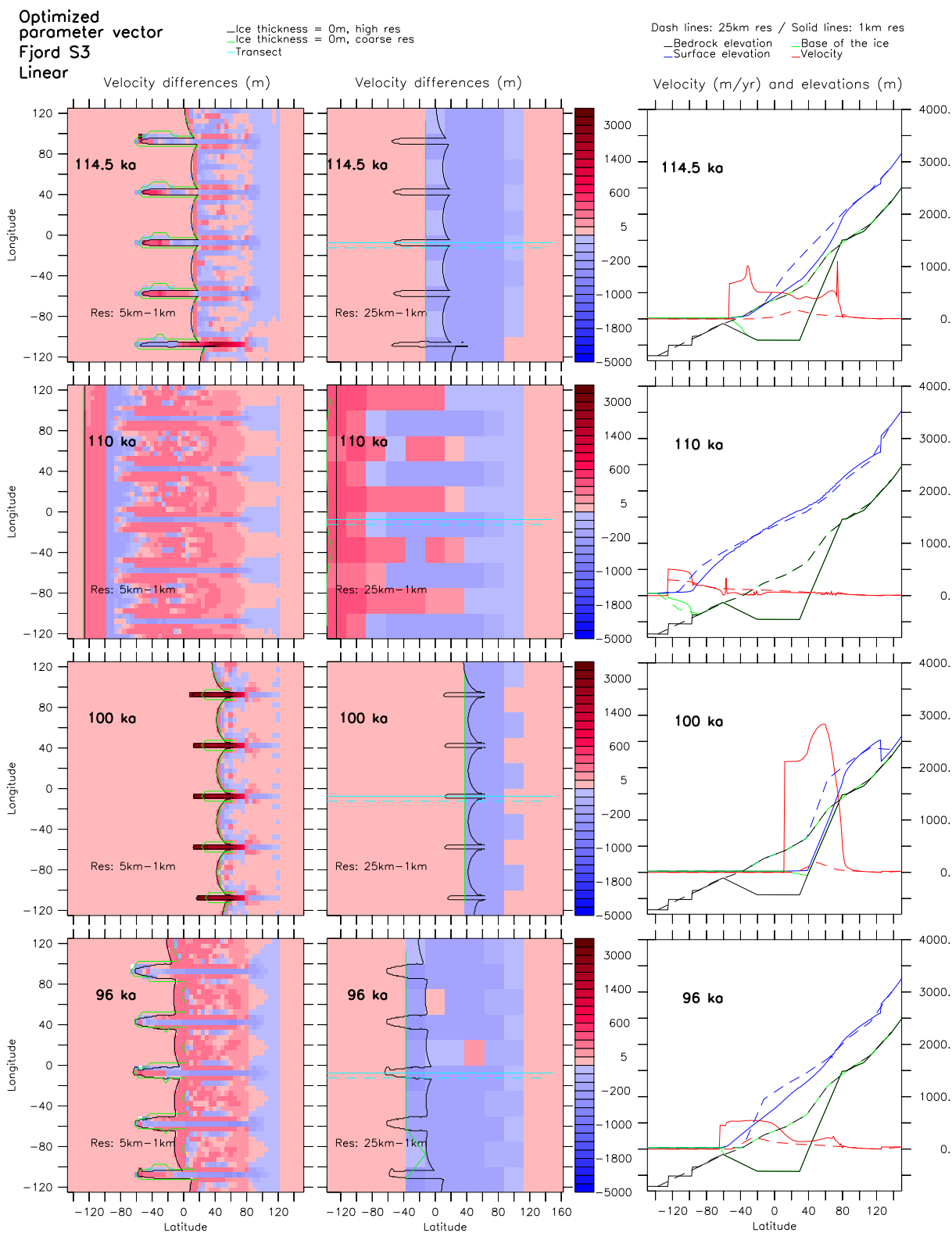


Figure 2.19: Results from a simulation using optimized parameters. Ice velocity fields at 5 km resolution (left panel) and 25 km resolution (central panel) compared to a 1 km resolution simulation at different time slices. The panel on the right side shows the surface, base and velocity evolution in the 25 and 1 km resolution simulations. These simulations use the baseline parameter vector and linear (Lin) sliding law over the region with five 2 km wide fjords.

2.5 Conclusion

Results from PSU/GSM model simulations run at 1 km resolution over regions of 300 km by 250 km with different fjord characteristics show that, independently of the sliding law used (linear or quadratic dependency to the basal stress):

- A region with no fjord generates on the order of 8 % (with a standard deviation over time of the order of 9 %) more ice than a reference region with a 5 km wide and 100 km long fjord over the full grid.
- Reducing the length/width of the fjord or increasing the resistive stresses (for example with the presence of bends in the fjords) increases the ice volume by up to 3 % (with a standard deviation over time on the order of 3.4 %) over the full grid.
- Compared to the reference fjord, increasing the number of fjords, the width of the fjords or adding branches reduces the total ice volume by up to 9.6 % (with a standard deviation of the order of 13 %).
- The impact of a fjord system on the ice evolution has dependence on more than just fjord area. Five 2 km wide fjords reduce the ice volume by approximately 8 % while a 10 km wide fjord reduces it by approximately 3.5 %.

No statistical relationships could be derived relating the ice drainage through fjords to the fjord characteristics.

Modelling ice evolution in fjord regions shows a grid resolution dependency of the surface elevation [RMSE](#) (compared to the 1 km). 25 km resolution simulations produce errors three times greater than at 5 km resolution. Surface elevation [RMSE](#) and ice volume difference misfits to the 1 km resolution simulations increase with the geometric complexity of the fjord system. Reducing the soft bed sliding coefficient proportionally to the fjord area in a coarse grid cell is not sufficient to reduce the impact of the overestimation of the fjord width at coarse resolution. However, the error in ice volume evolution and surface elevation [RMSE](#) are similar for different fjord geometry characteristics of a single fjord.

We reduce the PSU/GSM model resolution dependency at 5, 10, and 25 km resolution as follows. Following a different approach than [Calov et al. \(2015\)](#), we focus on the fjord regions and the differences generated by running a hybrid [SIA/SSA](#) model

at high (1 km) and low (5, 10 and 25 km) resolutions to tune the flow enhancement parameter, the hard bed sliding coefficient and the soft bed coefficient (Table 2.5 and 2.7 summarizes the parameters used at each resolutions) when using either a linear or quadratic basal sliding law. After tuning to minimize resolution dependence, the errors remaining in the 25 km resolution simulations are still twice as large as at 10 km resolution. In detail, tuning reduces the surface elevation [RMSE](#) (compared to the 1 km resolution) by 24.1% (with a standard deviation of 27.2%) for 5 km resolution simulation, by 17% (with a standard deviation of 28.6%) for 10 km resolution simulations and by 5% (with a standard deviation of 41.8%) for 25 km resolution simulations. However, the 25 km resolution simulations with resolution corrected parameters still shows a phase lag of approximately 2 kyr in ice growth after the first interstadial period compared to the 1 km resolution simulation.

Upscaling the basal elevation from the 1 km resolution grid to the coarse resolution grids using the deepest depth in the fjord(s), the fjord depth average, the average between the fjord average and the box average, or the average between the deepest depth in the fjord generates more misfit (in term of total ice volume and surface elevation [RMSE](#) with 1 km resolution simulation) compared to a box average upscaling.

We optimized over 20 different synthetic fjords with geometric characteristics that approximately span those that occur in reality. It is therefore applicable in any coastal region of fast flowing ice. This parameterization can be used in any ice sheet model using a hybrid shallow ice and shallow shelf approximation of the Stokes equations. The same methodology can be followed, comparing the 1 km resolution simulation using the hybrid model with the coarse resolution simulation using the [SIA](#) to improve the ice drainage through fjords in an ice sheet model that uses the [SIA](#).

Using a hybrid [SSA/SIA](#) model instead of a [HO](#) model decreases the total ice volume by 7.7% (with a standard deviation of 1.4% over different regions) at the end of an inception period in a 1 km resolution simulation. Thus the conclusion from continental scale model intercomparisons that hybrid [SSA/SIA](#) models generate more ice than [HO](#) models ([Pattyn et al., 2013](#)) is not valid in fjord regions.

The differences observed in ice volume and surface elevation [RMSE](#) when using a linear or quadratic sliding law are of the same order of magnitude as the resolution impact. This shows the need for improved constraint on the appropriate form of the sliding law.

We have shown that the number of fjords and the fjord area are the fjord characteristic that most impacts ice drainage. The differences in ice volume evolution

between a region with a fjord or not can be as large as the differences in ice volume evolution when the thermodynamic model is turned on and off. In addition, the ISM errors in representation of ice drainage through fjords increase with grid cell size. We reduce the model resolution dependency of ice drainage through fjords of different geometric characteristics by tuning the flow enhancement parameter, the hard bed sliding coefficient, and the soft bed coefficient.

The question remains whether the ice flux differences between coarse and high resolution simulations can be used in the tuning of the flow enhancement parameter, the hard bed sliding coefficient, and the soft bed coefficient parameters to reduce the misfits with the 1 km resolutions simulations. In addition, tests need to be implemented to examine the impact of this parameterization on the evolution of an ice sheet during the last glacial cycle. Finally, given the documented sensitivity to the value of the sliding exponent, there is a need for improved constraint on the appropriate form of the sliding law.

2.6 Author contribution

Kevin Le Morzadec and Lev Tarasov designed the experiments. Kevin Le Morzadec performed the simulations, the optimization and the data analysis with contributions from Lev Tarasov. Kevin Le Morzadec prepared the manuscript with some input and edits from Lev Tarasov.

2.7 Acknowledgements

Support provided by Canadian Foundation for Innovation, the National Science and Engineering Research Council, and ACEnet. Lev Tarasov holds a Canada Research Chair. We thank Mathieu Morlighem for his support with [ISSM](#) configurations.

Appendix A Thermodynamic impact

Inclusion of fully coupled thermodynamics is standard for ice sheet modelling. To compare the impact of fjord characteristics to the impact of another process on ice sheet evolution we run a set of simulations turning the thermodynamic model off.

Using the PSU/GSM model (with the baseline parameter vector) at 5, 10, and 25 km resolution, we prescribe climate fields, that simulate ice growth and decay observed using paleo-data from 120 ka to 70 ka, over the nine real fjord regions with the thermodynamic model turned on and off. To bound the impact of the bed temperature when the thermodynamic model is off we conduct an experiment with a constant frozen bed over the entire region and another experiment with frozen bed outside of the fjords and a bed at the pressure melting point within the fjords.

The average and standard deviation of the differences, when the thermodynamic model is turned on and off, are computed using results from simulations generated with the 9 Norwegian fjord regions. The "ice volume" is an average over 1000 yr centered around two stadials (110.5 to 109.5 and 90.5 and 89.5 ka) and two interstadials (101.5 to 100.5 and 80.5 to 79.5 ka) periods. The ice volume growth and decay rates in-between these periods are similar when the thermodynamic model is turned on or off. The total volume of ice present during stadial events however is affected by the amount of ice discharged through the fjords.

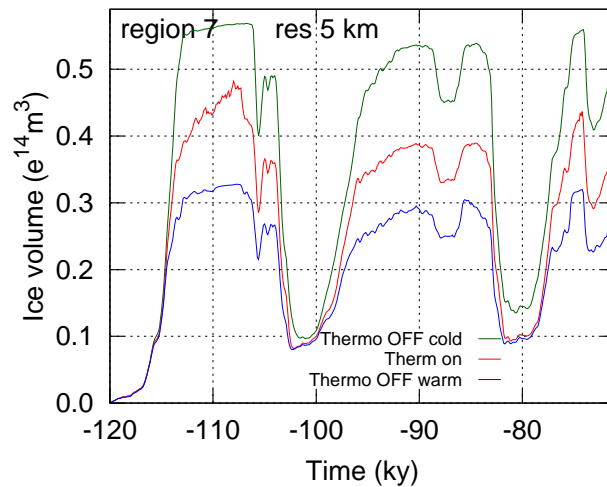


Figure A.1: Ice evolution over region 7, from Fig. A.1, when the thermodynamic model is turned on (red line), off with warm base (blue line) and off with cold base (green line).

During stadial periods the PSU/GSM, on average, overestimates the ice volume by 18% (with a standard deviation of 10%) when the fjords have a cold base and underestimates the ice volume by 19% (with a standard deviation of 8.3%) when the fjords base are at pressure melting point. The differences drop by two percents at 10 km resolution. At 25 km resolution, the differences with a warm base are

4.2% (with a standard deviation of 5.8%) over a cold base fjord and 15% (with a standard deviation of 6.3%) with a warm base. As most of the fjords are free of ice during interstadial phases the thermodynamic model has a limited impact on the ice evolution (see Fig.A.57(a) around 110 and 80 ka). Fig.A.57(a) shows an example of the thermodynamic impact on the ice volume for a simulation over region 7 at 5 km resolution. A more detailed table of the results is presented in the supplement (Table A.12) with an example of the ice volume time series at different resolution (Fig.A.57).

Chapter 3

A new sub-grid surface mass balance and flux model for continental-scale ice-sheet modelling: validation and last glacial cycle

3.1 Abstract

To investigate ice sheet evolution over the timescale of a glacial cycle, 3-D [ISM](#)s are typically run at “coarse” grid resolutions (10–50 km) that do not resolve individual mountains. This will introduce to-date unquantified errors in [SG](#) transport, accumulation and ablation for regions of rough topography. In the past, synthetic hypsometric curves, a statistical summary of the topography, have been used in [ISM](#)s to describe the variability of these processes. However, there has yet to be detailed uncertainty analysis of this approach.

We develop a new flow line [SG](#) model for embedding in coarse resolution models. A 1 km resolution digital elevation model was used to compute the local hypsometric curve for each [CG](#) cell and to determine local parameters to represent the hypsometric bins’ slopes and widths. The 1-D mass transport for the [SG](#) model is computed with the shallow ice approximation. We test this model against simulations from the 3-D [ISSM](#) run at 1 km grid resolution. Results show that none of the alternative

parameterizations explored were able to adequately capture [SG](#) surface mass balance and flux processes. Via glacial cycle ensemble results for North America, we quantify the impact of [SG](#) model coupling in an ISM. We show that [SG](#) process representation and associated parametric uncertainties, related to the exchange of ice between the [SG](#) and [CG](#) cells, can have significant (up to 35 m eustatic sea level equivalent for the North American ice complex) impact on modelled ice sheet evolution.

3.2 Introduction

The resolution used in any model of complex environmental systems (e.g. ice sheet models ([ISMs](#)), general circulation models or hydrological models) limits the processes that can be represented. For continental-scale glacial cycle contexts, [ISMs](#) are currently run at resolutions of about 10–50 km ([Pollard and DeConto, 2012](#); [Tarasov et al., 2012](#); [Colleoni et al., 2014](#)). Processes such as surface mass balance on mountain peaks, iceberg calving, and ice dynamics in fjords are sensitive to scales of about 100 m to a few kilometres and therefore have to be parameterized. For example, even at 10 km grid resolution, mountain peaks are smoothed to bumps in a plateau ([Payne and Sugden, 1990](#)), inducing errors in computed surface mass balance ([Marshall and Clarke, 1999](#); [Franco et al., 2012](#)). If the mean surface elevation of a coarse grid cell is below the [Equilibrium Line Altitude \(ELA\)](#), ice ablation is overestimated (e.g. [Tarasov and Peltier, 1997a](#)). Thus, coarser grid resolution can lead to temporal and spatial errors in ice sheet inception ([Abe-Ouchi and Blatter, 1993](#); [Abe-Ouchi et al., 2013](#)) and subsequent evolution ([Van den Berg et al., 2006](#); [Durand et al., 2011](#)).

Any model of complex environmental systems will have [SG](#) processes that are, by definition, not dynamically resolved. Accurate modelling of such systems must therefore determine whether the [SG](#) processes variability is relevant for the given context. If it is, some of the impact of this [SG](#) variability may be captured in a parameterized form ([Seth et al., 1994](#); [Leung and Ghan, 1995](#); [Marshall and Clarke, 1999](#); [Giorgi et al., 2003](#); [Ke et al., 2013](#)). For example, to improve surface mass balance in continental-scale ice sheet models, [Marshall and Clarke \(1999\)](#) used hypsometric curves, which represent the cumulative distribution function of the surface elevation. In this method, each individual glacier is not explicitly represented. Instead, 2-D topographic regions are parameterized with different hypsometric bins, representing a discrete number of elevations and their associated area. In addition to ablation and

accumulation at each **SG** bin, there is **SG** ice transport from high elevation regions to valleys where the average altitude is below the **ELA**. Starting with ice-free conditions, [Marshall and Clarke \(1999\)](#) found an increase in the total ice volume over North America after a 3 kyr¹ simulation when this hypsometric parameterization is coupled to an ice sheet model. The impact and accuracy of this **SG** model have yet to be quantified. The model was only validated against observations of a glacier located in the region used for tuning the parameterization ([Marshall et al., 2011](#)). Moreover, the communication between the **SG** and **CG** models was identified as a potentially important source of error ([Marshall and Clarke, 1999](#)), but its impact has not been documented.

In this chapter, we develop a new **SG** model extending the approach of [Marshall and Clarke \(1999\)](#) and [Marshall et al. \(2011\)](#). We use hypsometric curves that account for a much larger set of topographic information than just the maximum, minimum and median elevation. We present a new slope parameterization to compute the velocities that account for **SG** slope statistics. An effective width is added for the representation of the ice fluxes between **SG** bins. In contrast to the one-way communication used in the past, another modification to the original model is a two-way exchange of ice between the **SG** and **CG** cells. The **CG** ice thickness updating accounts for **SG** ice thickness, and the **SG** model accounts for ice flux out of the **CG** cell. For the first time, we evaluate the accuracy of the **SG** model against high resolution simulations by a higher order ice sheet model (**ISSM**; [Larour et al., 2012](#)). Sensitivities to the **SG** model configuration, such as the number of hypsometric bins, are assessed. We examine the extent to which the inclusion of further topographic statistics (e.g. the peak density in a region or the variance of the slopes) can improve computed sub-grid fluxes. We also evaluate the impact of embedding the **SG** model in the **GSM** (formerly the **MUNGSM**), our coarse grid model, for last glacial cycle simulations of the North American ice complex, using an ensemble of parameter vectors from a past calibration of the **GSM** ([Tarasov et al., 2012](#)). Special attention is given to the impact of the coupling between the **SG** model and the **GSM**.

¹In this chapter, “kyr” is used to represent time intervals and “ka” for time before present day.

3.3 Model description

3.3.1 Sub-grid model

The sub-grid model is a finite difference flow line model composed of a diagnostic equation for the ice velocities and a prognostic equation for ice thickness evolution. The surface mass balance is calculated using a [Positive Degree Day \(PDD\)](#) method. The elevation of a 3-D region is parameterized using a hypsometric curve. Differences between the new [SG](#) model and the [Marshall et al. \(2011\)](#) approach are summarized in [Table 3.1](#).

3.3.1.1 Hypsometric curves

[Marshall and Clarke \(1999\)](#) built their hypsometric curves, representing the basal elevation of a region, synthetically from the minimum, maximum and median elevation of the topography. We generate the hypsometric curves from the [GEBCO](#) 1 km resolution [DEM](#) ([Centre, 2010](#)). To select a region fitting the coarse resolution grid cell of the [GSM](#) (degrees), the [GEBCO](#) Cartesian coordinates are converted in degrees assuming the Earth as a perfect sphere with radius of 6370 km. The curves are obtained in a two-step process. First, the region is divided into N bins of equal altitude range. Then, to avoid empty bins, the surface elevation range of each empty bin is expanded (consequently decreasing the elevation ranges of the higher and lower adjacent bins) using as many adjacent bins as necessary until these bins represent approximately the same surface area. This process is repeated from the highest bin to the lowest as many times as necessary.

We use 1 km resolution gridded data, so that the area of each bin is proportional to the number of high resolution grid cells assigned to that bin. The alternative of using equal areas in each bin has been discarded as it smooths the results in regions of low peak density. A total of 10 bins have been selected in this study, based on the comparison against high resolution modelling (see [Sect. 3.4.1](#)). [Marshall and Clarke \(1999\)](#) and [Marshall \(2002\)](#) used, respectively, 10 and 16 hypsometric bins in their hypsometric curves.

At any time step, t , the surface slopes, S_k^t , for [SG](#) bin k , from 1 (highest) to N

Table 3.1: Differences between our new SG model and Marshall and Clarke (1999)/Marshall et al. (2011) models.

	New SG model	Marshall's model
Hypsometric curves		
Elevation	Computed from the DEM	Min, max and median elevation
Effective lengths	Computed from the DEM slopes	$\propto 50$ km
Width	\propto Number of cells in contact with adjacent levels	Not included
Number of levels (N)	10	10 to 16
SG fluxes		
Approximation	SIA	SIA
Ice rheology (T° equivalence)	0°C	-40°C
SG model activation		
Activated	Rough topography $\Delta h_b > 500\text{m}$ At least half of the area is above sea level	Every grid cell
Deactivated	Lowest SG level surface elevation reaches the bedrock elevation of the highest level	Lowest SG level filled
Reactivation	$H_{CG} < \frac{h_{b,SG(top)} - h_{b,CG}}{2}$	$H_{CG} < \frac{h_{b,SG(top)} - h_{b,SG(bottom)}}{N}$
SG \rightleftharpoons CG		
Ice thickness	SG to CG: Done as soon as the SG model is activated H_{CG} = Volume of lowest SG levels (total volume when SG is turned off) CG to SG: H_{SG} = Average between equal ice thickness and lowest levels filled	Done only when the lowest SG level is filled Not explained
Isostatic adjustment	CG adjustment applied at SG level	Not included
Flux to adjacent CG cells		
	Fluxes computed at CG level and limited to the fraction of the lowest SG levels area. Fluxes in or out of a CG cell redistributed over the lowest SG levels.	Fluxes computed at CG level only. No flux out of the cell treated at SG level. Fluxes coming from a CG cell to a SG cell redistributed over the lowest SG level.

(lowest), are computed from the surface elevation $h_{d,k}^t$ and an effective length L_k :

$$S_k^t = \frac{h_{d,k+1}^t - h_{d,k}^t}{L_k}. \quad (3.1)$$

To compute the slope at the lowest bin we assume an ice cliff boundary condition. The surface elevation $h_{d,N+1}$ is set to the basal elevation of the lowest hypsometric bin $h_{b,N}$. Instead of setting the hypsometric slopes with an effective length proportional to the horizontal extent of the CG cell (Marshall and Clarke, 1999), we account for the cubic dependence of ice flow on surface slope (see Eqs. 3.3 and 3.4). Specifically, for each hypsometric bin we compute the slope, S_k^0 , as the cube root of the mean of the cube of the magnitude of the slopes from the GEBCO data. The effective length, L_k , for SG bin k is computed from the basal elevation $h_{b,k}$:

$$L_k = \frac{(h_{b,k+1} - h_{b,k})}{S_k^0}, \quad (3.2)$$

where h_b is the basal elevation. As no information is extracted about the basal elevation downstream of the terminal SG cell, the effective length at the first upstream bin is used at the lowest hypsometric bin. A small effective length can generate unrealistically high velocities in that bin. To avoid this, the lowest bin effective length is set to the mean effective length of all the hypsometric bins when the altitude difference between the two lowest bins is less than 50 m.

The flow line model requires an effective width, W , for the representation of flux between hypsometric bins. W_k of each hypsometric bin is set to the total contact length of the SG cells assigned to the bin with adjacent lower hypsometric bin grid cells as detailed in Fig. 3.1.

3.3.1.2 Surface mass balance

We use the positive degree day method described in Tarasov and Peltier (1999a) to compute accumulation and ablation from monthly mean temperature and precipitation. A constant environmental lapse rate adjusts the temperature to the ice surface elevation. A parameterization of the elevation–desertification effect (Budd and Smith, 1981) reduces the precipitation by a factor of 2 for every kilometre increase in elevation. Snow is melted first and the remaining positive degree days are used to melt ice with allowance for the formation of superimposed ice. The Supplement B.1 includes a more

							6	6	
		6				8	7	7	5
	6	7	5				8	7	6
8	7	7	6				9	9	
8	7	7	6						
	6	6							
						6			
					8	7	6		
						8			

Figure 3.1: Schematic representation of the effective width of the 7th hypsometric bin for a region of 10 km by 10 km. Each square represents a high resolution (1 km) grid cell. The numbers define the hypsometric bin these SG grid cells belong to. The total length of all red lines (14 km) represents the effective width for the 7th bin.

detailed description of the surface mass balance module.

The [GSM](#) and [ISSM](#) compute the surface mass balance using the same [PDD](#) method.

3.3.1.3 Ice thickness evolution

The prognostic equation for the ice thickness (H) is computed, at each hypsometric bin, from the vertically integrated continuity equation as

$$\frac{\partial H}{\partial t} = \dot{M}_s - \nabla \cdot (\bar{\mathbf{u}}H) = \dot{M}_s + \nabla \cdot (DS). \quad (3.3)$$

S is the surface slope and \dot{M}_s is the surface mass balance rate (basal melt is computed in the [CG GSM](#) but ignored in the [SG](#) model). \bar{u} is the vertically integrated ice velocity of the [SG](#) model derived using the [SIA](#). The effective diffusivity D is given by

$$D = \frac{2}{n+2} (\rho g)^n A_0 H^{n+2} (S)^{n-1}. \quad (3.4)$$

The creep exponent n of Glen's flow law is set to 3. A_0 is the creep parameter in $\text{Pa}^{-3} \text{s}^{-1}$, $\rho = 910 \text{ kg m}^{-3}$ and $g = 9.81 \text{ m s}^{-2}$. Ice flow is insignificant when the ice thickness is on the order of 10 m. To avoid potential numerical instabilities, velocity is

set to 0 if ice thickness is less than 20 m.

In their most recent experiments, [Marshall et al. \(2011\)](#) tuned their revised model against the present day total ice volume (encompassing 27% uncertainties) in the eastern slopes of the Canadian Rockies. This tuning sets the ice rheology parameter for an ice temperature equivalence of approximately -40°C . As the [SG](#) model is used for regions that are either starting to accumulate ice or else deglaciating, basal ice temperature (where most deformation occurs) is likely close to freezing. The creep parameter is therefore fixed to a value corresponding to an ice temperature of 0°C using the Arrhenius relation from the [European Ice Sheet Modelling Initiative \(EISMINT\)](#) project ([Payne et al., 2000](#)).

Equation (3.3) is solved semi-implicitly using a central difference discretization as

$$\begin{aligned} \frac{\Delta x_k \Delta y_k}{\Delta t} (H_k^{t+1} - H_k^t) = & \\ + D_k^t (h_{b,k+1}^t + H_{k+1}^{t+1} - h_{b,k}^t - H_k^{t+1}) \frac{\Delta y_k}{\Delta x_k} - & \quad (3.5) \\ D_{k-1}^t (h_{b,k}^t + H_k^{t+1} - h_{b,k-1}^t - H_{k-1}^{t+1}) \frac{\Delta y_{k-1}}{\Delta x_{k-1}} + \dot{M}_s \Delta x_k \Delta y_k. & \end{aligned}$$

The superscripts t and $t + 1$ represent respectively the current and the subsequent time step. Δx is the effective length L and Δy is the effective width W defined in Sect. 3.3.1.1.

At the highest bin, we assume that no ice flows into the region. At the lowest bin ice is allowed to flow out of the region.

3.3.1.4 Model limitations

The shallow ice approximation, used to compute fluxes, is formally invalid for high surface slopes such as present in mountain ranges like the Rockies. Simulating ice evolution over a 3-D terrain using a flow line model limits the ice flow representation. Ice flows from one [SG](#) bin to another using an average slope. Our model configuration does not allow for ice at high elevations to flow into an adjacent coarse grid cell. Nor does it allow for ice present at low elevations, in isolated regions having a closed drainage basin, to stay in a coarse grid cell. Moreover, the Arrhenius coefficient is computed with a constant ice temperature of 0°C . High velocities processes, such as periodical surges ([Tangborn, 2013](#); [Clarke, 1987](#)), cannot be represented since basal sliding and basal hydrology are not present in the current study.

The hypsometric length parameterization inferred from the surface slopes are correct for ice free regions, but it is only an approximation once the ice starts building up. At the lowest hypsometric bin, slopes are computed assuming ice cliff boundary conditions.

For the comparison against [ISSM](#) results, the surface temperature is downscaled with a lapse rate of $6.5\text{ }^{\circ}\text{Ckm}^{-1}$. This typical value used in glacial modelling represents the average free-air lapse rate observed in the troposphere which need not match the impact of changing surface elevation. Studies over Iceland, Greenland, Ellesmere Island and the Canadian high Arctic report seasonal changes in the surface temperature lapse rates over mountain regions and glaciers, with a mean annual value of about $3.7\text{--}5.3\text{ }^{\circ}\text{C/km}$ ([Marshall and Losic, 2011](#)). Rates as low as $2\text{ }^{\circ}\text{C/km}$ are measured in the summer ([Gardner et al., 2009](#)). These values are tested in the [GSM](#) ensemble simulations where the lapse rate ranges between 4 and $8\text{ }^{\circ}\text{C/km}$.

3.3.2 GSM

The core of the [GSM](#) is a 3-D thermomechanically coupled ice sheet model. The model incorporates sub-glacial temperatures, basal dynamics, a visco-elastic bedrock response, climate forcing, surface mass balance, a surface drainage solver, ice calving and margin forcing. The grid resolution used for this study is 1.0° longitude by 0.5° latitude.

The thermomechanically coupled ice sheet model, described in detail in [Tarasov and Peltier \(2002\)](#), uses the vertically integrated continuity equation and computes the 3-D ice temperature field from the conservation of energy, taking into account 3-D advection, vertical diffusion, deformation heating, and heating due to basal motion. Velocities are derived from the [SIA](#) equations. The sub-glacial temperature field is computed with a 1-D vertical heat diffusion bedrock thermal model that spans a depth of 3 km ([Tarasov and Peltier, 2007](#)). If the base of the ice is at the pressure melting point, basal motion is assumed to be proportional to a power of the driving stress. The exponent for this Weertman-type power law is set to 3 for basal sliding and 1 for till deformation (detailed description in [Tarasov and Peltier, 2002, 2004a](#)). The geographic location of the sediment cover is determined from different data sets ([Laske and Masters, 1997](#); [Fulton, 1995](#); [Josenhans and Zevenhuizen, 1990](#)). Ice shelf flow is approximated with a linear function of the gravitational driving stress. At the base, ice melt is also computed from the energy balance.

The visco-elastic bedrock response is asynchronously coupled to the [GSM](#) with a 100-year interval. This module is based on the complete linear visco-elastic field theory for a Maxwell model of the Earth ([Tarasov and Peltier, 2002, 2007](#)).

At the surface, the parameterized climate forcing ([Tarasov and Peltier, 2004a, 2006, 2007](#)) is based on a linear interpolation between the present day climatology, derived from a 14-year average (1982–1995) of the 2m monthly mean reanalysis; [Kalnay et al., 1996](#)), and a [Last Glacial Maximum \(LGM\)](#) climatology. The [LGM](#) climatology field is derived from a linear combination of [Paleoclimate Modelling Intercomparison Project \(PMIP\)](#) I and II general circulation model results with the linear combination dependent on the maximum elevation of the Keewatin ice dome ([PMIP](#) I boundary conditions lacked a major Keewatin ice dome, while [PMIP](#) II had a large dome). The interpolation follows a glacial index derived from the [Greenland Ice-core Project \(GRIP\)](#) $\delta^{18}\text{O}$ record at the summit of the Greenland ice sheet ([Dansgaard et al., 1993; World Data Center-A for Paleoclimatology, 1997](#)). The surface mass balance is derived from this climatology using the same methodology as described in [Sect. B.1](#). A surface drainage solver is fully coupled asynchronously at 100-year time steps. It diagnostically computes downslope drainage, filling any depressions (lakes) if drainage permits ([Tarasov and Peltier, 2005, 2006](#)).

The calving module, described in detail in [Tarasov and Peltier \(2004a\)](#), is based on a height above buoyancy criterion with added mean summer sea surface temperature dependence. The inhibition of calving due to the presence of landfast sea ice is also parameterized. To reduce misfits between the model results and geological evidences of the ice configuration, the mass-balance forcing is nudged to promote compliance with geologically inferred deglacial margin chronologies ([Tarasov and Peltier, 2004a](#)).

3.3.3 GSM and sub-grid model coupling

In this section, we describe how the [SG](#) model is embedded in the [GSM](#) and the conditions applied to activate or deactivate the [SG](#) model in each [CG](#) cell. The [GSM](#) is run, at all times, over all the [CG](#) cells and the ice thickness is updated in cases where the [SG](#) model is activated. [Figure 3.2](#) gives a summary diagram of the coupling between the [GSM](#) and the [SG](#) model.

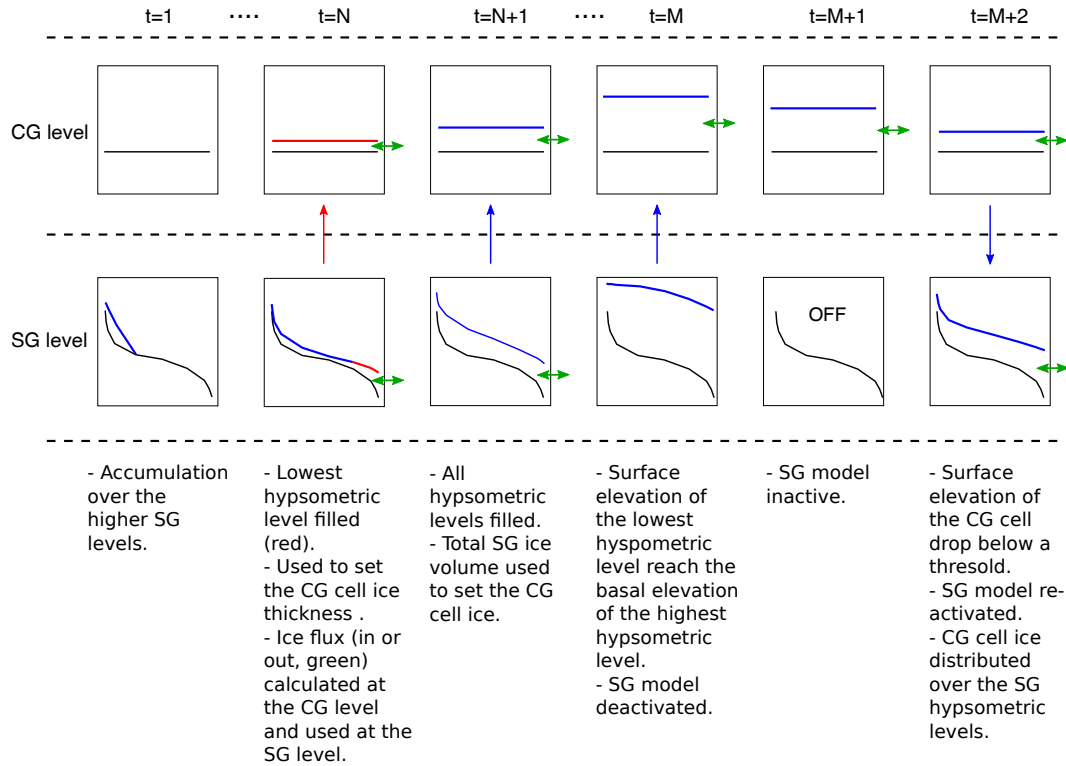


Figure 3.2: Communication between the GSM and the SG model for one CG cell.

3.3.3.1 Interaction between the sub-grid model and the GSM

There is two-way communication between the GSM and SG models to exchange information about ice thickness, surface mass balance, and surface temperature. Ice in a CG cell is added to the SG level² when the SG model switches from deactivated to activated for a given CG cell. The information about the ice evolution at the SG level is used to update the ice thickness, surface mass balance rate and surface temperature at the CG level.

Marshall et al. (2011) export SG ice to the CG level only when the lowest SG bin is filled and the SG model for the given CG cell is deactivated in the time step. In our model, SG–CG ice transfer is as follows. While the SG model is activated, CG ice volume is set to that of the filled SG bins. The rationale for this is the assumption that over a large mountainous region, such as the Rockies, an ice sheet grows by building up ice in major valleys (represented by the lowest hypsometric bins) from ice accumulation and ice flowing in from surrounding mountain peaks. A SG bin is

²SG level represents the hypsometric curve while CG level corresponds to a GSM cell.

classified as filled once its surface elevation reaches the basal elevation of the adjacent higher bin. The surface mass balance rate and surface temperature of the **CG** cells are updated to the new elevations. When the **SG** model switches from activated to deactivated, the total **SG** ice volume is transferred to the **CG** cell.

Once the **SG** model is reactivated in a **CG** cell during deglaciation, the ice volume present at the **CG** level is distributed over the different hypsometric bins. To account for the higher volume of ice in valleys, represented by the lowest hypsometric bins, the average of the following two mass-conserving distributions is used for **SG** initialization. The first is even distribution across every bin. The second keeps equal surface elevation for the lowest bins, starting from the lowest bin and using as many bins as necessary.

Marshall and Clarke (1999) have no ice flux to adjacent **CG** cells when the **SG** model is active. In our model, ice transport between **CG** cells, computed with the **GSM**, is modified using **SG** information. We assume that only the ice present in the filled bins flows out of the coarse grid region; therefore, only a fraction of the **CG** flux is permitted. This fraction is computed as the area of the filled **SG** bins divided by the total **CG** cell area. To avoid double counting of this inter **CG** flux, the **SG** model does not compute flux out of the lowest bin through Eq. (3.3) when coupled to the **GSM**. At every iteration, the **SG** model accounts for the **CG** ice flux. For **CG** ice flux into a cell with active **SG**, the ice fills the lowest hypsometric bin. Once that bin reaches the elevation of the next higher bin, the remaining ice is used to fill up the two bins at the same elevation. This process is repeated using as many bins as necessary to redistribute all the ice. For **CG** ice flux out of the cell, the same amount of ice is removed from all the filled **SG** bins. If the total volume of ice to be removed is not reached using that region of the **SG** cell, the excess remaining is used to empty higher bins one after another.

The **SG** model flux module is coupled asynchronously and runs at half the **SG** mass balance time step. Glacial isostatic adjustment from the **CG** level is imposed on the **SG** basal topography.

3.3.3.2 Sub-grid model activation/deactivation

Unlike Marshall and Clarke (1999), the **SG** model is activated only in cells above sea level with rough topography. A terrain is considered rough when the differences between the maximum and minimum basal elevation is higher than 500 m. To account for regions such as the Alaska Peninsula where **CG** cells represent regions including

basal topography both above and below sea level, cells where at least half of the area is above sea level are treated at the **SG** level. During inception, ice accumulates and can flow into valleys, filling them and thereby reducing the surface elevation variation. The **SG** treatment becomes less critical and is deactivated when the lowest hypsometric bin surface elevation reaches the bedrock elevation of the highest bin. This criterion keeps the **SG** model activated for a longer period of time than in [Marshall and Clarke \(1999\)](#) where the **SG** model is deactivated when ice reaches the lowest bin. During deglaciation, mountain peaks become uncovered and surface elevation variations increase, reaching a point where both ablation and accumulation are present. The **SG** model is reactivated when the ice thickness in the **CG** cell is lower than half of the difference between the basal elevation of the highest hypsometric bin and the basal elevation of the **CG** cell. This differs from [Marshall and Clarke \(1999\)](#), who use only **SG** information to set the threshold to a fraction of the variation in **SG** basal elevation.

3.3.4 Ice Sheet System Model (ISSM)

As a detailed description of the **ISSM** is given in [Larour et al. \(2012\)](#), only a brief description of the model components used in this study are presented here. The **ISSM** is a finite element 3-D thermomechanically coupled ice flow model. The mass transport module is computed from the depth-integrated form of the continuity equation. Using the ice constitutive equation, the conservation of momentum provides the velocities. The model offers the option of computing the velocities using full Stokes, higher-order Blatter–Pattyn, shelfy-stream or shallow ice approximation equations. The higher-order Blatter–Pattyn approximation is used in this study. As the velocity equations depend on the temperature, this field is computed from conservation of energy, including 3-D advection and diffusion. For this study, a new surface mass balance module identical to the one present in the sub-grid model, and detailed in [Sect. B.1](#), has been incorporated into the **ISSM**.

3.4 Sub-grid model performance and tests

The **SG** model computation time for a 3000-year simulation, using 10 hypsometric bins, is about 0.02 s. At a resolution of 1 km and using 10 cpus, **ISSM** run time is about 2–5 h (depending of the topographic region used). The sub-grid model adds 3–6 h

(depending of the parameter vector used) to the glacial cycle run time (approximately 4h) over North America.

3.4.1 Comparison with ISSM

We compare 2 kyr [ISSM](#) and [SG](#) simulations, applying constant sea level temperature and precipitation over an inclined bed and 21 different test regions in the Canadian Rockies. These regions, for both the [ISSM](#) and [SG](#) simulations, have a dimension of 30 km by 60 km and we use a [DEM](#) of 1 km resolution. To improve correspondence between the [ISSM](#) and the [SG](#) model, the minimum ice thickness allowed in the [SG](#) model is set to 10 m. The boundary conditions at the ice margin in the [ISSM](#) are computed as an ice–air interface. To isolate the impact of using the [SIA](#) to represent fluxes in a mountainous region containing steep slopes in the hypsometric parameterization, our current experiments have no basal sliding. As glaciers can experience sliding in this type of region, the next stage of this project will include sliding.

3.4.1.1 Inclined plane test

The bed topography for this test is an inclined plane topography with a constant slope of 0.014 and a maximum basal elevation of 800 m. For this case, the accuracy of the [SG](#) model correlates with the number of hypsometric bins as shown in Fig. 3.3 (ice and velocity profiles are shown in Fig. B1 in the Supplement). Reducing the number of [SG](#) bins increases the surface gradient between two hypsometric bins and thereby the computed ice velocities. With 10 hypsometric bins, the ice volume simulated by the [SG](#) model can be as low as 40 % of the [ISSM](#) prediction. The misfits are not significant in simulations where no ablation is present (e.g. for a temperature set to -5°C).

3.4.1.2 Rocky Mountains test

The [SG](#) model is tested on 21 regions from the Canadian Rockies, representing a wide range of topographic complexity (e.g. Fig. 3.4a), altitude (e.g. Fig. 3.4b) and slopes (e.g. Fig. 3.4c). The slopes of these regions are higher than in the inclined plane case. We focus on the results for simulations over the six test regions in Fig. 3.4 forced with sea level temperature of 0°C and a desertification effect factor of 0.5. The results of other simulations, using different regions and with similar forcing as used in the

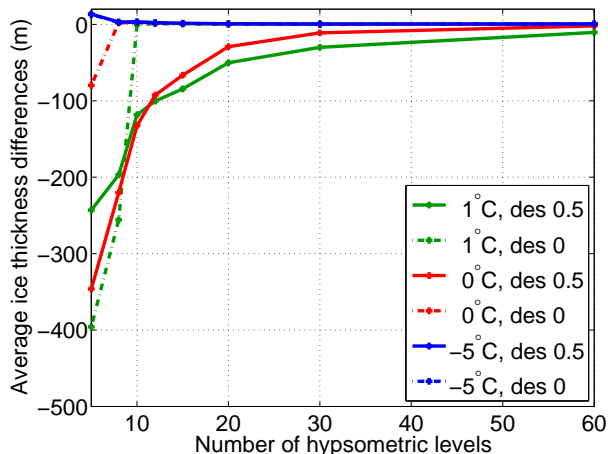


Figure 3.3: [SG](#) model vs. [ISSM](#) differences over an idealized inclined plane terrain. Average ice thickness differences ([SG](#) model - [ISSM](#)) are presented for simulations using different temperatures, desertification effect factors and number of hypsometric bins.

inclined plane experiments, are not shown as they present similar misfits against [ISSM](#) results.

In contradiction with the simplified inclined plane configuration, increasing the number of hypsometric bins does not reduce the misfits with [ISSM](#) simulations (Fig. 3.5). The [SG](#) model does not account for the build-up of ice in closed drainage basins where no flow is permitted out of the region before a threshold elevation is reached. Another complication for the “real” topography scenario comes from topographic “jumps” not addressed in the [SG](#) model. Some high resolution adjacent grid cells belong to non-adjacent hypsometric bins. The ice flow between these two locations is not accurately captured. The number of “jumps” increases with the number of bins used (Fig. B2 in the Supplement). A total of 10 hypsometric bins are then used to limit this effect. Even so, the [SG](#) model generates 45 % less to 15 % more ice than [ISSM](#) simulations (25 % less on average), depending on the regional topographic characteristics. No relation was found between the geographic complexity and the performance of the model, as explained in Sect. 3.4.2.

3.4.2 Test of alternative parameterizations

We examine the impact of including more topographic characteristics in the velocity parameterization. Characteristics considered include the flow direction, the terrain

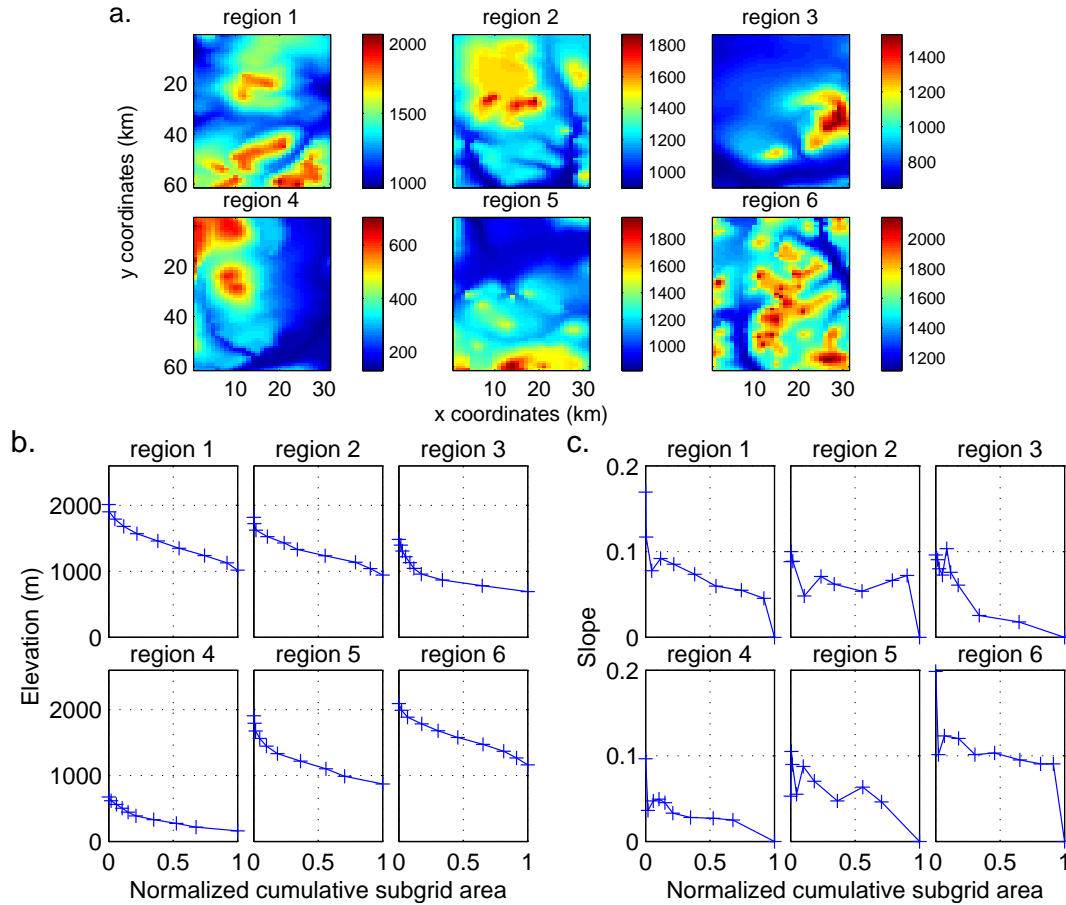


Figure 3.4: Topography characteristics for six regions over the Canadian Rockies. (a) summarizes surface elevations, (b) the hypsometric curves, and (c) the mean slope for each hypsometric bin.

ruggedness (measured as the variation in three-dimensional orientation using a radius of 5 grid cells around the grid cell of interest), the sum of the squared slopes, the variance in the slopes, the number of local maxima (tested with radius sizes of 2, 6 and 10 grid cells) and the standard deviation of the surface elevation topography.

The [ISSM](#) and the sub-grid model were run until steady state (2 kyr) for simulations with a constant precipitation rate of 1 mm/yr and a sea level temperature forcing of 0°C. The parameters minimizing ice volume differences were selected using a stepwise multilinear regression fit. The flow direction and the mean of the squared slope do not reduce the misfits. The slope variance does not improve the results when combined with the remaining two parameters (elevation standard deviation and terrain ruggedness). When used alone, it does reduce the errors but not as well as

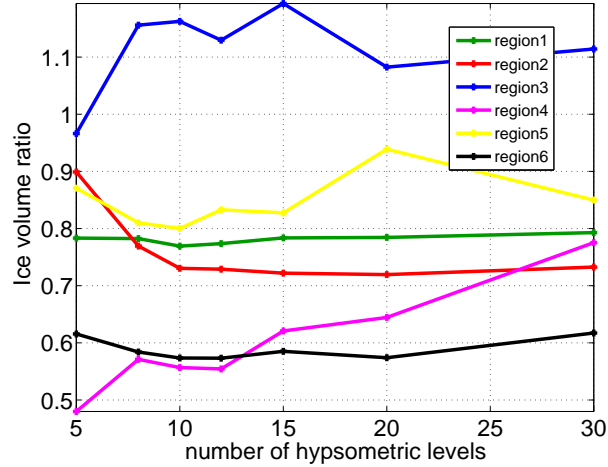


Figure 3.5: Ratio of the SG model over ISSM total ice volume for six different regions in the Rockies as a function of hypsometric bins. The simulations were run until steady state with a constant sea level temperature of 0°C and a desertification effect factor of 0.5. The steady state ice thicknesses, velocities and slopes from the ISSM and the SG model (using 10 hypsometric bins) are presented in Fig. B3 in the Supplement.

when the standard deviation of the topography is used. The terrain ruggedness and the peak density both represent the same physical characteristics and do not improve the results when used alone. Improvements are obtained when combined with the standard deviation of the topography. However, the improvement is not greater than with the standard deviation alone. The standard deviation of the topography is the parameter that correlates the most with the misfits. The average absolute value of the differences between the SG model and ISSM average ice thickness is 61 m. This difference is reduced to 21 m (see Fig. 3.6) when the regression model generated using the standard deviation of the topography is used. More details about the results of the stepwise regression fits are provided in the Supplement B.2.

To explore potential improvement from accounting for the standard deviation of the high resolution topography, S_{SD} , we test the following parameterization of the velocity, \bar{u}_1 :

$$\bar{u}_1 = \frac{2}{5} (\rho g)^3 A_0 (P_1 H S_{SD}^{P_2})^{P_3} \left(\frac{\partial h_d}{\partial x} \right)^3. \quad (3.6)$$

This equation is used in a simulation initialized with the ice thickness, velocities and slopes of ISSM values at steady state. The parameters P_1 , P_2 and P_3 (respectively 4.87, 0.016 and 2.8) are obtained using a least-squares approach that minimizes the differences between the velocities computed by ISSM and the SG model after one

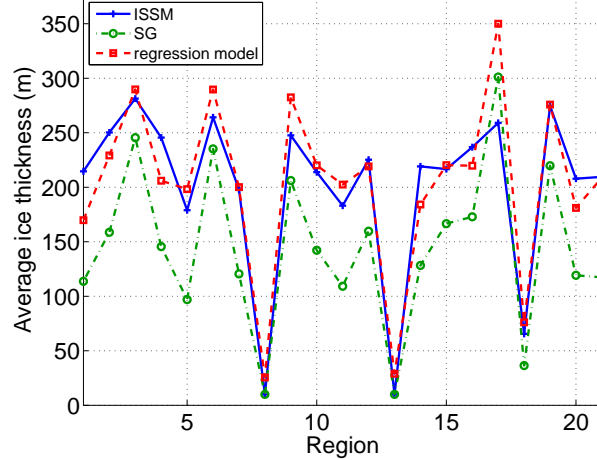


Figure 3.6: Average ice thickness in metres for different topographic regions in the Rockies. Results are shown for the [ISSM](#), the regression model (generated by the stepwise regression fit including only the standard deviation of the topography) and the [SG](#) model using 10 hypsometric bins.

iteration (0.01-year).

The lowest hypsometric bin has the most significant misfits (e.g. Fig. B4 in the Supplement). This is likely related to the margin ice cliff slope parameterization. To try to correct this, we test the following parameterization for the lowest hypsometric bin velocity:

$$\bar{u}_{2,N} = \frac{2}{5} (\rho g)^3 A_0 H_N^4 \left(P_4 H_N^{P_5} \frac{\partial h_{d,N}}{\partial x} \right)^3. \quad (3.7)$$

Using the same least-squares approach as above, the parameters P_4 and P_5 are respectively set to 5924.4 and -1.6383 . These two parameterizations do not reduce the ice thickness differences with [ISSM](#) transient results (see Fig. 3.7). Ice thickness, velocities and slopes over the six regions analysed are presented for the different parameterizations in Fig. B5 of the Supplement. As the model is highly non-linear, the improvement generated by the least-squares fit method for an initialization with [ISSM](#) steady state conditions does not persist over 1000-year runs.

The following modifications of the current version of the [SG](#) model have been explored but did not improve the model. The central difference discretization of the ice thickness in the effective diffusivity coefficient was replaced by an upwind scheme. Simulations with different values of the Arrhenius coefficient, the power of the ice thickness and the slope, in Eq. (3.4), were analysed. An extra parameter was added in the velocity equation to account for neglected stresses. Turning off the internal

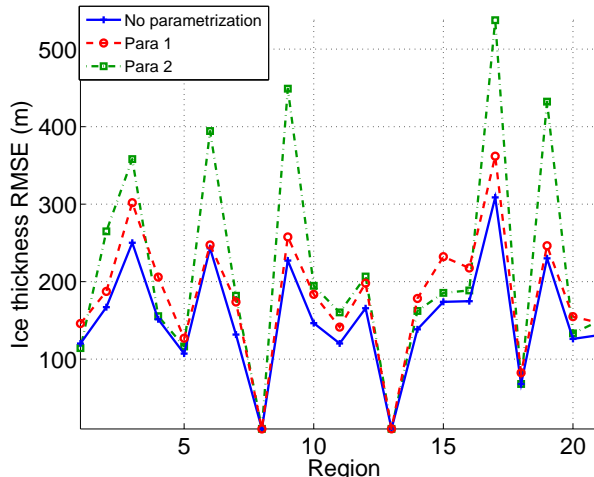


Figure 3.7: Average ice thickness root mean square error (RMSE) between the [ISSM](#) and the [SG](#) model for different topographic regions. Simulations are run over 2 kyr using a constant precipitation rate of 1 m/yr and a sea level temperature forcing of 0 °C. Different [SG](#) parameterizations are presented. Para 1 is the standard deviation of the topography parameterization (Eq. 3.6) and Para 2 the lowest hypsometric slope parameterization (Eq. 3.7).

[SG](#) model flux term increased the misfits with [ISSM](#) simulations by a minimum of 100% (as shown in Fig. 3.8). The basal elevation downstream of the terminus has been computed using a linear extrapolation of two or three upstream bins. The lowest hypsometric bin effective length generated with these basal elevations did not reduce the misfits with [ISSM](#) results.

3.5 Behaviour of the sub-grid model in the [GSM](#)

We present results of simulations over the last glacial cycle. The 39 “ensemble parameters” of the [GSM](#) (attempting to capture the largest uncertainties in climate forcing, ice calving, and ice dynamics) have been subject to a Bayesian calibration against a large set of palaeoconstraints for the deglaciation of North America, as detailed in [Tarasov et al. \(2012\)](#). We use a high-scoring sub-ensemble of 600 parameter vectors from this calibration to compare the [GSM](#) behaviour when the [SG](#) model is turned on and off. The primary supplement of [Tarasov et al. \(2012\)](#) includes a tabular description of the 39 ensemble parameters as well as input data sets. For the purposes of clarity and computational cost, we examined model sensitivity to different coupling and flux parameters using five parameter vectors (of the 600 members ensemble) that

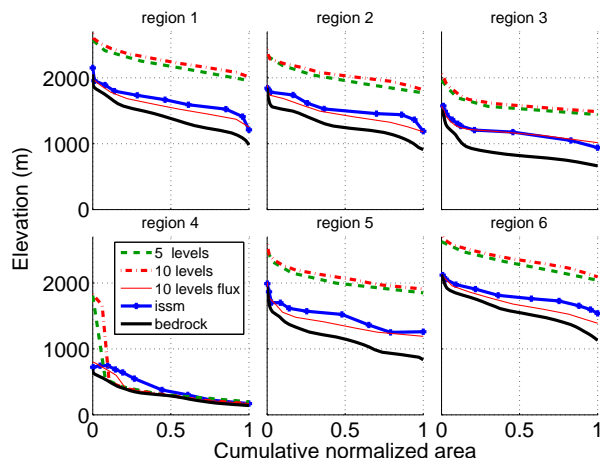


Figure 3.8: Surface elevation generated by the [ISSM](#) (solid blue line), the [SG](#) model with no flux term, using 5 and 10 hypsometric bins, (dotted lines) and the [SG](#) model including the flux term (solid thin red line). These simulations use a constant sea level temperature of 0°C and a desertification effect factor of 0.5. Results are shown at steady state after 2 kyr for six different regions with different topographic characteristics.

gave some of the best fits to the calibration constraints. As these five parameter vectors display similar behaviour, we present sensitivity results using the parameter vectors for the two runs described in detail in [Tarasov et al. \(2012\)](#) (identified in that paper as runs nn9894 and nn9927). For ease of interpretation, the ice volumes are presented as [Eustatic Sea Level \(e.s.l.\)](#) equivalent³.

3.5.1 Last glacial cycle simulations over North America

The [SG](#) model can significantly alter the pattern of ice accumulation and loss. Figure 3.9 shows an example, for one of the parameter vectors of the ensemble of simulations, where [SG](#) ice accumulates while it melts at the [CG](#) level (Fig. 3.9a), and an example where [CG](#) ice is about 60% greater than the [SG](#) ice (Fig. 3.9b).

The ensemble of simulations of the last glacial cycle over North America with the [SG](#) model activated generates, on average, between 0 and 1 m [e.s.l.](#) more ice than when the [SG](#) model is turned off (Fig. 3.10).

The impact of the [SG](#) model depends, however, on the climate forcing and the ice sheet extent and elevations. During inception, when the [SG](#) model is turned on,

³Using a conversion factor of $2.519 \text{ m.e.s.l.}/10^{15} \text{ m}^3$ of ice

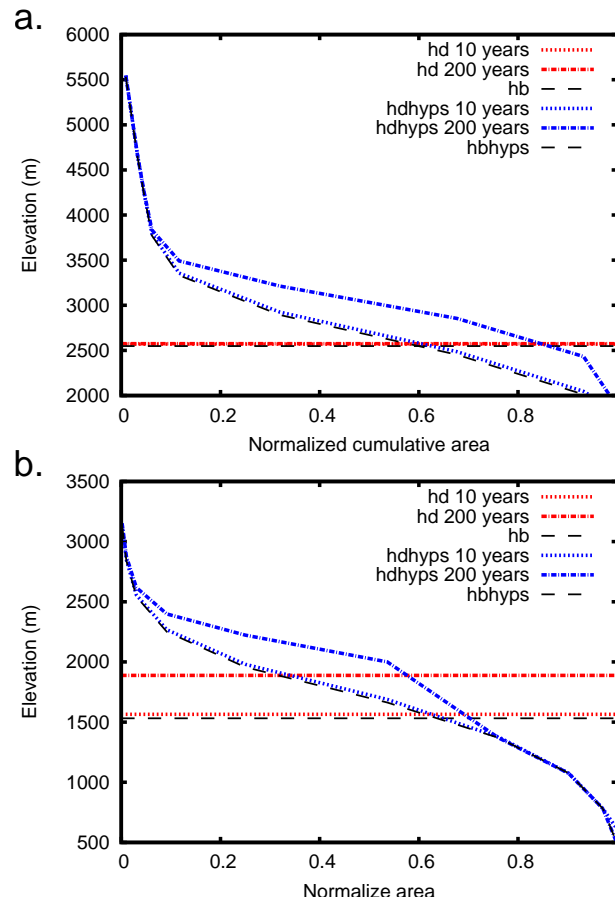


Figure 3.9: Elevation comparisons when the **SG** model is turned on (blue) or off (red) at different time steps using the parameter vector nn9894. h_d 10 years is the **CG** surface elevation after 10 years. h_{dhyps} 10 years is the **SG** surface elevation. h_b is the basal elevation. **(a)** and **(b)** represent cases where the **ELA** is above and below the coarse grid surface elevation.

ice accumulating in higher regions flows downhill and accumulates in regions close to the **ELA** and in valleys (Fig. 3.11). This allows, for example, ice to build up in the northern part of Alaska. For typical runs, the ice generated by the **SG** model in the Alaskan Peninsula is, however, insufficient as compared to geological inferences (Dyke, 2004). The ensemble mean and standard deviation of the differences between runs with **SG** on and off at 110 ka, are respectively 0.4 and 1 m *e.s.l.* However, at specific time slices, the differences can be much larger. Once the ice sheet has grown to a sizeable fraction of **LGM** extent, for example at 50 ka, the standard deviation of the ensemble-run differences (between **SG** on and off) reaches 5 m *e.s.l.* Figure 3.12 shows an example where ice in a region of low altitude in the centre of Canada is not allowed

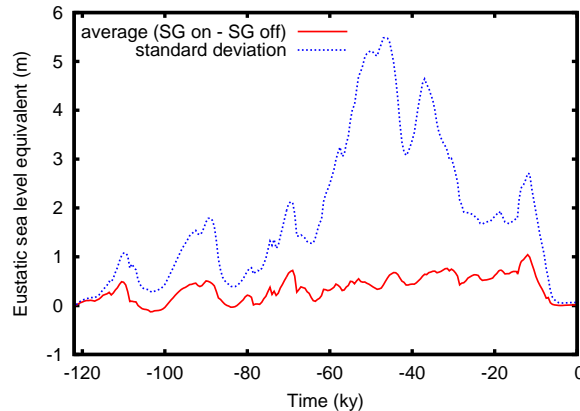


Figure 3.10: Ensemble mean (solid red line) and standard deviation (dotted blue line) eustatic sea level equivalent of the total ice volume differences when the **SG** model is turned on and off, for an ensemble run over the last glacial cycle.

to grow when the **SG** model is used. On the other hand, a simulation using different ensemble parameters generates ice in this region only when the **SG** model is turned on (Fig. B6 in the Supplement). In extreme cases, differences can reach tens of m *e.s.l.* (Fig. B7 in the Supplement). We could not identify a reason for the strong sensitivity of ice volume around 50 ka other than the inherent non-linearity of the **GSM**.

3.5.2 Sensitivity of the model to different flux and coupling parameters

The accounting of **SG** fluxes has varying impacts over a glacial cycle simulation (Fig. 3.13). At 50 ka, for example, the total ice volume with parameter vector nn9894 is reduced by 50 % when **SG** fluxes are included. During inception, on the other hand, inclusion of **SG** fluxes increases the total amount of **CG** ice (Fig. 3.14, again with nn9894).

To better understand the range of responses to **CG** ice flow between grid cells that have **SG** activated, three case scenarios can be considered. Case 1: ice flows out of the lowest **SG** bins located above the **ELA** into the lowest **SG** bins located above the **ELA** of another **CG** cell. There is limited impact of not allowing ice to flow out of the **CG** cell as in both cases ice accumulates. Case 2: ice flows out of the lowest **SG** bins located above the **ELA** into the lowest **SG** bins located below the **ELA** of another **CG** cell. In that case, turning off the fluxes between **CG** cells tends to reduce the total melt. Case 3: ice flows out of the lowest **SG** bins located below the **ELA** into the

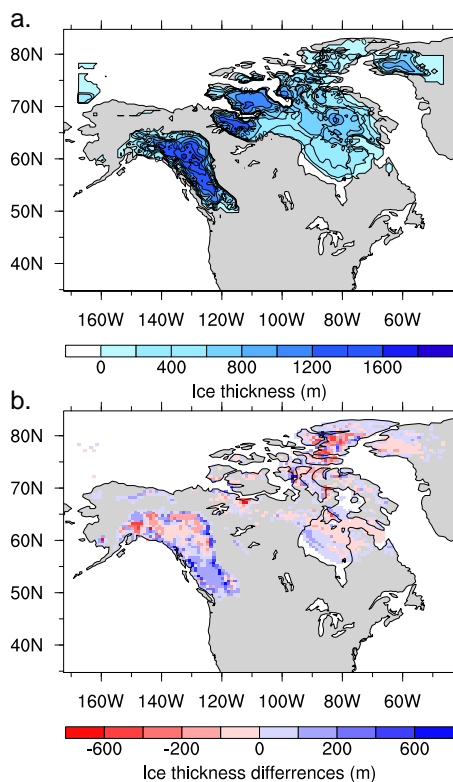


Figure 3.11: Ice field during inception at 115 ka for a simulation using one of the parameter vectors that generates best fits to the calibration constraints (nn9894). **(a)** Ice thickness with **SG** turned on. **(b)** Ice thickness differences between simulations with the **SG** model turned on and off. Zero differences are presented in the same colour as the continent.

lowest **SG** bins located below the **ELA** of another **CG** cell. Ice flowing into lower **SG** bins generates higher melting rates, so permitting fluxes between **CG** cells will in this case tend to increase ice mass loss. In cases 2 and 3, the combination of ice flowing below the **ELA** from the adjacent **CG** cell and from the bins above the **ELA** can raise the surface elevation of lower bins above the **ELA** and reduce the melt. Depending on the proportion of each of these cases, not allowing ice fluxes out of coarse grid cells with **SG** activated generates higher or lower ice volumes (Fig. 3.13). Moreover, 50 ka is an example of a 60% increase of the total ice volume when the fluxes out of coarse grid cells (with **SG** activated) are not allowed. As a counter-example, 35 ka presents a case where turning off the fluxes out of (**SG** activated) coarse grid cells decreases the total ice volume.

With Marshall et al.'s (2011) flux equation, differences between runs with **SG** fluxes turned on versus off are negligible over the full glacial cycle (Fig. 3.14).

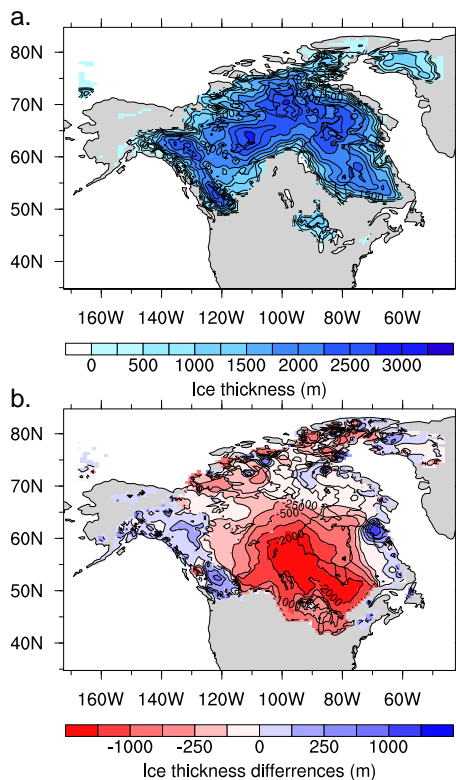


Figure 3.12: Ice field at 50 ka for a simulation using parameter nn9894. **(a)** Ice thickness with **SG** turned on. **(b)** Ice thickness differences between simulations with the **SG** model turned on and off.

As described in Sect. 3.3.3.1, the **CG** ice thickness used by the **GSM** conserves the ice volume of the filled **SG** bins (volume conservation, **Volume Conservation (VC)**, method). As this ice is redistributed over the total area of the coarse grid cell, the surface elevation of the ice, and consequently the fluxes, are underestimated. The surface gradient between adjacent cells is then lower than the gradient at the **SG** level. We tested setting the **CG** surface elevation to the maximum value between the surface elevation of the coarse grid cell and the lowest hypsometric bin (surface conservation **Surface Conservation (SC)** method). We also implemented a method using the maximum surface elevation generated by the two former methods (**maximum conservation (MC)** method). During inception (between 118 and 114 ka) the **VC** method generates between 10 and 20% (which is equivalent to 0.5–1 m **e.s.l.**) more ice than the two other methods (Fig. 3.15). During the first 60 kyr of simulation, the difference in total ice volume stays under 1 m **e.s.l.** independently of the flux redistribution methods (Fig. B8 in the Supplement). Between 60 ka and the **LGM**, the

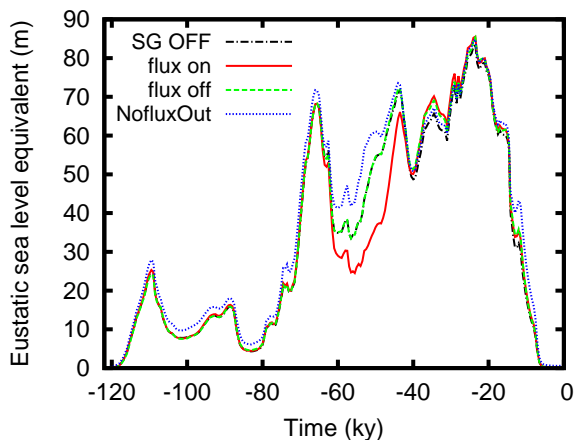


Figure 3.13: Total ice volume evolution for a simulation using parameter vector nn9894. “flux on” and “flux off” both include the **SG** surface mass balance calculations but the latter has no **SG** ice fluxes. “NofluxOut” has **SG** on, but no **SG** ice flux between coarse grid cells. The “**SG OFF**” line is most of the time hidden under the “flux off” line.

SC method generates between 1 and 12 m *e.s.l.* less ice than the two other methods (Fig. B8). The **VC** method was used for the ensemble runs as it generates more ice over the Alaska Peninsula, northern and southern mountain ranges, thereby reducing misfits against geological inferences.

Figure 3.16 shows the results of the glacial cycle simulation when the **SG** model is turned off and when the minimum altitude variation **SG** activation threshold is set to 50, 150, 300 and 500 m. A non-linear dependence on the threshold can be observed. At 50 ka, for example, setting the threshold to 50 m generates the lowest total ice volume while a threshold of 150 m leads to the highest ice volume. The difference between these two runs is 34.5 m *e.s.l.* at 50 ka. Thresholds of 300 and 500 m generate intermediate total ice volumes. Moreover, simulations using different parameter vectors (not shown) result in different behaviours. No conclusion could be drawn about the optimal threshold.

3.6 Conclusions

Our new sub-grid surface mass balance and flux model extends the initial work of Marshall and Clarke (1999) and Marshall et al. (2011). The evaluation of the model, done for the first time against results from a high resolution higher order model (**ISSM**),

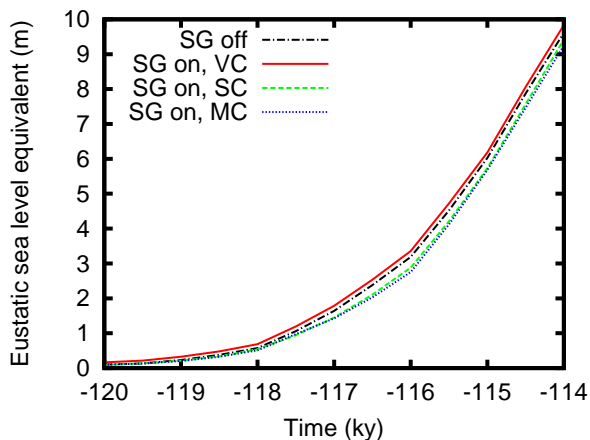


Figure 3.14: Ice volume evolution for a simulation over North America (parameter vector nn9894) with the **SG** model turned on during inception. “our flux” represents the flux code used in our **SG** model and “Marshall flux” the flux code used in [Marshall et al. \(2011\)](#) experiment. “flux off” represents the simulation with no ice flux between **SG** bins and “NofluxOut” has no **SG** flux between coarse grid cells (but **SG** fluxes within each coarse grid cell are still enabled).

demonstrates that

- Depending on the regional topographic characteristics, the new **SG** model simulates ice volumes 45 % lower to 15 % higher than simulated by the **ISSM** (using 10 hypsometric bins). Increasing the number of hypsometric bins to more than 10 did not reduce misfits for simulations over rough topographic regions extracted from the Canadian Rockies.
- Turning off the **SG** internal fluxes increases the ice volume misfits with **ISSM** simulations by a minimum of 100 %.
- Increasing the number of topography characteristics used in the **SG** model, as suggested by [Marshall and Clarke \(1999\)](#), did not reduce the misfits with the high resolution model during transient runs.

An ensemble of simulations over the last glacial cycle of the North American ice complex shows, on average, an increase of ice generated with inclusion of the **SG** model. The ensemble mean for each time step is between 0 and 1 m *e.s.l.*, with a standard deviation of a minimum of twice the mean and reaching 5 m *e.s.l.* at 50 ka. At the end of inception, at 110 ka, the increase of ice volume from **SG** model inclusion is still insufficient over the Alaska Peninsula when compared to geological inferences. Over

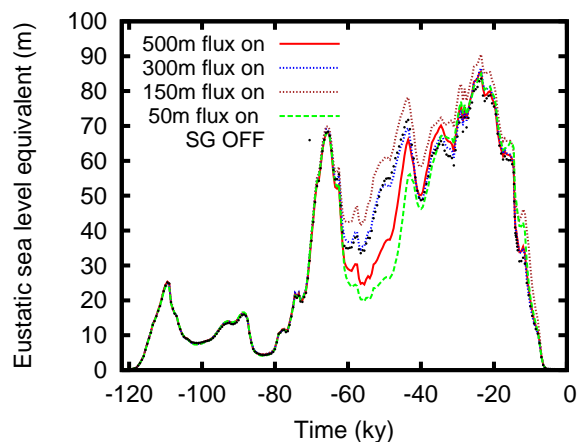


Figure 3.15: Total ice volume evolution for a simulation over North America during inception with the **SG** model turned on (**SG** on) using the parameter vector of run nn9927. Different methods of ice redistribution at the **CG** level are compared. **VC** is for ice volume conservation, **SC** for surface elevation conservation and **MC** uses the maximum of the previous two methods. “**SG** off” represents a run where the **SG** model has been turned off.

the glacial cycle, the **SG** model generates different patterns of ice extent. In some instances, the **SG** model prevents ice growth, while in others it enables extra ice build up over thousands of square kilometres.

Simulated ice evolution is sensitive to the treatment of ice fluxes within the **SG** model and between the **SG** and **CG** levels.

- The flux term has an important impact on the **SG** model. Not allowing ice to flow between hypsometric bins increases the total ice volume with a maximum increase of 50% at 50 ka (in a glacial cycle run). During inception, however, the flux module can generate more ice. Different parameterizations of the flux term impact the results. A **SG** ice rheology parameter corresponding to ice at about -40°C (as used in Marshall et al., 2011) generates the same amount of ice during inception as when the flux term is off.
- The flux term used in the Marshall et al. (2011) study, with the ice rheology parameter representing ice at about -40°C , generates an ice volume higher than when a flux parameterization with a rheology value representing ice at about 0°C is used.
- Not allowing ice to flow out of a **CG** cell where **SG** is activated increases or

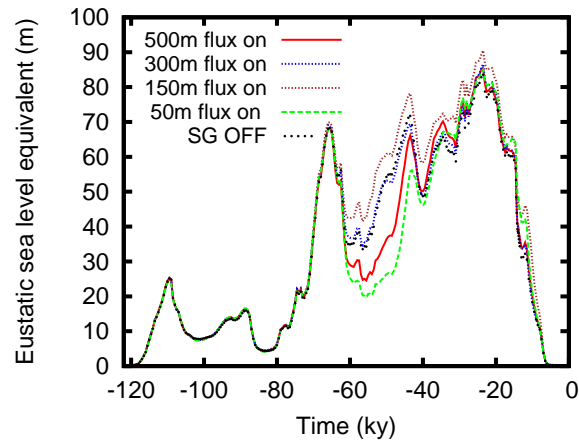


Figure 3.16: Total ice volume evolution for a simulation using parameter vector nn9894. Different curves represent simulations with different minimum altitude variation thresholds used for the **SG** activation.

decreases the total ice volume depending of the ice configuration. At 50 ka, the total increases by 60 %.

- The ice configuration from simulations over the last glacial cycle of North America is sensitive to the choice of **SG** to **CG** ice redistribution scheme.

We have identified the representation of **SG** fluxes between **CG** cells to be a challenging issue that can significantly impact modelling ice sheet evolution.

We have shown that the above geometric and ice dynamics factors can have significant impacts on modelled ice sheet evolution (with up to a 35 m.e.s.l. difference in North American ice volume at 50 ka). Therefore, significant potential errors may arise if sub-grid mass-balance and fluxes are not accounted for in the coarse resolutions required for glacial cycle ice sheet models. Other alternatives to the hypsometric parameterization, such as running a high resolution **SIA** model in the region of rough topography, could be considered. One issue we have not examined is the downscaling of the climatic forcing. Temperature and especially precipitation can exhibit strong vertical gradients in mountainous regions. Whether this can have significant impact on **CG** scales is unclear. Improvements of the precipitation representation are possible using, for instance, a linear model of orographic precipitation for downscaling climatic inputs (Jarosch et al., 2012).

Code availability

The sub-grid code is available upon request from the first two authors.

Author contribution

Kevin Le Morzadec and Lev Tarasov designed the experiments. Kevin Le Morzadec developed the [SG](#) model code and performed the simulations. Kevin Le Morzadec and Lev Tarasov coupled the [SG](#) model into the [GSM](#). Mathieu Morlighem and Helene Seroussi supported [ISSM](#) installation and helped build a new surface mass balance module for the [ISSM](#). Kevin Le Morzadec prepared the manuscript with contributions from Lev Tarasov and the other co-authors. Lev Tarasov heavily edited the manuscript.

Acknowledgements

We thank Vincent Lecours and Rodolphe Devillers for extracting some of the topographic characteristics. Support provided by the Canadian Foundation for Innovation, the National Science and Engineering Research Council, and ACEnet. Tarasov holds a Canada Research Chair. We finally thank Philippe Huybrechts, as well as Fuyuki Saito and an anonymous reviewer, whose comments helped significantly improve the clarity of the manuscript.

Chapter 4

Conclusion

4.1 Summary

The objectives of this thesis were to:

- Document the impact of fjord geometry on ice discharge.
- Document the impact of higher order ice dynamics physics on fjord discharge.
- Document the impact of basal sliding representation on ice discharge.
- Document the resolution dependence of modelled fjord ice discharge.
- Reduce the topographic scale dependency of an ice sheet model in purely terrestrial regions of rough topography (mountain ranges) and outlet glaciers (fjords).

The impact on ice discharge of fjord area and resistive stresses induced by different fjord shapes is documented in Chapter Two. This impact, quantified below, shows the uncertainties introduced in modelling the present and future state of current ice sheets if the basal topography in coastal regions is not known at resolution of at least 1 km. I analyzed regions with dimensions of 300 km by 250 km. A region with a 5 km wide and 100 km long fjord (a typical scale) generates 8% (with a standard deviation over time of the order of 8%) less ice than a region with no fjords. The fjord geometry characteristics increase or decrease the time-averaged ice volume by, respectively, 3% and 9.6% (with a standard deviation of the order of 3% and 10%) compared to a straight fjord.

[ISMs](#) underestimate the ice volume in fjord regions when representing fjords in coarse grid cells by the average of the SG high resolution topography and when reducing the basal sliding coefficient proportionally to the total fjord area fraction. This error increases with grid cell size. Simulations over regions with dimension of 300 km by 250 km, presented in Chapter Two, show surface elevation RMSEs (compared to simulation at 1 km resolution) of 11 % at 5 km resolution, 17.6 % at 10 km resolution and, 31 % at 25 km resolution. Fjords drain an important fraction of past and present ice sheets and therefore their representational uncertainties in models need to be quantified.

My comparison of ice evolution representations in simulations using different ice dynamics approximations and different sliding laws, done in Chapter Two, confirms the need for a better representation of ice dynamics and sliding in coarse resolution [ISMs](#) to capture ice drainage through fjords. A continental-scale [ISM](#) intercomparison ([Pattyn et al., 2013](#)) showed that pure membrane models generate more ice than models using a HO approximation. My results contradict this for regions with fjords. The literature to date has been ambiguous about the appropriate law to use for basal sliding. I have shown that even after optimizing some of the ice flow parameters, the impact of using a linear power law compared to a quadratic one has as much impact as the grid resolution on ice drainage (presented in the previous paragraph).

By modifying ice flow parameters, I improve, in Chapter Two, the ice evolution representations at 5, 10, and 25 km resolution. However, at 25 km resolution, simulations still have a lag of one to three thousand years before growing ice after an interstadial period compared to the 1 km resolution simulations. Using the optimisation presented in Chapter Two, simulations have to be done at resolutions higher than 25 km to match the timing of total ice volume growth and decay generated in simulations done at 1 km resolution. In detail, tuning reduces the surface elevation RMSE (compared to the 1 km resolution) on average by 24.1 % for the simulations at 5 km resolution, by 17 % for the simulations at 10 km simulations, and by 5 % for the simulations at 25 km resolution. Upscaling the basal elevation from the 1 km resolution grid to the coarse resolution grids using the deepest depth in the fjord(s), the fjord depth average, the average between the fjord average and the box average, or the average between the deepest depth in the fjord generates more misfits (in term of ice volume and surface elevation RMSE with respect to the 1 km reference resolution simulation) compared to a simple box average regridding.

In Chapter Three, I treat the topographic scale dependency of an [ISM](#) in purely terrestrial regions of rough topography and improve the representation of accumulation

and ablation zones in a single coarse grid cell. Extending the approach of [Marshall and Clarke \(1999\)](#) and [Marshall et al. \(2011\)](#), I develop a new subgrid surface mass balance and flux model (available as a supplement of the thesis) that was coupled to the [GSM](#) model. Compared to results from a high resolution higher order model ([ISSM](#)) the new [SG](#) model simulates ice volumes 45 % lower to 15 % higher than simulated by the [ISSM](#) (25 % less on average). An ensemble of simulations over the last glacial cycle of the North American ice complex shows, on average, an increase of ice generated with inclusion of the [SG](#) model. The ensemble mean for each time step is between 0 and 1 m [e.s.l.](#), with a standard deviation of a minimum of twice the mean and reaching 5 m [e.s.l.](#) at 50 ka. Some simulations generate differences up to a 35 m [e.s.l.](#) in North American ice volume at 50 ka.

Models of complex environmental systems have [SG](#) processes not resolved at the simulation resolution. I have documented the modelled resolution dependence of surface mass balance and ice flow in topographically complex regions. I have also developed parametrizations for these contexts to account for [SG](#) topography. Together, my two parameterizations better account for accumulation zones, ablation zones and different flow regimes within a coarse grid cell. Including these parameterizations in [ISMs](#) reduces the uncertainties in representing events such as inception and deglaciation sensitive to topographically relevant [SG](#) processes. Further work may improve these parametrizations. However, the remaining uncertainties related to ice flow and [Surface Mass Balance \(SMB\)](#) in regions with rough topography are likely small compared to the uncertainties introduced by the climate forcings.

4.2 Future work

This thesis has documented the impact of rough topography on [SG](#) surface mass balance and ice dynamics, as well as developed a [SG](#) parameterization to reduce the [ISM](#) scale dependency related to these processes in regions of rough topography. This study is an initial attempt towards a scale independent [ISM](#). In mountain regions the new [SG](#) parameterization captures both accumulation and ablation zones in a single coarse grid cell but still underestimate ice volume by 25 % (on average over the different regions analyzed). However, it is unclear what other steps could be done to improve this given the detailed approach taken.

In coastal regions of rough topography, the new coarse grid parameterization partly

captures the [SG](#) impact of fjord geometric characteristics on ice drainage in coarse resolution models. Errors remain in the representation of the ice dynamic through fjords leading, for example, to lags of one to three thousand years in the evolution of ice growth in 25 km resolution simulations. Given time constraints, this work is less complete than that carried out for the [SG](#) hypsometric model and there are some further steps that could be carried out to potentially further reduce coarse resolution [ISM](#) errors.

The differences in basal elevation between coarse resolution and high resolution reduces the ice thickness in fjord regions during coarse resolution simulations. The resulting differences in basal temperature impact ice dynamic. The extent of this impact needs to be investigated. [Pollard and DeConto \(2012\)](#) describes a potential approach to compensate for this. My coarse resolution fjord characteristics may be improved by taking into account the number of fjords in a coarse grid cell. More work needs to be done, as well, to analyze the impact on the ice drainage of the fjord position on the grid. Does a fjord located in a grid cell and a fjord located between two grid cell generate the same response of the model? The parameterization has been tested on synthetic fjords and needs to be tested in regions with real topography. I chose to use a forced upstream boundary condition to isolate the topographic impacts. It would be worth exploring whether the optimal parametrizations would change if the fluxes were not forced at the boundary. Finally, it would be worth repeating the exercise with the adaptive grid [BISICLES](#) model to increase confidence that the current results are not biased by limitations of the [ISSM](#) and the hybrid model.

The two parameterizations developed in Chapters Two and Three reduce the [ISM](#) topographic grid resolution dependency. The impact of combining these two [SG](#) parametrizations in a continental scale ice sheet simulation over the last glacial cycle still needs to be investigated. Norwegian fjords are an ongoing challenge for data-calibrated ice sheet modelling given persistent misfits between computed [Relative Sea Level \(RSL\)](#) and relevant proxy records ([Lev Tarasov](#) personal communication). Tests will soon be implemented examining whether my new [SG](#) parametrizations can partly explain these misfits.

The question remains whether a better representation of [SG](#) processes such as subglacial hydrology, grounding line migration and calving in [ISM](#) could improve ice sheets evolution reconstruction with glaciological models or if improving the climate forcings would be sufficient. An adaptive grids model (e.g. [BISICLES](#), [Cornford et al., 2013](#)) could become an alternative as it allows increased resolution in areas of interest

while maintaining coarse resolution in the main part of the ice sheet. However, these models are still too computationally expensive to run ensemble simulation, necessary to extract the model uncertainties, in a continental scale over a glacial cycle.

The representation of the climate and ocean forcings are major uncertainties in the reconstruction of past ice sheets. Coupled ISMs and climate models of different complexity (Energy Balance Models, Earth system Models of Intermediate Complexity, and General Circulation Models) are being used to test the ability of these coupled models to reduce the misfits between ice evolution reconstruction and paleo-data constraints. Another issue we have not examined, but that has been shown to have an impact on ice evolution, is the downscaling of the climatic forcing (e.g. [Seguinot et al., 2014](#)). Temperature and especially precipitation can exhibit strong vertical gradients in mountainous regions. Whether this can have a significant impact on CG scales is unclear. Improvements of the precipitation representation are possible using, for instance, a linear model of orographic precipitation for downscaling climatic inputs ([Jarosch et al., 2012](#)).

Appendix A

Supplementary material for: Subgrid fjords in ice sheet models

A.1 Forcings

A.1.1 Basal topography

A.1.1.1 Realistic fjord

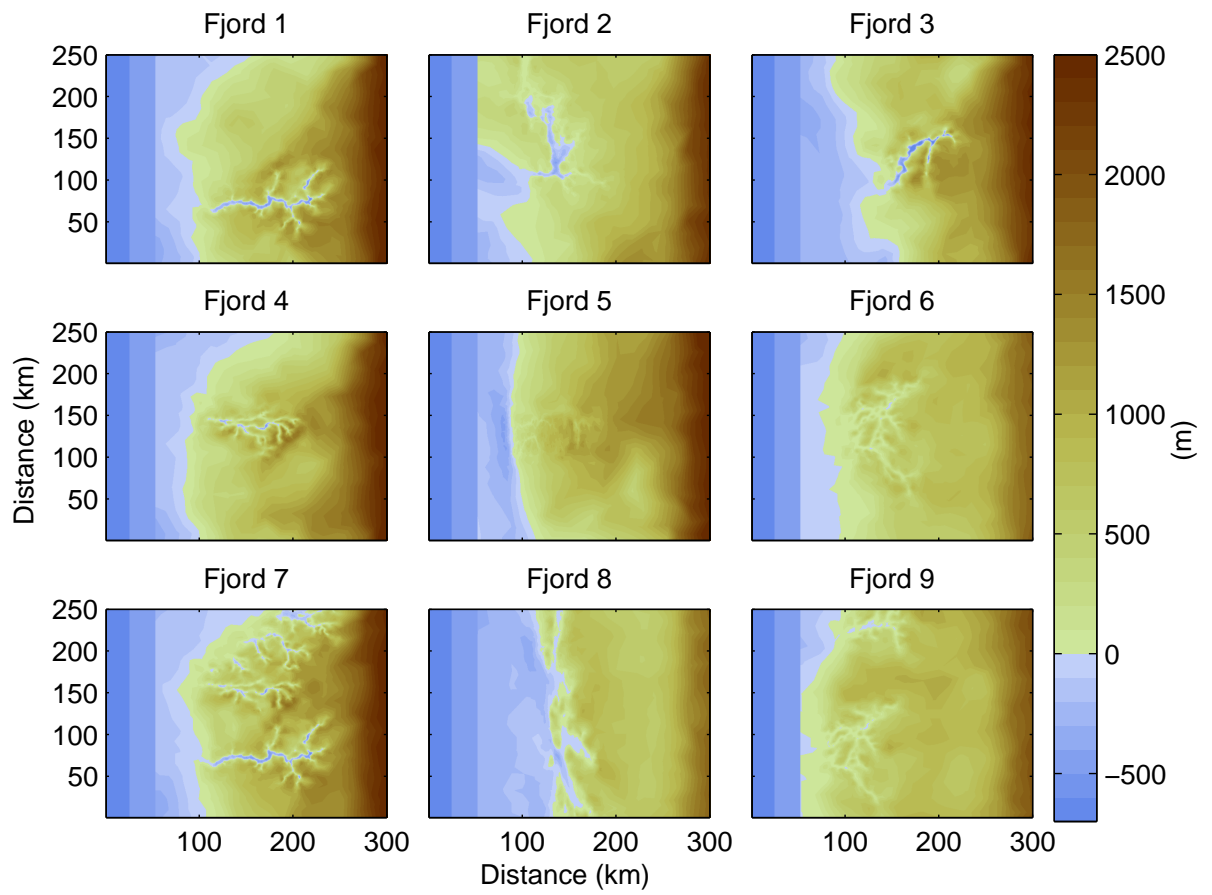


Figure A.1: Basal topography representing real fjord topography.

A.1.1.2 Synthetic fjords

Region S21, S22 and S23 have, respectively, the same fjord has region S1, S4 and S5 but the fjord is in between two grid cell at every resolution.

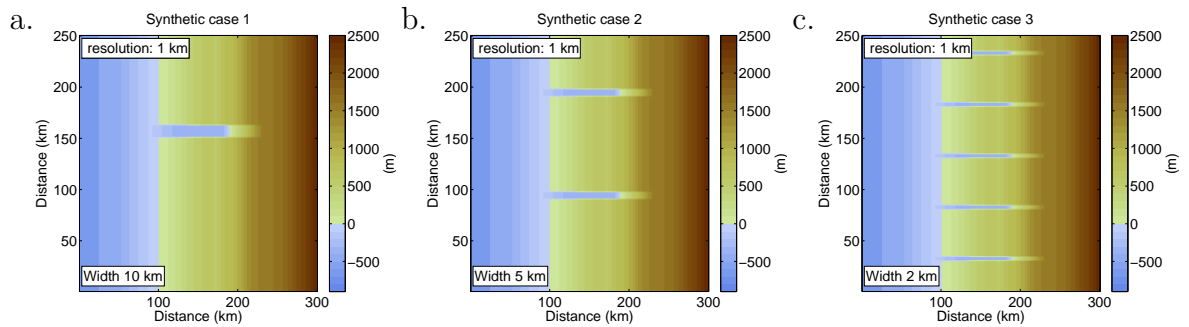


Figure A.2: Different number of fjords.

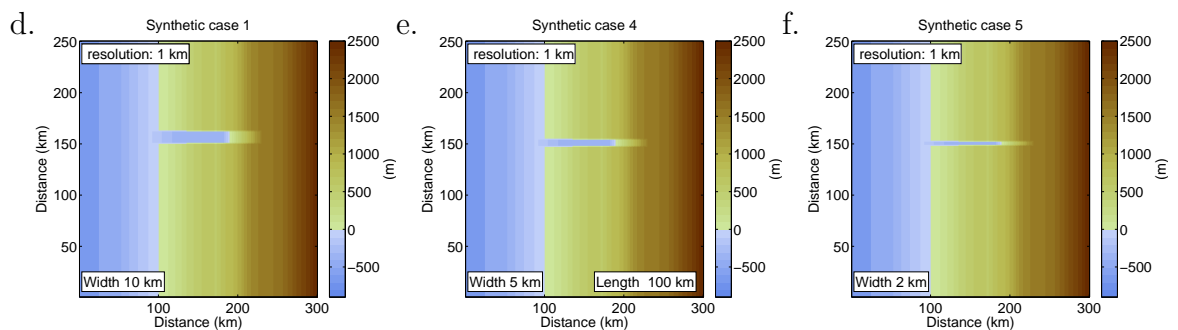


Figure A.3: Different fjord width.

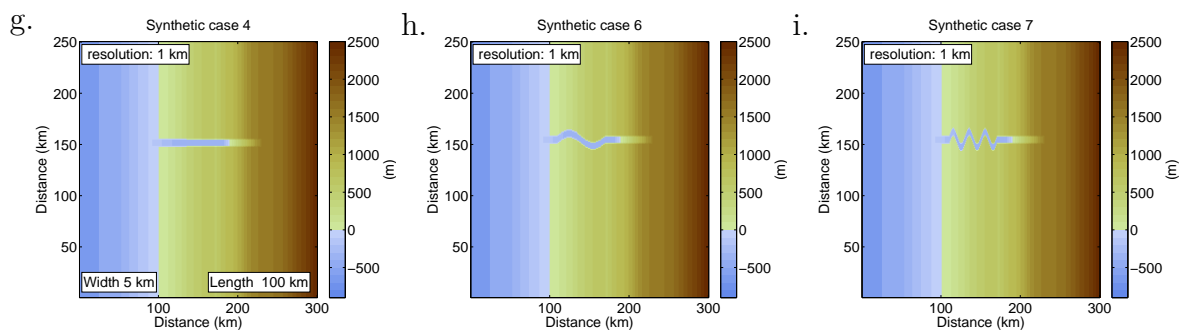


Figure A.4: Different number of bends.

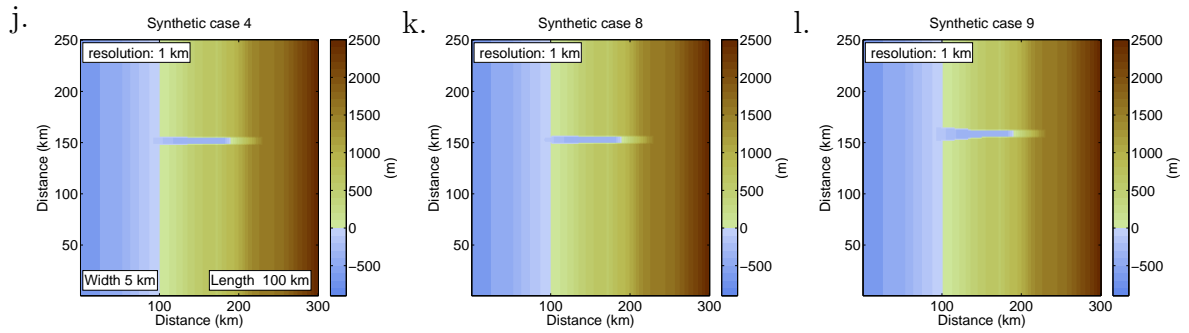


Figure A.5: Different fjord width at the mouth of the fjord.

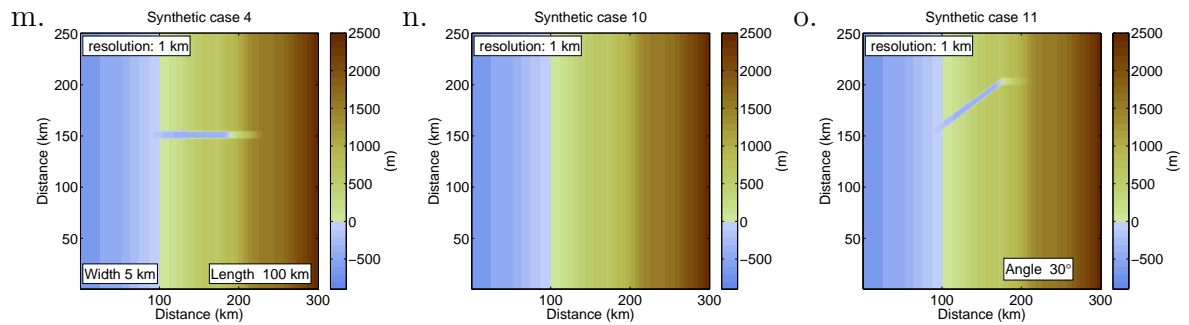


Figure A.6: Regions with no fjords and with an inclined fjord.

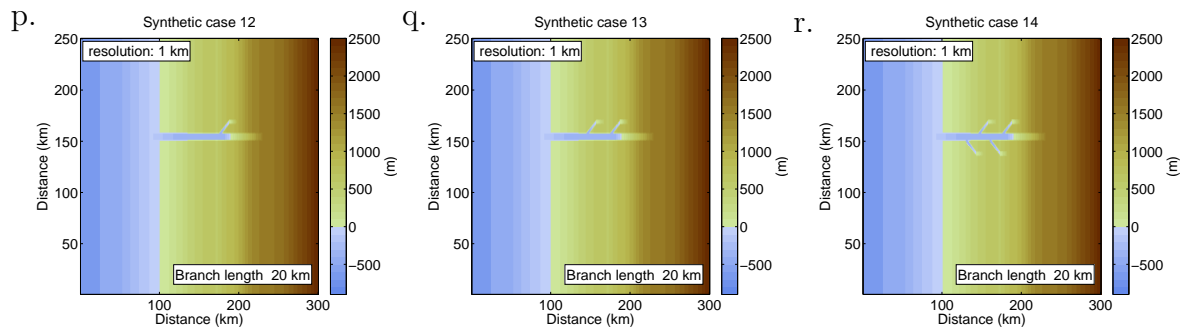


Figure A.7: Different number of branches.

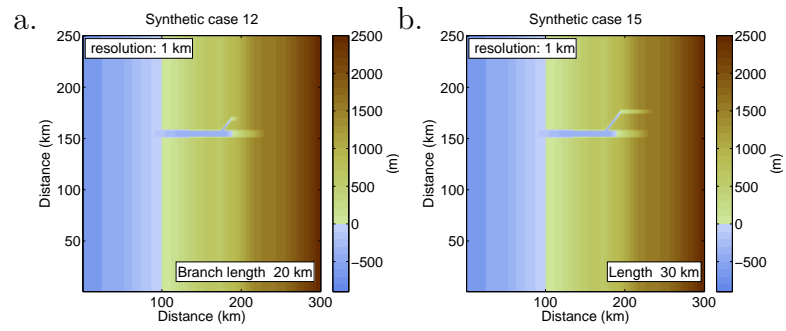


Figure A.8: Different branches length.

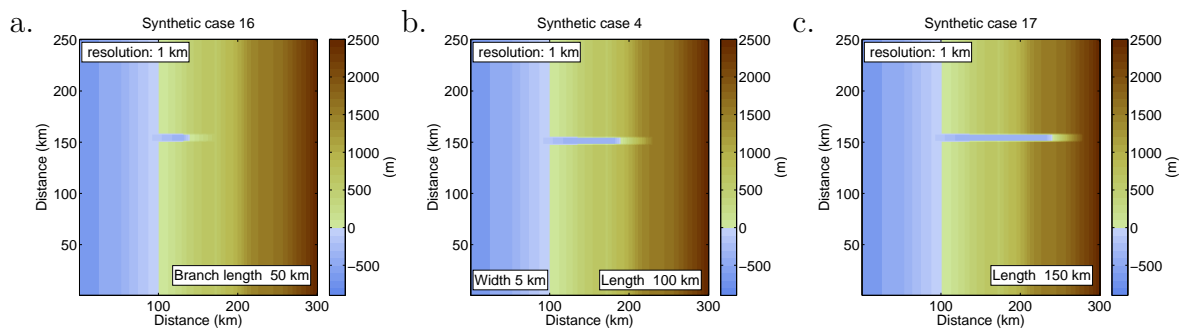


Figure A.9: Different fjord length.

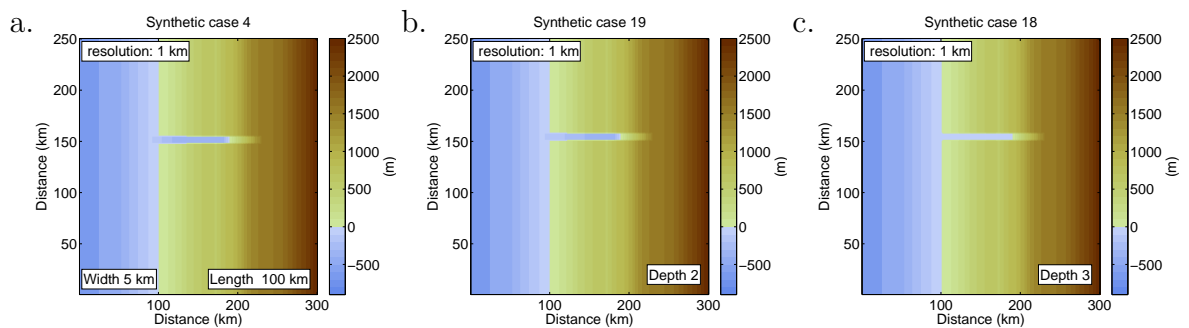


Figure A.10: Different depth profile.

A.1.1.3 Reasoning for the selection of the synthetic fjords

1. Sinusoidal shape (5 km width)

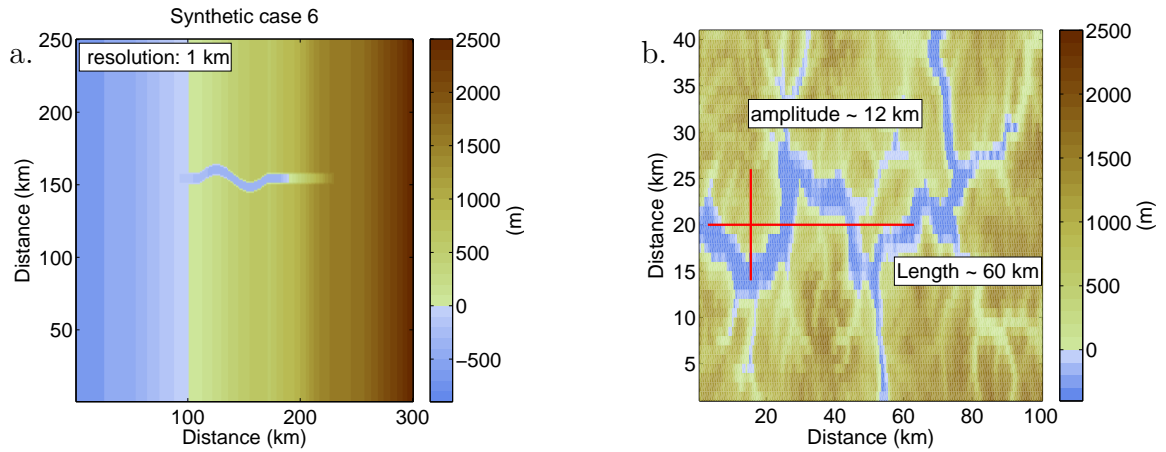


Figure A.11: Fjord id 6. Amplitude 12 km over 60 km.

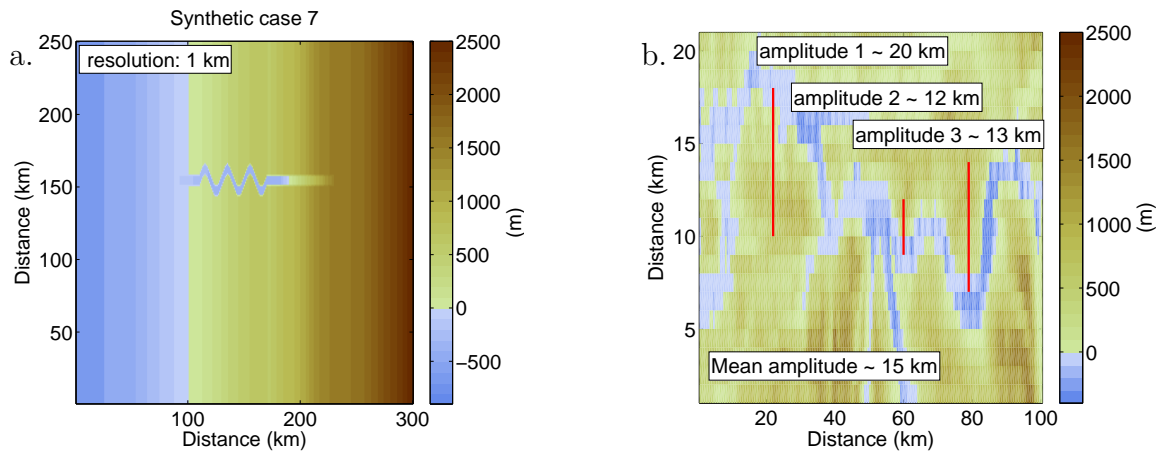


Figure A.12: Fjord id 7. Amplitude 15 km. 3 sinusoid over 60 km.

2. Fjord length

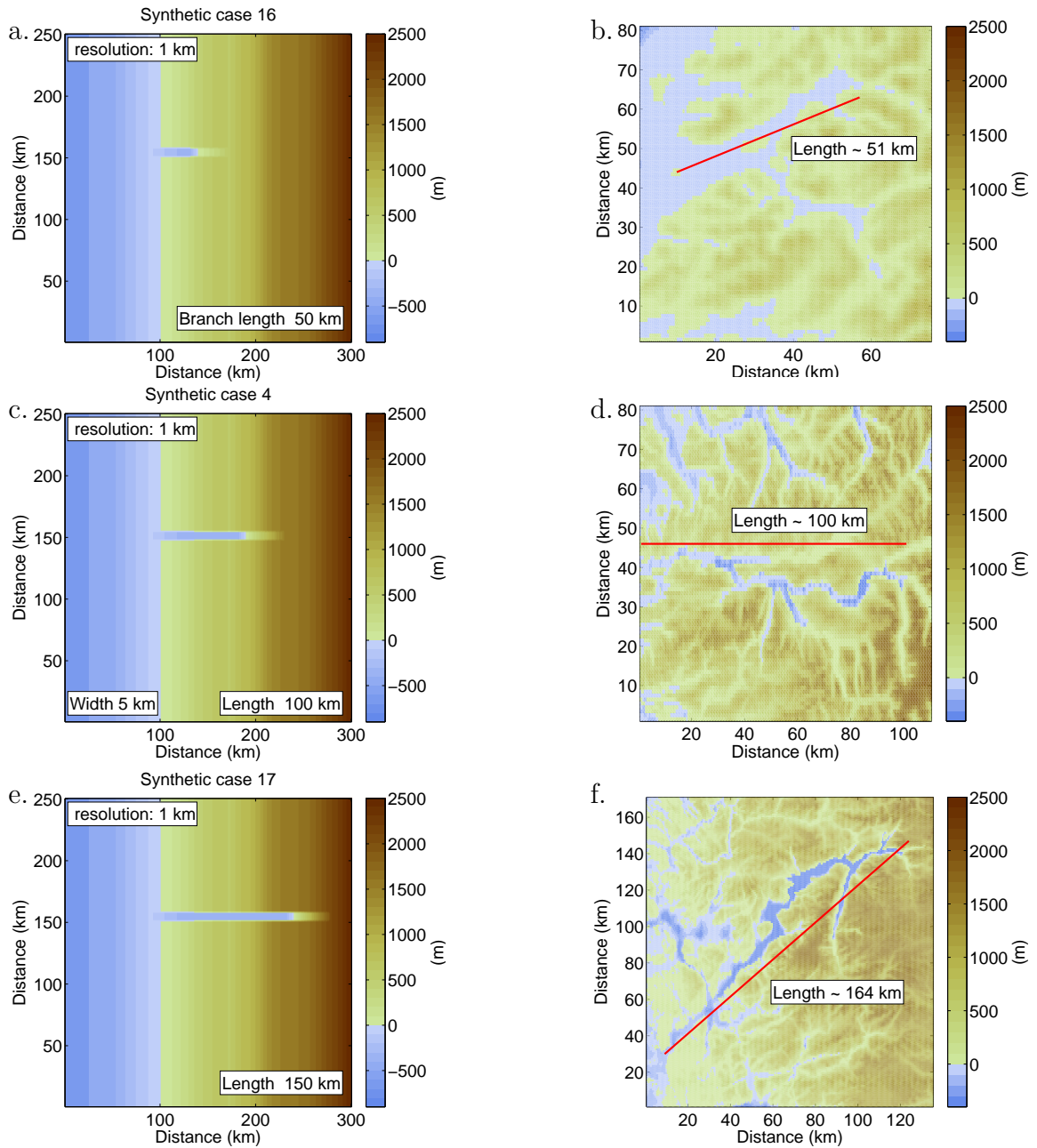


Figure A.13: Fjord id 17,4, 18. Different fjords length. A.13(a) 50 km long fjord. A.16(c) 100 km long fjord. A.13(e) 150 km long fjord.

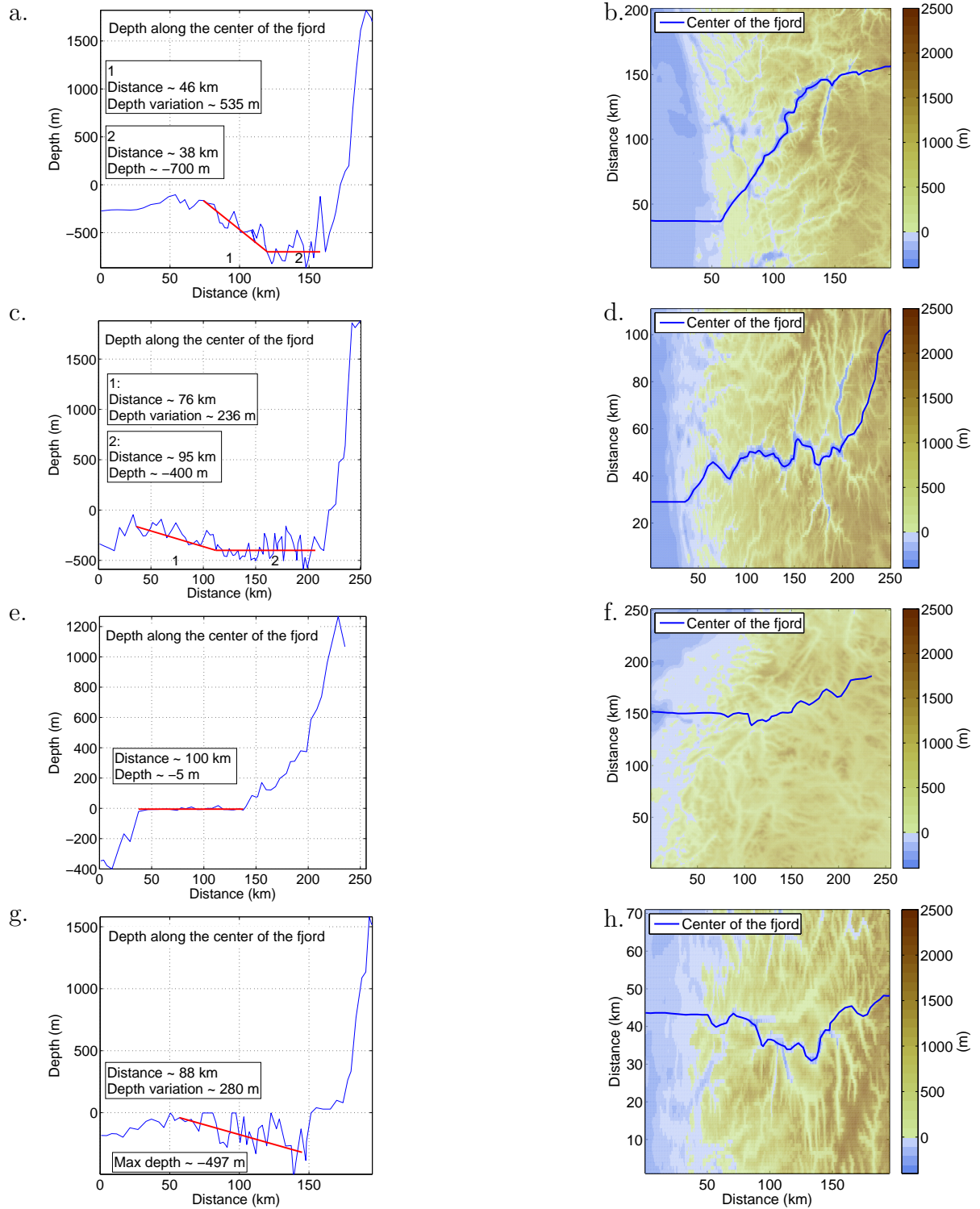


Figure A.15: Different depth variations along the fjord center for different regions.

4. Fjords width

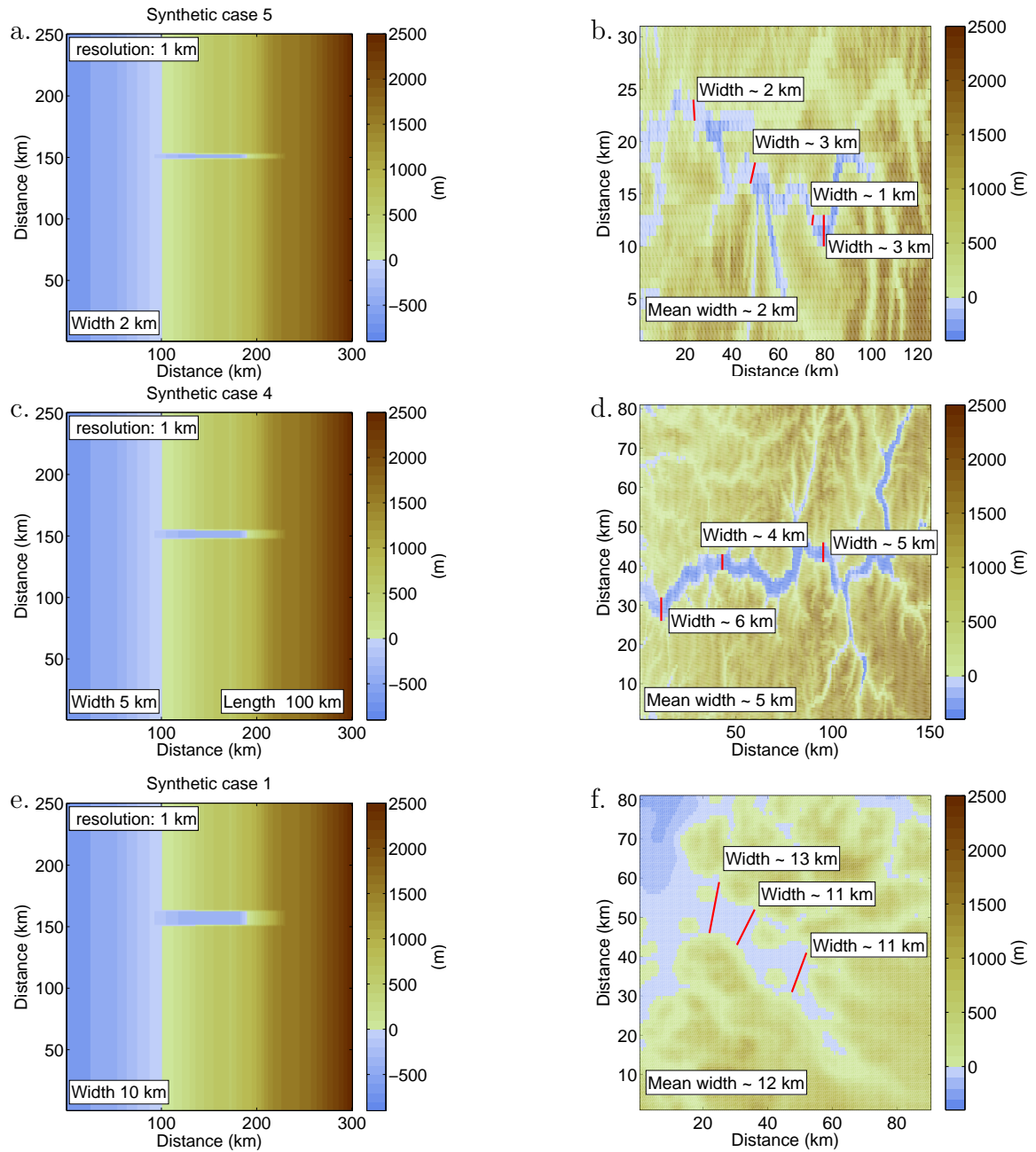


Figure A.16: Fjord id 5, 4, 1. Different fjords width. A.16(a) 2 km width. A.16(c) 5 km width. A.20(c) 10 km width.

5. Width variation toward the mouth

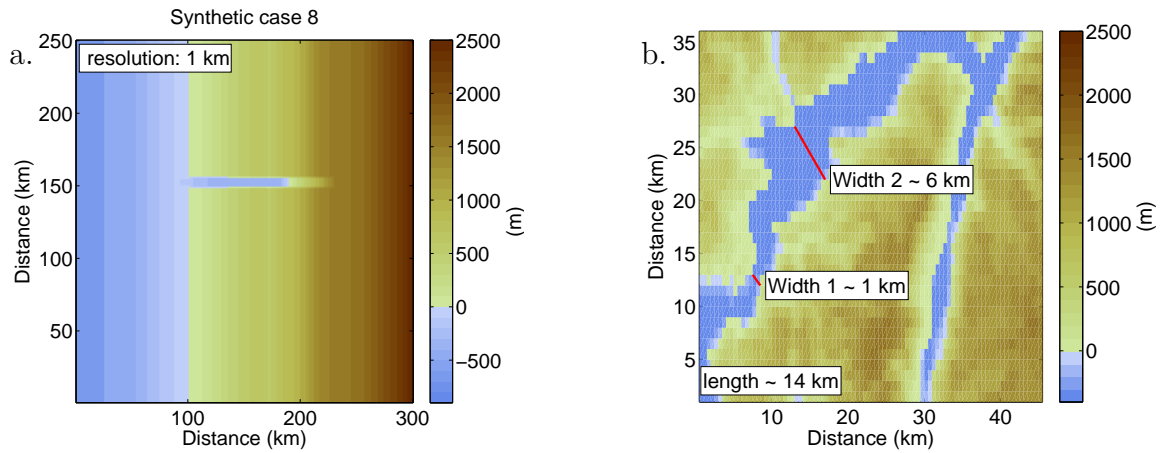


Figure A.17: Fjord id 8.1 km width at the mouth to 5 km upstream. Reduction done over 15 km.

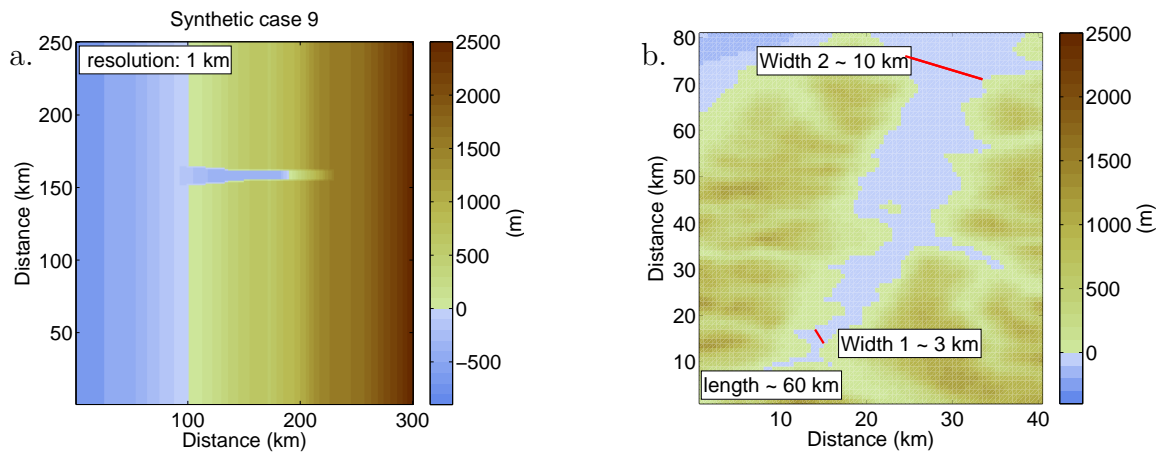


Figure A.18: Fjord id 9. 12 km width at the mouth to 5 km upstream. Reduction done over 60 km.

6. Branches

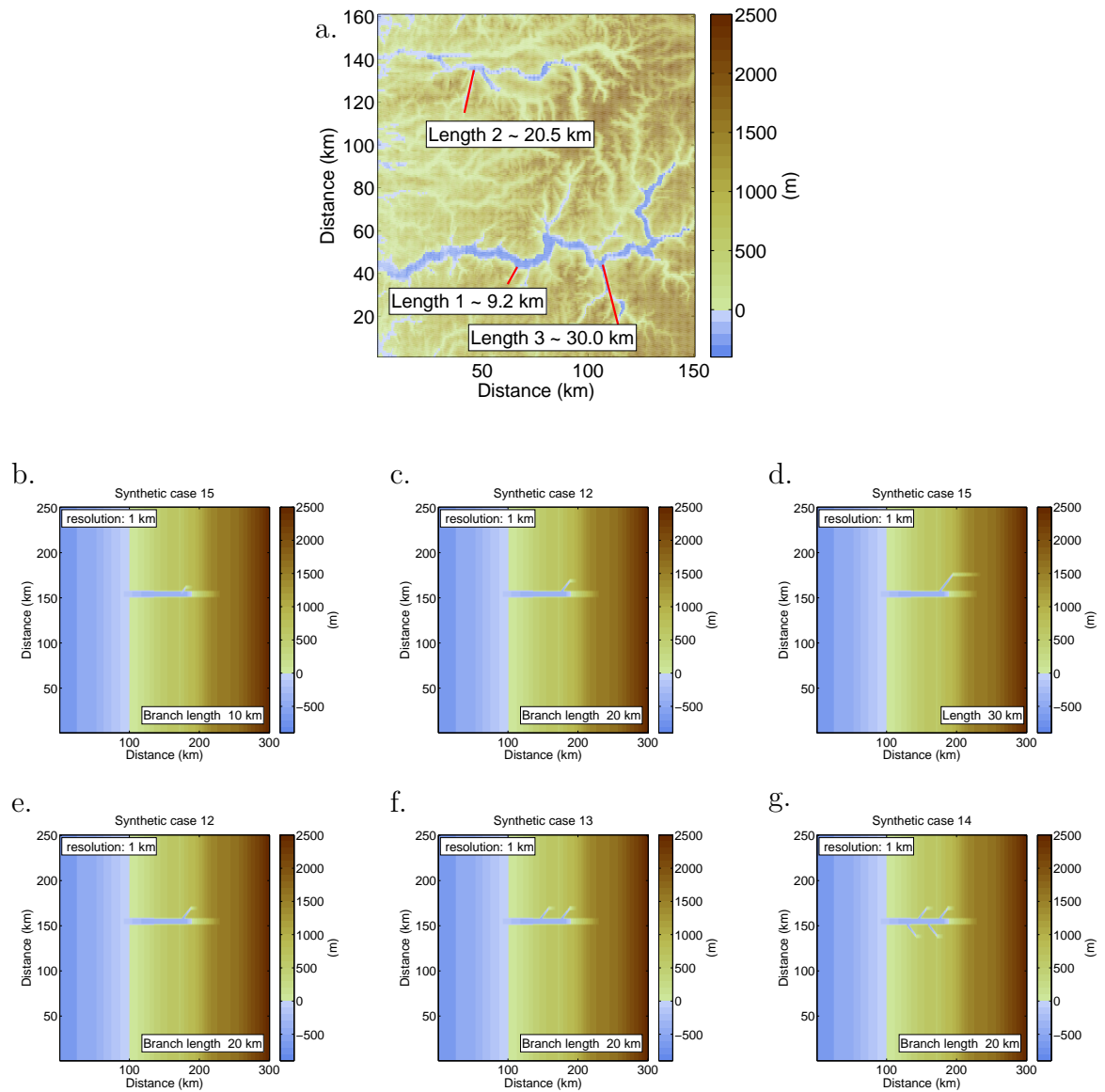


Figure A.19: Fjord id 15,12,16,12,13. Branches are 2 km wide and 10 (A.19(b)), 20 (A.19(e)), and 30 (A.19(d)) km long. A.19(e),A.19(f), A.19(g) 20 km length branches.

7. Multiple fjords

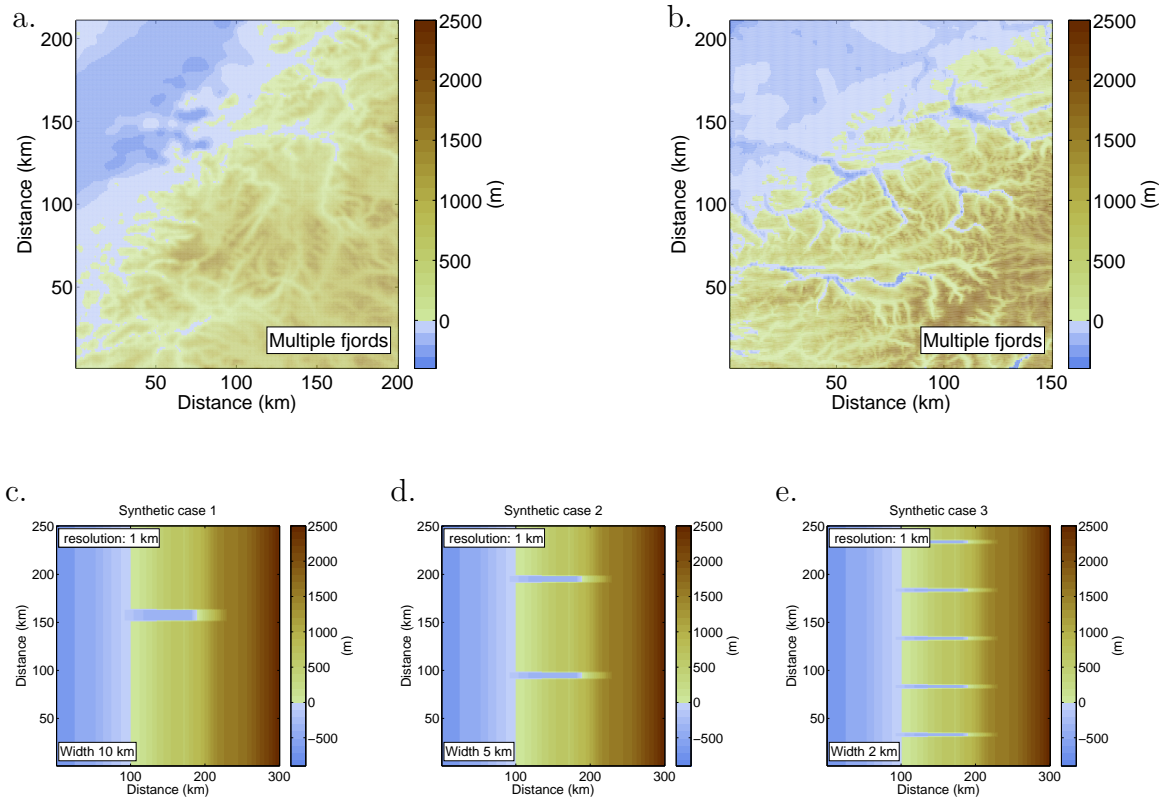


Figure A.20: Fjord id 1, 2, 3. Different number of fjords. A.20(c) one 10 km width fjord. A.20(d) two 5 km width fjord. A.20(e) five 2 km width fjord.

8. Different angles (constant 5 km width fjord)

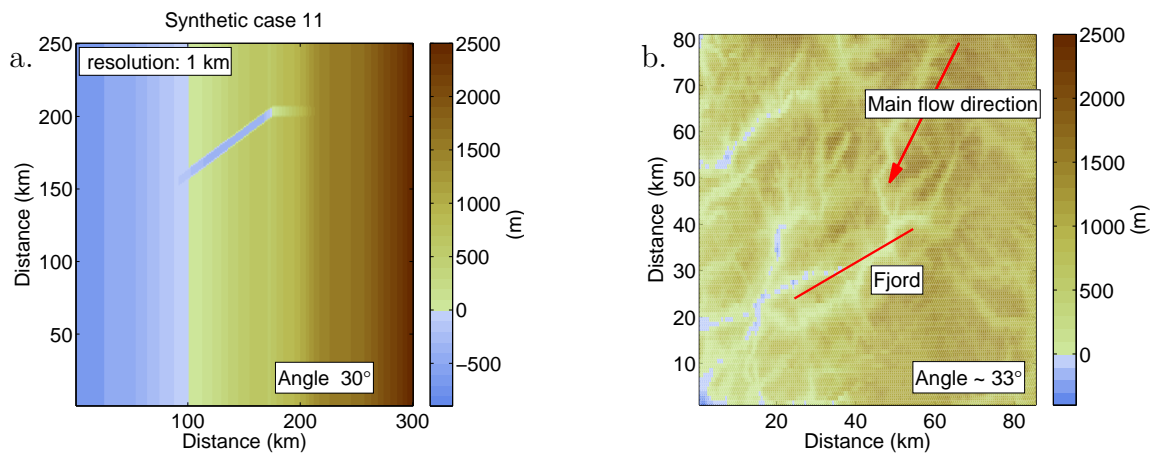


Figure A.21: Fjord id 11. 30 degrees angle

A.1.1.4 Example of one real and one synthetic fjord at different resolutions

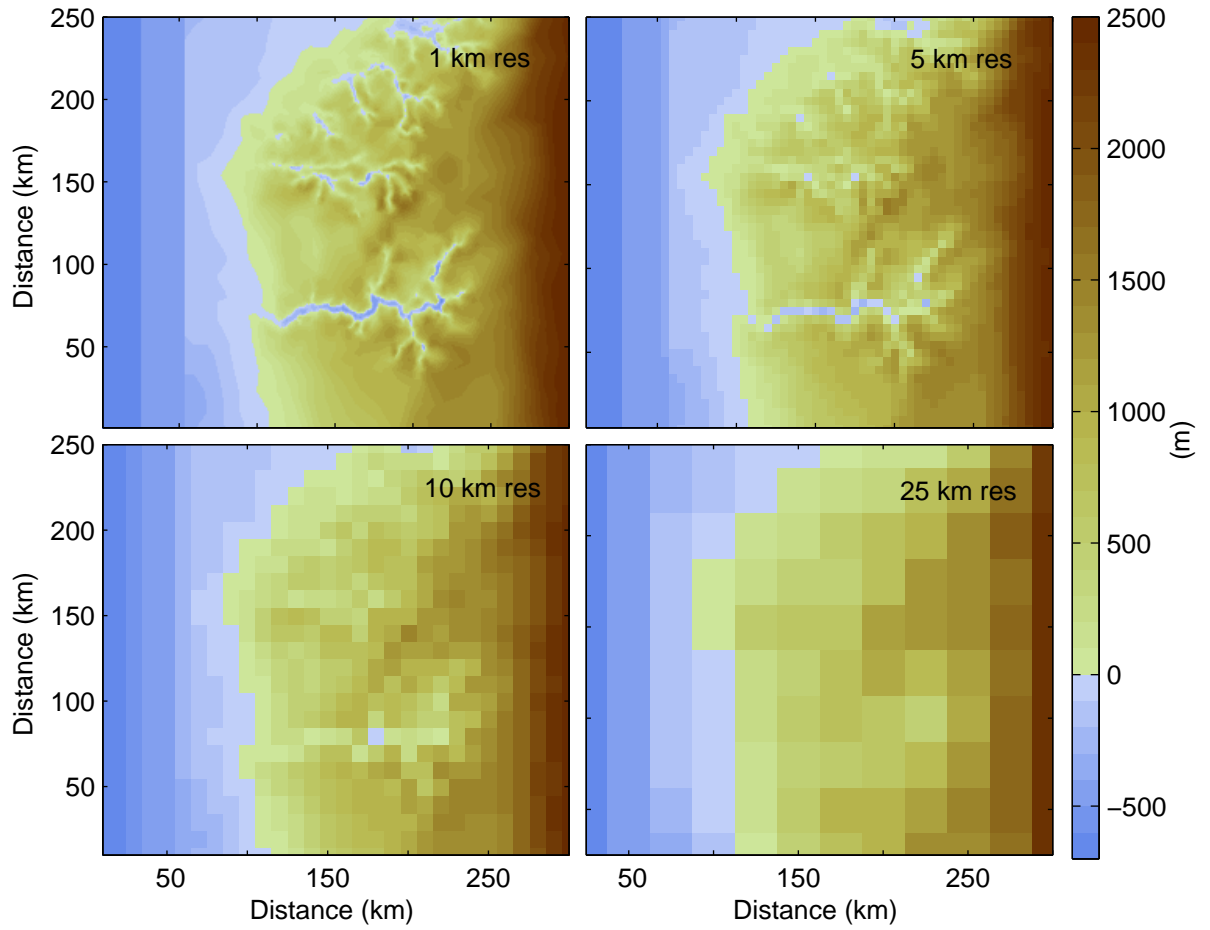


Figure A.22: Fjord 7 basal topography at different resolutions.

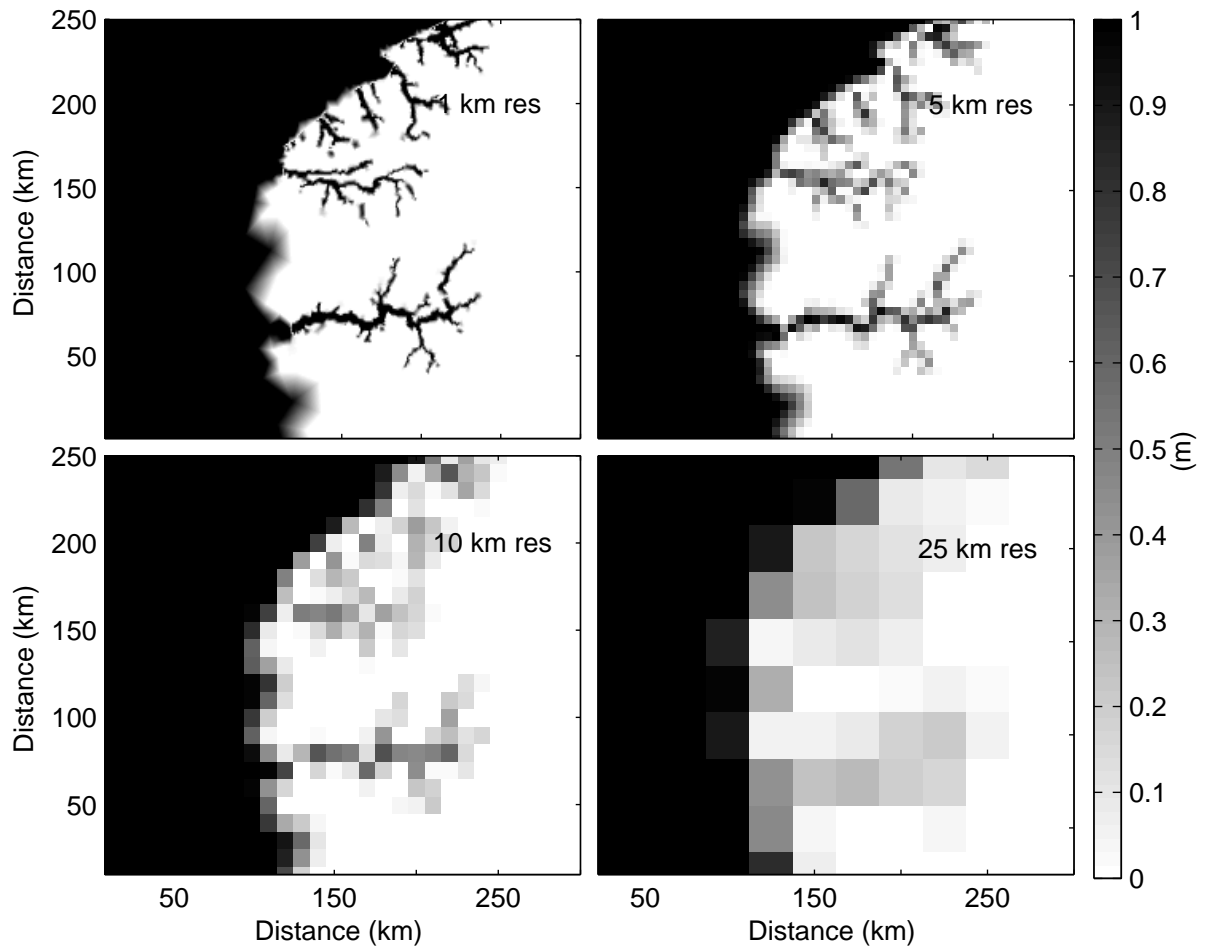


Figure A.23: Fjord 7 mask at different resolutions.

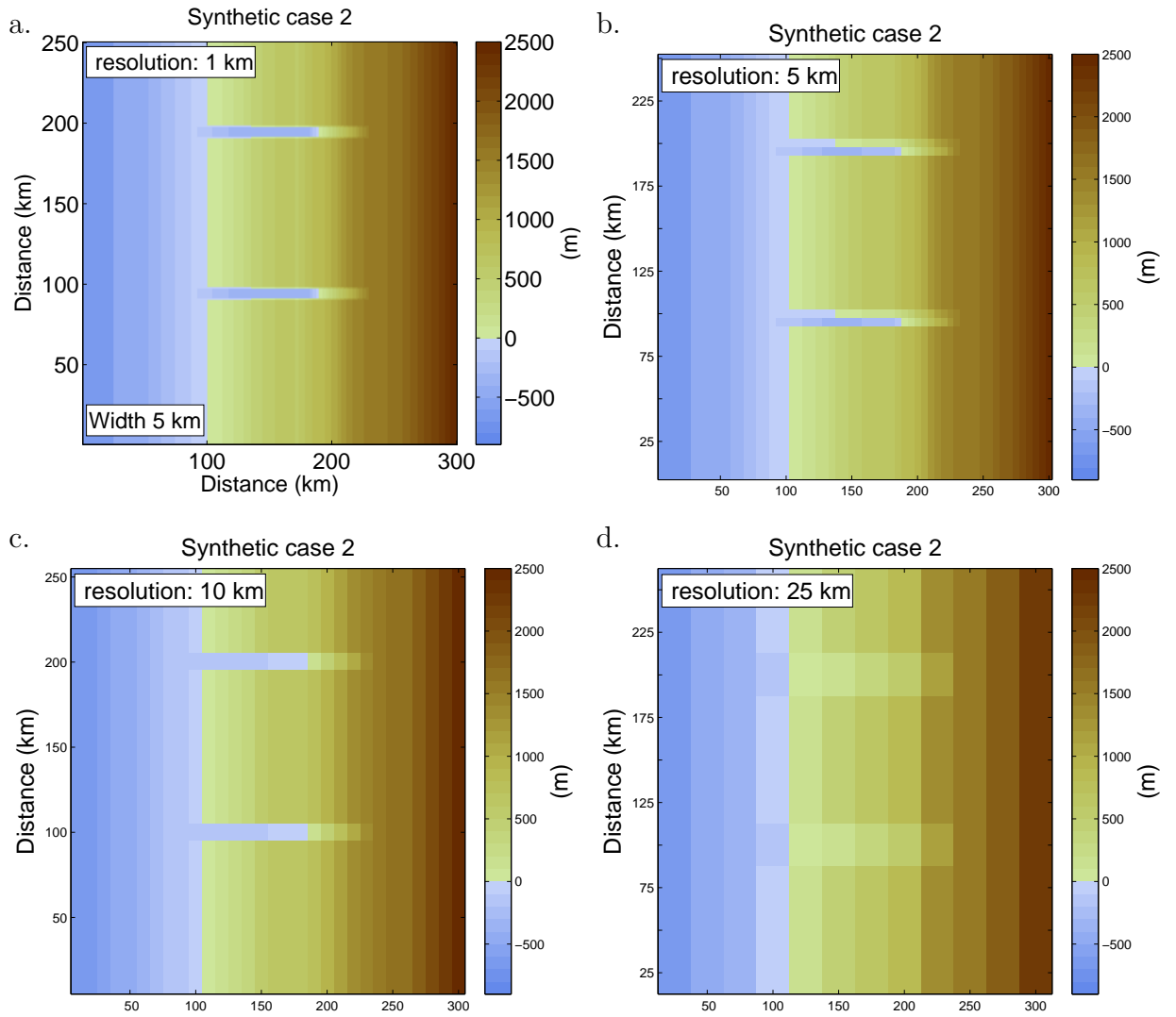


Figure A.24: Basal topography for synthetic fjord 2 at different resolutions.

A.1.2 Present day and LGM temperature and precipitation

A.1.2.1 Interpolation definition

The monthly temperature, T , is computed from the sea level LGM, T_{LGM} , and PD, T_{PD} , temperature as

$$T = Tdiff (T_{LGM} - T_{PD}) + T_{PD} - \lambda max(st, 0.001 sealev) \quad (A.1)$$

The lapse rate λ is defined as

$$\lambda = Tdiff \lambda_{LGM} + (1 - Tdiff) \lambda_{PD}. \quad (A.2)$$

The monthly precipitation ((m/yr)) is computed as:

$$P = min \left(1.5, P_{PD} \left(\frac{P_{LGM}}{P_{PD}} \right)^{Pfac} \right) \quad (A.3)$$

The parameters $Tdiff$, $Pfac$ are glacial indexes and $sealev$ represent the sea level evolution.

A.1.2.2 PD and LGM temperature and precipitation fields

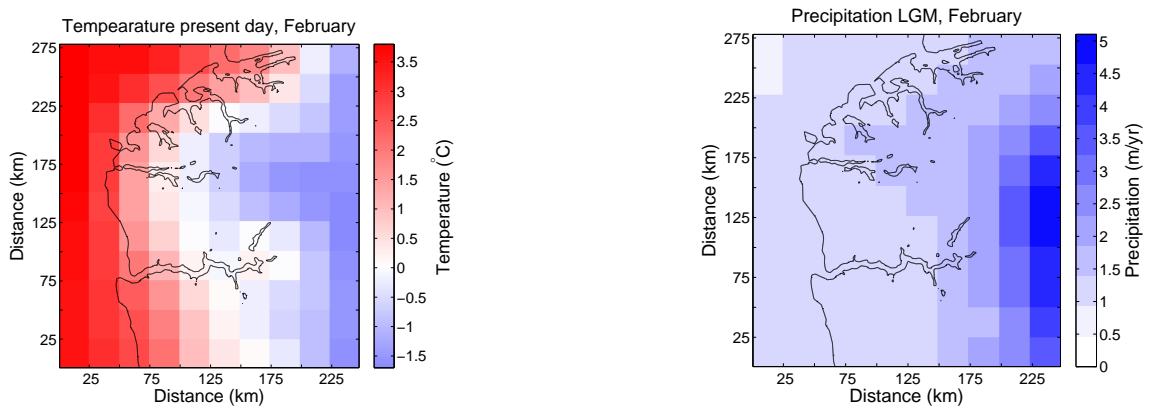


Figure A.25: Present day temperature and precipitation fields at 25 km resolution.

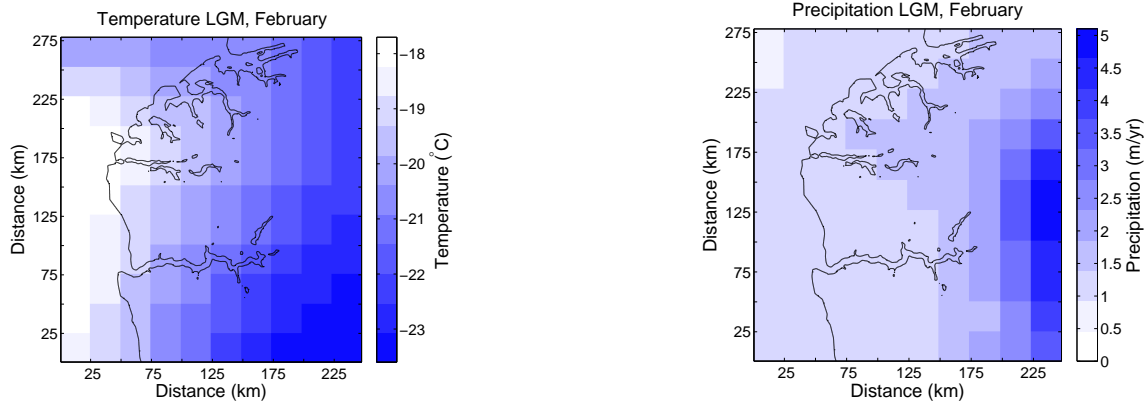


Figure A.26: Last glacial maximum temperature and precipitation fields at 25 km resolution.

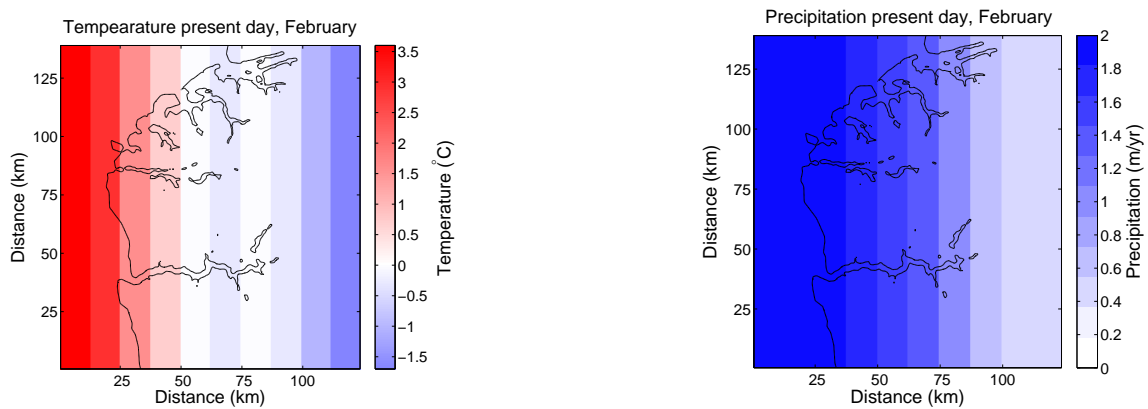


Figure A.27: Latitudinally constant present day temperature and precipitation fields at 25 km resolution.

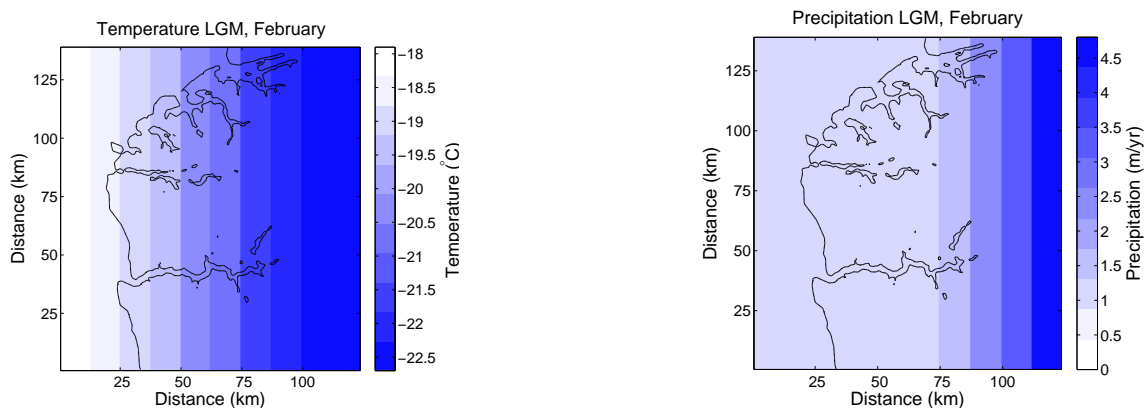


Figure A.28: Latitudinally constant last glacial maximum temperature and precipitation fields at 25 km resolution.

A.1.3 Climate parameters

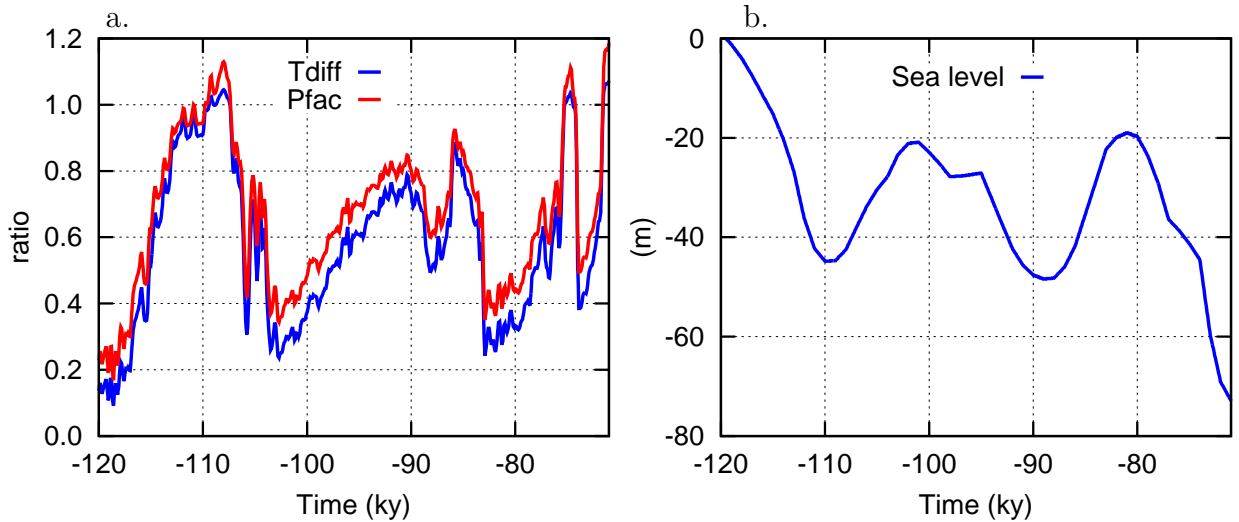


Figure A.29: Climate forcing parameters. The parameters $Tdiff$, $Pfac$ are glacial indexes (see Section A.1.2.1) and $sealev$ represent the sea level evolution.

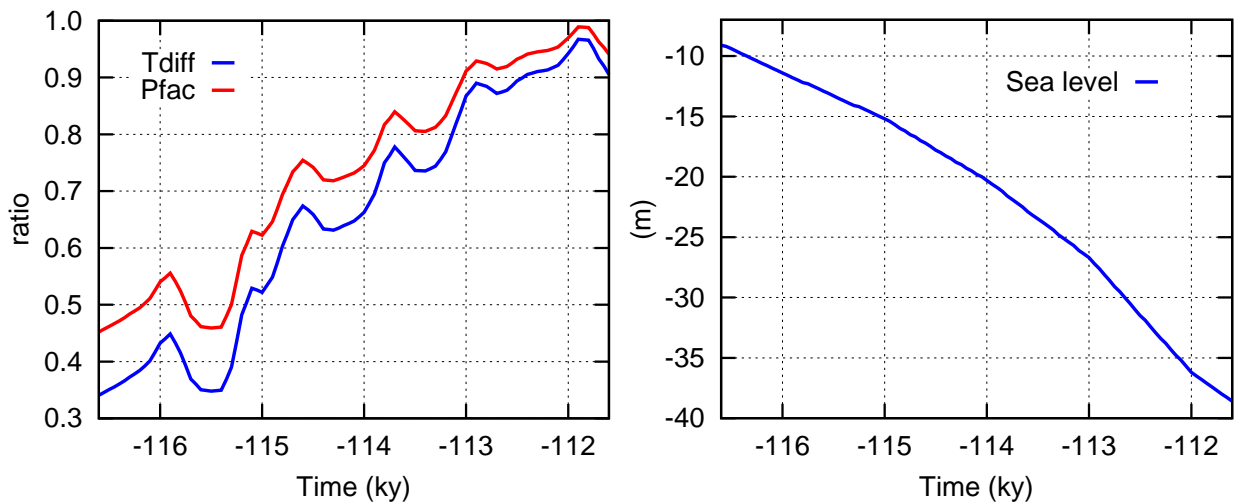


Figure A.30: Climate forcing parameters starting during inception starting at starting at 116.6 ka. The parameters $Tdiff$, $Pfac$ are glacial indexes (see Section A.1.2.1) and $sealev$ represent the sea level evolution.

A.1.4 Upstream boundary forcing

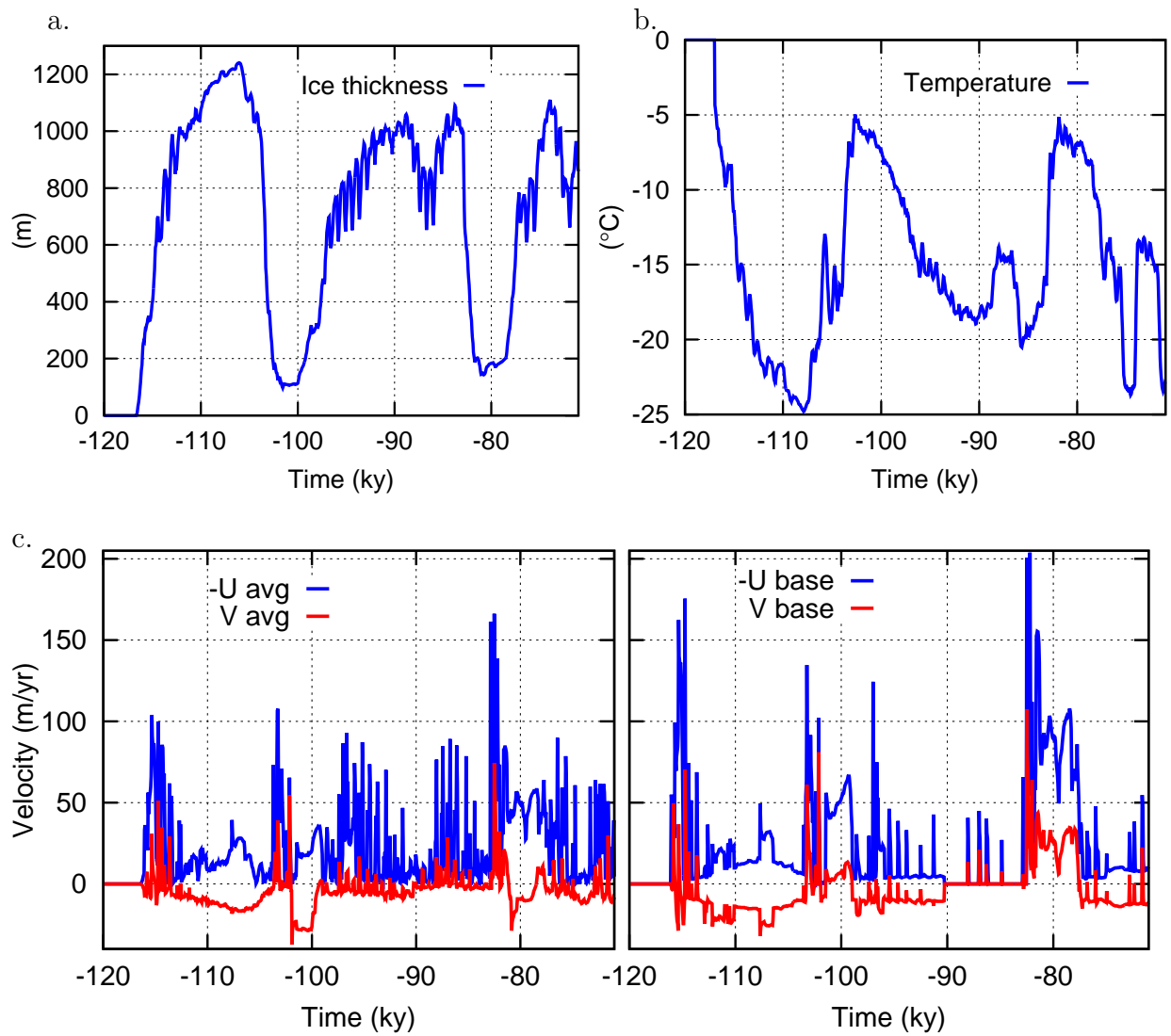


Figure A.31: Upstream ice thickness (a.), temperature (b.) and velocity forcing (c.). U_{avg} represents the vertically and latitudinally average velocity in the x direction (left to right on the topography maps). V_{avg} represents the vertically and latitudinally average velocity in the y direction (bottom to top on the topography maps). U_{base} and V_{base} represent the latitudinally average velocities at the base of the ice.

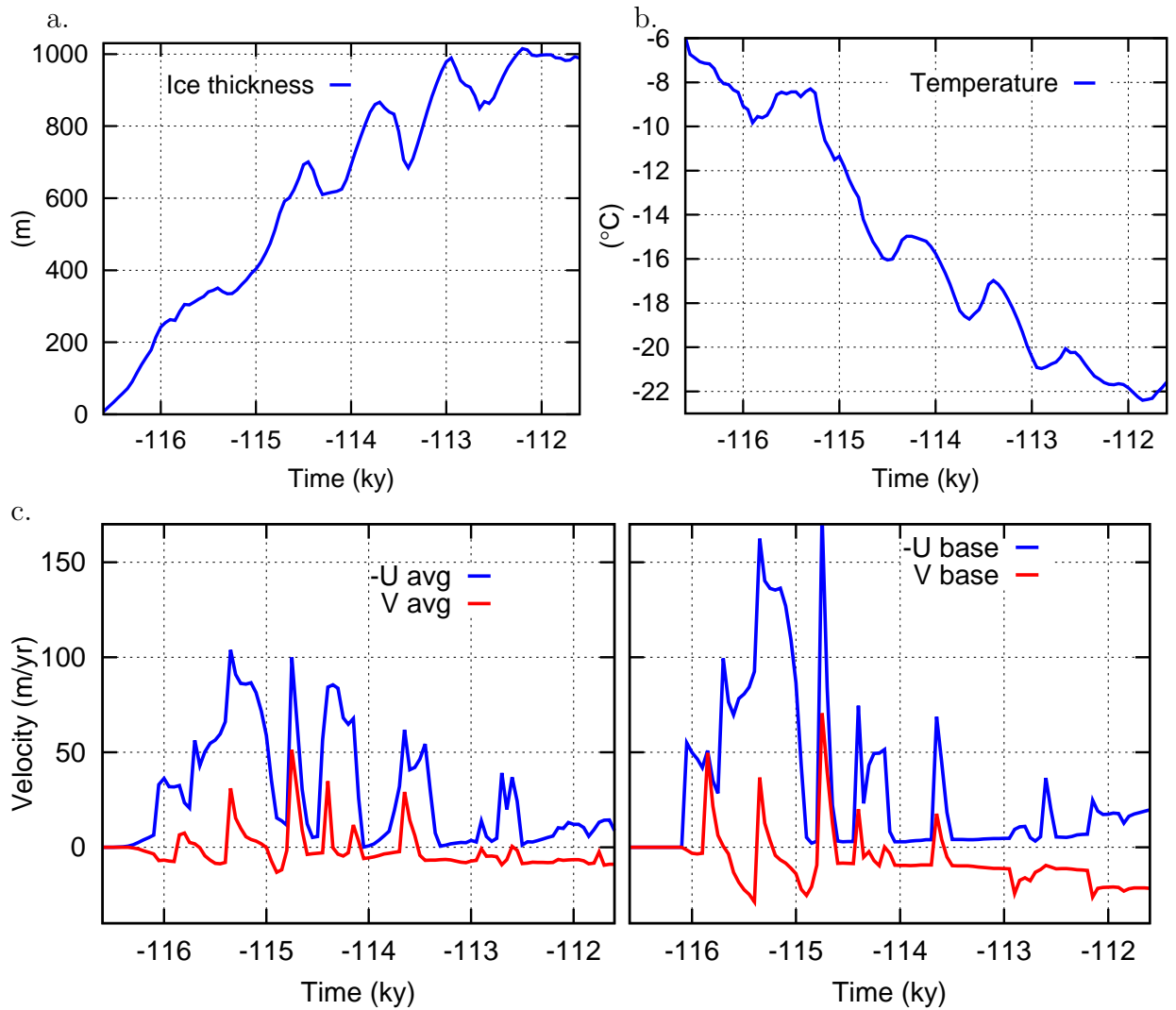


Figure A.32: Upstream ice thickness (a.), temperature (b.) and velocity forcing (c.) used in inception simulations. U_{avg} represents the vertically and latitudinally average velocity in the x direction (left to right on the topography maps). V_{avg} represents the vertically and latitudinally average velocity in the y direction (bottom to top on the topography maps). U_{base} and V_{base} represent the latitudinally average velocities at the base of the ice.

A.1.4.1 Geothermal heat flux during inception

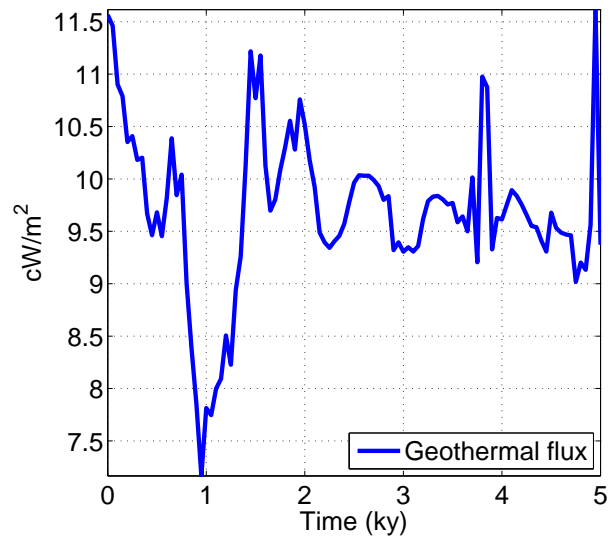


Figure A.33: Near basal geothermal heat flux evolution. Positive values have an upward heat flux).

A.2 PSU/GSM parameter vector

A.2.1 Impact of the flow enhancement coefficient for shelf flow (fnshelf)

Table A.2: Total ice volume difference between the base run and different fnshelf parameters showing a impact of less than 1 % (on average) of differences between simulations using the parameters tested (listed in table A.1) and simulation using the baseline parameter vector.

	res (km)	Volume (10^{14} m ³)				Percentage (%)			
		stadial		interstadial		stadial		interstadial	
		avg	std	avg	std	avg	std	avg	std
fnShelf1	5	0.00045	0.0012	-2.5e-05	0.00011	0.11	0.29	-0.027	0.18
fnShelf2	5	-0.0035	0.0036	2.2e-05	0.00013	-0.91	0.9	0.02	0.22
fnShelf1	10	0.00067	0.0031	1.1e-05	0.00011	0.17	0.75	0.063	0.29
fnShelf2	10	-0.0018	0.0029	5.6e-05	0.00029	-0.48	0.76	0.08	0.6
fnShelf1	25	0.0012	0.0054	-4e-05	0.00058	0.33	1.5	0.091	1.3
fnShelf2	25	-0.00076	0.0044	-0.0005	0.0019	-0.15	1.2	-1.2	3.8

A.2.2 Impact of the calving and sub-shelf melt parameters

Table A.3: Total ice volume difference between the base run and different calving and sub-shelf melt parameters showing a impact of less than 1 % (on average) of differences between simulations using the parameters tested (listed in table A.1) and simulation using the baseline parameter vector.

	res (km)	Volume (10^{14} m ³)				Percentage (%)			
		stadial		interstadial		stadial		interstadial	
		avg	std	avg	std	avg	std	avg	std
CM1	5	-0.0015	0.0021	-1.4e-05	7.1e-05	-0.38	0.53	-0.014	0.095
CM2	5	-0.001	0.0021	-1.1e-05	6.2e-05	-0.26	0.5	-0.026	0.12

CM1	10	-0.0019	0.003	9.7e-05	0.00034	-0.48	0.71	0.13	0.5
CM2	10	-0.00069	0.0026	0.00015	0.00038	-0.21	0.63	0.29	0.6
CM1	25	0.0011	0.0055	8e-06	0.00078	0.29	1.4	0.0034	1.2
CM2	25	-0.00027	0.0057	-0.00042	0.0021	-0.04	1.5	-1.3	5.1

A.2.3 Example of the impact of the flow enhancement coefficient for shelf flow, calving and sub-shelf melt parameters

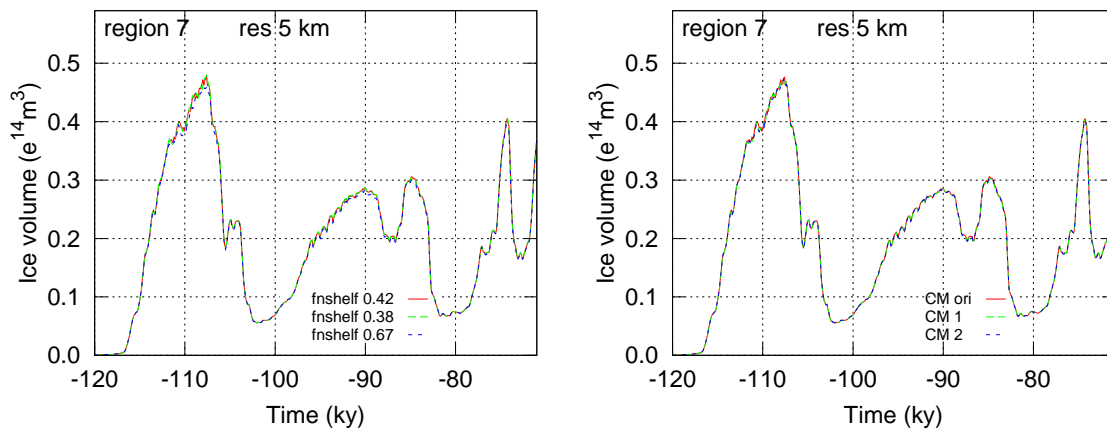


Figure A.34: Total ice volume evolution over fjord region 7 for different fn_{shelf} parameters (left panel) and for different calving and sub-shelf melt parameters (right panel) showing the limited impact of these parameters on the total ice volume evolution.

A.3 Experimental design

A.3.0.1 Soft bed parameters

Table A.1: Lists of the baseline parameter vector. Values are rounded to 2 decimal places.

Definition	Parameter	Original		fnshelf1	fnshelf2	CM1	CM2
		Quadratic	Linear				
Ice dynamics							
soft bed basal sliding coef.	slidsedC	0.4	8	8	8	8	8
hard bed basal sliding coef.	slidhardC	8	4	4	4	4	4
Flow enhancement coef. for grounded ice	flowC	4.28	4.28	4.28	4.28	4.28	4.28
Flow enhancement coef. for shelf flow	shelfflowC	0.42	0.42	0.38	0.67	0.47	0.47
Calving and sub-shelf melt							
Maximum calving velocity, tidewater glacier	calvmaxV/10	0.28	0.28	0.28	0.28	0.57	0.32
Grounding line zone SSM coef. (large shelves)	SSMGLz1C	1.18	1.18	1.18	1.18	1.13	0.88
Shelf front SSM coef. (large shelves)	SSMfrontC	2.89	2.89	2.89	2.89	2.23	1.90
Grounding line zone SSM coef. (large shelves)	SSMGLz1C	1.33	1.33	1.33	1.33	1.10	2.35
Ice shelf calving minimum thickness threshold	Hshelfcrit	0.64	0.64	0.64	0.64	0.84	0.53
Ice shelf calving coef.	shelfcalvC	2.35	2.35	2.35	2.35	2.10	1.02
Thin ice calving temperature-dependent coef.	calvthinC	0.41	0.41	0.41	0.41	0.50	0.32
Ice shelf calving sub-Hshelfcrit enhancement coef.	shelfcalv2C	0.19	0.19	0.19	0.20	1.21	0.41
Shelf front melt climate-dependence coef.	SSMfrontTC	0.67	0.67	0.68	0.68	1.08	0.86

Table A.4: Lists of soft bed parameter tested when using a linear or a quadratic sliding law.

		20 kPa velocity equivalence (m/yr)
Linear	Quadratic	
0	0	0
0.1	0.005	20
0.25	0.0125	50
0.5	0.025	100
2	0.1	400
8	0.4	1600
15	0.75	3000
30	1.5	6000
45	2.25	9000

A.4 Results

A.4.1 Fjord geometry impact

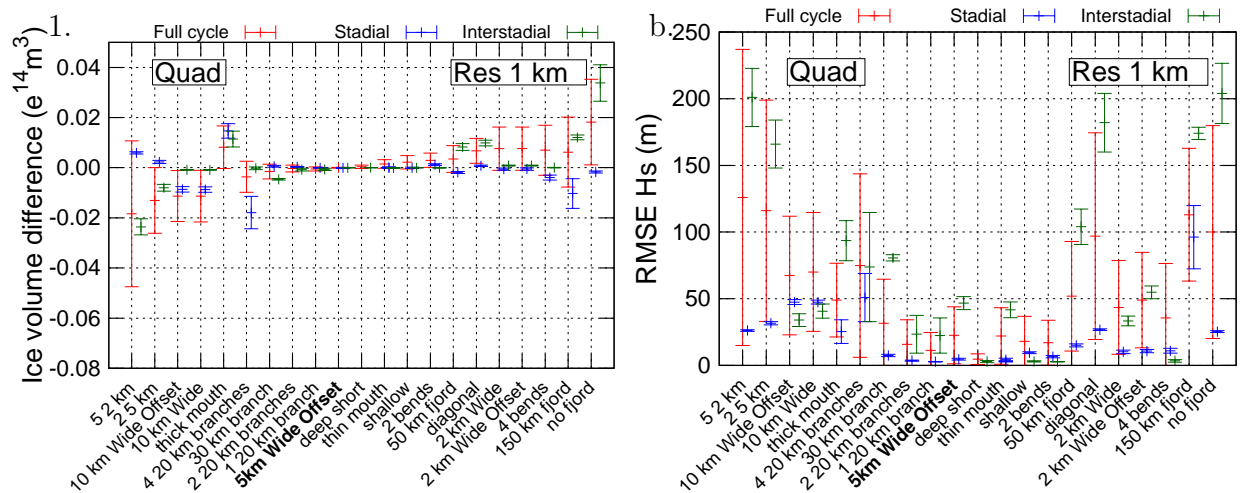


Figure A.35: Fjord characteristics impact compared to a 5 km wide and 100 km long fjord showing a relation between the fjord area and resistive stresses to the ice drainage. The left panel shows the total ice volume differences. The right panel shows the surface elevation [RMSE](#). Red represents the average and standard deviation over 50 kyr, blue at the end of inception (111 to 107 ka) and green at the end of the first interstadial event (102 to 100 ka). These simulations use the baseline parameter vector and a quadratic (Quad) sliding law. The x axis represent the different fjords region listed in Section [A.1.1.2](#) of the supplement. The boldface 5 km fjord, in the x axis, represents limit between regions generating less ice than the reference fjord (on the left) and the region with more ice (on the right).

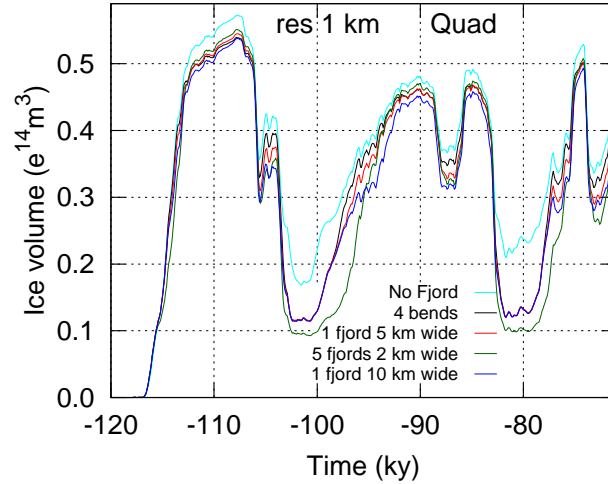


Figure A.36: Range of ice evolution generated with different fjord characteristics. These simulations use the baseline parameter vector and a quadratic (Quad) sliding law.

A.4.1.1 Ice volume evolution

Out of the following characteristics, number of fjords (Fig.A.37(a)), fjord width (Fig.A.37(b)), fjord length (Fig.A.38(a)), fjord terminus width (Fig.A.38(b)), fjord flow direction (Fig.A.39(a)), fjord number of bends (Fig.A.39(b)), fjord number of branches (Fig.A.40(a)), fjord branches length (Fig.A.40(b)), and the fjord depth profile (Fig.A.41) only the number of fjords and total size of fjords has a discernible impact on the rate of glaciation, non have an impact on deglacial rates.

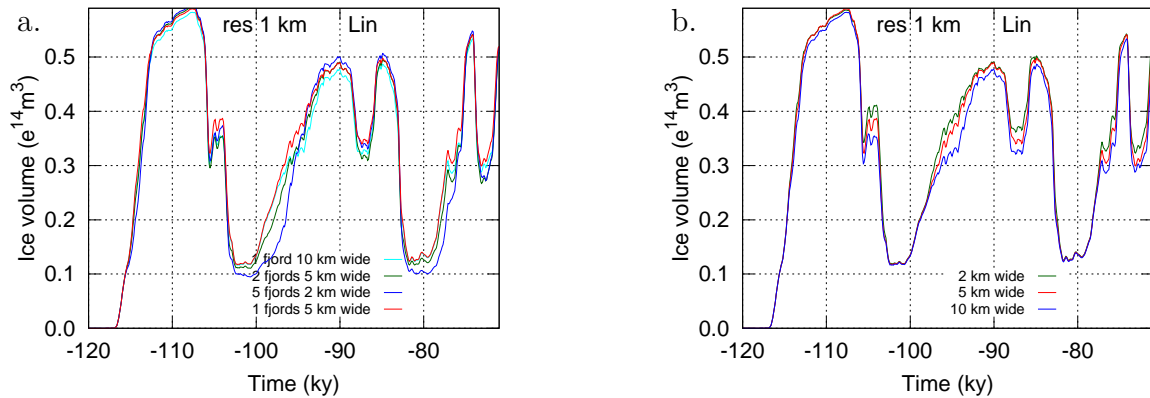


Figure A.37: Impact of fjord regions with a. different number of fjords with different width as shown in Fig.A.2 and b. one fjord of different width as shown in Fig.A.3 on the total ice volume evolution. These simulations use the baseline parameter vector and a linear (Lin) sliding law.

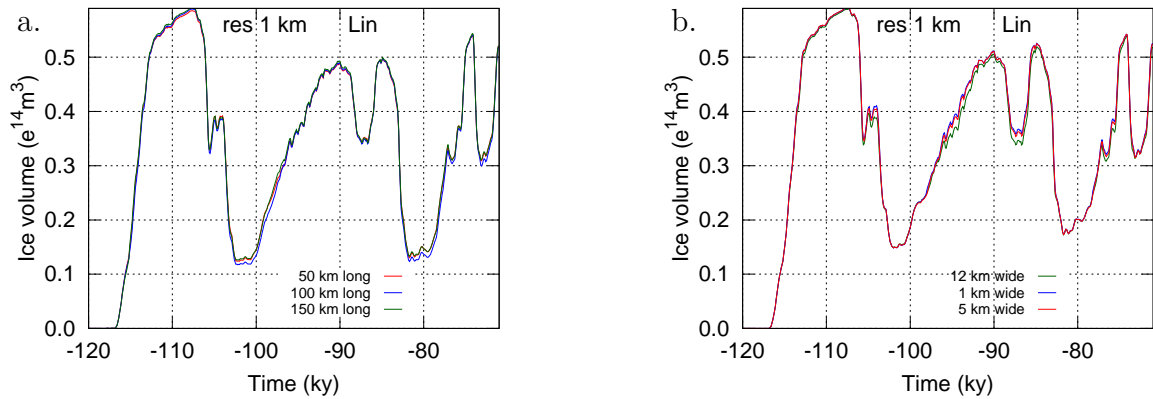


Figure A.38: Impact of fjord regions with a. different fjord length as shown in Fig.A.9 and b. different width at the mouth of the fjord as shown in Fig.A.5 on the total ice volume evolution. These simulations use the baseline parameter vector and a linear (Lin) sliding law.

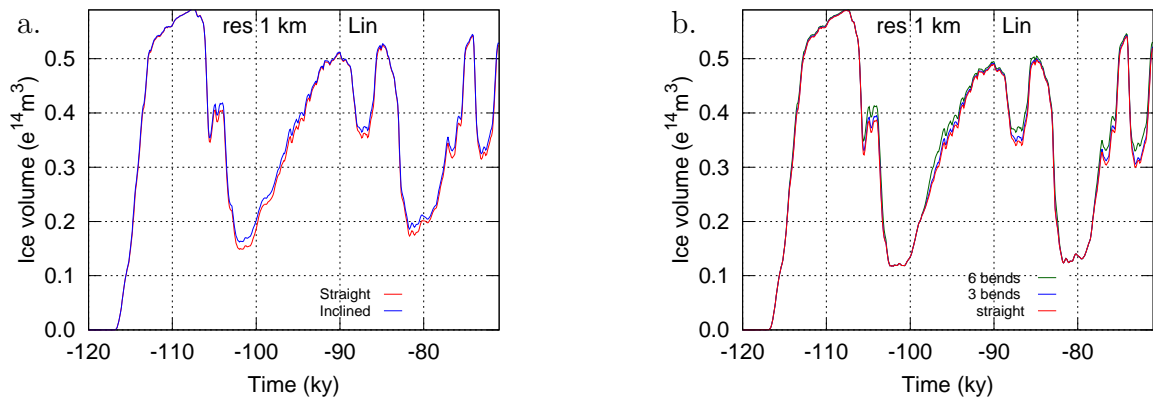


Figure A.39: Impact of fjord regions with a. fjord direction as shown in Fig.A.6 and b. different number of bends in the fjord as shown in Fig.A.4 on the total ice volume evolution. These simulations use the baseline parameter vector and a linear (Lin) sliding law.

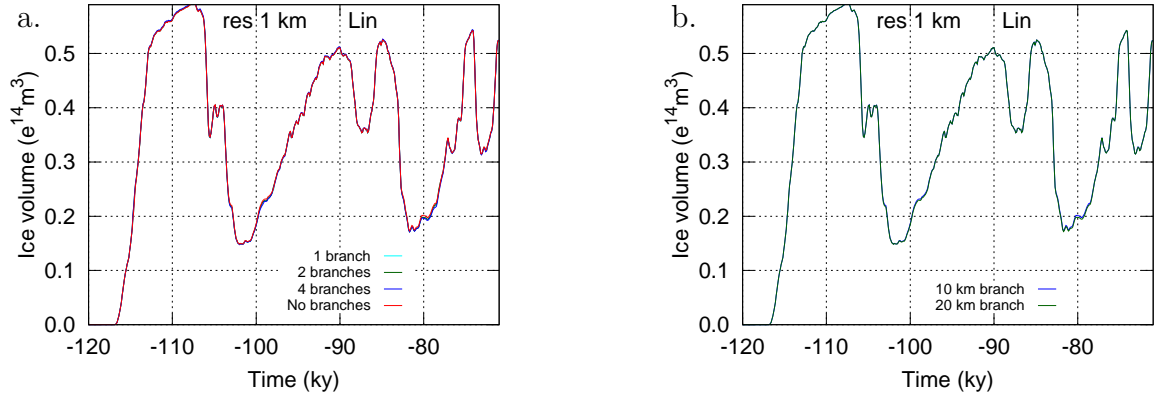


Figure A.40: Impact of fjord regions with a. different number of branches as shown in Fig.A.7 and b. one branch of different length as shown in Fig.A.8 on the total ice volume evolution. These simulations use the baseline parameter vector and a linear (Lin) sliding law.

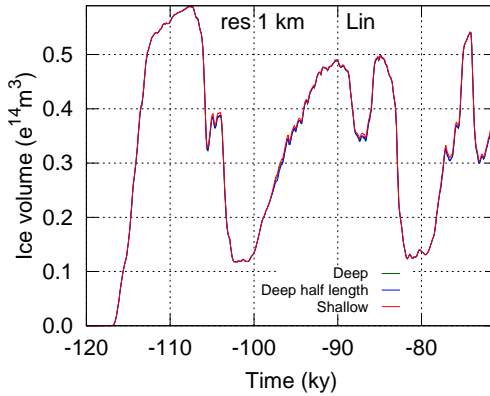


Figure A.41: Impact of fjord regions with different depth profile as shown in Fig.A.14 on the total ice volume evolution. These simulations use the baseline parameter vector and a linear (Lin) sliding law.

A.4.1.2 Statistics

Out of the following characteristics, number of fjords (Fig.A.37(a)), fjord width (Fig.A.37(b)), fjord length (Fig.A.38(a)), fjord terminus width (Fig.A.38(b)), fjord flow direction (Fig.A.39(a)), fjord number of bends (Fig.A.39(b)), fjord number of branches (Fig.A.40(a)), fjord branches length (Fig.A.40(b)), and the fjord depth profile (Fig.A.41) only the number of fjords and total size of fjords has a discernible impact on total ice volume evolution (table A.5) and surface elevation RMSE (table A.7) compared to a single fjord 5 km wide and 100 km long. The largest differences are

generated with five 2 km fjord that reduces the total ice volume on average by 9.6% (table A.5) and have surface elevation of 128 m (which is 24.6% of the average ice thickness, table A.7). We find the same conclusions when using a quadratic sliding law (table A.5 and A.8) instead of a linear sliding law.

Table A.5: Total ice volume evolution differences between regions with different characteristics and a region with a 5 km wide and 100 km long strait fjord (reference fjord) using a **linear** sliding law. Fjords with a wider area or with multiple fjords drain more ice than fjords with narrower fjords or increase resistive stresses (compared to the reference fjord).

Fjord	Volume (10^{14} m ³)						Percentage (%)					
	TS		SD		ISD		TS		SD		ISD	
	avg	std	avg	std	avg	std	avg	std	avg	std	avg	std
1 10 km	-0.0124	0.0111	-0.00744	0.000771	-0.00113	8.56e-05	-3.43	2.87	-1.3	0.159	-0.928	8.56e-05
2 5 km	-0.0138	0.0145	0.00365	0.000254	-0.00808	0.00139	-5.39	5.1	0.636	0.041	-6.59	0.00139
5 2 km	-0.0198	0.0326	0.007	0.000539	-0.0244	0.00422	-9.57	13.1	1.22	0.119	-19.9	0.00422
1 2 km	0.00763	0.00926	-0.00153	0.000655	0.00071	0.000118	2.45	2.8	-0.264	0.11	0.583	0.000118
2 bends	0.00276	0.00283	0.00071	0.000335	-1.43e-05	4.78e-05	0.819	0.862	0.125	0.0609	-0.0108	4.78e-05
4 bends	0.00985	0.0104	0.00223	0.000492	6.19e-05	8.65e-05	3.04	3.38	0.391	0.0941	0.0523	8.65e-05
thin mouth	0.0015	0.00188	-0.000344	0.000278	-0.000329	0.000174	0.457	0.549	-0.0592	0.0469	-0.205	0.000174
thick mouth	-0.0053	0.00577	-0.00255	0.000487	0.000795	0.000304	-1.36	1.52	-0.444	0.0895	0.498	0.000304
no fjord	0.0188	0.0191	-0.00351	0.000804	0.0535	0.00719	8.19	9.79	-0.607	0.13	33.7	0.00719
included	0.00663	0.0054	-8.54e-05	0.000543	0.0159	0.00168	2.62	2.61	-0.0131	0.0946	10	0.00168
1 20 km branch	-0.000497	0.000924	0.000202	0.000221	-0.000852	0.000498	-0.247	0.448	0.0353	0.0378	-0.521	0.000498
2 20 km branches	-0.000312	0.00136	0.00082	0.000131	-0.000924	0.000583	-0.197	0.615	0.142	0.0224	-0.563	0.000583
4 20 km branches	-0.000197	0.00227	0.00193	0.000393	-0.00132	0.000665	-0.261	0.941	0.336	0.07	-0.811	0.000665
30 km branch	-0.00153	0.00329	0.00124	0.000186	-0.00496	0.000476	-1.05	1.83	0.217	0.0347	-4.06	0.000476
50 km fjord	0.00338	0.00541	-0.0029	0.000431	0.00818	0.00135	2.01	2.94	-0.504	0.0662	6.67	0.00135
150 km fjord	0.00561	0.00501	0.00258	0.000579	0.00996	0.000594	2.52	3.32	0.452	0.111	8.15	0.000594
shallow	0.00195	0.00236	-0.000393	0.000473	-1.43e-05	4.78e-05	0.601	0.703	-0.0669	0.0814	-0.0109	4.78e-05
deep	0.000196	0.00101	0.00011	0.000184	-3.81e-05	6.69e-05	0.044	0.338	0.0194	0.0324	-0.0303	6.69e-05
10km Wide Offset	-0.0124	0.0112	-0.0073	0.00105	-0.00115	8.73e-05	-3.44	2.89	-1.28	0.205	-0.943	8.73e-05
5km Wide Offset	-8.72e-05	0.000252	-0.000141	0.00023	-2.86e-05	7.17e-05	-0.0275	0.0885	-0.024	0.0399	-0.0224	7.17e-05
2km Wide Offset	0.00762	0.00926	-0.00154	0.000607	0.000719	0.000121	2.45	2.8	-0.267	0.102	0.591	0.000121

Table A.6: Total ice volume evolution differences between regions with different characteristics and a region with a 5 km wide and 100 km long strait fjord (reference fjord) using a quadratic sliding law. Fjords with a wider area or with multiple fjords drain more ice than fjords with narrower fjords or increase resistive stresses (compared to the reference fjord).

Fjord	Volume (10^{14} m^3)						Percentage (%)					
	TS		SD		ISD		TS		SD		ISD	
	avg	std	avg	std	avg	std	avg	std	avg	std	avg	std
1 10 km	-0.0113	0.0103	-0.00872	0.0011	-0.000886	9.64e-05	-3.24	2.76	-1.66	0.243	-0.747	9.64e-05
2 5 km	-0.0131	0.0131	0.0023	0.000621	-0.00798	0.00135	-5.3	4.9	0.433	0.111	-6.69	0.00135
5 2 km	-0.0184	0.0291	0.00594	0.000433	-0.0236	0.00319	-9.29	12.5	1.12	0.0847	-19.8	0.00319
1 2 km	0.00761	0.00864	-0.00061	0.000477	0.000871	0.000174	2.53	2.74	-0.114	0.0887	0.731	0.000174
2 bends	0.00296	0.00285	0.00125	0.000358	-3.81e-05	7.4e-05	0.9	0.925	0.237	0.0715	-0.0321	7.4e-05
4 bends	0.00698	0.01	-0.00395	0.001	3.81e-05	6.69e-05	2.36	3.24	-0.745	0.175	0.0331	6.69e-05
thin mouth	0.00147	0.00172	9.76e-06	0.000296	-0.000105	6.69e-05	0.468	0.565	0.000902	0.0523	-0.0701	6.69e-05
thick mouth	0.00819	0.00848	0.0147	0.0029	0.0114	0.00316	2.55	2.35	2.64	0.522	7.66	0.00316
no fjord	0.0182	0.0171	-0.0017	0.000424	0.0338	0.00729	7.96	8.78	-0.304	0.0733	22.7	0.00729
included	0.00675	0.00498	0.000754	0.000257	0.00985	0.00112	2.67	2.32	0.135	0.0468	6.66	0.00112
1 20 km branch	-0.000469	0.000822	-7.32e-05	0.000167	-0.000681	0.000453	-0.233	0.42	-0.0135	0.0302	-0.447	0.000453
2 20 km branches	-0.000304	0.00136	0.00032	0.000176	-0.000757	0.000539	-0.173	0.637	0.0569	0.031	-0.496	0.000539
4 20 km branches	-0.00364	0.00618	-0.0179	0.00649	-0.00021	0.000539	-0.966	1.35	-3.19	1.14	-0.125	0.000539
30 km branch	-0.0015	0.00294	0.00058	0.000391	-0.00463	0.000292	-1.02	1.74	0.11	0.0739	-3.9	0.000292
50 km fjord	0.00347	0.00536	-0.00186	0.000402	0.00827	0.00138	2.08	3.01	-0.352	0.0703	6.93	0.00138
150 km fjord	0.00623	0.014	-0.0103	0.00588	0.0121	0.000955	3.5	5.43	-1.93	1.09	10.2	0.000955
shallow	0.00219	0.00268	-8.05e-05	0.00027	-4.76e-06	4.98e-05	0.71	0.874	-0.0145	0.0509	-0.00419	4.98e-05
deep	0.000367	0.00067	-2.44e-06	0.000216	9.52e-06	5.39e-05	0.105	0.212	9.05e-05	0.0409	0.00813	5.39e-05
10km Wide Offset	-0.0113	0.0102	-0.0086	0.00109	-0.000867	9.66e-05	-3.23	2.74	-1.63	0.24	-0.731	9.66e-05
5km Wide Offset	-3.61e-05	0.000138	-8.78e-05	0.000224	-1.43e-05	5.73e-05	-0.0128	0.0451	-0.0164	0.0418	-0.0119	5.73e-05
2km Wide Offset	0.00761	0.00863	-0.000529	0.00049	0.000871	0.000174	2.53	2.74	-0.0985	0.0915	0.731	0.000174

Table A.7: Surface elevation **RMSE** differences between regions with different characteristics and a region with a 5 km wide and 100 km long strait fjord (reference fjord) using a **linear** sliding law. The errors are proportional to the differences in the fjords area and resistive stresses generated by the shape of the fjords compared to the reference fjord.

Fjord	RMSE h_s (m)						Percentage (%)					
	TS		SD		ISD		TS		SD		ISD	
	avg	std	avg	std	avg	std	avg	std	avg	std	avg	std
1 10 km	72.2	46.6	42.1	2.89	40.1	4.11	11.8	6.25	5.06	0.448	9.17	4.11
2 5 km	113	86.3	18	1.88	168	20.8	21.3	16.7	2.17	0.276	38.8	20.8
5 2 km	128	118	16.2	0.354	206	25.4	24.6	22.8	1.94	0.0834	47.4	25.4
1 2 km	41.8	34.8	5.32	1.91	34.7	4.54	7.33	5.45	0.644	0.246	7.94	4.54
2 bends	16.2	15.5	3.87	0.838	3.22	1.79	2.67	2.56	0.467	0.111	0.735	1.79
4 bends	41.7	42.7	9.14	1.6	3.96	1.65	6.86	6.96	1.1	0.218	0.905	1.65
thin mouth	21.6	20.9	3.63	0.959	42.8	5.45	4.03	4.04	0.434	0.109	8.74	5.45
thick mouth	44.1	28.7	11.7	1.15	69.2	8.49	7.78	5.3	1.4	0.156	14.2	8.49
no fjord	100	86.1	16.1	2.79	252	15.4	19.5	18.7	1.94	0.377	60.2	15.4
included	95.1	82	17.3	2.42	197	23.2	17.9	16.3	2.08	0.336	43	23.2
1 20 km branch	11.3	14.6	2.29	0.417	25.5	12.9	2.11	2.78	0.273	0.0451	5.18	12.9
2 20 km branches	15.1	17.9	3.19	1.16	26.7	14.1	2.77	3.35	0.38	0.132	5.42	14.1
4 20 km branches	17.9	21.9	3.7	1.59	28.6	16.1	3.3	4.1	0.44	0.181	5.8	16.1
30 km branch	29.4	34.3	4.76	0.485	81.3	4.04	6.3	7.71	0.571	0.0502	18.6	4.04
50 km fjord	49.8	42.7	8.92	1.55	107	12.9	9.99	9.52	1.08	0.212	25.3	12.9
150 km fjord	81.6	57.6	31.1	1.74	171	5.87	20.3	28.7	3.73	0.14	41.8	5.87
shallow	15.7	14.7	6.91	1.71	3.18	1.05	2.52	2.38	0.834	0.222	0.725	1.05
deep	5.24	7.34	2.47	0.552	3.6	1.52	0.881	1.24	0.296	0.0672	0.824	1.52
10km Wide Offset	69.8	47.4	41.1	4.33	34.7	5.38	11.3	6.35	4.95	0.614	7.94	5.38
5km Wide Offset	21.9	21.9	3.41	0.501	47.4	7.9	4.48	4.78	0.409	0.0533	10.9	7.9
2km Wide Offset	47.6	36.2	5.68	1.82	56.4	6.41	8.71	6.21	0.687	0.236	13	6.41

Table A.8: Surface elevation **RMSE** differences between regions with different characteristics and a region with a 5 km wide and 100 km long strait fjord (reference fjord) using a **quadratic** sliding law. The errors are proportional to the differences in the fjords area and resistive stresses generated by the shape of the fjords compared to the reference fjord.

Fjord	RMSE hs (m)						Percentage (%)					
	TS		SD		ISD		TS		SD		ISD	
	avg	std	avg	std	avg	std	avg	std	avg	std	avg	std
1 10 km	70.1	44.5	47.5	1.52	40.7	5.3	11.8	6.04	6.18	0.334	9.48	5.3
2 5 km	116	83	31.6	1.26	166	17.9	22.2	16.3	4.11	0.23	39.2	17.9
5 2 km	126	111	26.2	0.644	201	21.8	24.8	22.1	3.4	0.108	47.2	21.8
1 2 km	43.5	35.2	10.2	1.29	33.3	3.63	7.8	5.72	1.33	0.191	7.77	3.63
2 bends	17	16.8	6.66	0.907	2.78	0.249	2.84	2.83	0.865	0.123	0.645	0.249
4 bends	35.6	40.8	11	1.82	3.46	0.932	6.01	6.83	1.42	0.201	0.802	0.932
thin mouth	22.1	21.2	4.42	0.992	41.7	5.84	4.2	4.2	0.545	0.113	8.83	5.84
thick mouth	49	27.6	25.4	8.84	93.6	15	8.92	5.73	3.14	1.1	20.6	15
no fjord	100	79.9	25.4	0.669	204	22.6	19.7	17.3	3.15	0.147	48.3	22.6
included	97	77.5	26.8	0.617	182	22	18.5	15.7	3.31	0.148	40.5	22
1 20 km branch	11.3	13.4	2.79	0.127	22.4	13.2	2.14	2.63	0.345	0.0172	4.73	13.2
2 20 km branches	15.9	18.3	3.63	0.45	23.4	14.1	2.95	3.48	0.45	0.0627	4.92	14.1
4 20 km branches	74.9	68.8	50.9	18	73.8	40.9	13.5	13	6.26	2.19	15.7	40.9
30 km branch	31.7	32.9	7.5	0.831	80.7	2.41	6.75	7.56	0.973	0.0909	18.8	2.41
50 km fjord	51.9	41.1	15.1	1.14	104	13.3	10.5	9.32	1.96	0.172	24.9	13.3
150 km fjord	113	49.8	96.2	23.7	174	4.68	25.9	27.1	12.5	2.93	44.1	4.68
shallow	18	18.8	9.56	0.654	3.04	0.428	3	3.21	1.24	0.0703	0.705	0.428
deep	4.76	4.02	3.04	0.354	2.92	0.75	0.794	0.633	0.395	0.0399	0.676	0.75
10km Wide Offset	67.4	44.5	47.5	1.81	34	4.74	11.2	6.03	6.18	0.338	7.91	4.74
5km Wide Offset	22.6	21.4	4.78	0.689	46.7	4.87	4.68	4.75	0.619	0.0779	10.9	4.87
2km Wide Offset	49	35.8	10.8	1.23	54.9	4.78	9.13	6.3	1.4	0.182	12.8	4.78

A.4.2 Model sensitivities: resolution and order of ice dynamics approximation

A.4.2.1 Model resolution dependency

1. Summary statistics (table A.9) showing an increase of the surface elevation **RMSE** with resolution

Table A.9: Surface elevation **RMSE** at 5, 10 and 25 km resolution compared to the 1 km resolution simulations using the **quadratic** sliding law. The data are averaged over all the synthetic fjords and over the whole time series (TS), over the first stadial (SD) and over the first interstadial (ISD).

res (km)	RMSE h_s (m)						Percentage (%)					
	TS		SD		ISD		TS		SD		ISD	
	avg	std	avg	std	avg	std	avg	std	avg	std	avg	std
5	63.7	20.6	40.9	2.61	54.6	7.84	12	4.87	5.38	0.381	12.7	7.84
10	94.4	17.8	80.7	6.42	114	5.99	18.7	5.28	11	0.949	27	5.99
25	145	10.4	65.5	3.94	143	9.21	32.1	6.65	8.83	0.524	30.6	9.21

2. Total ice volume and surface elevation **RMSE**

The impact of model resolution on the total ice volume using a linear sliding law described in Section 2 of the main article is the same when using a quadratic sliding law (see Fig.A.42). Specifically, regions with a single fjord with different characteristic all generate differences in the total ice volume (compared to the reference fjord) of the same order of magnitude. This shows that the impact of different fjord characteristics are partly taken into account in coarse resolution simulations with the basal sliding coefficient parameterization based on the fjords area. In addition, multiplying the numbers of fjords in a region without increasing the total fjords area (compare five 2 km fjords, two 5 km fjords and one 10 km fjord in Fig.A.42) increases the errors generated at 5 and 10 km resolution. The surface elevation **RMSE** using either a linear (Fig.A.43) or a quadratic (Fig.A.44) law confirm the conclusion drawn with the total ice volume differences between coarse and high resolution simulations in Section 2 of the main document.

The model resolution dependency described in Section of the main article when

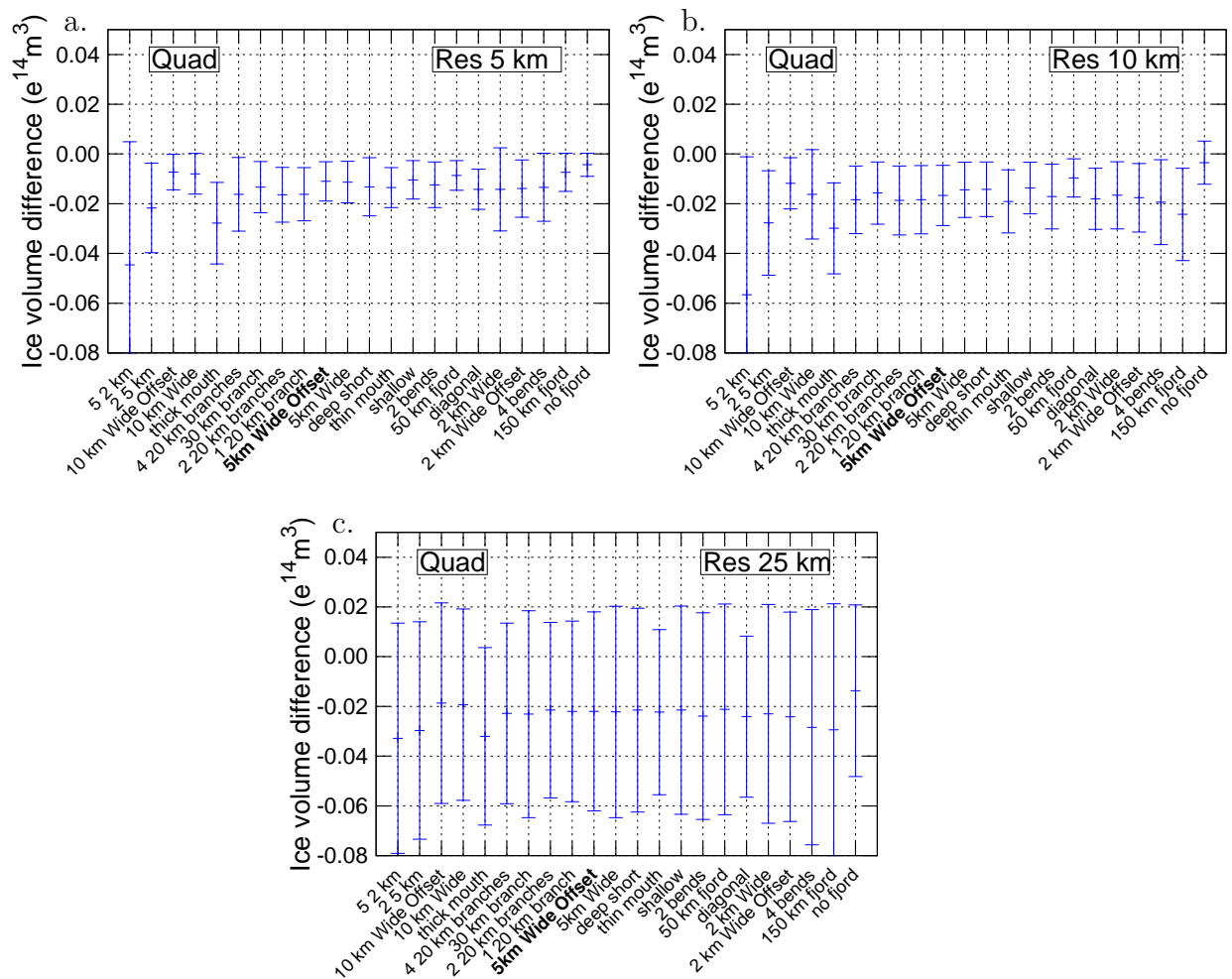


Figure A.42: Fjord characteristics impact for: a. a simulation at 5 km resolution, b. a simulation at 10 km resolution and c. a simulation at 25 km resolution compared to a 1 km simulation of a 5 km wide and 100 km long fjord. Red represents the average and standard deviation over 50 kyr, blue at the end of inception (111 to 107 ka) and green at the end of the first interstadial event (102 to 100 ka). These simulations use the baseline parameter vector and **quadratic** (Quad) sliding law.

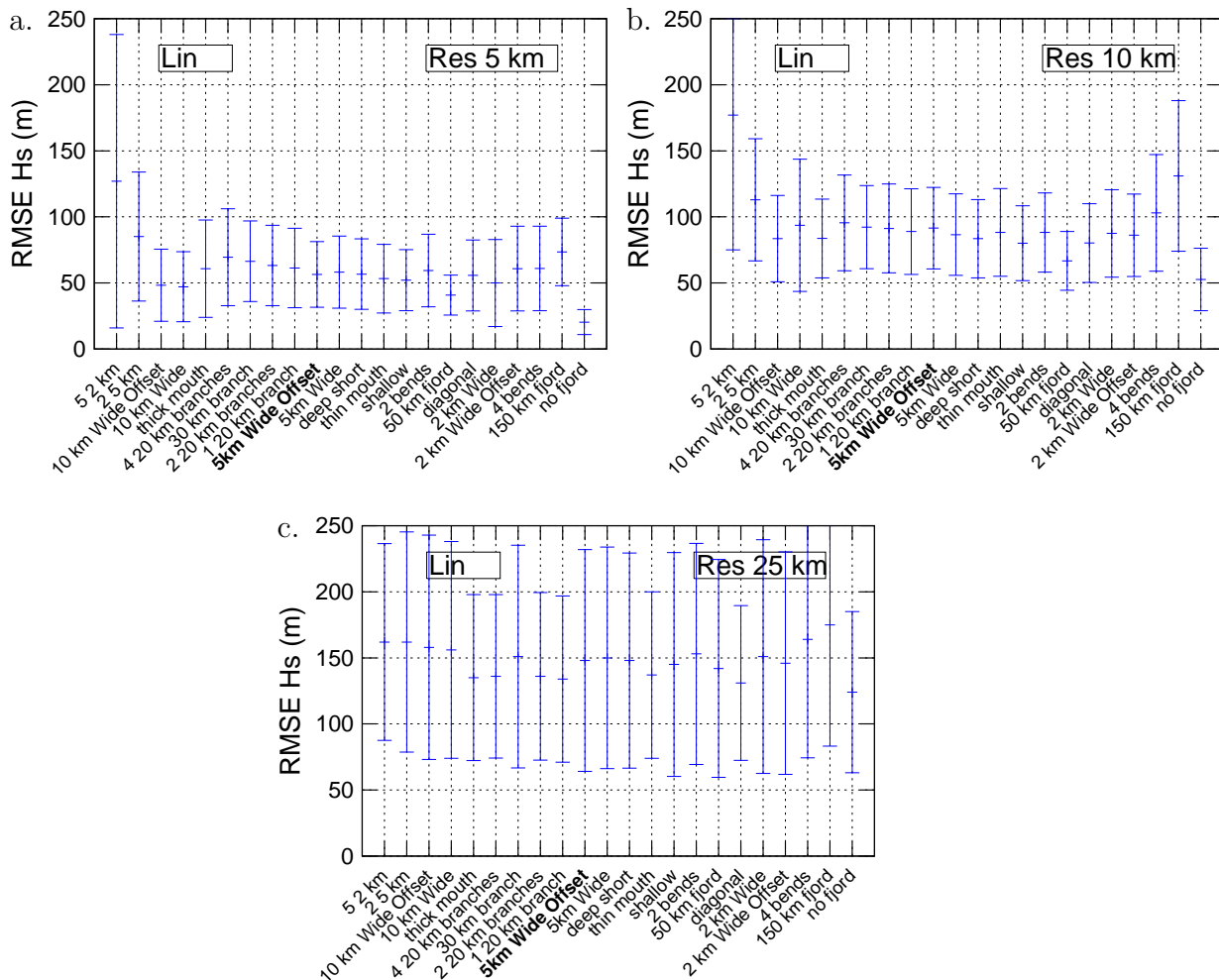


Figure A.43: Fjord characteristics impact on the surface elevation RMSE for: a. a simulation at 5 km resolution, b. a simulation at 10 km resolution and c. a simulation at 25 km resolution compared to a 1 km simulation of a 5 km wide and 100 km long fjord. Red represents the average and standard deviation over 50 kyr, blue at the end of inception (111 to 107 ka) and green at the end of the first interstadial event (102 to 100 ka). These simulations use the baseline parameter vector and **linear** (Lin) sliding law.

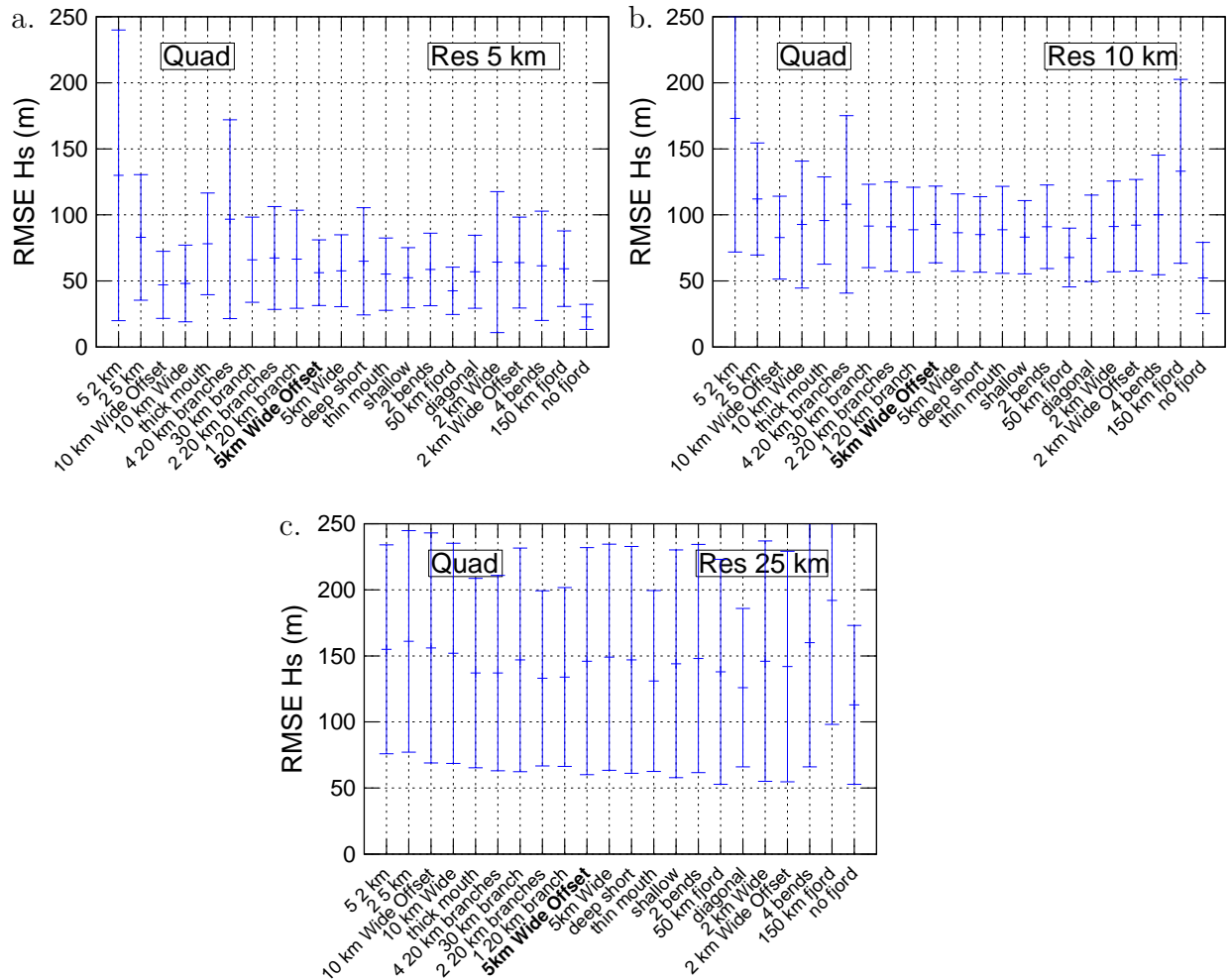


Figure A.44: Fjord characteristics impact on the surface elevation **RMSE** for: a. a simulation at 5 km resolution, b. a simulation at 10 km resolution and c. a simulation at 25 km resolution compared to a 1 km simulation of a 5 km wide and 100 km long fjord. Red represents the average and standard deviation over 50 kyr, blue at the end of inception (111 to 107 ka) and green at the end of the first interstadial event (102 to 100 ka). These simulations use the baseline parameter vector and **quadratic** (Quad) sliding law.

using a linear sliding law is similar when using a quadratic sliding law (compare Fig.A.45 with Fig.2.6 in the main article). Specifically, simulations at 25 km resolutions generates a lag of about 3 kyr during the beginning of the second stadial event around 100 or 97 ka depending of the region analyzed (Fig.A.45).

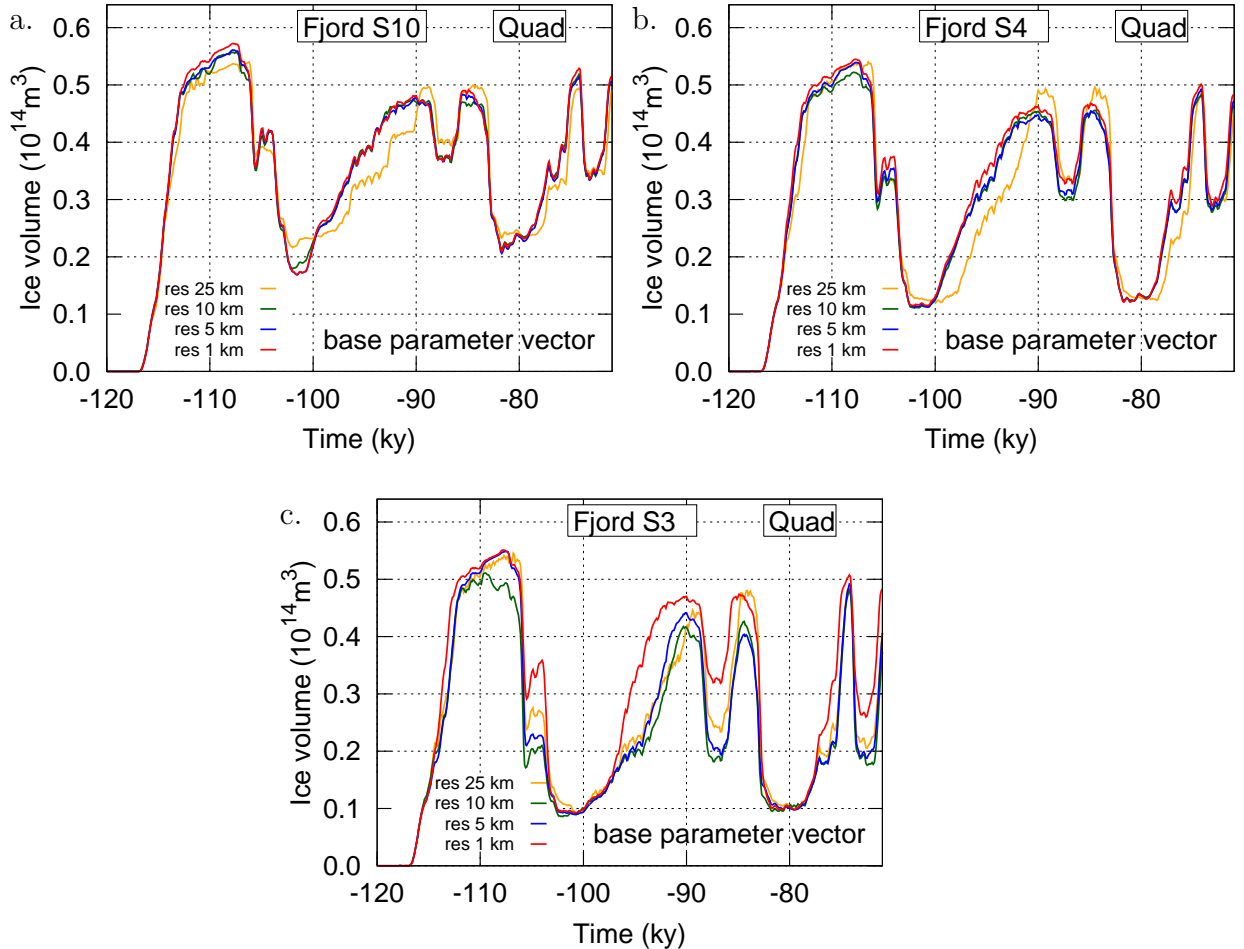


Figure A.45: Resolution impact on the total ice volume. Examples for a region with no fjords (a. S10), with one 5 km wide and 100 km long fjord (b. S4) and five 2 km wide fjords (c. S3). These simulations use the baseline parameter vector and **quadratic** (Quad) sliding law.

3. Velocity differences

The impact of resolution on the velocity fields differs in the same manner when using a quadratic sliding law (Fig.A.46) than when using a linear sliding law (see Fig.2.7 in the main paper). More precisely, the impact of resolution on the velocity fields differs nonlinearly with resolution and time.

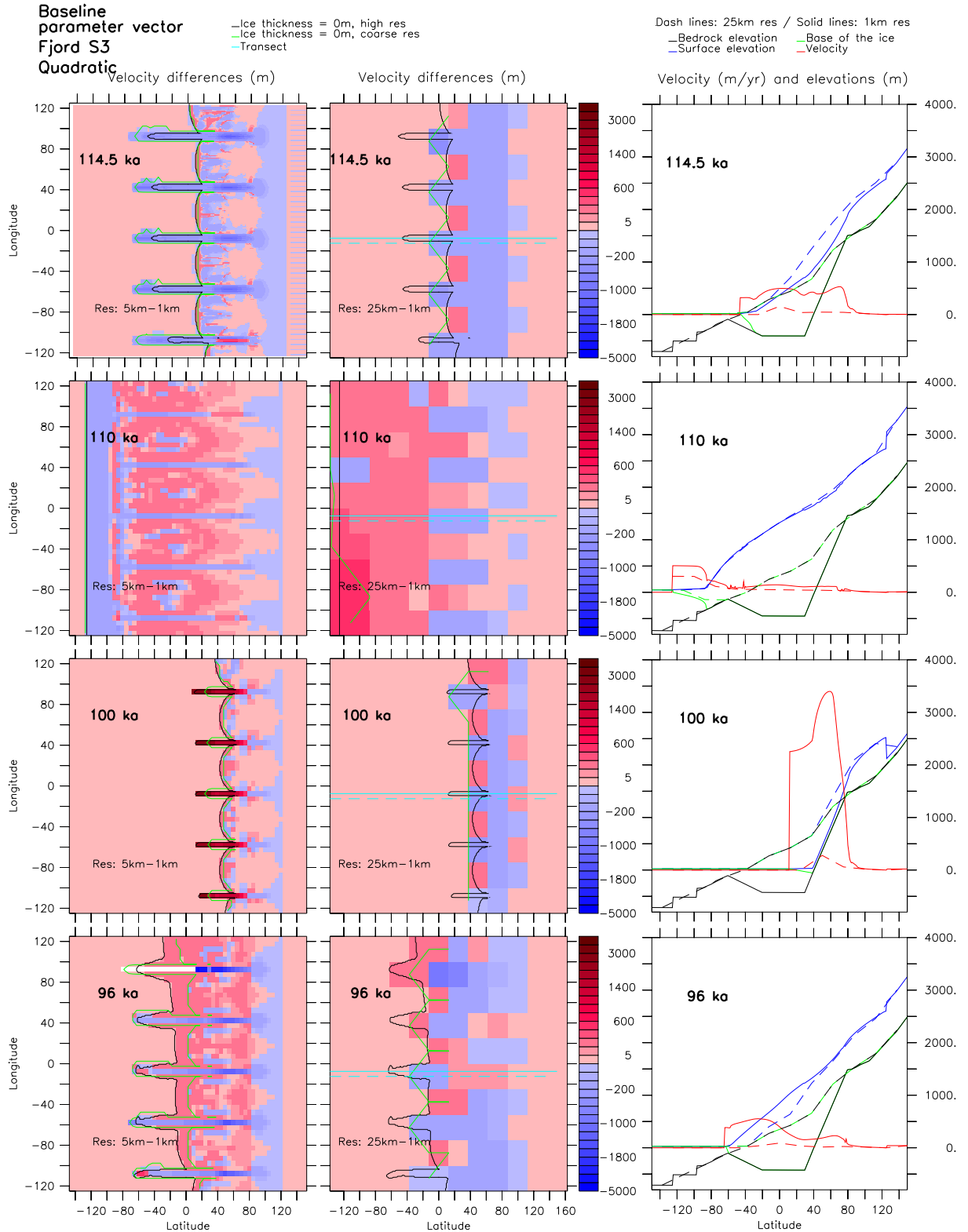


Figure A.46: Ice velocity fields at 5 km resolution (left panel) and 25 km resolution (central panel) compared to a 1 km resolution simulation at different time slices. The panel on the right side shows the surface, base and velocity evolution in the 25 and 1 km resolution simulations. These simulations use the baseline parameter vector and **quadratic** (Quad) sliding law over the region with five 2 km wide fjords.

A.4.2.2 Higher order ice dynamic physics

Simulations that compute the ice velocity using the [HO](#) model generates region with thicker ice and higher velocities in fjord regions compared to simulations that compute the ice velocity using the hybrid [SIA/SSA](#) model.

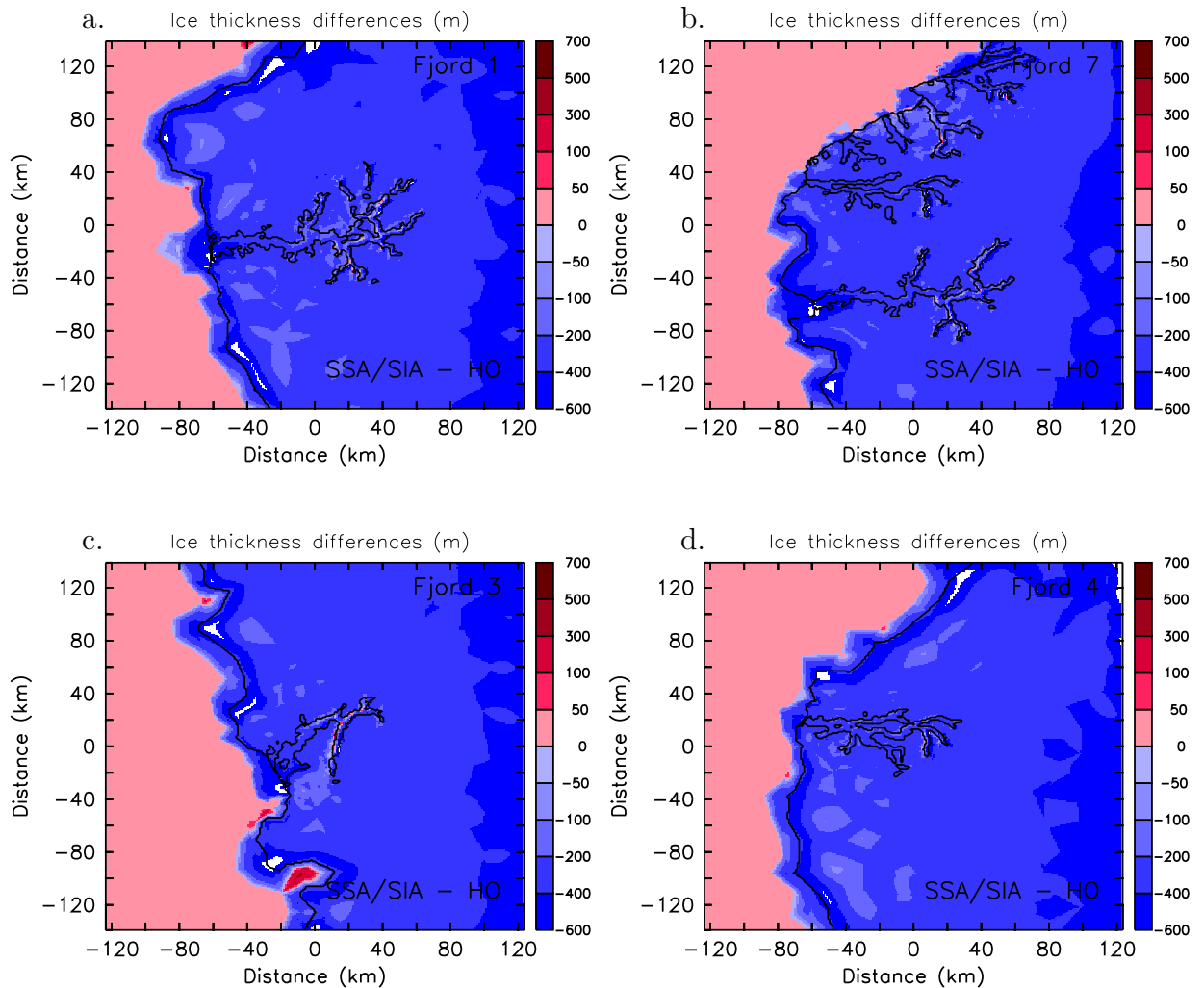


Figure A.47: Ice thickness differences between [ISSM](#) simulations solving the [HO](#) model for ice flow and [PSU/GSM](#) simulations solving the hybrid [SIA/SSA](#) model at the end of inception after a 5000 years. Results are shown for topographic regions 1, 7, 3, and 4 presented on [Fig.A.1](#). The [HO](#) model generates more ice than the hybrid [SIA/SSA](#) model.

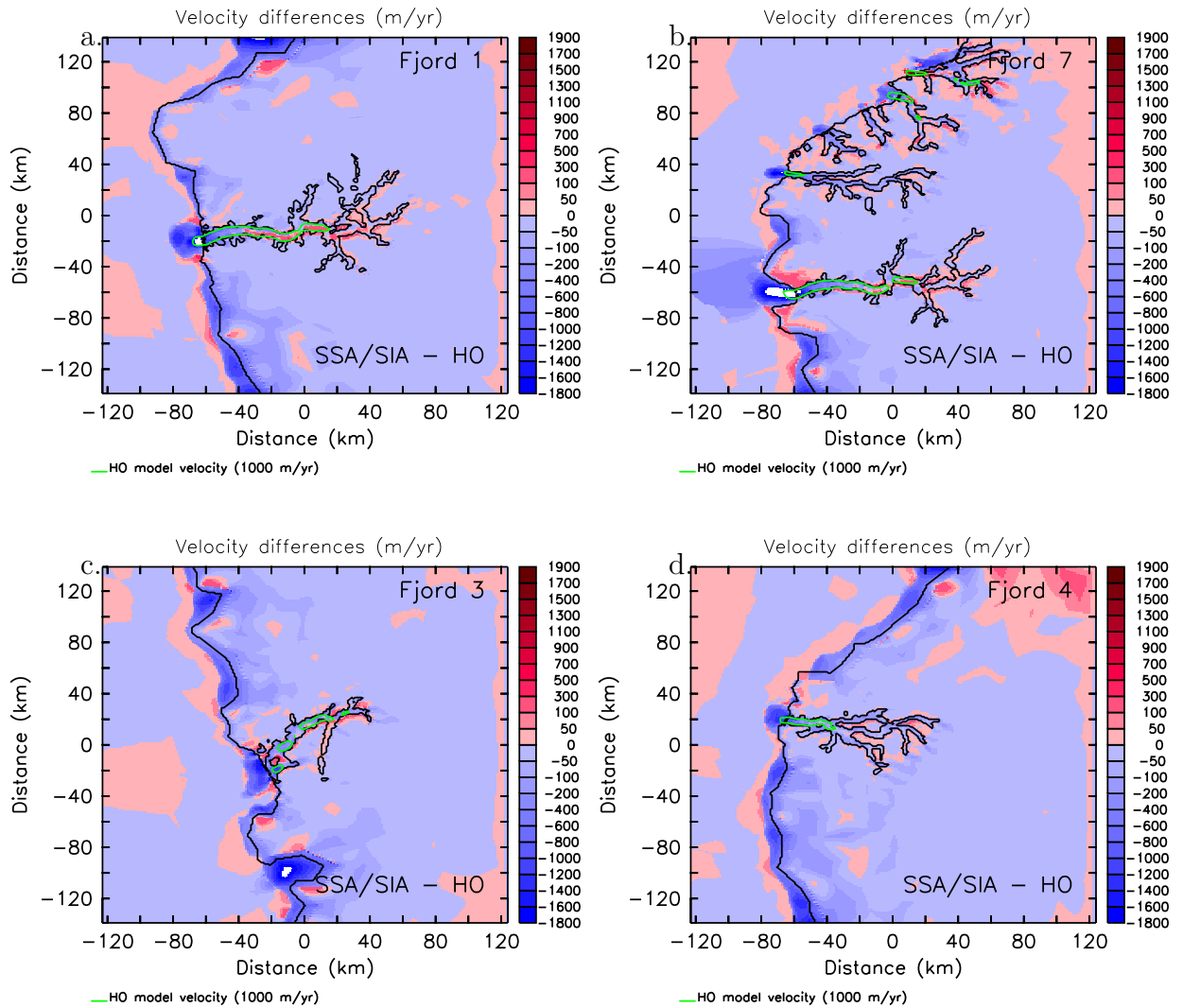


Figure A.48: Vertically average velocity differences between ISSM simulations solving the HO model for ice flow and PSU/GSM simulations solving the hybrid SIA/SSA model at the end of inception after a 5000 years run. Results are shown for the topographic regions 1, 7, 3, and 4 presented on Fig.A.1. The HO model generates higher velocities than the hybrid SIA/SSA model in the fjords.

A.4.3 Resolution dependency minimization

A.4.3.1 Hard bed parameters

The metric (defined in Section 2.4.3) minimum values in Fig.A.49 and A.50 represent the set of parameters (presented in table 2.5 of the main text) that reduces the most the differences in total ice volume evolution and surface elevation RMSE between coarse resolution and high resolution simulations.

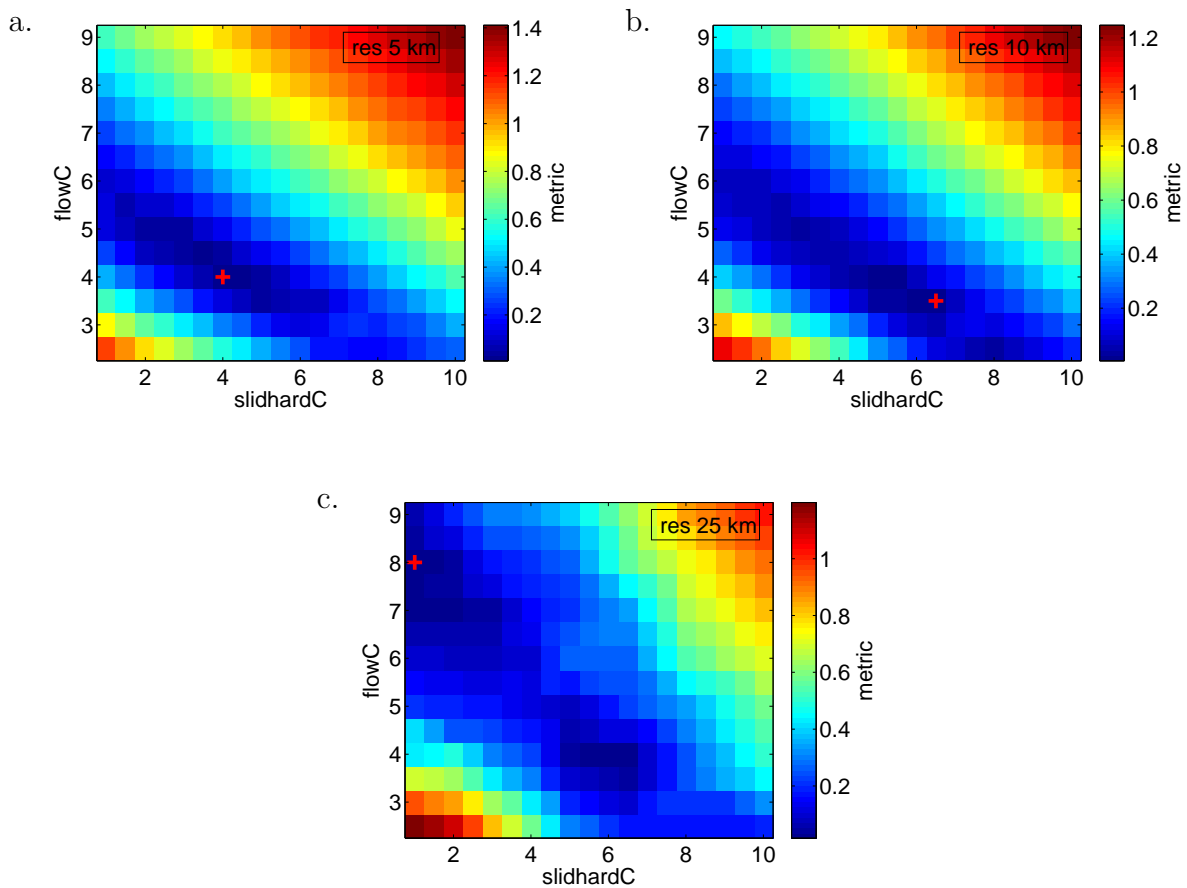


Figure A.49: Impact the combination of different flow enhancement factor (flowC) and the hard bed sliding coefficient (slidhardC) on simulations run at, a. 5 km resolution, b. 10 km resolution, and c. 25 km resolution. A lower metric (defined in Section 2.4.3) represent a better fit to the 1 km resolution simulation. The red cross represent the lowest differences compared to the high resolution simulations. Sliding is represented as a **linear** flow law.

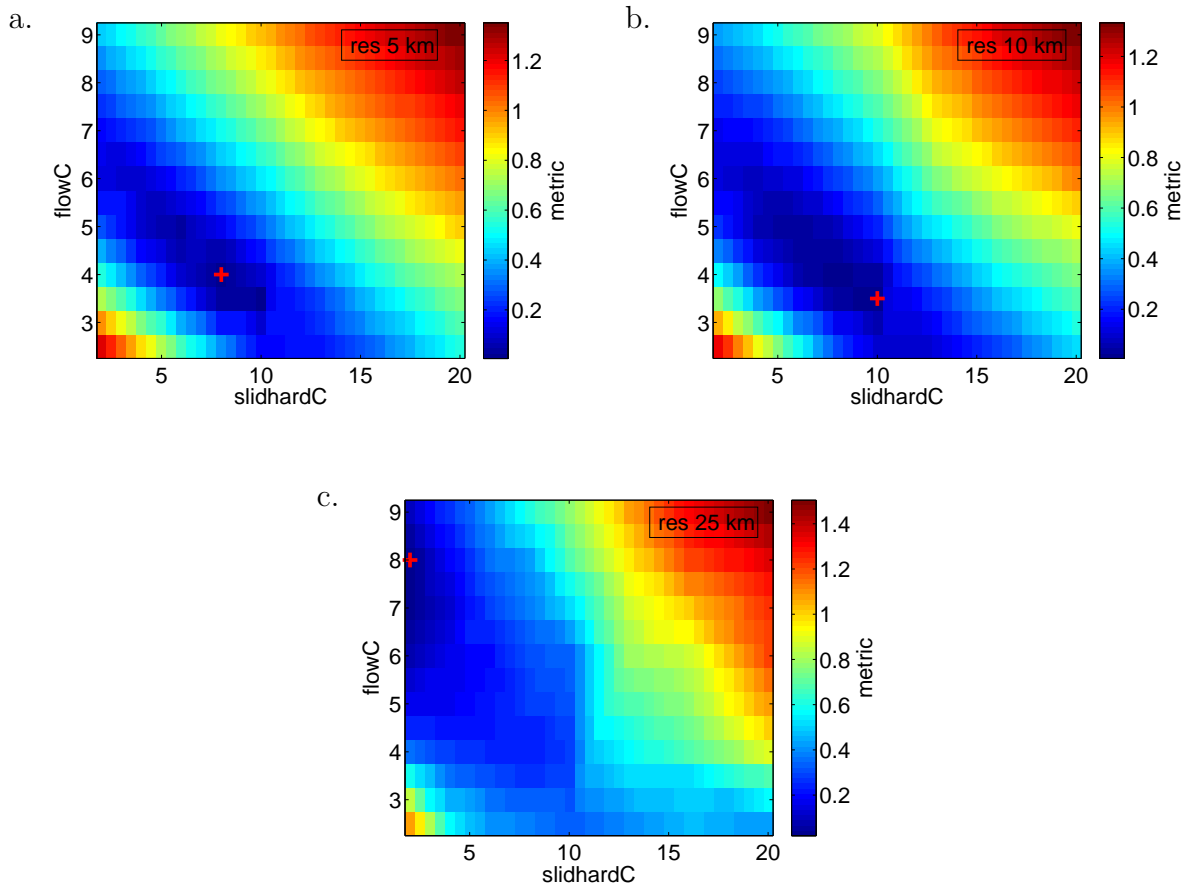


Figure A.50: Impact the combination of different flow enhancement factor (flowC) and the hard bed sliding coefficient (slidhardC) on simulations run at, a. 5 km resolution, b. 10 km resolution, and c. 25 km resolution. A lower metric (defines in Section 2.4.3) represent a better fit to the 1 km resolution simulation. The red cross represent the lowest differences compared to the high resolution simulations. Sliding is represented as a **quadratic** flow law.

Table A.10: Improvement generated with the optimal Fnslid/Fnflow parameters in the representation of total ice volume and surface elevation **RMSE** compared to the simulation using the baseline parameter vector. **Quadratic** sliding law.

	res (km)	Volume diff		hs RMSE (m)	
		sum (10^{14} m^3)	Improvement (%)	sum (m)	Improvement (%)
Base	5	2.5		2290	
Optimal	5	2.1	17.2	2360	-2.68
Base	10	3.6		5200	
Optimal	10	3.5	3.01	5110	1.6
Base	25	15		11300	
Optimal	25	12	17.8	10500	7.32

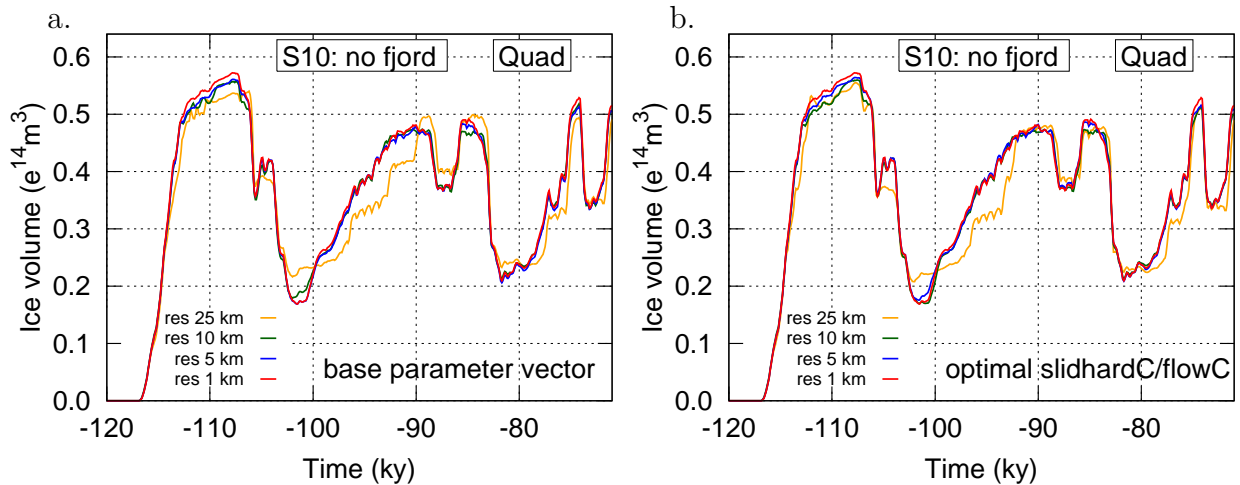


Figure A.51: Total ice volume evolution at different resolutions with: a. the baseline parameter vector and, b. the optimal sets of slidhardC and flowC parameters. These simulations use the **quadratic** (Quad) sliding law. The main difference compared to the 1km resolution simulation at the end of inception, between 112 and 98 ka, are reduced to a few percents with the optimum parameter set. The optimization did not reduce the differences in the 25 km resolution simulation after 102 ka.

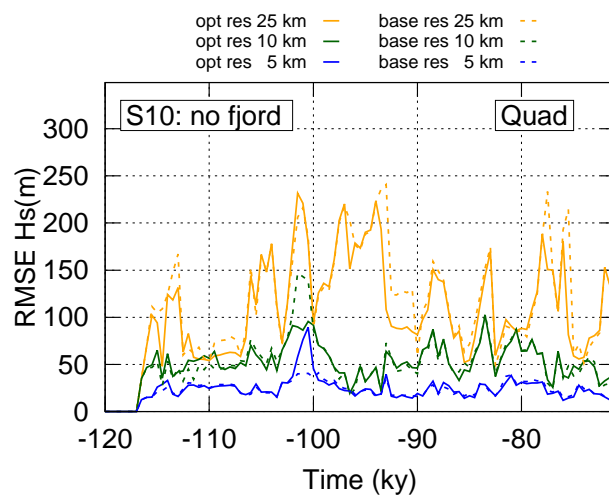


Figure A.52: Surface elevation **RMSE** (compared to the 1 km resolution simulation) when using the baseline parameter vector (dotted lines) and the optimal sets of slidhardC and flowC parameters (solid lines). The different colours represent different resolutions. These simulations use the **quadratic** (Quad) sliding law. The surface elevation **RMSE** are significantly improve only in the 25 km resolution simulation, however high errors remains.

A.4.3.2 Soft bed parameters and basal topography upscaling methods

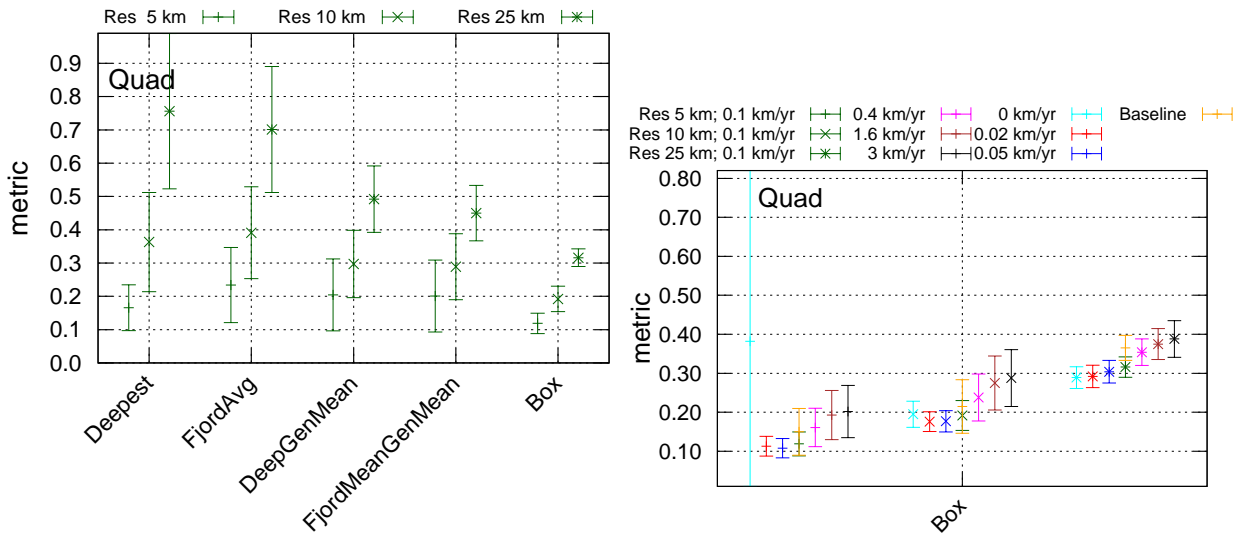


Figure A.53: Metric (normalized total ice volume differences plus normalized surface elevation **RMSE** compared to the 1 km resolution simulation using the base parameter vector) averaged over time and all the synthetic fjords. The left panel shows the impact of different topography interpolation methods (deepest fjord depth, *Deepest*, fjord depth average, *FjordAvg*, the average between the deepest depth in the fjord, *DeepGenMean*, the average between the fjord average and the box average, *FjordMeanGenMean*, and the box average, *Box*) when the 0.1 km/yr basal sliding coefficient is used. This shows that the *Box* average method generate the small errors in ther of total ice volume and surface elevation **RMSE** compared to the 1 km resolution simulation. The right panels focus on the impact of parameters when the box average is used for the interpolation. These simulations use the **quadratic** (Quad) sliding law. The optimum parameters presented in table 2.7 of the main paper are extracted from Fig.A.53(b)

Table A.11: Total ice volume difference and surface elevation **RMSE** between the base run and the optimal Fnsed/Fnslid/Fnflow parameters. These results show the reduction of errors generated with the optimization of the parameter vector twice large for the total ice volume than for the surface elevation **RMSE**. Reductions in the total ice volume difference are on average around 50 % at 5 km resolution, 20 % at 10 km resolution and 25 % at 25 km resolution. **Quadratic** sliding law.

		Volume diff (10^{14} m ³)				hs RMSE (m) (10^{14} m ³)			
		Improvement (%)		Improvement (%)		Improvement (%)		Improvement (%)	
res (km)		avg	std	avg	std	avg	std	avg	std
Base	5	0.014	0.017			63.7	20.9		
Optimal	5	0.0054	0.0076	47.2	61.3	32	17.4	29	35
Base	10	0.018	0.02			94.4	17.6		
Optimal	10	0.0076	0.0077	38.6	64.1	63.6	30	19.1	26.1
Base	25	0.035	0.032			145	15.1		
Optimal	25	0.021	0.019	18.5	71.1	120	69.2	6.37	30.5

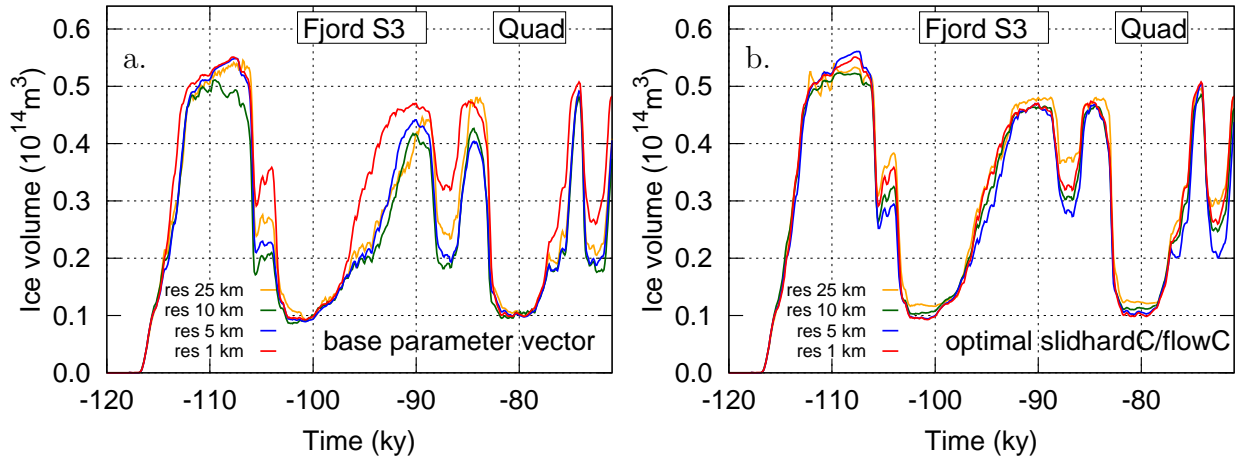


Figure A.54: Total ice volume evolution in a region (S3) with five 2 km wide, 100 km long fjords using: a. the baseline parameter vector and, b. the optimal set of parameters. These simulations use the **quadratic** (Quad) sliding law. Fig.A.54(b) shows a reduction in the differences in amplitude and timing of the total ice volume between coarse and high resolution simulations.

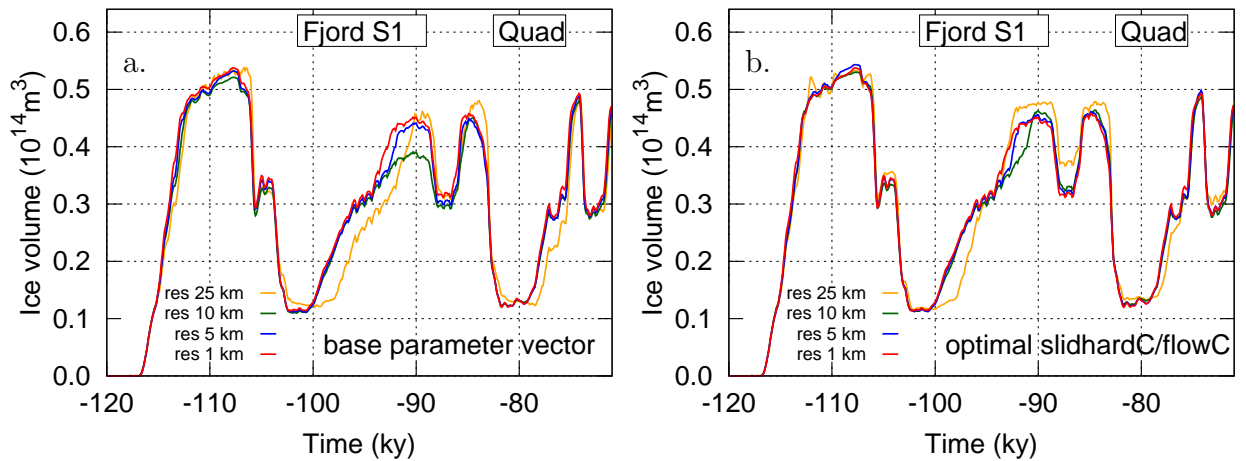


Figure A.55: Total ice volume evolution in a region (S1) with a 10 km wide, 100 km long fjord using: a. the baseline parameter vector and, b. the optimal set of parameters. These simulations use the **quadratic** (Quad) sliding law. Fig.A.55(b) shows a reduction in the differences in amplitude and timing of the total ice volume between coarse and high resolution simulations.

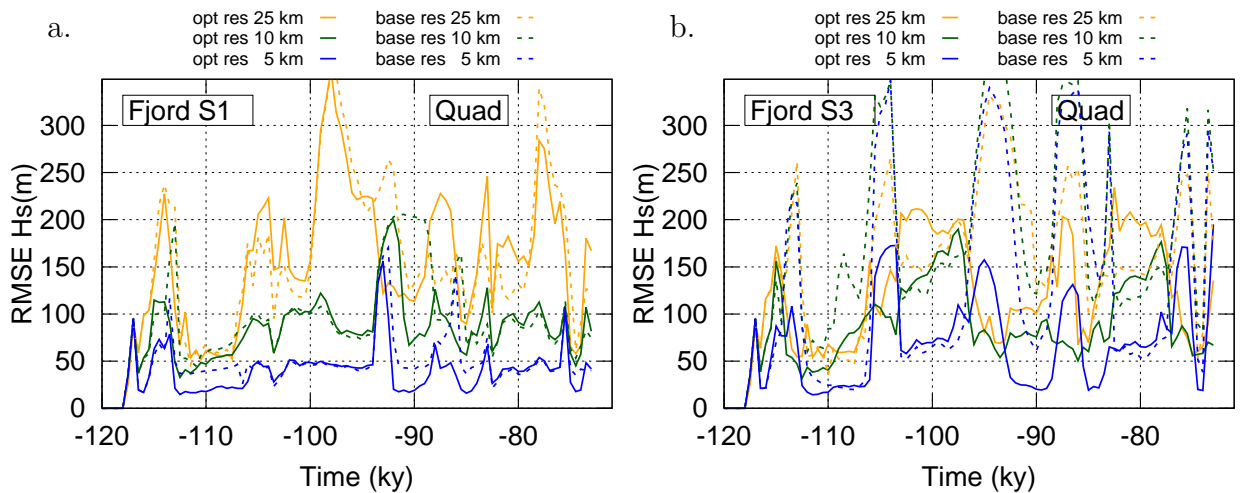


Figure A.56: Surface elevation **RMSE** evolution (compared to the 1 km resolution simulation) using the in a baseline (dotted lines) and the optimal (solid lines) parameter vector. These simulations use the **quadratic** (Quad) sliding law over: a. a region (S1) with a 10 km wide, 100 km long fjord and, b. a region with five 2 km wide, 100 km long fjords. Fig.A.56(b) shows a reduction in the differences in amplitude and timing of the total ice volume between coarse and high resolution simulations.

A.4.4 Thermodynamic off on

Results of simulation with the thermodynamic model turned on and off shows that even with upstream forcing, significant differences can be obtained in the total ice volume evolution differences (see differences between the simulation with and without the thermodynamic model during stadial event in Fig.A.57).

Table A.12: Total ice volume difference between simulation with the thermodynamic model turn OFF (with cold base or warm base) and ON.

base	res (km)	Volume (10^{14} m ³)				Percentage (%)			
		stadial		interstadial		stadial		interstadial	
		avg	std	avg	std	avg	std	avg	std
Cold	5	0.08	0.041	0.054	0.039	18	10	81	200
Cold	10	0.072	0.043	0.055	0.038	16	10	140	350
Cold	25	0.017	0.026	0.027	0.021	4.2	5.8	64	87
Warm	5	-0.09	0.043	0.0067	0.019	-19	8.3	12	48
Warm	10	-0.084	0.041	0.0074	0.025	-17	7.6	30	110
Warm	25	-0.07	0.033	-0.0031	0.016	-15	6.3	0.22	25

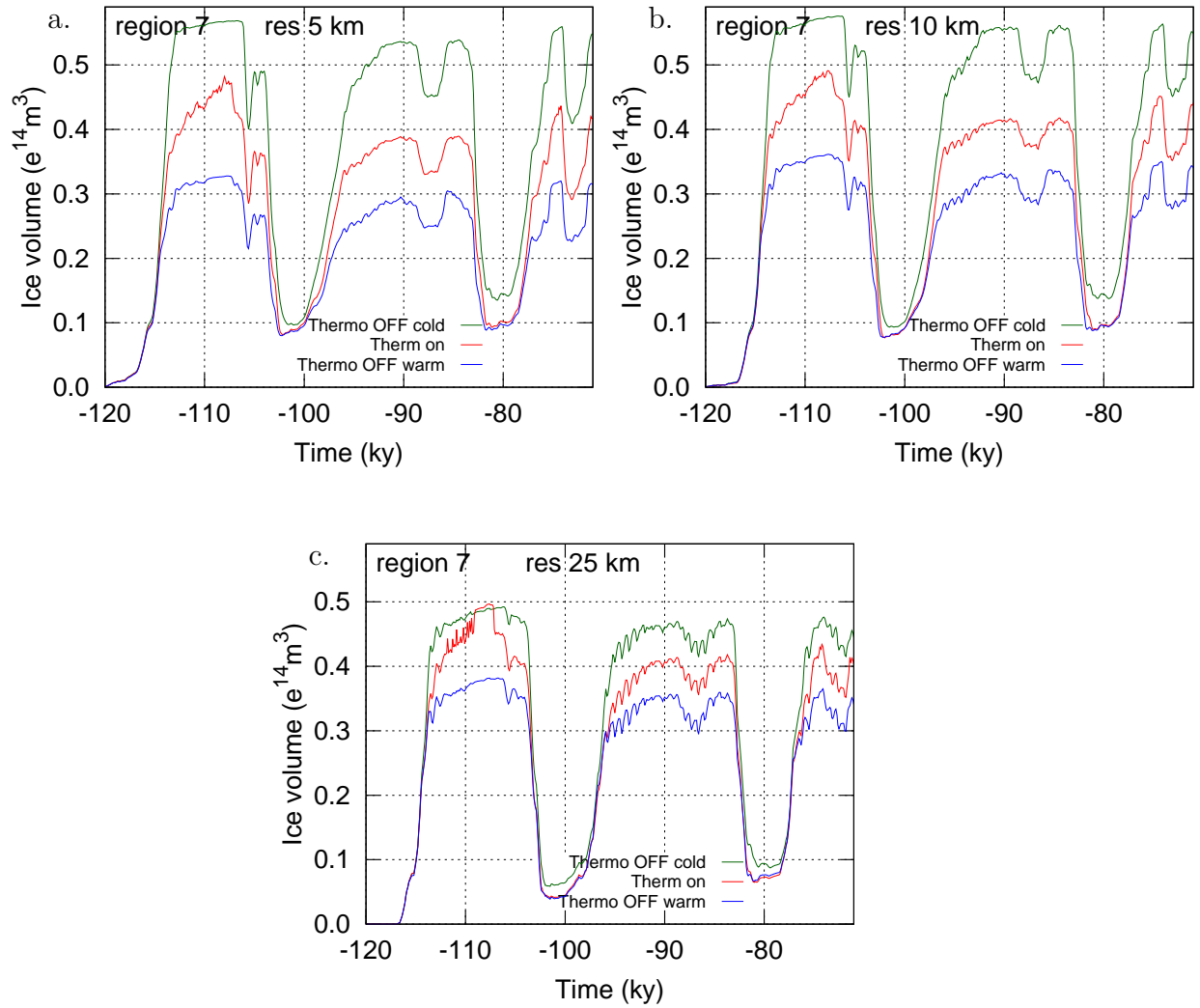


Figure A.57: Impact of the thermodynamic component of the model at different resolution for fjord region 7.

Appendix B

Supplementary material for: A new sub-grid surface mass balance and flux model for continental-scale ice-sheet modelling: validation and last glacial cycle

B.1 Surface mass balance module

Positive degree day methods have been widely used in surface mass balance models (Johannesson et al., 1995; Tarasov and Peltier, 1999a; Hock, 2003; Shea et al., 2009; Barrand et al., 2013). Here, we use the PDD method described in Tarasov and Peltier (1999a) to compute the ice ablation and accumulation from the temperature and precipitation fields. Ablation rates are derived from monthly mean temperature (T_m). To increase the accuracy, hourly temperatures are considered normally distributed, with a standard deviation (σ_{PDD}) of 5.5 °C, around the monthly mean. A lapse rate is also used to adjust the temperature forcing to the ice surface elevation. The number of days where the temperature is above 0 °C in a year is computed as:

$$\text{PDD} = \frac{1}{\sigma_{PDD}\sqrt{2\pi}} \int_0^{\text{1year}} \int_{0^\circ\text{C}}^{T_m+2.5\sigma_{PDD}} \text{Exp}\left[\frac{-(T - T_m)^2}{2\sigma_{PDD}^2}\right] dT dt \quad (\text{B.1})$$

The amount of snow and ice are assumed to melt proportionally to the number of positive degree days. Snow is melted first and the remaining positive degree days are used to melt ice. The ablation rate factors for snow (γ_{snow}) and ice (γ_{ice}) have a mean June/July/August temperature (T_{jja}) dependence extracted from energy balance modelling (Braithwaite, 1995; Tarasov and Peltier, 2002, 2003):

$$\gamma_{\text{ice}} = \begin{cases} 17.22 \text{ mm/PDD} & T_{jja} \leq -1^\circ\text{C}, \\ (0.0067 \times (10 - T_{jja})^3 + 8.3) \text{ mm/PDD} & -1^\circ\text{C} < T_{jja} < 10^\circ\text{C}, \\ 8.3 \text{ mm/PDD} & 10^\circ\text{C} \leq T_{jja} \end{cases}$$

and

$$\gamma_{\text{snow}} = \begin{cases} 2.65 \text{ mm/PDD} & T_{jja} \leq -1^\circ\text{C}, \\ (0.15 \times T_{jja} + 2.8) \text{ mm/PDD} & -1^\circ\text{C} < T_{jja} < 10^\circ\text{C}, \\ 4.3 \text{ mm/PDD} & 10^\circ\text{C} \leq T_{jja} \end{cases}$$

In addition, the amount of superimposed ice for a year is computed as per Janssens and Huybrechts (2000):

$$\begin{cases} \min[P_r + M, 2.2 \times (P_s - M) - d \times c_i/L \times \min(T_{\text{surf}}, 0^\circ\text{C})] & M < P_s, \\ \min[P_r + M, d \times c_i/L \times \min(T_{\text{surf}}, 0^\circ\text{C})] & M > P_s \end{cases}$$

where P_r is the rainfall in a year, P_s is the snow fall in a year, M is the snow melt in a year, 2.2 is the capillarity factor, d is the active thermodynamic layer (set to 1 m), c_i is the ice specific heat capacity ($152.5 + 7.122T$) in $\text{Jkg}^{-1} \text{K}^{-1}$, L is the latent heat fusion (3.35×10^5) in Jkg^{-1} , and T_{surf} is the surface temperature.

A normal distribution of the hourly temperature is also used to compute the amount of snow accumulation from the precipitation. A lower standard deviation $\sigma_{\text{RS}} = \sigma_{\text{PDD}} - 0.5$ is assumed in that case to account for the smaller temperature variability during cloudy days. Precipitation is assumed to fall as snow when the temperature is below 2°C .

$$\frac{\text{accumulation}}{\text{precipitation}} = \frac{\rho_i}{\rho_w \sigma_{\text{RS}} \sqrt{2\pi}} \int_0^{1\text{year}} \int_{T_m - 2.5\sigma_{\text{RS}}}^{2^\circ\text{C}} \exp\left[\frac{-(T - T_m)^2}{2\sigma_{\text{RS}}^2}\right] dT dt \quad (\text{B.2})$$

A parameterization of the elevation-desertification effect (Budd and Smith, 1981) reduces the precipitation by a factor of two for every kilometre increase in elevation.

This exponential reduction is a function of the surface height difference to that of present-day with an ensemble parameter threshold for activation ([Tarasov and Peltier, 2006](#); [Tarasov et al., 2012](#)).

B.2 Results for the stepwise regression fit

A regression model is constructed to minimizing ice volumes results misfits between the sub-grid model and [ISSM](#). To determine which topographic characteristics significantly reduce the misfits, a stepwise multilinear regression method is used. Simulations are run to steady state (2 kyr) using a constant precipitation rate of 1 m/yr and a sea level temperature forcing of 0°C. These simulations are performed over 3 sets of 7 topographic regions.

Using the flow direction, the number of local maxima (tested with radius sizes of 2, 6 and 10 grid cells) and the sum of the squared slopes in the regression model did not reduce the misfits. The other characteristics tested are the terrain ruggedness, the variance in the slopes, *slopevarNorm*, and the standard deviation of the surface elevation topography S_{SD} .

Table [B.1](#) summarizes the results of the stepwise regression fit when these parameters are used in different combinations (cases 1 to 8). 'In' indicates that this variable does reduce the differences between the ice volume generated by [ISSM](#) and the model generated with the stepwise regression fit. 'Out' indicates no reduction and the variable is not kept in the regression model. The stepwise regression fit is tested on experiments using the first and third topographic data set ("ids1"), the first and the second ("ids2") and the second and the third ("ids3"). A fourth experiment ("all ds") uses all the data. In that last case, no data are left to test the model obtained. 'rmse*10¹⁰ (3ds)' represents the root mean square error, in 10³ m³ of ice, between the ice volume generated by [ISSM](#) and the model generated by the stepwise regression fit results, using the three data sets. The regression model, V_{regmod} , that generates the lowest misfits accounts only for the standard deviation of the topography (case 7) and is define as:

$$V_{regmod} = 0.79V_{SG} + 2.2017e^8 S_{SD} \quad (\text{B.3})$$

Table B.1: Stepwise regression fit results

	ids1	ids2	ids3	all ds	rmse sum
case 1					
Ice volume SG	'In'	'In'	'In'	'In'	
terrain ruggedness	'In'	'Out'	'In'	'In'	
slopevarNorm	'In'	'Out'	'In'	'In'	
S _{SD}	'In'	'In'	'In'	'In'	
rmse*10 ¹⁰ (3ds)	7.3981	2.3025	8.9690	7.3981	26.068 (6)
case 2					
Ice volume SG	'In'	'In'	'In'	'In'	
terrain ruggedness	'Out'	'Out'	'In'	'In'	
S _{SD}	'In'	'In'	'Out'	'In'	
rmse*10 ¹⁰ (3ds)	2.9883	2.3025	5.6907	2.9883	13.970 (2)
case 3					
Ice volume SG	'In'	'In'	'In'	'In'	
terrain ruggedness	'Out'	'Out'	'In'	'In'	
slopevarNorm	'Out'	'In'	'Out'	'Out'	
rmse*10 ¹⁰ (3ds)	8.2247	2.6692	5.6907	8.2247	24.809 (4)
case 4					
Ice volume SG	'In'	'In'	'In'	'In'	
slopevarNorm	'Out'	'Out'	'Out'	'Out'	
S _{SD}	'In'	'In'	'In'	'In'	
rmse*10 ¹⁰ (3ds)	2.9883	2.3025	2.1609	2.9883	10.440 (1)
case 5					
Ice volume SG	'In'	'In'	'In'	'In'	
terrain ruggedness	'Out'	'Out'	'In'	'In'	
rmse*10 ¹⁰ (3ds)	8.2247	4.1280	5.6907	8.2247	26.268 (7)
case 6					
Ice volume SG	'In'	'In'	'In'	'In'	
slopevarNorm	'Out'	'In'	'In'	'In'	
rmse*10 ¹⁰ (3ds)	8.2247	2.6692	3.1347	8.2247	22.253 (3)
case 7					
Ice volume SG	'In'	'In'	'In'	'In'	
S _{SD}	'In'	'In'	'In'	'In'	
rmse*10 ¹⁰ (3ds)	2.9883	2.3025	2.1609	2.9883	10.440 (1)
case 8					
Ice volume SG	'In'	'In'	'In'	'In'	
rmse*10 ¹⁰ (3ds)	8.2247	4.1280	5.3374	8.2247	25.915 (5)

B.3 Surface elevation and velocities on an inclined plane when different numbers of hypsometric bins are used (Fig.B.1)

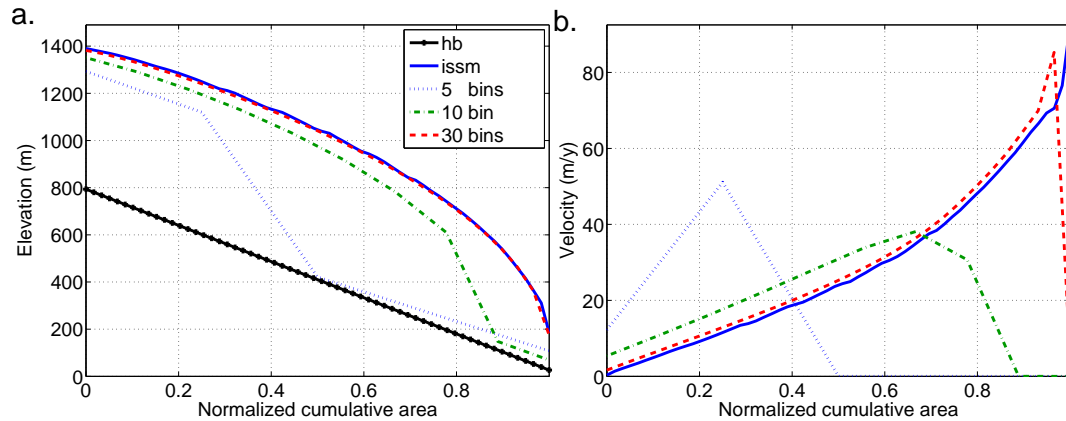


Figure B.1: Sensitivity to the number of hypsometric bins for an experiment using a sea level temperature set to 0°C and the desertification factor to 0.5. **a.** shows the surface elevation and **b.** the velocity profiles after 2 kyr.

B.4 Percentage of hypsometric bins jumps (Fig.B.2)

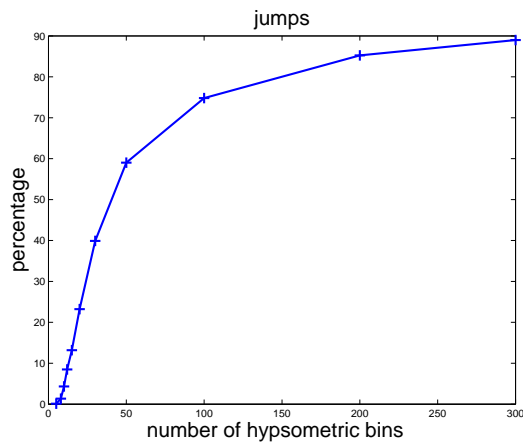


Figure B.2: Average percentage of hypsometric bin jumps in the 21 regions analyzed when different numbers of hypsometric bins are used. "Hypsometric bin jumps" is used to represent some high resolution adjacent grid cells that belong to non-adjacent hypsometric bins.

B.5 Sensitivity to number of hypsometric bins at steady state for six different regions in the Canadian Rockies (Fig.B.3)

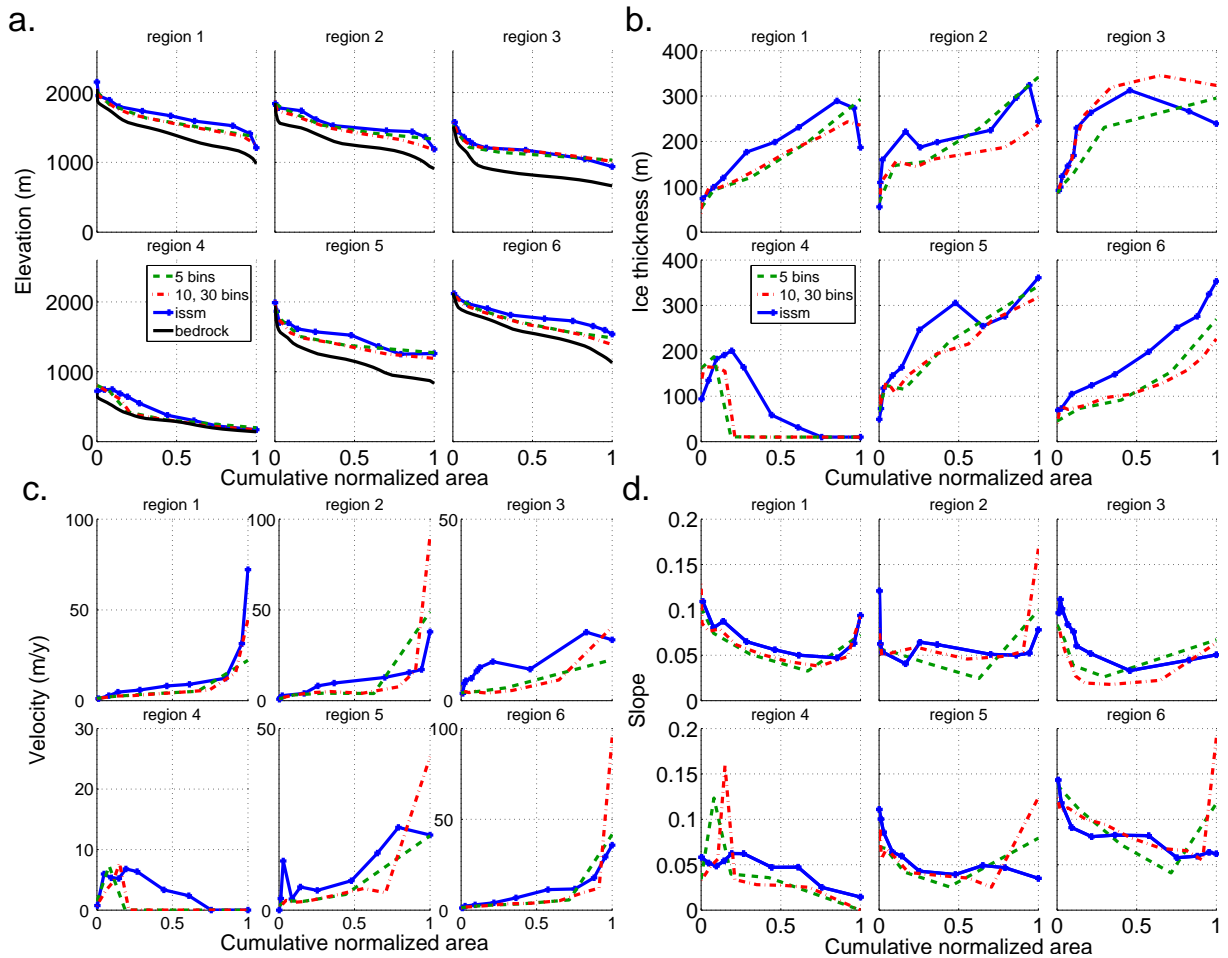


Figure B.3: Comparison of ice grid cell characteristics when different hypsometric bins are used in the SG model. Steady state results are shown (after 2 kyr simulation) for six different regions. **a.** displays the surface elevation, **b.** the ice thickness, **c.** the velocities and **d.** the slopes. The solid black line represents the bed topography using 30 hypsometric bins. The solid blue lines are for ISSM results. The other lines correspond to the SG model results using 5 (dashed green lines) and 10 (dashed-dotted red lines) hypsometric bins. The differences between the 10 and 30 bins runs are too small to be differentiated.

B.6 Ice evolution on an inclined plane for different forcings (Fig.B.4)

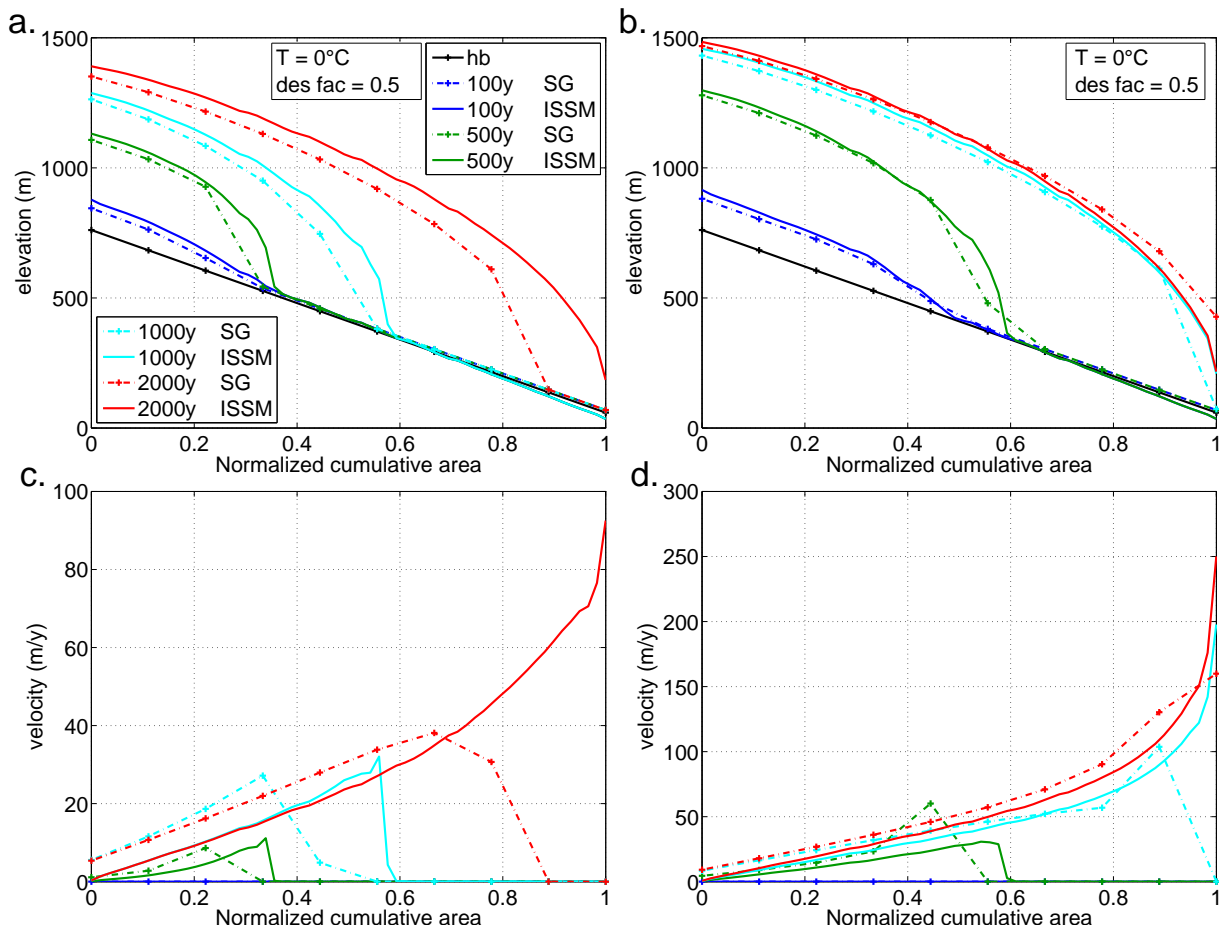


Figure B.4: Surface elevation and velocities evolution over an inclined plane for the ISSM and the SG model. Simulations use a sea level temperature forcing of 0°C and an elevation desertification factor of 0.5 in **a** and **c**, and 0 in **b** and **d**.

B.7 Sensitivity to different SG model parameterizations (Fig.B.5)

Here we compare different SG model parameterizations. The first parameterization of the velocities at every bin (Para 1) uses the standard deviation of the topography in the velocity equation (Eq.6 in the manuscript). The second parameterization adjust the lowest hypsometric bin velocity as described in Eq.7 of the manuscript.

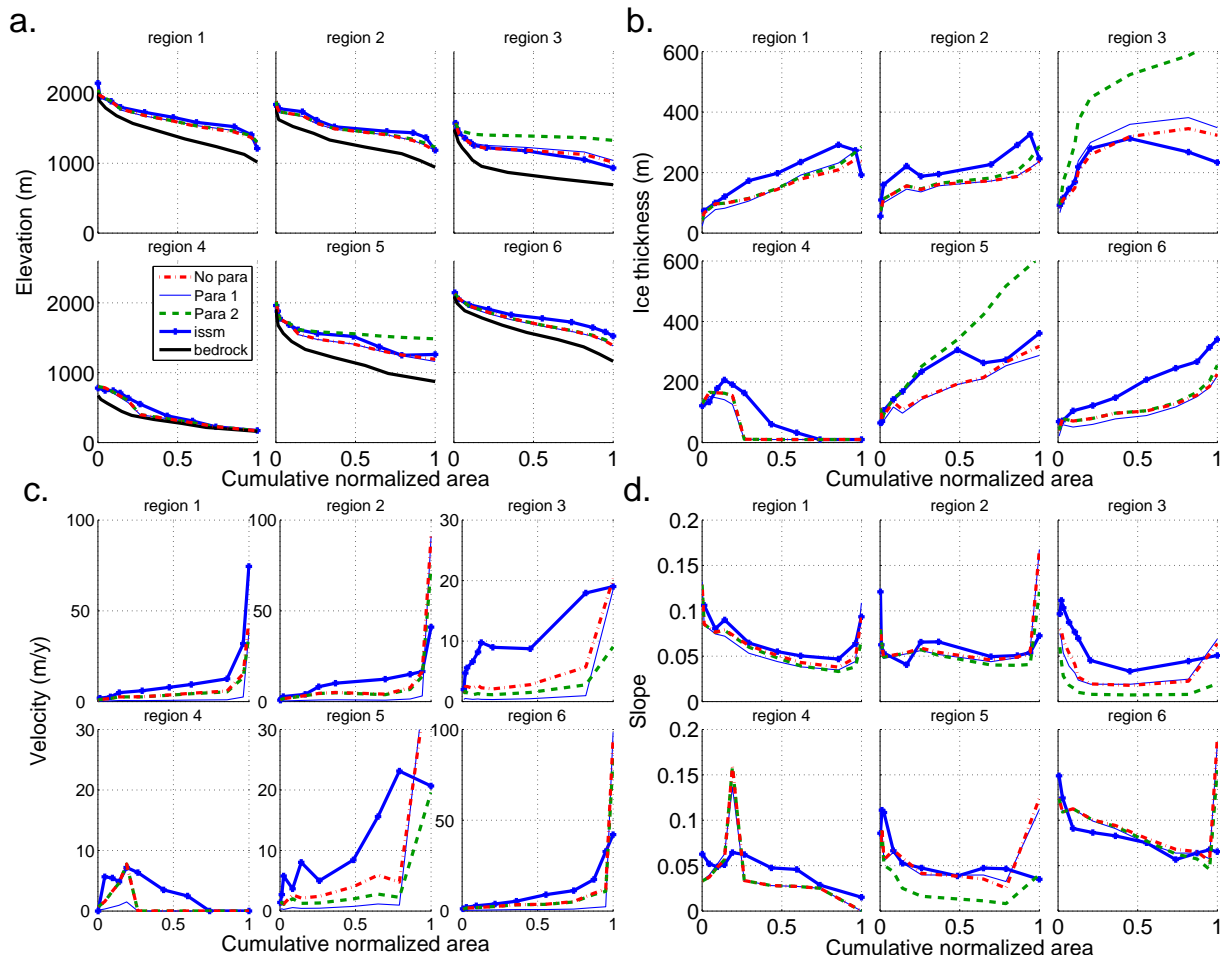


Figure B.5: Comparison of ice grid cell characteristics when different parameterizations are used in the SG model. Results are shown at steady state after 2 kyr of simulation for six different regions. **a.** displays the surface elevation, **b.** the ice thickness, **c.** the velocities and **d.** the slopes. The solid black line represents the bed topography using 30 hypsometric bins. The solid blue lines are from ISSM runs. The other lines correspond to the SG model results with no additional parameterization (dashed red lines), the parameterization of the velocities at every bin (Para 1, solid cyan lines) and the parameterization of the slope at the lowest bin (Para 2, dashed-dotted green lines). 10 hypsometric bins are used throughout.

B.8 Results for a simulation where more ice is generated when the SG model is activated (Fig.B.6)

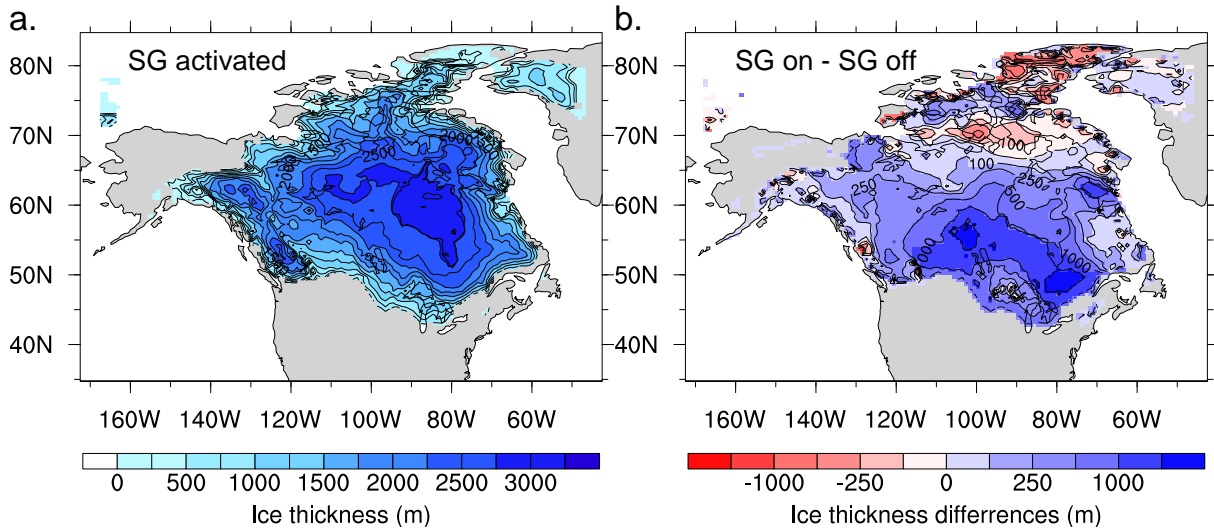


Figure B.6: Ice thickness comparison at 50 ka, using a parameter vector that gives an increase of ice thickness when the SG model is used. **a.** Ice thickness when SG is activated. **b.** Ice thickness difference between simulations with the SG model turned on and off.

B.9 Maximum positive and negative differences (Fig.B.7)

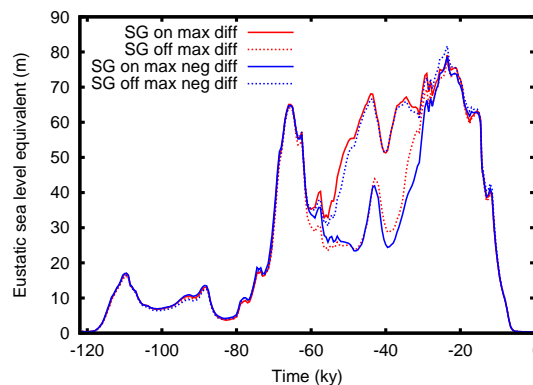


Figure B.7: Ice volume evolution using the ensemble parameter vectors that give the maximum positive (red) and negative (blue) differences between simulations with the SG model activated or not.

B.10 Ice volume redistribution on coarse grid (Fig.B.8)

Of the five runs that generate a better fit to calibration constraints in [Tarasov et al. \(2012\)](#), we focus here on results using the ensemble parameter vector of run nn9894 as they all display similar behaviour.

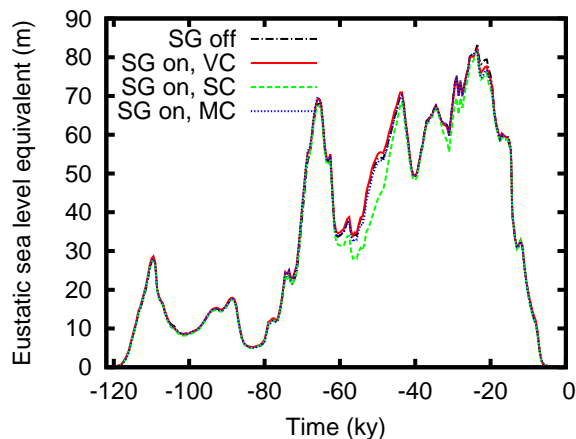


Figure B.8: Total ice volume evolution for a simulation over North America with the **SG** model turned on (**SG on**) using the parameter vector of run nn9894. Different methods of ice redistribution at the **CG** level are compared. "VC" is for ice volume conservation, "SC" for surface elevation conservation and "MC" uses the maximum of the previous two methods. "SG off" represents a run where the **SG** model has been turned off.

Bibliography

Abe-Ouchi, A. and Blatter, H.: On the initiation of ice sheets, *Annals of Glaciology*, 18, 203–203, 1993.

Abe-Ouchi, A., Saito, F., Kawamura, K., Raymo, M. E., Okuno, J., Takahashi, K., and Blatter, H.: Insolation-driven 100,000-year glacial cycles and hysteresis of ice-sheet volume, *Nature*, 500, 190–193, 2013.

Albrecht, T., Martin, M., Haseloff, M., Winkelmann, R., and Levermann, A.: Parameterization for subgrid-scale motion of ice-shelf calving fronts, *The Cryosphere*, 5, 35–44, 2011.

Alley, R. B.: Deforming-bed origin for southern Laurentide till sheets?, *Journal of Glaciology*, 37, 67–76, 1991.

Amundson, J. and Truffer, M.: A unifying framework for iceberg-calving models, *Journal of Glaciology*, 56, 822–830, 2010.

Applegate, P. J., Kirchner, N., Stone, E. J., Keller, K., and Greve, R.: An assessment of key model parametric uncertainties in projections of Greenland Ice Sheet behavior, *The Cryosphere*, 6, 589–606, 2012.

Bamber, J., Griggs, J., Hurkmans, R., Dowdeswell, J., Gogineni, S., Howat, I., Mouginot, J., Paden, J., Palmer, S., Rignot, E., et al.: A new bed elevation dataset for Greenland, *The Cryosphere*, 7, 499–510, 2013.

Barber, D., McCullough, G., Babb, D., Komarov, A., Candlish, L., Lukovich, J., Asplin, M., Prinsenberg, S., Dmitrenko, I., and Rysgaard, S.: Climate change and ice hazards in the Beaufort Sea, *Elementa: Science of the Anthropocene*, 2, 000 025, 2014.

Barnett, T. P. L. D., Schlese, U., Roeckner, E., and Latif, M.: The Effect of Eurasian Snow Cover on Regional and Global Climate Variations, *Journal of the Atmospheric Sciences*, 46, 661–686, 1989.

Barrand, N., Vaughan, D., Steiner, N., Tedesco, M., Kuipers Munneke, P., Broeke, M., and Hosking, J.: Trends in Antarctic Peninsula surface melting conditions from observations and regional climate modeling, *Journal of Geophysical Research: Earth Surface*, 118, 315–330, 2013.

- Bartholomaus, T. C., Larsen, C. F., and O'Neel, S.: Does calving matter? Evidence for significant submarine melt, *Earth and Planetary Science Letters*, 380, 21–30, 2013.
- Bartholomaus, T. C., Stearns, L. A., Sutherland, D. A., Shroyer, E. L., Nash, J. D., Walker, R. T., Catania, G., Felikson, D., Carroll, D., Fried, M. J., et al.: Contrasts in the response of adjacent fjords and glaciers to ice-sheet surface melt in West Greenland, *Annals of Glaciology*, pp. 1–14, 2016.
- Bassis, J.: The statistical physics of iceberg calving and the emergence of universal calving laws, *Journal of Glaciology*, 57, 3, 2011.
- Bassis, J. N. and Ma, Y.: Evolution of basal crevasses links ice shelf stability to ocean forcing, *Earth and Planetary Science Letters*, 409, 203–211, 2015.
- Benn, D., Warren, C., and Mottram, R.: Calving processes and the dynamics of calving glaciers, *Earth-Science Reviews*, 82, 143–179, 2007.
- Bevan, S., Luckman, A., and Murray, T.: Glacier dynamics over the last quarter of a century at Helheim, Kangerdlugssuaq and 14 other major Greenland outlet glaciers, *The Cryosphere*, 6, 923–937, 2012.
- Braithwaite, R. J.: Positive degree-day factors for ablation on the Greenland ice sheet studied by energy-balance modelling, *Journal of Glaciology*, 41, 153–160, 1995.
- Briggs, R., Pollard, D., and Tarasov, L.: A glacial systems model configured for large ensemble analysis of Antarctic deglaciation, *The Cryosphere*, 7, 1949–1970, 2013.
- Broecker, W. S. and Denton, G. H.: The role of ocean-atmosphere reorganizations in glacial cycles, *Geochimica et Cosmochimica Acta*, 53, 2465–2501, 1989.
- Brown, C., Meier, M., Post, A., and (US), G. S.: Calving speed of Alaska tidewater glaciers, with application to Columbia Glacier, US Dept. of the Interior, Geological Survey, 1983.
- Budd, W. F. and Smith, I.: The growth and retreat of ice sheets in response to orbital radiation changes, *Sea Level, Ice, and Climatic Change*, pp. 369–409, 1981.
- Calov, R., Robinson, A., Perrette, M., and Ganopolski, A.: Simulating the Greenland ice sheet under present-day and palaeo constraints including a new discharge parameterization, *The Cryosphere*, 9, 179–196, 2015.
- Carr, J., Vieli, A., Stokes, C., Jamieson, S., Palmer, S., Christoffersen, P., Dowdeswell, J., Nick, F., Blankenship, D., and Young, D.: Basal topographic controls on rapid retreat of Humboldt Glacier, northern Greenland, *Journal of Glaciology*, 61, 137–150, 2015.
- Carr, J. R., Stokes, C. R., and Vieli, A.: Recent progress in understanding marine-terminating Arctic outlet glacier response to climatic and oceanic forcing Twenty years of rapid change, *Progress in Physical Geography*, 37, 436–467, 2013a.
- Carr, J. R., Vieli, A., and Stokes, C.: Influence of sea ice decline, atmospheric warming, and glacier width on marine-terminating outlet glacier behavior in northwest Greenland at seasonal to interannual timescales, *Journal of Geophysical Research: Earth Surface*, 118, 1210–1226, 2013b.

- Carr, J. R., Stokes, C., and Vieli, A.: Recent retreat of major outlet glaciers on Novaya Zemlya, Russian Arctic, influenced by fjord geometry and sea-ice conditions, *Journal of Glaciology*, 60, 155–170, 2014.
- Cazenave, A. and Llovel, W.: Contemporary sea level rise, *Annual Review of Marine Science*, 2, 145–173, 2010.
- Centre, B. O. D.: The GEBCO_08 Grid, version 20091120, <http://www.gebco.net>, 2010.
- Chaulagain, N. P.: Socio-economic Dimension of Snow and Glacier Melt in the Nepal Himalayas, in: *Dynamics of Climate Change and Water Resources of Northwestern Himalaya*, pp. 191–199, Springer, 2015.
- Church, J., Clark, P., Cazenave, A., Gregory, J., Jevrejeva, S., Levermann, A., Merrifield, M., Milne, G., Nerem, R., Nunn, P., Payne, A., Pfeffer, W., Stammer, D., and Unnikrishnan, A.: Sea Level Change, *Climate Change 2013: The Physical Science Basis. Contribution of Working Group I to the Fifth Assessment Report of the Intergovernmental Panel on Climate Change*, 2013.
- Clarke, G. K.: Fast glacier flow: ice streams, surging, and tidewater glaciers, *Journal of Geophysical Research: Solid Earth* (1978–2012), 92, 8835–8841, 1987.
- Clarke, G. K.: Subglacial processes, *Annual Review of Earth and Planetary Sciences*, 33, 247–276, 2005.
- Colleoni, F., Masina, S., Cherchi, A., Navarra, A., Ritz, C., Peyaud, V., and Otto-Bliesner, B.: Modeling Northern Hemisphere ice-sheet distribution during MIS 5 and MIS 7 glacial inception, *Climate of the Past*, 10, 269–291, 2014.
- Cornford, S. L., Martin, D. F., Graves, D. T., Ranken, D. F., Le Brocq, A. M., Gladstone, R. M., Payne, A. J., Ng, E. G., and Lipscomb, W. H.: Adaptive mesh, finite volume modeling of marine ice sheets, *Journal of Computational Physics*, 232, 529–549, 2013.
- Csatho, B. M., Schenk, A. F., van der Veen, C. J., Babonis, G., Duncan, K., Rezvanbehbahani, S., van den Broeke, M. R., Simonsen, S. B., Nagarajan, S., and van Angelen, J. H.: Laser altimetry reveals complex pattern of Greenland Ice Sheet dynamics, *Proceedings of the National Academy of Sciences*, 111, 18 478–18 483, 2014.
- Cuffey, K. and Paterson, W.: *The physics of glaciers*, Elsevier, ed, 4, 693, 2010.
- Damsgaard, A., Egholm, D. L., Piotrowski, J. A., Tulaczyk, S., Larsen, N. K., and Tylmann, K.: Discrete element modeling of subglacial sediment deformation, *Journal of Geophysical Research: Earth Surface*, 118, 2230–2242, 2013.
- Dansgaard, W., Johnsen, S., Clausen, H., Dahl-Jensen, D., Gundestrup, N., Hammer, C., Hvidberg, C., Steffensen, J., Sveinbjörnsdottir, A., Jouzel, J., and Bond, G.: Evidence for general instability of past climate from a 250-kyr ice-core record, *Nature*, 364, 218–220, 1993.

- Das, I., Hock, R., Berthier, E., and Lingle, C. S.: 21st-century increase in glacier mass loss in the Wrangell Mountains, Alaska, USA, from airborne laser altimetry and satellite stereo imagery, *Journal of Glaciology*, 60, 283–293, 2014.
- Depoorter, M., Bamber, J., Griggs, J., Lenaerts, J., Ligtienberg, S., van den Broeke, M., and Moholdt, G.: Calving fluxes and basal melt rates of Antarctic ice shelves, *Nature*, 502, 89–92, 2013.
- Dewey, K. F.: Daily Maximum and Minimum Temperature Forecasts and the Influence of Snow Cover, *Monthly Weather Review*, 105, 1594–1597, 1977.
- Drouet, A.-S., Docquier, D., Durand, G., Hindmarsh, R., Pattyn, F., Gagliardini, O., Zwinger, T., et al.: Grounding line transient response in marine ice sheet models, *The Cryosphere*, 7, 395–406, 2013.
- Durand, G., Gagliardini, O., De Fleurian, B., Zwinger, T., and Le Meur, E.: Marine ice sheet dynamics: Hysteresis and neutral equilibrium, *Journal of Geophysical Research: Earth Surface*, 114, 2009a.
- Durand, G., Gagliardini, O., Zwinger, T., Le Meur, E., and Hindmarsh, R. C.: Full Stokes modeling of marine ice sheets: influence of the grid size, *Annals of Glaciology*, 50, 109–114, 2009b.
- Durand, G., Gagliardini, O., Favier, L., Zwinger, T., and Le Meur, E.: Impact of bedrock description on modeling ice sheet dynamics, *Geophysical Research Letters*, 38, L20 501, doi:10.1029/2011GL048892, 2011.
- Dyke, A. S.: An outline of North American deglaciation with emphasis on central and northern Canada, *Quaternary glaciations - Extent and chronology*, 2, 373–424, 2004.
- Enderlin, E., Howat, I., and Vieli, A.: High sensitivity of tidewater outlet glacier dynamics to shape, *The Cryosphere*, 7, 1007–1015, 2013a.
- Enderlin, E., Howat, I., and Vieli, A.: The sensitivity of flowline models of tidewater glaciers to parameter uncertainty, *The Cryosphere*, 7, 1579–1590, 2013b.
- Enderlin, E. M., Howat, I. M., Jeong, S., Noh, M.-J., Angelen, J. H., and Broeke, M. R.: An improved mass budget for the Greenland ice sheet, *Geophysical Research Letters*, 41, 866–872, 2014.
- Feldmann, J., Albrecht, T., Khroulev, C., Pattyn, F., and Levermann, A.: Resolution-dependent performance of grounding line motion in a shallow model compared with a full-Stokes model according to the MISMIP3d intercomparison, *Journal of Glaciology*, 60, 353–360, 2014.
- Fowler, A.: Weertman, Lliboutry and the development of sliding theory, *Journal of Glaciology*, 56, 2010.
- Franco, B., Fettweis, X., Lang, C., and Erpicum, M.: Impact of spatial resolution on the modelling of the Greenland ice sheet surface mass balance between 1990–2010, using the regional climate model MAR, *The Cryosphere*, 6, 695–711, 2012.

Fretwell, P., Pritchard, H. D., Vaughan, D. G., Bamber, J. L., Barrand, N. E., Bell, R., Bianchi, C., Bingham, R. G., Blankenship, D. D., Casassa, G., Catania, G., Callens, D., Conway, H., Cook, A. J., Corr, H. F. J., Damaske, D., Damm, V., Ferraccioli, F., Forsberg, R., Fujita, S., Gim, Y., Gogineni, P., Griggs, J. A., Hindmarsh, R. C. A., Holmlund, P., Holt, J. W., Jacobel, R. W., Jenkins, A., Jokatz, W., Jordan, T., King, E. C., Kohler, J., Krabill, W., Riger-Kusk, M., Langley, K. A., Leitchenkov, G., Leuschen, C., Luyendyk, B. P., Matsuoka, K., Mouginot, J., Nitsche, F. O., Nogi, Y., Nost, O. A., Popov, S. V., Rignot, E., Rippon, D. M., Rivera, A., Roberts, J., Ross, N., Siegert, M. J., Smith, A. M., Steinhage, D., Studinger, M., Sun, B., Tinto, B. K., Welch, B. C., Wilson, D., Young, D. A., Xiangbin, C., and Zirizzotti, A.: Bedmap2: improved ice bed, surface and thickness datasets for Antarctica, *The Cryosphere*, 7, 375–393, doi:10.5194/tc-7-375-2013, , 2013.

Fulton, R.: Surficial Materials Map of Canada, Natural Resources Canada, Ottawa, Canada, 1995.

Ganopolski, A. and Calov, R.: Simulation of glacial cycles with an Earth system model, in: *Climate Change*, pp. 49–55, Springer, 2012.

Gardner, A. S., Sharp, M. J., Koerner, R. M., Labine, C., Boon, S., Marshall, S. J., Burgess, D. O., and Lewis, D.: Near-surface temperature lapse rates over Arctic glaciers and their implications for temperature downscaling, *Journal of Climate*, 22, 4281–4298, 2009.

Giorgi, F., Francisco, R., and Pal, J.: Effects of a subgrid-scale topography and land use scheme on the simulation of surface climate and hydrology. Part I: Effects of temperature and water vapor disaggregation, *Journal of Hydrometeorology*, 4, 317–333, 2003.

Gladstone, R. M., Payne, A. J., and Cornford, S. L.: Resolution requirements for grounding-line modelling: sensitivity to basal drag and ice-shelf buttressing, *Annals of glaciology*, 53, 97–105, 2012.

Goldberg, D., Holland, D., and Schoof, C.: Grounding line movement and ice shelf buttressing in marine ice sheets, *Journal of Geophysical Research: Earth Surface*, 114, 2009.

Greve, R. and Hutter, K.: Polythermal three-dimensional modelling of the Greenland ice sheet with varied geothermal heat flux, *Annals of Glaciology*, 21, 8–12, 1995.

Gudmundsson, G., Krug, J., Durand, G., Favier, L., and Gagliardini, O.: The stability of grounding lines on retrograde slopes, *The Cryosphere*, 6, 1497–1505, 2012.

Guo, W., Wang, C., Zeng, X., Ma, T., and Yang, H.: Subgrid parameterization of the soil moisture storage capacity for a distributed rainfall-runoff model, *Water*, 7, 2691–2706, 2015.

Hebeler, F., Purves, R. S., and Jamieson, S. S.: The impact of parametric uncertainty and topographic error in ice-sheet modelling, *Journal of Glaciology*, 54, 899–919, 2008.

Hindmarsh, R. C. and Le Meur, E.: Dynamical processes involved in the retreat of marine ice sheets, *Journal of Glaciology*, 47, 271–282, 2001.

Hirsch, P. E., Schillinger, S., Weigt, H., and Burkhardt-Holm, P.: A Hydro-Economic Model for Water Level Fluctuations: Combining Limnology with Economics for Sustainable Development of Hydropower, *PLoS one*, 9, e114889, 2014.

- Hock, R.: Temperature index melt modelling in mountain areas, *Journal of Hydrology*, 282, 104–115, 2003.
- Hock, R.: Glacier melt: a review of processes and their modelling, *Progress in physical geography*, 29, 362–391, 2005.
- Holland, P.: Climate change: Warm bath for an ice sheet, *Nature Geoscience*, 3, 147–148, 2010.
- Horton, B. P., Rahmstorf, S., Engelhart, S. E., and Kemp, A. C.: Expert assessment of sea-level rise by AD 2100 and AD 2300, *Quaternary Science Reviews*, 84, 1–6, 2014.
- Hughes, T.: The Jakobshavn Effect, *Geophysical Research Letters*, 13, 46–48, 1986.
- Huybrechts, P.: Report of the third EISMINT workshop on model intercomparison, European Science Foundation (Strasbourg), 1998.
- Huybrechts, P., Letreguilly, A., and Reeh, N.: The Greenland ice sheet and greenhouse warming, *Palaeogeography, Palaeoclimatology, Palaeoecology*, 89, 399–412, 1991.
- Ingólfsson, Ó., Benediktsson, Í. Ö., Schomacker, A., Kjær, K. H., Brynjólfsson, S., Jónsson, S. A., Korsgaard, N. J., and Johnson, M. D.: Glacial geological studies of surge-type glaciers in Iceland—Research status and future challenges, *Earth-Science Reviews*, 2015.
- Iverson, N. R., Hooyer, T. S., and Baker, R. V.: Ring-shear studies of till deformation: Coulomb-plastic behavior and distributed strain in glacier beds, *Journal of Glaciology*, 44, 634–642, 1998.
- Jacobs, S., MacAyeal, D., and Ardai Jr, J.: The recent advance of the Ross Ice Shelf, Antarctica, *J. Glaciol*, 32, 464–474, 1986.
- Jamieson, S. S., Vieli, A., Livingstone, S. J., Cofaigh, C. Ó., Stokes, C., Hillenbrand, C.-D., and Dowdeswell, J. A.: Ice-stream stability on a reverse bed slope, *Nature Geoscience*, 5, 799–802, 2012.
- Janssens, I. and Huybrechts, P.: The treatment of meltwater retention in mass-balance parameterizations of the Greenland ice sheet, *Annals of Glaciology*, 31, 133–140, 2000.
- Jarosch, A. H., Anslow, F. S., and Clarke, G. K.: High-resolution precipitation and temperature downscaling for glacier models, *Climate dynamics*, 38, 391–409, 2012.
- Jenkins, A.: Convection-driven melting near the grounding lines of ice shelves and tidewater glaciers, *Journal of Physical Oceanography*, 41, 2279–2294, 2011.
- Johannesson, T., Sigurdsson, O., Laumann, T., and Kennett, M.: Degree-day glacier mass-balance modelling with applications to glaciers in Iceland, Norway and Greenland, *Journal of Glaciology*, 41, 345–358, 1995.
- Josenhans, H. and Zevenhuizen, J.: Dynamics of the Laurentide ice sheet in Hudson Bay, Canada, *Marine Geology*, 92, 1–26, 1990.

Joughin, I., Smith, B. E., and Medley, B.: Marine Ice Sheet Collapse Potentially Under Way for the Thwaites Glacier Basin, West Antarctica, *Science*, 344, 735–738, 2014.

Kalnay, E., Kanamitsu, M., Kistler, R., Collins, W., Deaven, D., Gandin, L., Iredell, M., Saha, S., White, G., Woollen, J., Zhu, Y., Leetmaa, A., Reynolds, R., Chelliah, M., Ebisuzaki, W. and Higgins, W., Janowiak, J., Mo, K. C., Ropelewski, C., Wang, J., Jenne, R., and Joseph, D.: The NCEP/NCAR 40-year reanalysis project, *Bulletin of the American Meteorological Society*, 77, 437–471, 1996.

Ke, Y., Leung, L., Huang, M., and Li, H.: Enhancing the representation of subgrid land surface characteristics in land surface models, *Geoscientific Model Development*, 6, 1609–1622, 2013.

Lambrecht, A. and Mayer, C.: Temporal variability of the non-steady contribution from glaciers to water discharge in western Austria, *Journal of hydrology*, 376, 353–361, 2009.

Larour, E., Seroussi, H., Morlighem, M., and Rignot, E.: Continental scale, high order, high spatial resolution, ice sheet modeling using the Ice Sheet System Model (ISSM), *Journal of Geophysical Research*, 117, F01022, doi:10.1029/2011JF002140, 2012.

Laske, G. and Masters, G.: A global digital map of sediment thickness, *Eos Trans. AGU*, 78, F483, 1997.

Lazzara, M., Jezek, K., Scambos, T., MacAyeal, D., and Van der Veen, C.: On the recent calving of icebergs from the Ross Ice Shelf, *Polar Geography*, 23, 201–212, 1999.

Le Morzadec, K., Tarasov, L., Morlighem, M., and Seroussi, H.: A new sub-grid surface mass balance and flux model for continental-scale ice sheet modelling: testing and last glacial cycle, *Geoscientific Model Development*, 8, 3199–3213, 2015.

Lemke, P., Ren, J., Alley, R. B., Allison, I., Carrasco, J., Flato, G., Fujii, Y., Kaser, G., Mote, P., Thomas, R. H., et al.: Observations: changes in snow, ice and frozen ground., Titel: *Climate change 2007: the physical science basis; summary for policymakers, technical summary and frequently asked questions. Part of the Working Group I contribution to the Fourth Assessment Report of the Intergovernmental Panel on Climate Change*, pp. 337–383, 2007.

Letrégouilly, A., Reeh, N., and Huybrechts, P.: The Greenland ice sheet through the last glacial-interglacial cycle, *Palaeogeography, Palaeoclimatology, Palaeoecology*, 90, 385–394, 1991.

Leung, L. R. and Ghan, S.: A subgrid parameterization of orographic precipitation, *Theoretical and applied climatology*, 52, 95–118, 1995.

Levermann, A., Albrecht, T., Winkelmann, R., Martin, M., Haseloff, M., and Joughin, I.: Kinematic first-order calving law implies potential for abrupt ice-shelf retreat, *The Cryosphere Discussions*, 5, 2699–2722, 2011.

Li, X., Sun, B., Siegert, M. J., Bingham, R. G., Tang, X., Zhang, D., Cui, X., and Zhang, X.: Characterization of subglacial landscapes by a two-parameter roughness index, *Journal of Glaciology*, 56, 831–836, 2010.

- Lliboutry, L.: Contribution à la théorie du frottement du glacier sur son lit, *Comptes Rendus Hebdomadaires des Seances de l'Academie des Sciences*, 247, 318–320, 1958.
- Luckman, A., Murray, T., De Lange, R., and Hanna, E.: Rapid and synchronous ice-dynamic changes in East Greenland, *Geophysical Research Letters*, 33, 2006.
- Ma, Y., Gagliardini, O., Ritz, C., Gillet-Chaulet, F., Durand, G., and Montagnat, M.: Enhancement factors for grounded ice and ice shelves inferred from an anisotropic ice-flow model, *Journal of Glaciology*, 56, 805–812, 2010.
- MacAyeal, D.: Large-scale ice flow over a viscous basal sediment- Theory and application to ice stream B, Antarctica, *Journal of Geophysical Research*, 94, 4071–4087, 1989.
- MacAyeal, D., Abbot, D., and Sergienko, O.: Iceberg-capsize tsunamigenesis, *Annals of Glaciology*, 52, 51, 2011.
- Marshall, S.: Modelled nucleation centres of the Pleistocene ice sheets from an ice sheet model with subgrid topographic and glaciologic parameterizations, *Quaternary International*, 95, 125–137, 2002.
- Marshall, S. and Clarke, G.: Ice sheet inception: subgrid hypsometric parameterization of mass balance in an ice sheet model, *Climate Dynamics*, 15, 533–550, 1999.
- Marshall, S. and Oglesby, R.: An improved snow hydrology for GCMs. Part 1: Snow cover fraction, albedo, grain size, and age, *Climate Dynamics*, 10, 21–37, 1994.
- Marshall, S. J. and Losic, M.: Temperature lapse rates in glacierized basins, in: *Encyclopedia of Snow, Ice and Glaciers*, pp. 1145–1150, Springer, 2011.
- Marshall, S. J., White, E. C., Demuth, M. N., Bolch, T., Wheate, R., Menounos, B., Beedle, M. J., and Shea, J. M.: Glacier water resources on the eastern slopes of the Canadian Rocky Mountains, *Canadian Water Resources Journal*, 36, 109–134, 2011.
- McFadden, E. M., Howat, I. M., Joughin, I., Smith, B. E., and Ahn, Y.: Changes in the dynamics of marine terminating outlet glaciers in west Greenland (2000–2009), *Journal of Geophysical Research: Earth Surface* (2003–2012), 116, 2011.
- Meier, M. and Post, A.: Fast tidewater glaciers, *Journal of Geophysical Research: Solid Earth* (1978–2012), 92, 9051–9058, 1987.
- Moon, T., Joughin, I., and Smith, B.: Seasonal to multi-year variability of glacier surface velocity, terminus position, and sea ice/ice mélange in northwest Greenland, *Journal of Geophysical Research: Earth Surface*, 2015.
- Morlighem, M., Rignot, E., Mouginot, J., Seroussi, H., and Larour, E.: Deeply incised submarine glacial valleys beneath the Greenland ice sheet, *Nature Geoscience*, 7, 2014.
- Motyka, R., Hunter, L., Echelmeyer, K., and Connor, C.: Submarine melting at the terminus of a temperate tidewater glacier, LeConte Glacier, Alaska, USA, *Annals of Glaciology*, 36, 57–65, 2003.

- Motyka, R. J., Beget, J., and Bowen, P.: Recent retreat of LeConte Glacier and associated calving and iceberg hazards, State of Alaska, Dept. of Natural Resources, Division of Geological and Geophysical Surveys, p. 9, 1998.
- Motyka, R. J., Truffer, M., Fahnestock, M., Mortensen, J., Rysgaard, S., and Howat, I.: Submarine melting of the 1985 Jakobshavn Isbræ floating tongue and the triggering of the current retreat, *Journal of Geophysical Research: Earth Surface* (2003–2012), 116, 2011.
- Neumann, B., Vafeidis, A. T., Zimmermann, J., and Nicholls, R. J.: Future coastal population growth and exposure to sea-level rise and coastal flooding—a global assessment, *PloS one*, 10, e0118571, 2015.
- Nijzink, R. C. and Savenije, H. H.: The importance of topography-controlled sub-grid process heterogeneity and semi-quantitative prior constraints in distributed hydrological models, *Hydrology and Earth System Sciences*, 20, 1151, 2016.
- Nowicki, S., Bindschadler, R. A., Abe-Ouchi, A., Aschwanden, A., Bueller, E., Choi, H., Fastook, J., Granzow, G., Greve, R., Gutowski, G., et al.: Insights into spatial sensitivities of ice mass response to environmental change from the SeaRISE ice sheet modeling project II: Greenland, *Journal of Geophysical Research: Earth Surface*, 118, 1025–1044, 2013.
- O’Leary, M. and Christoffersen, P.: Calving on tidewater glaciers amplified by submarine frontal melting, *The Cryosphere*, 7, 119–128, 2013.
- Parry, M. L., Canziani, O. F., and Palutikof, J.: *Climate Change 2007: impacts, adaptation and vulnerability: contribution of Working Group II to the fourth assessment report of the Intergovernmental Panel on Climate Change*, Cambridge Univ Pr, 2007.
- Pattyn, F., Perichon, L., Aschwanden, A., Breuer, B., De Smedt, B., Gagliardini, O., Gudmundsson, G. H., Hindmarsh, R., Hubbard, A., Johnson, J. V., et al.: Benchmark experiments for higher-order and full Stokes ice sheet models (ISMIP-HOM), *The Cryosphere Discussions*, 2, 111–151, 2008.
- Pattyn, F., Schoof, C., Perichon, L., Hindmarsh, R., Bueller, E., Fleurian, B. d., Durand, G., Gagliardini, O., Gladstone, R., Goldberg, D., et al.: Results of the marine ice sheet model intercomparison project, MISIP, *The Cryosphere Discussions*, 6, 267–308, 2012.
- Pattyn, F., Perichon, L., Durand, G., Favier, L., Gagliardini, O., Hindmarsh, R. C., Zwinger, T., Albrecht, T., Cornford, S., Docquier, D., et al.: Grounding-line migration in plan-view marine ice-sheet models: results of the ice2sea MIMIP3d intercomparison, *Journal of Glaciology*, 59, 410–422, 2013.
- Payne, A. and Sugden, D.: Topography and ice sheet growth, *Earth Surface Processes and Landforms*, 15, 625–639, 1990.
- Payne, A., Huybrechts, P., Abe-Ouchi, A., Calov, R., Fastook, J., Greve, R., Marshall, S., Marsiat, I., Ritz, C., Tarasov, L., and Thomassen, M. P. A.: Results from the EISMINT model intercomparison: the effects of thermomechanical coupling, *Journal of Glaciology*, 46, 227–238, 2000.

- Pelto, M. and Warren, C.: Relationship between tidewater glacier calving velocity and water depth at the calving front, *Annals of glaciology*, 15, 115–118, 1991.
- Phillips, E., Lee, J. R., and Burke, H.: Progressive proglacial to subglacial deformation and syntectonic sedimentation at the margins of the Mid-Pleistocene British Ice Sheet: evidence from north Norfolk, UK, *Quaternary Science Reviews*, 27, 1848–1871, 2008.
- Pollack, H. N., Hurter, S. J., and Johnson, J. R.: Heat flow from the Earth's interior: Analysis of the global data set, *Rev. Geophys.*, 31, 267–280, 1993.
- Pollard, D.: Some ice-age aspects of a calving ice-sheet model, in: *Milankovitch and Climate: Understanding the Response to Astronomical Forcing*, p. 541, 1984.
- Pollard, D. and DeConto, R.: Modelling West Antarctic ice sheet growth and collapse through the past five million years, *Nature*, 458, 329–332, 2009.
- Pollard, D. and DeConto, R.: Description of a hybrid ice sheet-shelf model, and application to Antarctica, *Geoscientific Model Development*, 5, 1273–1295, 2012.
- Pollard, D., Chang, W., Haran, M., Applegate, P., and DeConto, R.: Large ensemble modeling of last deglacial retreat of the West Antarctic Ice Sheet: comparison of simple and advanced statistical techniques, *Geoscientific Model Development Discussions*, 8, 9925–9963, 2015.
- Rignot, E. and Kanagaratnam, P.: Changes in the velocity structure of the Greenland Ice Sheet, *Science*, 311, 986, 2006.
- Rignot, E. and Mouginot, J.: Ice flow in Greenland for the international polar year 2008–2009, *Geophysical Research Letters*, 39, 2012.
- Rignot, E., Koppes, M., and Velicogna, I.: Rapid submarine melting of the calving faces of West Greenland glaciers, *Nature Geoscience*, 3, 187–191, 2010.
- Rignot, E., Jacobs, S., Mouginot, J., and Scheuchl, B.: Ice-shelf melting around Antarctica, *Science*, 341, 266–270, 2013.
- Rind, D., Peteet, D., and Kukla, G.: Can Milankovitch orbital variations initiate the growth of ice sheets in a general circulation model?, *Journal of Geophysical Research-Atmospheres*, 94, 1989.
- Rosenau, R., Schwalbe, E., Maas, H.-G., Baessler, M., and Dietrich, R.: Grounding line migration and high-resolution calving dynamics of Jakobshavn Isbræ, West Greenland, *Journal of Geophysical Research: Earth Surface*, 118, 382–395, 2013.
- Rutt, I., Hagdorn, M., Hulton, N., and Payne, A.: The Glimmer community ice sheet model, *J. Geophys. Res.*, 114, 1–22, 2009.
- Schoof, C.: Ice sheet grounding line dynamics: Steady states, stability, and hysteresis, *J. Geophys. Res.*, 112, 2007.

- Schrama, E., Wouters, B., Rietbroek, R., and van de Wal, W.: Mass contribution of ice sheets and land glaciers to sea level rise, in: EGU General Assembly Conference Abstracts, vol. 16, p. 5688, 2014.
- Sciascia, R., Straneo, F., Cenedese, C., and Heimbach, P.: Seasonal variability of submarine melt rate and circulation in an East Greenland fjord, *Journal of Geophysical Research: Oceans*, 118, 2492–2506, 2013.
- Seguinot, J., Khroulev, C., Rogozhina, I., Stroeven, A. P., and Zhang, Q.: The effect of climate forcing on numerical simulations of the Cordilleran ice sheet at the Last Glacial Maximum, *The Cryosphere*, 8, 1087–1103, 2014.
- Seth, A., Giorgi, F., and Dickinson, R. E.: Simulating fluxes from heterogeneous land surfaces: explicit subgrid method employing the biosphere-atmosphere transfer scheme (BATS), *Journal of Geophysical Research*, 99, 18 651–18 667, 1994.
- Shea, J. M., Moore, R. D., and Stahl, K.: Derivation of melt factors from glacier mass-balance records in western Canada, *Journal of Glaciology*, 55, 123–130, 2009.
- Stouffer, R. J., Yin, J., Gregory, J., Dixon, K., Spelman, M., Hurlin, W., Weaver, A., Eby, M., Flato, G., Hasumi, H., et al.: Investigating the causes of the response of the thermohaline circulation to past and future climate changes, *Journal of Climate*, 19, 1365–1387, 2006.
- Straneo, F., Curry, R., Sutherland, D., Hamilton, G., Cenedese, C., Våge, K., and Stearns, L.: Impact of fjord dynamics and glacial runoff on the circulation near Helheim Glacier, *Nature Geoscience*, 2011.
- Stroeven, A. P.: Numerical simulations of the Cordilleran ice sheet through the last glacial cycle, *The Cryosphere*, 10, 639, 2016.
- Tangborn, W.: Mass balance, runoff and surges of Bering Glacier, Alaska, *The Cryosphere*, 7, 867–875, 2013.
- Tarasov, L. and Peltier, W.: Impact of thermomechanical ice sheet coupling on a model of the 100 kyr ice age cycle, *Journal Of Geophysical Research-Atmospheres*, 104, 9517–9545, 1999a.
- Tarasov, L. and Peltier, W.: Greenland glacial history and local geodynamic consequences, *Geophysical Journal International*, 150, 198–229, 2002.
- Tarasov, L. and Peltier, W.: Greenland glacial history, borehole constraints, and Eemian extent, *J. geophys. Res.*, 108, 2143, doi:10.1029/2001JB001731, 2003.
- Tarasov, L. and Peltier, W.: A geophysically constrained large ensemble analysis of the deglacial history of the North American ice-sheet complex, *Quaternary Science Reviews*, 23, 359–388, 2004a.
- Tarasov, L. and Peltier, W.: Arctic freshwater forcing of the Younger Dryas cold reversal, *Nature*, 435, 662–665, 2005.

- Tarasov, L. and Peltier, W.: A calibrated deglacial drainage chronology for the North American continent: evidence of an Arctic trigger for the Younger Dryas, *Quaternary Science Reviews*, 25, 659–688, 2006.
- Tarasov, L. and Peltier, W.: Coevolution of continental ice cover and permafrost extent over the last glacial-interglacial cycle in North America, *Journal of Geophysical Research*, 112, F02S08, doi:10.1029/2006JF000661, 2007.
- Tarasov, L. and Peltier, W. R.: Terminating the 100 kyr Ice Age cycle, *J. Geophys. Res.*, 102, 21 665–21 693, 1997a.
- Tarasov, L. and Peltier, W. R.: A high-resolution model of the 100 kyr Ice Age cycle, *Ann. Glaciol.*, 25, 58–65, 1997b.
- Tarasov, L. and Peltier, W. R.: Impact of thermomechanical ice sheet coupling on a model of the 100 kyr ice age cycle, *J. Geophys. Res.*, 104, 9517–9545, 1999b.
- Tarasov, L. and Peltier, W. R.: A geophysically constrained large ensemble analysis of the deglacial history of the North American ice sheet complex, *Quat. Sci. Rev.*, 23, 359–388, 2004b.
- Tarasov, L., Dyke, A. S., Neal, R. M., and Peltier, W.: A data-calibrated distribution of deglacial chronologies for the North American ice complex from glaciological modeling, *Earth and Planetary Science Letters*, 315, 30–40, 2012.
- Turner, J. K. J.: *Antarctic meteorology and climatology*, 1997.
- Van den Berg, J., Van de Wal, R., and Oerlemans, J.: Effects of spatial discretization in ice-sheet modelling using the shallow-ice approximation, *Journal of Glaciology*, 52, 89–98, 2006.
- Van Den Broeke, M., Bamber, J., Ettema, J., Rignot, E., Schrama, E., Van de Berg, W., Van Meijgaard, E., Velicogna, I., and Wouters, B.: Partitioning recent Greenland mass loss, *Science*, 326, 984, 2009.
- Van der Veen, C.: Calving glaciers, *Progress in Physical Geography*, 26, 96, 2002.
- Verbitsky, M. and Oglesby, R.: The effect of atmospheric carbon dioxide concentration on continental glaciation of the Northern Hemisphere, *Journal of Geophysical Research-Atmospheres*, 97, 1992.
- Vieli, A. and Payne, A.: Assessing the ability of numerical ice sheet models to simulate grounding line migration., *Journal of Geophysical Research: Earth Surface*, 110, F01 003, 2005.
- Vieli, A., Funk, M., and Blatter, H.: Flow dynamics of tidewater glaciers: a numerical modelling approach, *Journal of Glaciology*, 47, 595–606, 2001.
- Walland, David J.; Simmonds, I.: Sub-Grid Topography and the Simulation of Northern Hemisphere Snow Cover, *International Journal of Climatology*, 16, 961–982, 1996.

- Weertman, J.: On the sliding of glaciers, *Journal of Glaciology*, 3, 33–38, 1957.
- Weertman, J.: Stability of the junction of an ice sheet and an ice shelf, *Journal of Glaciology*, 13, 3–11, 1974.
- Wilby, R. L. and Wigley, T.: Downscaling general circulation model output: a review of methods and limitations, *Progress in Physical Geography*, 21, 530–548, 1997.
- Winkelmann, R., Martin, M., Haseloff, M., Albrecht, T., Bueller, E., Khroulev, C., and Levermann, A.: The Potsdam Parallel Ice Sheet Model (PISM-PIK)–Part 1: Model description, *The Cryosphere*, 5, 715–726, 2011.
- World Data Center-A for Paleoclimatology, National Geophysical Data Center, B.: The Greenland Summit Ice Cores CD-ROM, CD-ROM, 1997.
- Xu, C.: From GCMs to river flow: a review of downscaling methods and hydrologic modelling approaches, *Progress in Physical Geography*, 23, 229, 1999.
- Xu, Y., Rignot, E., Menemenlis, D., and Koppes, M.: Numerical experiments on subaqueous melting of Greenland tidewater glaciers in response to ocean warming and enhanced subglacial discharge, *Annals of Glaciology*, 53, 229–234, 2012.